DoE/DP/40070-1

FLUID MECHANICS OF FUSION LASERS

FINAL REPORT

For The Period

11 September 1978 - 5 June 1980

J. Shwartz, V. A. Kulkarny, D. A. Ausherman,
H. H. Legner* and B. Sturtevant**

TRW
Systems and Energy
One Space Park
Redondo Beach, CA 90278

Prepared For The
Department of Energy
Nevada Operations Office
Under Contract DE-AC08-78DP 40070

*Dr. H. Legner is currently with Physical Sciences Inc., Woburn, Mass. 01801

**Professor B. Sturtevant, of Caltech, is a TRW Consultant

DISCLAIMER

The following pages are an exact representation of what is in the original document folder.

NOTICE

Printed in the United States of America

Available from:

National Technical Information Service
U.S. Department of Commerce
5285 Port Royal Road
Springfield, Virginia 22161

Price: Printed Copy $_____
Microfiche $3.00

2

ABSTRACT

Flow loop components required to operate continuous-flow, repetitively-pulsed CO_2 and KrF laser drivers for ICF were identified and their performance requirements were specified. It was found that the laser flow loops can have a major effect on the laser beam quality and overall efficiency. The pressure wave suppressor was identified as the most critical flow loop component. The performance of vented side-wall suppressors was evaluated both analytically and experimentally and found capable of meeting the performance requirements of the CO_2 and KrF fusion lasers. All other laser flow loop components are essentially similar to those used in conventional, low speed wind tunnels and are therefore well characterized and can be readily incorporated into fusion laser flow system designs.

CONTENTS

1. INTRODUCTION

The general objective of this program was to study the problems of developing flow systems for repetitively pulsed gaseous lasers which can meet the requirements of laser-driven ICF power generation. More specifically, the objective was to identify the most critical elements of such flow systems, to determine if existing state-of-the-art technologies and components can be used, and to initiate the development of those elements for which presently available solutions are found to be inadequate. Another objective was to compare the different candidate laser drivers for ICF power generation on the basis of their flow system requirements and the technical risks and difficulties involved in meeting such requirements.

The lasers considered under this program are primarily the CO_2 and KrF lasers. The most important requirements imposed on the flow systems of these and similar lasers, based on laser-fusion systems considerations are:

a. that they produce a uniform flow in the cavity, with a high degree of media homogeneity just prior to the lasing pulse so that the laser beam can be focused onto small fusion targets; and

b. that the power required to regenerate and recirculate the gas through the cavity be minimized.

The media homogeneity in the cavity, prior to each lasing pulse, will be affected mainly by cavity inlet flow conditions (i.e., the density uniformity of the cavity feed gas) and by the pressure waves produced in the cavity subsequent to each lasing pulse.

The power required to regenerate and recirculate the gas will depend on the type and extent of chemical and thermal regeneration which is required for any specific laser system, and it will depend also on the pumping power required to flow and recirculate the gas through the laser system. The latter is determined to a large extent by the overall pressure drop in the flow system.

The design of low-pressure-drop recirculating flow systems is a standard practice in wind tunnel technology. Flow-conditioners are also used in wind tunnels when a highly uniform flow is required in the test sections. Such technologies can be readily adapted to the recirculating flow system of a repetitively pulsed fusion laser.

The subject of pressure wave attenuation in repetitively pulsed gaseous lasers has recently received considerable attention under several DoD-funded pulsed laser programs. At least some of the concepts and techniques of pressure wave attenuation, developed for DoD applications, should be useful also for fusion lasers. There are, however, some differences: The repetitively pulsed CO_2 and chemical lasers being developed for DoD utilize an open-loop, high-pressure-drop gas feed system, most often in the form of a choked feed plate, which effectively isolates the fresh incoming gas (which is upstream of the cavity) from the spent gas and the pressure reverberations in the cavity. Such large pressure drops are clearly unacceptable for fusion lasers, where flow efficiency is of primary importance. Low-pressure-drop, closed-loop flow systems are required in the DoD pulsed UV & visible laser programs. However, here too there are differences between the DoD and the fusion laser requirements. The pressure drop and flow efficiency requirements will be more stringent in a fusion laser, whereas in the DoD-type lasers there will be more emphasis on media homogeneity and beam quality.

The simultaneous requirements for entrance flow conditioning and acoustic wave suppression in a low-pressure-drop recirculating flow system thus represent the major challenge. The present program was designed to address this challenge by developing an analytical and experimental base which can be used in the design of fusion laser flow systems which can meet these requirements.

Simplified analytical models, presented in Section 2, were used to establish the design and performance requirements for flow systems of repetitively pulsed fusion lasers. The requirements on lasing-media uniformity are derived from the beam quality considerations. The requirements on flow efficiency are based on estimates of overall target gains and other system efficiencies.

The need for gas temperature control, to small fractions of 1°C, was identified as an important technical problem, but no attempt has been made so far to specify techniques and devices which can be used to meet this requirement.

The problem of pressure wave suppression, particularly upstream of the laser cavity and under small-pressure-drop conditions, is addressed in Section 3. Our major effort in this area was toward the development of an experimental facility which can simulate the pressure waves generated in pulsed lasers. So far we have used this facility mainly to help upgrade and validate a code which can be used to analyze pressure wave propagation and decay in the presence of various pressure wave suppression devices. The experiments have also been used to highlight potential problems associated with one particular pressure suppression device (the vented side-wall absorber, see Section 3.1).

Along with the experimental effort we have continued the development of our analytical capabilities in modeling pressure wave suppression processes and devices. Recent code modifications and comparisons of code predictions on experimental results are presented in Section 3.2.

2. FLOW SYSTEM STUDIES

2.1 GENERAL CONSIDERATIONS FOR FUSION LASER FLOW SYSTEMS

The fusion laser flow system can be viewed as a conventional wind tunnel with the laser cavity replacing the test section. The flow system design must reflect the requirements imposed on the laser as a reactor driver. The beam generated by this laser will have to be focused down onto a small target, typically of the order of 1 mm. This requirement places restrictions on the density nonuniformities in the cavity just prior to initiation. The flow system thus must deliver a highly uniform gas to the laser cavity. It must also be efficient; namely, the power required to generate the continuous and uniform flow must not be large compared to the average power extracted from the laser. The analysis of these two key aspects of flow system requirements is presented in subsection 2.1.1.

The heat and overpressure generated in the cavity of a pulsed laser is a major source of flow nonuniformities. These overpressures must be suppressed to some predetermined level (dictated by the beam quality requirements), on a time scale that is shorter than the pulse interval and without undue cost to the flow system pressure drop and flow recirculation power. Meeting the beam quality and flow efficiency requirements will depend critically on our ability to develop the necessary pressure wave suppression techniques and devices. The status of pulsed laser pressure wave suppression is briefly reviewed in subsection 2.1.2, and the special requirements and problems anticipated in fusion-type lasers are emphasized.

There are additional problems associated with recirculating fusion laser flow systems that could severely limit the ability to attain the required operating conditions. The two flow features that will probably require careful consideration are the temperature uniformity requirement -- which is quite formidable for large fusion laser systems -- and the control of flow nonuniformities produced by flow separation, flow turning, and the nonsteady energy addition. These are briefly reviewed in subsection 2.1.3.

2.1.1 Flow System Requirements

Figure 2-1 illustrates the basic configuration and essential components of a fusion laser final amplifier. The cavity configuration assumed for this study is shown in Figure 2-2. The major laser parameters, which will affect the design and performance of the flow system, are indicated on this figure. As far as the flow system is concerned, the laser performance can be characterized by three nondimensional parameters: the extracted energy density, S (expressed, e.g., in J/lit-atm or similar dimensionless form), the beam quality, BQ (to be defined below) and the pulse repetition frequency (PRF). The subsystem used for laser excitation or initiation (be it on e-beam, a discharge or a photolytic source), is characterized for our purposes by the power consumed by this system, P_I. Similarly, the flow system is characterized mainly by the power it takes to drive the compressor, P_F, and the flow Mach No. in the cavity, M. The lasing media itself is characterized by the gas properties in the cavity (pressure, temperature, molecular weight, ratio of specific heats, γ, and index of refraction, η or β), and by the sensible heat, ΔQ, which develops in the cavity after laser excitation and pulse extraction.

2.1.1.1 Beam Quality and Media Homogeneity

Beam Quality

For the purpose of this study, the beam quality is defined as

$$BQ \quad \frac{d_{min} D}{2 \lambda F} \qquad (1)$$

where λ is the laser wavelength, F is the focal length of the focusing mirror, D is the characteristic size of the laser beam aperture in the near field and d_{min} is the minimum spot size which can be obtained in the far field (or focal plane) that contains 90% of the beam power and energy.

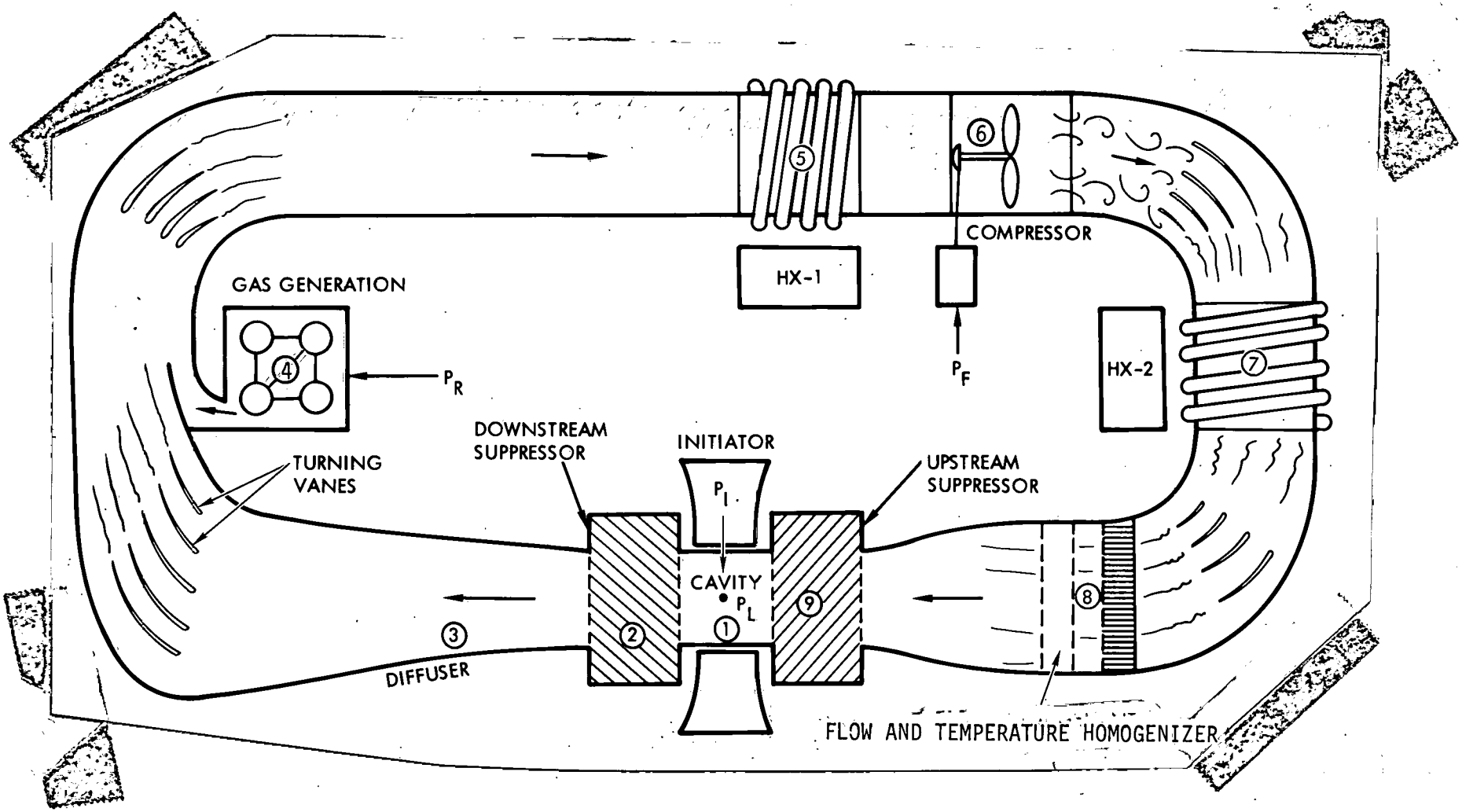

Figure 2-1. Schematic of a Fusion Laser Flow System

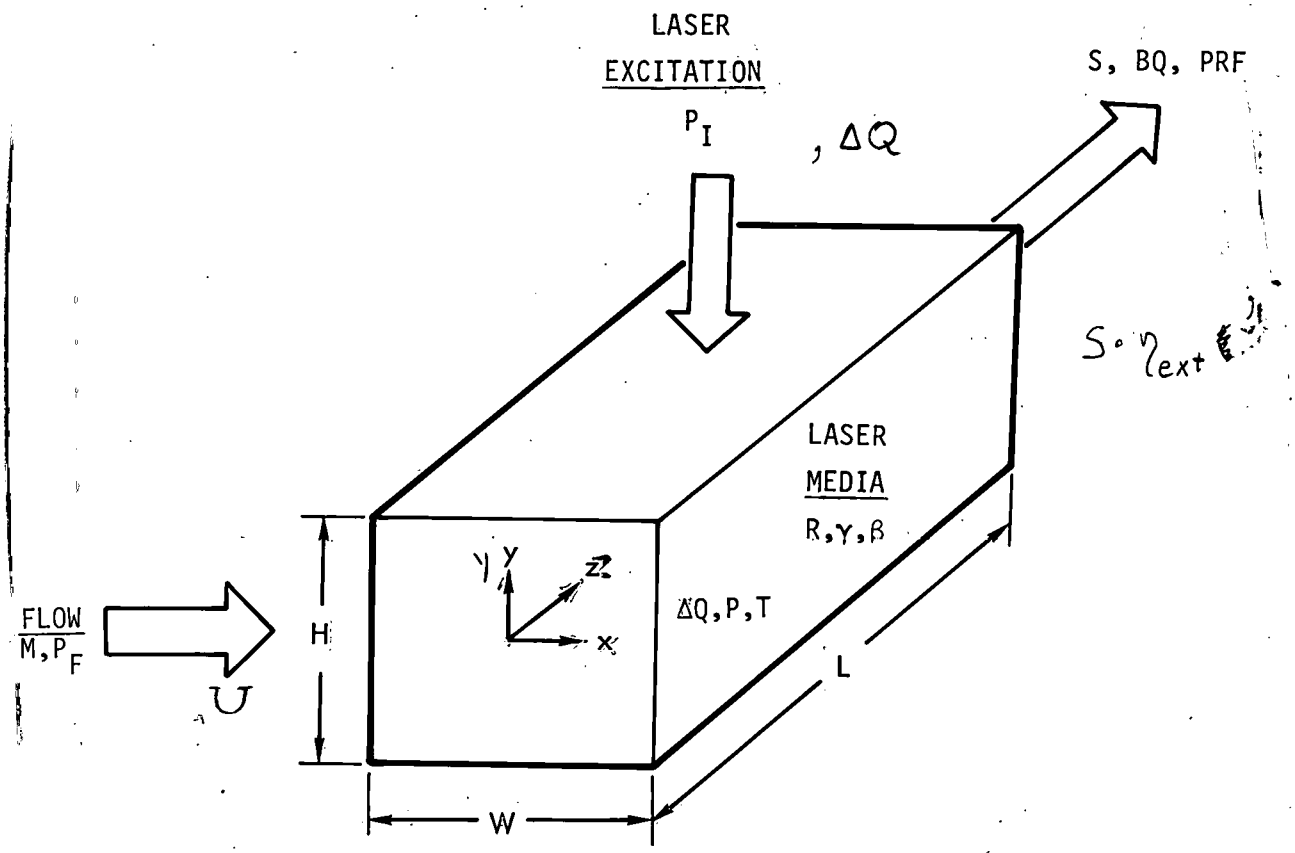

Figure 2-2. Schematic of a Laser Cavity

The focused beam spot size, d_{min}, should be equal to or smaller than the fusion target, which is typically assumed to be of the order of 1 mm. For an ideal diffraction-limited beam, which has a uniform phase and a Gaussian intensity distribution across the beam, it can be shown that the minimum spot diameter which contains 90% of the beam energy is given by

$$d_{min} = d_{dif} = \frac{1.8\,\lambda F}{D}$$

We will assume that the input beam to the final amplifier has uniform phase and a nearly uniform intensity distribution. If the amplifier medium has a perfectly uniform index of refraction, the amplified beam could be focused down to a spot diameter d_{dif}. If the index of refraction is not uniform across the amplifier, the beam exiting the amplifier will have an aberrated phase and its minimum spot diameter will be larger than d_{dif}. The minimum spot size depends both on the magnitude of these phase aberrations and on their shape or distribution across the beam aperture.

The index of refraction variations in an amplifier medium of a uniform composition (which is the only kind of medium considered in this report) are related to the density variations through

$$\Delta n = n - 1 = \beta \left(\frac{\rho}{\rho_a}\right)\left(\frac{\Delta\rho}{\rho}\right) \qquad (2)$$

where β is the Gladstone-Dale constant and ρ_a is the reference density for which β is known. The optical path difference (measured in wavelengths) for a ray traversing an amplifier of length L (refer to Figure 2-2) is given by

$$OPD\,(x,y) = \int_0^L \frac{\Delta n\, dz}{\lambda} = \frac{L}{\lambda} \langle \Delta n \rangle = \frac{L}{\lambda}\,\beta \left(\frac{\rho}{\rho_a}\right)\left\langle\left\langle \frac{\Delta\rho}{\rho} \right\rangle\right\rangle \qquad (3a)$$

and the phase difference is given by

$$\Delta\phi(x,y) = 2\pi \cdot OPD(x,y) \tag{3b}$$

We will now try to relate the amplifier density and index of refraction variations to the minimum focused spot size and beam quality. Such relationships will allow us to determine subsequently the media homogeneity requirements when the desired minimum spot size and beam quality are given.

When the phase aberrations are ordered and small (say, OPD < 0.1), diffraction analysis leads to the relationship

$$\frac{d_{min}}{d_{dif}} \approx \exp\left[\frac{1}{2}(\Delta\phi)^2_{RMS}\right], \tag{4}$$

independent of the shape and distribution of the aberrations. For random phase aberrations of a length scale Λ (e.g., such as would be created by turbulent velocity and density fluctuations in the amplifier cavity), Reference 2-1 shows that the minimum spot size is given by

$$\frac{d_{min}}{d_{dif}} \approx \exp\left[\frac{1}{2}\frac{\Lambda}{L}(\Delta\phi)^2_{RMS}\right] \tag{5a}$$

when $\Lambda < D$, and by

$$\frac{d_{min}}{d_{dif}} \approx \exp\left[\frac{1}{2}\frac{D^2}{\Lambda L}(\Delta\phi)^2_{RMS}\right] \tag{5b}$$

when $\Lambda > D$. Expressions (5a) and (5b) are valid for both small and large aberrations, independent of shape, provided they are randomly distributed.

There are no equivalent simple expressions for large but ordered phase aberrations. In such cases the shape of the aberration critically affects the minimum achievable beam quality and spot size.

A first-order estimate of the minimum focused spot diameter (or minimum blur circle) and beam quality can be obtained by using simple geometric optics considerations. Any given ordered aberration can be expressed as a Fourier series of m components, i.e.,

$$\Delta\phi(x,y) = \sum_{i=1}^{m} \Delta\phi_i \; F_i(x,y)$$

and similarly,

$$\langle\Delta n\rangle(x,y) = \sum_{i=1}^{m} \Delta n_i \; f_i(x,y)$$

The geometric beam spreading angle produced by each Fourier component of the aberration function is given approximately by

$$\theta_i(\text{geo.}) \approx \frac{4L\,\Delta n_i}{\ell_i} \tag{6}$$

where ℓ_i is the wavelength of the i^{th} component. The total spreading angle can now be expressed as

$$\theta_{TOT}^2 = \theta_{dif}^2 + \sum_{i=1}^{m} \theta_i^2(\text{geo.}) \tag{7}$$

where θ_{dif} is the spreading angle of the diffraction-limited beam given by λ/D. The minimum focused spot diameter then becomes

$$d_{min} \approx 2\left[\theta_{dif}^2 + \sum_{i=1}^{m} \theta_i^2\right]^{1/2} F = \left[1 + \sum_{i=1}^{m} \left(\frac{\theta_i}{\theta_{dif}}\right)^2\right]^{1/2} d_{dif} \tag{8}$$

and

$$BQ^2 \approx 1 + \sum_{i=1}^{m} \left(\frac{\theta_i}{\theta_{dif}}\right)^2 = 1 + \sum_{i=1}^{m} \left[\left(\frac{4L\,\Delta n_i}{\lambda}\right)\left(\frac{D}{\ell_i}\right)\right]^2 \tag{9}$$

Expressions of this form have been compared with results obtained by more rigorous methods of calculations (typically involving numerical solutions of the physical optics equations) and were found to give reasonable first-order estimates.

Equations (8) and (9) are used in this report for evaluating the effect of large ordered aberrations (OPD > 0.1) on the minimum spot size and the beam quality. Each such aberration will have to be characterized by its maximum OPD and "wavelength" ℓ (or number of cycles) across the beam aperture, D.

Media Inhomogeneities

The residual pressure fluctuations are related to the density fluctuations by the acoustic limit of the isentropic relation $p \sim \rho^{\gamma}$, i.e., for small residual fluctuations

$$\frac{\Delta\rho}{\rho_1} \approx \frac{1}{\gamma}\left(\frac{\Delta p}{p_1}\right)_r \tag{10}$$

There is, however, one other mechanism by which pressure fluctuation in the cavity can generate density inhomogeneities. If a non-isentropic flow element is located upstream of the cavity, pressure fluctuation in the cavity will imprint an entropy (temperature) and density variation on the gas entering the cavity. This variation does not decay with time even if the entropy generating pressure fluctuations do. For small pressure and entropy fluctuations it can be shown that

$$\frac{\Delta\rho}{\rho_1} \approx \frac{\gamma-1}{\gamma}\left(\frac{\Delta p}{p_1}\right)_e \tag{11}$$

Requirement (11) is roughly a factor of two or so less restrictive than the requirement for residual pressure fluctuations.

The required temperature uniformity can be obtained from the logarithmic differentiation of the ideal gas law ($p = \rho RT$). Under isobaric conditions, we find that

$$\frac{\Delta\rho}{\rho_1} \approx -\frac{\Delta T}{T_1} \qquad (12)$$

Thus, the required density uniformity prescribes the required level of temperature uniformity. Typical permissible $\Delta\rho/\rho_1$ values require temperature control to fractions of a degree.

It is interesting to compare these requirements against the initial disturbance levels in the laser cavity just after the initiation process. The constant-volume (density) initiation process allows one to simply determine the temperature (pressure) rise using the first law of thermodynamics and the gas law. The result is

$$\left(\frac{\Delta p}{p_1}\right)_{init} = \left(\frac{\Delta T}{T_1}\right)_{init} = \frac{(\gamma-1)\,\Delta Q(J/lit\text{-}atm)}{101.3} \qquad (13)$$

The typical range of laser parameters leads to values of $(\Delta p/p_1)_{init}$ that are O(1). In some cases, as will be seen for the Raman Cell of the KrF system, $(\Delta p/p_1)_{init}$ will be very small [$O(10^{-3})$]; however, in general, the initial overpressure levels calculated from (13) will require acoustic pressure suppression of between 10^2 and 10^4 due to the medium quality requirements described previously. The temperature uniformities required also necessitate "control" by factors similar to the pressure suppression factors.

The requirements on the flow uniformity are also connected to the beam-quality specified medium homogeneity ($\Delta\rho/\rho_1$). From the energy equation along a streamline, $C_pT + (1/2)\,U^2 = C$, which is valid just prior to the initiation pulse, one finds that

$$\frac{\Delta\rho}{\rho_1} \approx (\gamma-1)\,M^2\,\frac{\Delta U}{U} \qquad (14)$$

where M is the flow Mach number and $\Delta U/U$ is the large-scale velocity variation allowed in the cavity.

At very low Mach numbers ($\lesssim 0.03$), the velocity uniformity is not restrictive, however, when $M \gtrsim 0.3$, the $\Delta U/U$ requirement may be very difficult to meet. Once $\Delta U/U$ becomes small enough, it is difficult to distinguish a vortical or large-scale ordered disturbance from the smaller-scale random inhomogeneities (turbulence). The density inhomogeneities associated with turbulence velocity fluctuations are given by

$$\frac{\Delta\rho}{\rho} \lesssim M^2 \left(\frac{u}{U}\right)^2 \qquad (15)$$

where u'' is the rms turbulence intensity. This relationship is a consequence of the fact that turbulent pressure fluctuations are related to the turbulent velocity fluctuations through $\Delta P \sim \rho u'^2$, and that $\Delta P = C^2 \Delta\rho$ for adiabatic disturbances.

The medium quality requirements described above are summarized in Table 2-1 and will be evaluated for specific fusion laser systems in Sections 2.2 and 2.3. The above discussion completes our general analysis of the laser gas medium uniformity requirements just prior to initiation. In the next subsection, the overall flow efficiency and pressure-drop requirements will be examined and the pressure-drop contributions of the various elements of the flow system will be evaluated to first order.

2.1.1.2 Flow Efficiency Definition and Requirements

The flow system associated with a fusion laser must be closed-cycle in order to make ICF economically feasible. In addition to conserving gas, the closed-cycle system must also use a minimum of power to transport the laser gas around the circuit while maintaining the medium homogeneity requirements defined in 2.1.1.1.

A schematic of a fusion laser flow system is shown in Figure 2-1. The various elements in the system will be identified now beginning with the laser cavity (denoted as station 1).

Table 2-1. Factors Influencing the Medium Homogeneity $\left(\frac{\Delta\rho}{\rho}\right)$.

Influencing Factors	Analytic Relationship
Residual Pressure Fluctuations	$\left(\frac{\Delta\rho}{\rho_1}\right) = \frac{1}{\gamma}\left(\frac{\Delta p}{p_1}\right)_r$
Pressure Induced "Entropy Waves"	$\left(\frac{\Delta\rho}{\rho_1}\right) = \frac{\gamma-1}{\gamma}\left(\frac{\Delta p}{p_1}\right)_e$
Temperature Fluctuations	$\left(\frac{\Delta\rho}{\rho_1}\right) = -\left(\frac{\Delta T}{T_1}\right)$
Large-Scale Velocity Fluctuations	$\left(\frac{\Delta\rho}{\rho_1}\right) = (\gamma-1)\, M^2 \frac{\Delta u}{U}$
Turbulent Velocity Fluctuations	$\left(\frac{\Delta\rho}{\rho_1}\right) = M^2 \left(\frac{u'}{U}\right)^2$

The characteristics and purposes of the various elements of the flow system are summarized in Table 2-2. The flow in the laser cavity is initially at a given state (p_1, T_1). After the laser gas is initiated (e.g., with an electric discharge), the constant-volume heat addition process leads to an overpressure Δp and a temperature excess ΔT. The overpressure Δp is suppressed by acoustic elements upstream (9) and downstream (2) of the cavity. Both of these elements are entropy-producing and necessarily must contribute to the flow pressure drop p^* of the entire system. A diffuser (3) is needed only when the gas flows at a fairly high Mach number, say $M \geq 0.2$, to convert the dynamic head (or kinetic energy) of the flow to static pressure (potential energy), with minimum losses. A gas regenerator (4) will be required if the gas undergoes nonreversible chemical changes in the cavity.. Heat exchangers (5) and (7) are required to extract the excess heat deposited in the cavity, the heat generated by the compressor and heat that may be added to the cycle by the regeneration process. The location of the heat exchangers may vary, and in some applications, one heat exchanger may suffice. A compressor (6) will be required to circulate the gas around the flow loop. The rate of mass flow through the flow loop and the overall pressure drop will determine the power required to drive the compressor. Flow management devices (8) will be needed to control the velocity and temperature fluctuations in the gas near the entrance to the cavity to meet the beam quality requirements. It is possible that the functions of velocity and temperature control could be combined with the pressure wave suppression function of the upstream absorber (9) and performed all by one element.

The overall laser efficiency η_L, defined as the laser output power, P_L, divided by the total input power, $p_{TOT} = P_I + P_F + P_R$ (where P_I, P_F and P_R are the initiation, flow and chemical refeneration powers, respectively), is a key parameter in the evaluation of laser fusion. This definition permits us to write

$$\frac{1}{\eta_L} = \frac{1}{\eta_I} + \frac{1}{\eta_F} + \frac{1}{\eta_{CR}} \qquad (16)$$

Table 2-2. Major Elements of a Fusion Laser Flow System

Element Number	Element Name	Element Function, Characterization or Requirements
①	Laser Cavity	Requires Homogeneous Medium at T_1, p_1 Prior to Initiation. $T_1 + \Delta T$ and $p_1 + \Delta p$ Produced After Initiation.
②	Downstream Acoustics	Suppresses Δp at Low Pressure Drop and Minimizes Reflection into Cavity
③	Subsonic Diffuser	Recovers Driving Pressure.
④	Gas Regenerator	Chemically Reconstitutes the Recirculating Gas.
⑤	Heat Exchanger (1)	Reduces Temperature to Near T_1.
⑥	Compressor	Increases Pressure Sufficiently to Transport Flow. Also Increases Temperature to $T_1 + \Delta T_c$.
⑦	Heat Exchanger (2)	Reduced Compressor-Heated Gas Temperature to T_1.
⑧	Flow Management Devices	Produce Uniform Flow at p_1 and T_1; Control both Velocity and Temperature Fluctuations.
⑨	Upstream Acoustics	Suppress Δp at Low Pressure Drop Without Perturbing Other Media Properties.

where η_I is the initiation (electrical) efficiency, η_F is the flow efficiency, and η_{CR} is the chemical regeneration efficiency of the laser. In this report we will not discuss the gas regeneration aspects of the flow system, since the two candidate fusion lasers which are specifically considered here, CO_2 and KrF, will require only minimal chemical regeneration. Equation (16) is thus simplified with the last r.h.s. term eliminated. The effect of the flow efficiency on the overall laser efficiency can thus be readily predicted.

No attempt was made in this study to estimate the minimum required overall laser efficiency for ICF power generation or to evaluate the benefits which can be derived from an increased laser efficiency. Simple arguments indicate, however, that the absolutely minimum acceptable laser efficiency is of the order of one percent and that substantial gains can be derived in net power production if the laser efficiency is increased from 1 to 10%*. We will thus focus our attention on this range of overall laser efficiencies.

* The 1% minimum efficiency is based on an assumed pellet gain of $G = 10^3$ and a yield of $Y = \eta_L G = 10$, resulting in a recirculating power fraction of about 30%. This fraction is relatively high but still acceptable. For a more detailed discussion of this subject, see Ref. 2-2, p. 25.

Figure 2-3 is a plot of Equation (16) with $P_R \to 0$. Given an initiation efficiency, η_I, and a desired laser efficiency, η_L, this figure can be conveniently used to determine the minimum required flow efficiency, η_F. Consider, for example, a laser with a 10% initiation efficiency. The overall efficiency will vary from $\approx$ 1.7% to 9.1% as the flow efficiency varies from 2% to 100%. Suppose we choose 5% as the goal for the overall laser efficiency. Then, based on Figure 2-3, if $0.05 \leq \eta_I \leq 0.1$, η_F must be well above 10%. We will show below that there is a tradeoff between η_F and the overall flow-cycle pressure drop. Low values of η_F permit high pressure drops in the flow system and, hence, allow for the greatest freedom of design to meet the medium quality requirements.

The flow efficiency is coupled to the flow system pressure drop and the laser energy extraction. The connection between these parameters is now derived. Specifically, the flow efficiency is defined as

$$\eta_F = P_L / P_F \tag{17}$$

where P_L is the average power out of the laser module and P_F is the power required to recirculate the laser gas. The average laser power (in watts) is

$$P_L = p_1 V_1 S \boxed{PRF} \tag{18}$$

where p_1 is the cavity pressure in atmospheres, V_1 is the cavity volume in liters, S is the extracted energy density in J/lit-atm and PRF is the pulse repetition frequency. The flow power P_F, in watts, required to pump the laser gas around the flow loop is given by (2-3)

$$P_F = (1.013 \times 10^2) \frac{p_1 V_1 C PRF}{\eta_{comp}} \left(\frac{\gamma}{\gamma-1}\right) \left[\left(\frac{p_6}{p_5}\right)^{\frac{\gamma-1}{\gamma}} - 1\right] \frac{T_5}{T_1} \tag{19}$$

where p_1 is again in atm, and V_1 in liters, and C is the flush factor (defined as the volume of gas pumped per pulse through the laser cavity

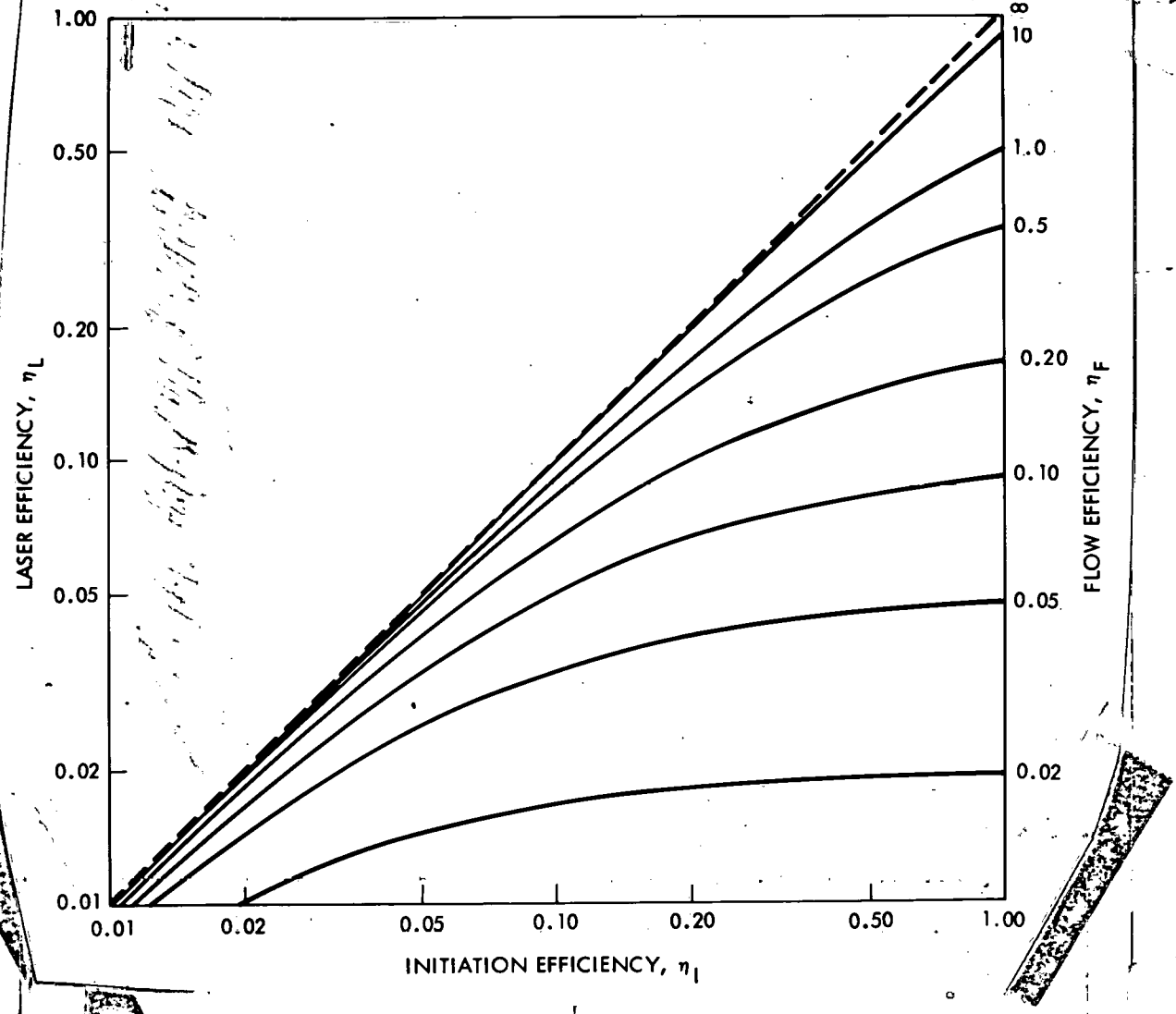

Figure 2-3. Overall Laser Efficiency Versus Initiation and Flow Efficiencies.

divided by the cavity volume, η_{comp} is the compressor efficiency, T_5/T_1 is the ratio of the gas temperature entering the compressor to the temperature in the cavity, and p_5 and p_6 are the static pressure upstream and downstream of the compressor, respectively. If we combine (17), (18) and (19), we obtain

$$\eta_F \cdot f\left(\frac{p_6}{p_5}, \gamma\right) = \frac{S \cdot \eta_{comp}}{101.3\ C(T_5/T_1)} \tag{20}$$

where

$$f(p_6/p_5, \gamma) = \frac{\gamma}{\gamma-1}\left[\left(\frac{p_6 - p_5}{p_5} + 1\right)^{\frac{\gamma-1}{\gamma}} - 1\right] \tag{21}$$

and $(p_6 - p_5)/p_5 \equiv \Delta p^*/p_5$ is the "system" pressure drop. Since efficient flow systems will require small pressure drops, we can expand Eq. 21 and obtain a linearized term for f:

$$f \approx \frac{\Delta p^*}{p_5} \tag{22}$$

The flow efficiency, η_F, can now be computed from

$$\eta_F \cdot \frac{\Delta p^*}{p_5} = \frac{S \cdot \eta_{comp}}{101.3\ C(T_5/T_1)} \tag{23}$$

This expression is accurate to within 7% for

$$\frac{\Delta p^*}{p_5} < 0.2 \text{ and } \gamma > 1.4 \tag{24}$$

For larger pressure drops and/or smaller γ the exact expression for f (Eq. 21) should be used.

The tradeoff between η_F and $\Delta p^*/p_5$ can now be readily presented (see Figure 2-4). Note the importance of the extraction energy density. This parameter varies by an order of magnitude for different fusion laser candidates. For an advanced CO_2 system with S = 5 J/lit-atm, and a realistic flow efficiency of 20%, Figure 2-4 implies an allowable pressure drop for the entire system of 10%. This value for $\Delta p^*/p_5$ is a factor of 20 to 30 larger than the typical low-speed wind tunnel pressure drop ($\approx$0.004). Hence, for this example there appears to be enough available $\Delta p^*/p_5$ to meet the requirements of the fusion laser "wind tunnel" which include acoustics, flow management, and heat exchangers. The various contributors to pressure drop in the system are described in subsequent paragraphs.

The primary sources of pressure drop in the flow system are defined in Table 2-3. The pressure drop will be identified with an asterisk (*) to distinguish it from initiation-produced overpressures and with a subscript to indicate the location of the pressure losses. The numbered subscripts shown in Table 2-3 refer back to Figure 2-1 and Table 2-2. The lettered subscripts refer to losses distributed throughout the system.

Pressure losses in flow systems are typically referenced to the dynamic pressure of the flow entering the loss element. The dynamic pressure q_i is defined as $\rho_i U_i^2/2$ where ρ_i is the gas density and U_i is the gas velocity at location i in the system. The pressure drop is then given by

$$\Delta p^* = K \rho_i U_i^2/2 = K q_i \qquad (25)$$

where the coefficient K [typically O(1)] depends upon the specific pressure loss source.

Analytic estimates for the various pressure-drop elements will be presented below with the determination of K as the goal. We proceed in the same order as indicated in Table 2-3.

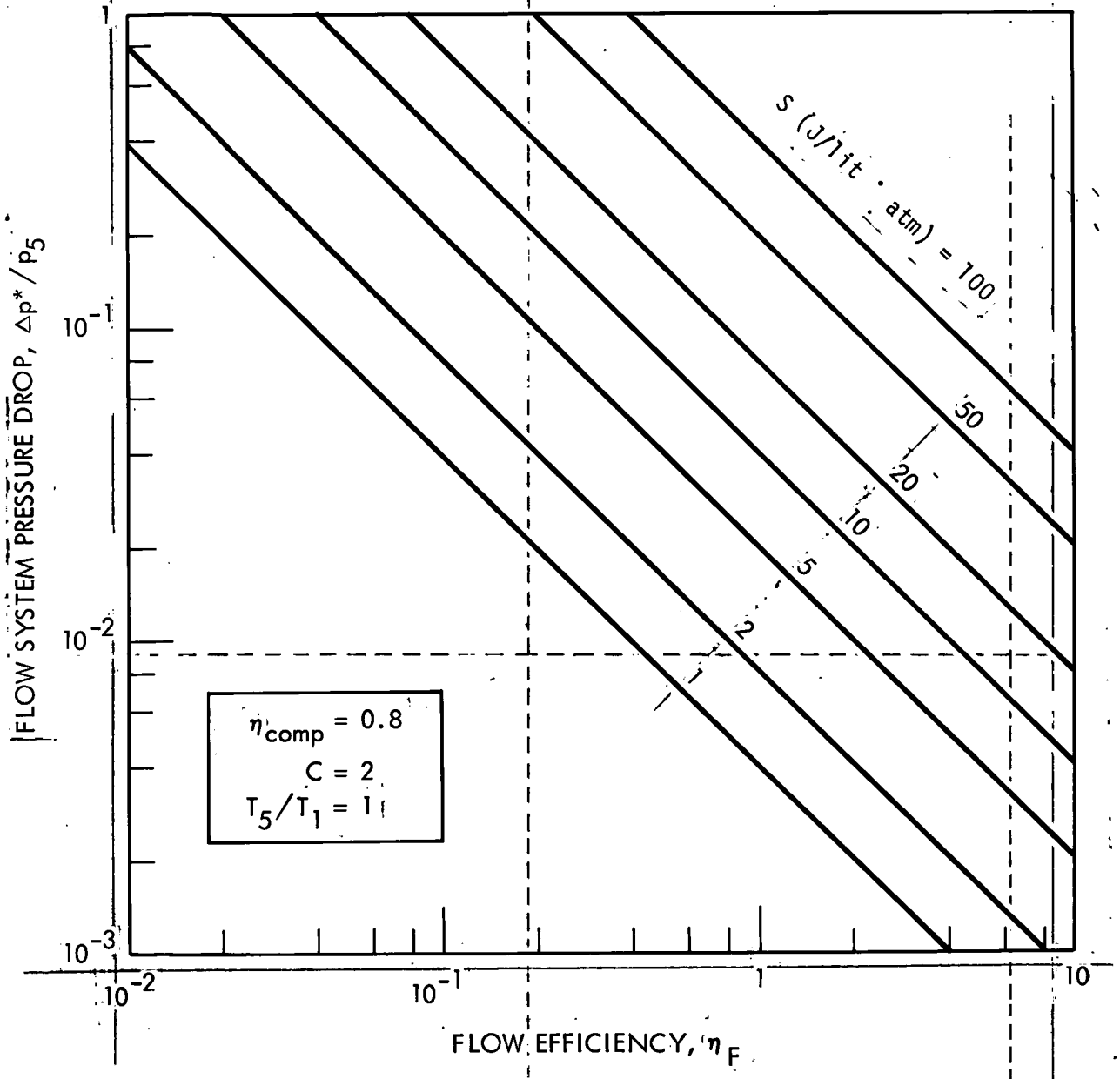

Figure 2-4. Flow Efficiency Versus Pressure Drop.

BOTTOM OF PAGE
BOTTOM OF PAGE

Table 2-3. Sources of Pressure Drop in Fusion Laser Flow Systems

Pressure Drop Sources		Location	Features
Heat Addition	Δp_1^*	Laser Cavity	Constant Volume Heat Addition with Entropy-Producing Disturbances.
Diffuser	Δp_2^*	Downstream of Acoustics	Frictional Pressure Drop, Flow Separation Should be Avoided.
Pressure Suppressor	$\Delta p_9^*/\Delta p_2^*$	Up/Downstream of Cavity	Pressure Drop is Design Dependent.
Flow Turns (4)	Δp_T^*	Corners of Flow System	Frictional Losses/Flow Disturbances, Design Dependent.
Flow Conditioning	Δp_c^*	Upstream of Cavity	Includes Convergent Section, Screens, Honeycombs (for velocity and temperature control).
Heat Exchangers (2)	$\Delta p_5^*/\Delta p_7^*$	Up/Downstream of Compressor	Pressure Drop Proportional to Temperature Change.
Boundary Layer Friction	Δp_F^*	Entire Flow System	General Frictional Losses, Separation Should be Avoided.

Cavity Heat Addition

A drop in stagnation pressure occurs in the laser cavity due to the heat addition caused by the initiation process and subsequent lasing. The stagnation temperature rise can be calculated from the heat deposited into the flow, ΔQ. The change in stagnation temperature is given by

$$\frac{\Delta T_{01}}{T_{01}} = \frac{T_{02} - T_{01}}{T_{01}} = \frac{(\Delta Q \cdot p_1)\, p_1}{\rho_1 C_p T_{01}} \tag{26}$$

The quantity $\Delta T_{01}/T_{01}$ is related to M_2, the Mach number after the heat addition, as follows:(2-4)

$$\frac{\Delta T_{01}}{T_{01}} = \frac{M_2^2 \left(1 + \gamma M_1^2\right)^2}{M_1^2 \left(1 + \gamma M_2^2\right)^2} \frac{\left(1 + \frac{\gamma-1}{2} M_2^2\right)}{\left(1 + \frac{\gamma-1}{2} M_1^2\right)} - 1 \tag{27}$$

Equations (26) and (27) enable one to relate the heat addition to the stagnation pressure loss. After some algebraic manipulations, using basic gas-dynamic relationships, one can write

$$P_{01} - P_{02} = K_1 \left(\frac{\rho_1 V_1^2}{2}\right) = \Delta p_1^* \tag{28}$$

where

$$K_1 = K_1(M_2) = \frac{-2}{\gamma M_1^2} \left[\frac{\left(1 + \gamma M_1^2\right)}{\left(1 + \gamma M_2^2\right)} \left(1 + \frac{\gamma-1}{2} M_2^2\right)^{\frac{\gamma}{\gamma-1}} - \left(1 + \frac{\gamma-1}{2} M_1^2\right)^{\frac{\gamma}{\gamma-1}} \right] \tag{29}$$

In general, this contribution to the overall pressure drop will not be larger. Note that the evaluation made above considers the single pulse situation. We can take the repetitively pulsed nature of the heating into account by dividing the single pulse ΔT_{01} by the flush factor C.

Subsonic Diffuser

The behavior of subsonic diffusers is described in detail in Reference 2-5. The pressure drop through the diffuser is given by

$$p_3^* = K_3 \left(\frac{\rho_3 V_3^2}{2} \right) \tag{30}$$

where K_3 is somewhat geometry-dependent and the dynamic pressure ($\rho_3 V_3^2/2$) is evaluated at the diffuser inlet. Long diffusers with $L_3/H \gtrsim 10$ and small area ratios ($A_{outlet}/A_{inlet} \lesssim 2.5$), operate efficiently without significant stall. The loss coefficient for these geometries is in the range $0.25 \lesssim K_3 \lesssim 0.4$.

Pressure Suppressors

The acoustic suppression elements upstream and downstream of the laser cavity are the key elements of the fusion laser flow system. They are unavoidable if we are to meet the stringent beam quality and flow uniformity requirements. Several concepts for performing the pressure suppression have been under study for several years in the pulsed-laser community. The two primary candidates are flow-through absorbers and side-wall muffler absorbers. These suppression elements may represent the major contributors to the allowable pressure drop for the fusion laser flow system. Due to the "special" nature of these system flow elements, quantitative discussion of pressure drops arising from these elements is deferred to Section 2.1.2.2 and to further specific laser system discussion in Sections 2.2 and 2.3.

Flow Turns

In a closed-cycle fusion laser flow system there are typically four (4) corners (see Figure 2-1) where the flow turns by 90°. The flow encounters losses as it turns around the corners. If the corner is abrupt without vanes then a 100% loss of dynamic pressure can result,[2-5] i.e., $K_T = 1$. Careful design of the corner duct and corner vanes can lead to values of K_T as low as 0.11 according to Pope.[2-5] A reasonable value is $K_T = 0.15$, which we will utilize for each corner. Note that, if necessary,

the vanes can be utilized to help cool the hot laser gas by flowing a coolant through the vanes.

Flow Conditioning

The flow conditioning pressure drop sources include any elements in the flow system specifically designed to minimize and control flow non-uniformities as well as possible thermal inhomogeneities. The main purpose of these elements is to suppress vortical and turbulent velocity fluctuations; however, thermal management can also be affected through the use of cooled flow conditioning elements if necessary. Three types of losses are considered. The losses associated with flow through the contraction section upstream of the cavity, and with flow through screens and honeycombs.

The loss coefficient for the contraction section or contraction cone (in wind-tunnel terminology) is given by[2-5]

$$K_{c1} = 0.32\ C_f\ \ell_c/H\ . \qquad (31)$$

where C_f is the skin-friction coefficient, ℓ_c is the length of the contraction section and H is the cavity height. This loss term is predominantly frictional and is typically less than 3% total pressure drop in a conventional low-speed wind tunnel.

At high Reynolds number ($Ud/\beta\nu > 10^3$), the screen pressure drop coefficient is given by

$$K_{c2} = 0.8\ \frac{1-\beta}{\beta^2} \qquad (32)$$

where d is the wire diameter and β is the porosity of the screen, i.e., $\beta \equiv$ open area/total area. Screens operate without instabilities for values of $\beta \gtrsim 0.6$. Typical values of K_{c2} range from approximately 0.10 to approximately 2. We will utilize a value of $K_{c2} = 1$ for every screen employed in the flow system.

Losses in honeycombs are typically small since they are very open. For honeycombs with a length/diameter ratio of 6 and equal tube areas,

Pope[2-5] quotes a range for K_{c3} from 0.30 (circular tubes) to 0.20 (hexagonal tubes). We will use a value of $K_{c3} = 0.25$.

Heat Exchangers

The pressure-drop coefficients for the heat exchangers depend on the gas entrance and exit temperature, as well as on the coolant temperature. For the first heat exchanger that serves to take out most of the laser cavity heat addition, we have[2-5]

$$K_5 = 2 \frac{T_{02} - T_{01}}{T_{02} - T_5} \tag{33}$$

where T_5 is the coolout temperature, entering the heat exchanger. The second heat exchanger serves to take out the thermal energy introduced into the flow by the compressor. Hence

$$K_6 = 2 \frac{T_{06} - T_{05}}{T_{06} - T_7} \tag{34}$$

Note that further fine-tuning of the temperature may be necessary to achieve the small density inhomogeneity levels of interest. Adding an extra heat exchanger will not produce much pressure drop because the total temperature change introduced by such a heat exchanger will be small.

Boundary-Layer Friction

Frictional losses occur along the entire flow loop. Some of these losses are found in area-change regions such as the contraction upstream of the cavity, the diffuser downstream of the cavity, and the corner flow turns. However, these contributions have been separately taken into account as described above. Hence, the boundary-layer friction losses only need to be computed for the straight-wall sections. The pressure drop in a duct of length ℓ is

$$\Delta p_F^* = K_F \left(\frac{1}{2} \rho V^2\right) \tag{35}$$

DOCUMENT NO.
PAGE NO.

where K_F is simply $C_f \ell/D_h$ (where D_h is the hydraulic diameter of the duct cross section and C_f is the skin-friction coefficient which is Reynolds-number dependent and typically in the range of 3×10^{-3} to 10^{-2}). The friction contribution is typically quite small for low-speed wind tunnels.

The various pressure-drop coefficients (K_s) for the sources described above are summarized in Table 2-4. The major contributions are underlined.

T2-4

2.1.1.3 Mean-Flow Requirements

The preceding discussion has centered around the pressure drop of the flow system and the (maximum) permissible pressure drop. There are also other specific requirements on the flow itself, e.g., the gas velocity or Mach number which must be related to the cavity geometry, the PRF, and the "flush factor" C. These three parameters require some discussion before specific flow velocity requirements can be established.

F 2-5

First, consider the cavity geometry. Cavities considered in this report are limited to rectangular geometries as shown in the sketch of Figure 2-5(a). The dimension in the beam (optical-axis) direction is is denoted by L. This is limited by small-signal-gain considerations and the growth of parasitic modes. A typical range of cavity lengths we will consider here is L = 1-to-5 m. The initiation height is limited by the specific initiation process. For an e-beam-controlled discharge, H is limited here to be approximately 0.15 m. These dimensions of the laser cavity are "flow-independent" and will be considered as fixed in our flow system calculations. The flow length W remains to be determined. It is an important parameter for flow system scaling studies.

The pulse repetition frequency (PRF) required for laser fusion power generation is yet to be determined. The widest range which can be considered is 1-to-100 Hz, with the most likely range limited to 10-to-20 Hz. Since this frequency is strongly flow-system-dependent, we will leave it as a variable parameter. There will obviously be other important considerations as well which will eventually determine the required pulse repetition frequency.

The mass utilization per pulse or "flush factor" C (the gas volume which flows through the cavity per pulse, divided by the active, lasing

BOTTOM OF PAGE
BOTTOM OF PAGE

Table 2-4. Summary of Pressure Drop Loss Coefficients.

Pressure Drop Source	Loss Coefficient	Approximate Range of Values
Heat Addition	$K_1 = \frac{\Delta T_{01}}{T_{01}}$ (small M)	0.1 - 1
Diffuser	K_3 = Constant	0.25 - 0.40
Pressure Suppressors	K_2, K_9	0.1 - 5
Flow Turns	K_T (one turn)	0.1 - 1
Flow Conditioning		
Contraction	$K_{c1} = 0.32\ C_f\ \ell_c/H$	10^{-3} - 0.1
Screen	K_{c2} = constant	0.1 - 2
Honeycomb	K_{c3} = constant	0.2 - 0.3
Heat Exchangers	K_5, K_7 = constant	0.5 - 2
Boundary-Layer Friction	$K_F = C_f\ \ell/D_h$	10^{-2} - 1.0

DOCUMENT NO.
PAGE NO

(a) CAVITY GEOMETRY

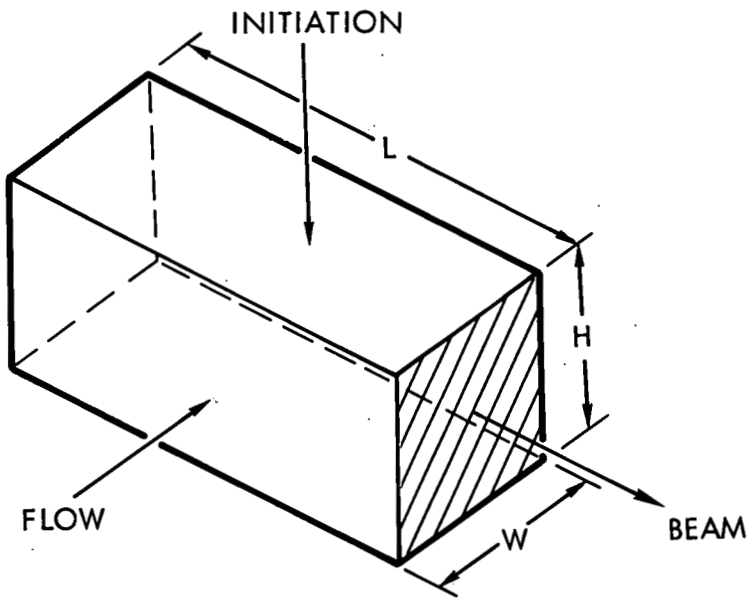

(b) FLOW GEOMETRY

$$C = \frac{\text{TOTAL GAS VOLUME}}{\text{INITIATED GAS VOLUME}} \leq 2$$

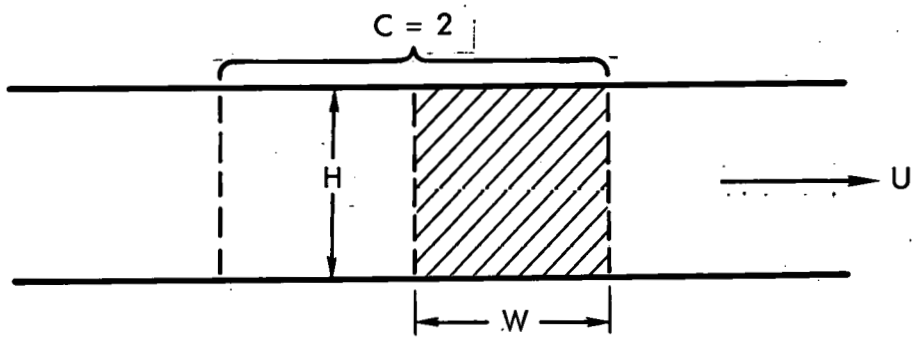

Figure 2-5. Cavity and Flow Geometries.

BOTTOM OF PAGE

volume) has a minimum (by definition) of unity. Because of potential mixing nonuniformity and the need for time (space) to suppress the initiation-generated pressure waves, $C > 1$. If the initial overpressure is small enough, it may be possible to achieve values for C that are close to unity; a realistic goal for C is 1.5, however due to the medium homogeneity constraints we will utilize a conservative value of $C = 2$ which will allow more time for acoustic quieting.

The flow velocity requirement can now be established. The volume passed through the cavity per pulse is $C \times W \times H \times L$ and the related gas velocity must be

$$U = CW \times PRF \tag{36}$$

At a given PRF, $U \sim W$. It is convenient to define a dimensionless PRF as follows:

$$\overline{PRF} = \frac{W \times PRF}{a} = \frac{\text{Acoustic Time}}{\text{Pulse Interval}} \tag{37}$$

where the acoustic time is defined as the time it takes a sound wave to travel across the width of the cavity and the pulse interval is the time elapsed between two consecutive pulses. We would like $\overline{PRF} << 1$ since this would allow for many transits of the acoustic waves in the cavity region within a pulse interval, thereby promoting successive pressure suppression with each bounce. If we now divide the velocity (36) by the acoustic speed a, we obtain the Mach number

$$M = C\,\overline{PRF} \tag{38}$$

Acoustic suppression will thus be facilitated when $M << 1$. Increasing pressure drop with M also suggests that $M << 1$. These two reinforcing Mach number constraints will lead to restrictions on the permissible values of W and PRF.

2.1.1.4 Summary of Flow System Requirements

There are essentially two sets of requirements imposed on the flow system of a fusion laser. One pertains to the required laser beam quality and the related cavity media homogeneity. The desired focal spot size and

the focal length of the focusing optics, the laser wavelength, the cavity dimensions and the laser media composition and pressure will determine the level of cavity media homogeneity which must be maintained by the flow system. These requirements dictate, e.g., that the lasing medium in the cavity be completely exchanged between successive pulses and that acoustic suppression and flow conditioning devices be employed in the flow system.

Another set of requirements is determined by flow efficiency considerations. The flow efficiency (laser power divided by power required to recirculate the gas) must be at least as good as, or somewhat better than, the initiation or regeneration efficiencies. This requirement will dictate low-pressure-drop designs for the flow system.

These general requirements (good media homogeneity and high flow efficiency) are basically in conflict. The overall objective of the flow system studies can be viewed as an attempt at finding the optimal trade-off between these two requirements.

2.1.2 Pressure Wave Suppression in Pulsed Lasers

The subject of pressure wave suppression in pulsed lasers has received considerable attention following the development of repetitively pulsed, high energy gas lasers. The atmospheric pressure, CO_2 electric discharge laser was probably the forerunner of this class of lasers. The development of acoustic suppressors for pulsed CO_2 lasers has a fairly long history (see, e.g. Refs. [2-6, 2-7]). Similar attempts were made to analyze pressure wave generation and suppression phenomena in pulsed CO lasers. [(2-8,2-9)] More recently, several studies were performed aimed at developing pressure wave suppressors for repetitively pulsed DF and KrF lasers. [(2-10 – 2-13)] There is of course a vast body of now classical literature on acoustic wave suppression in other flow systems. Studies related to fan and jet engine noise quieting are prominent examples. We will not attempt to review here this literature. It should be noted, however, that this literature deals mostly with suppression of lower overpressures (acoustic waves) than those generated in pulsed lasers and therefore are not always applicable to the pulsed laser pressure suppression problem.

Pressure wave suppressors which are used in repetitively pulsed lasers and in other similar flow systems can be divided into two generic types -- those which act on the mean flow (which we will call "active" absorbers), and those which do not (here referred to as "passive" absorbers). In the first class we include porous flow-through absorbers, dust or droplet laden absorbing media (such as in Ref. [2-11]) and any abrupt changes in the flow direction and/or cross section. In a sense, the orifice plate which is normally placed upstream of the cavity in repetitively pulsed lasers, to separate the feed gas from any disturbances in the cavity, can be considered as an active absorber. Examples of several active absorbers are presented in Figure 2-6.

The second class includes all side-wall absorbers, of either the vented duct design (Ref. [2-10]) or the porous side wall muffler design (Ref. [2-13]), which do not interact with the quiescent mean flow but affect the flow and pressure fields whenever pressure waves are generated. Typical examples are shown in Figure 2-7. There are, of course, various combinations of these two generic classes of absorbers. Wedge or diamond-shaped porous materials inserted in a flow duct affect the mean flow, due

BOTTOM OF PAGE
BOTTOM OF PAGE

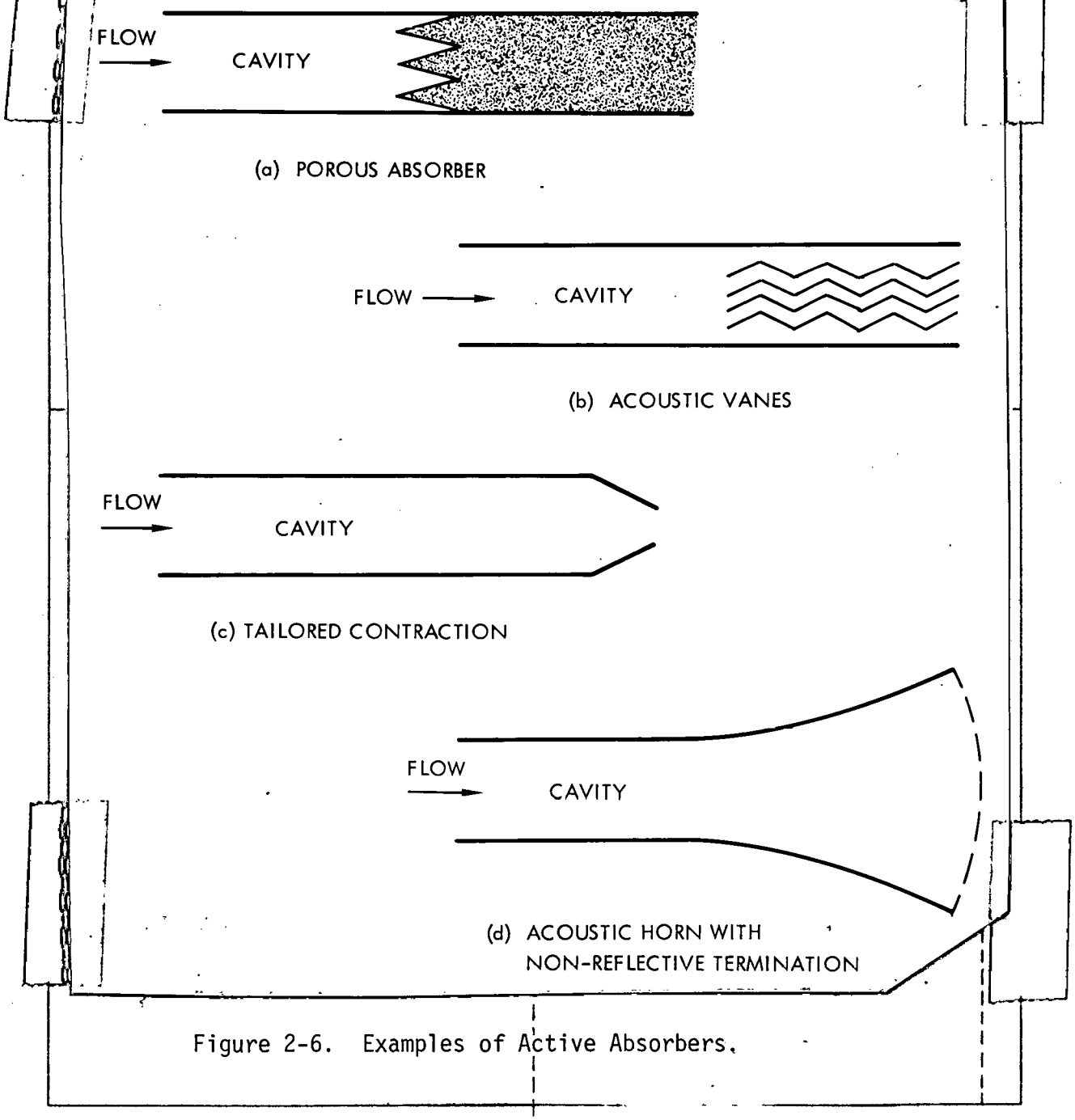

Figure 2-6. Examples of Active Absorbers.

DOCUMENT NO.
PAGE NO.

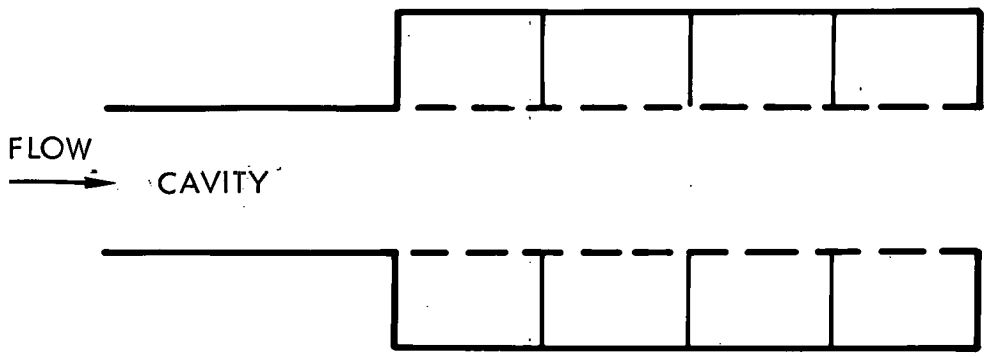

(a) VENTED SIDE WALL ABSORBER

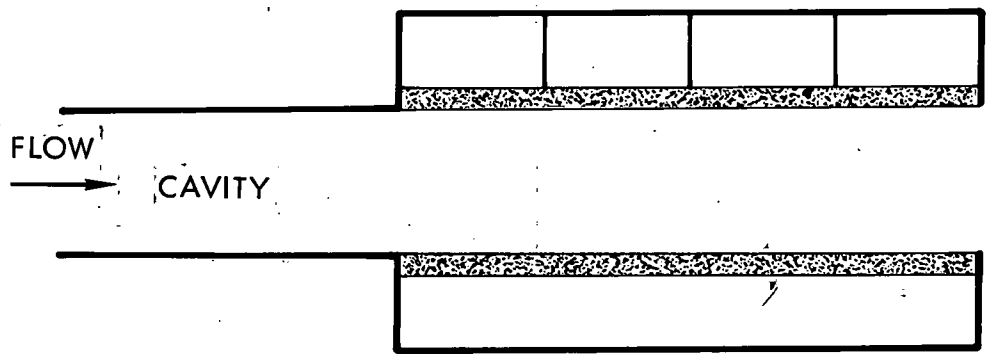

(b) POROUS SIDE WALL ABSORBER

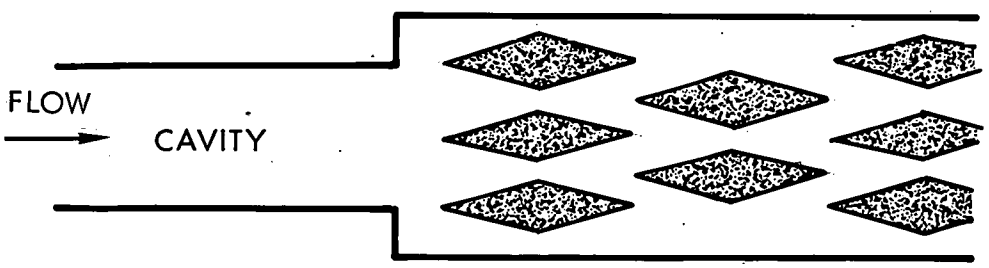

(c) DIAMOND SHAPED POROUS ABSORBERS

Figure 2-7. Examples of Passive (a & b) and Combined Active/ Passive (c) Absorbers.

to the flow contractions which they introduce, and have a secondary important effect on the pressure waves, whenever these are generated, since these waves force the fluid into the porous material and amplify the absorption and attenuation processes.

The pressure wave suppressors described briefly above all absorb the pressure energy by viscous damping and by shedding of vorticity from rigid or porous surfaces. Both active and passive absorbers have the potential for achieving the pressure wave suppression levels required for the different types of repetitively pulsed lasers developed to date (see Refs. 2-7, 2-10 – 2-13).

The development of pressure wave suppressors for pulsed fusion lasers can benefit greatly from the experience gained in the past work on pulsed laser suppressors. It should be noted, however, that many pulsed laser pressure wave suppressors developed to date have utilized choked orifice plates upstream of the cavity, to positively isolate the cavity feed gas from the pressure disturbances in the cavity. This feed plate reflects all pressure waves generated in the cavity and preserves the density homogeneity of the feed gas. The feed gas is thus ready to be introduced into the cavity when the pressure disturbances there have subsided sufficiently. A pressure wave absorber is placed in such lasers downstream of the cavity and acts on both the pressure waves propagated directly from the cavity and those reflected from the feed plate. The role of the downstream absorber is thus essentially to minimize any pressure wave reflections into the cavity. 100% reflection for the upstream feed plate and zero reflection for the downstream absorber are the ideal design goals for these two flow elements.

In fusion-type lasers the requirement for a highly efficient flow system with minimal pressure drops precludes the use of fully-reflecting choked-orifice plates upstream of the cavity (except, perhaps, for very high-energy-density lasers, such as the HF system). In such lasers, low-pressure-drop absorbers will have to be placed both upstream and downstream of the cavity. Passive absorbers, with their inherently low pressure drop characteristics (for the mean flow), will be the natural choice for the downstream absorber. The selection of an upstream absorber is considerably more complex.

The upstream pressure wave absorption in a fusion-type laser, subject to the requirements of high mass utilization (small C) and high flow efficiency (low Δp^*), represents a unique and fundamentally difficult problem. The difficulty arises from the fact that upstream absorption must take place in a region where the fresh cavity feed gas resides. This gas must retain a high degree of density uniformity before it is convected into the cavity. All pressure wave suppression processes are basically high-loss and non-isentropic. They should not take place in a region where gas uniformity is of primary concern.

Active flow-through absorbers will not be appropriate, most probably, because of their non-isentropic interaction with the pressure waves. A simple calculation can be used to demonstrate this point. Consider, for example, any flow-through absorber such as is shown schematically in Figure 2-8. If the pressure fluctuations in front of this absorber are slow (relative to the characteristic flow times), a steady state analysis can be applied, assuming that the flow is quasi-steady. A relationship between the pressure and density fluctuations inside the porous medium can be derived from the general one-dimensional flow conservation equations. Continuity requires that

$$\frac{d(\rho u)}{dx} = 0 \tag{39}$$

The absorbing media presents a resistence to the gas flow characterized by a force "k" per unit volume. The momentum conservation equation is therefore written as

$$\rho u \frac{du}{dx} + \frac{dp}{dx} = -k(\rho,u) \tag{40}$$

We will assume, for simplicity, that no heat is exchanged between the flow and the absorbing media (adiabatic flow), and energy conservation therefore prescribes

$$C_p \frac{dT}{dx} + u \frac{du}{dx} = 0 \tag{41}$$

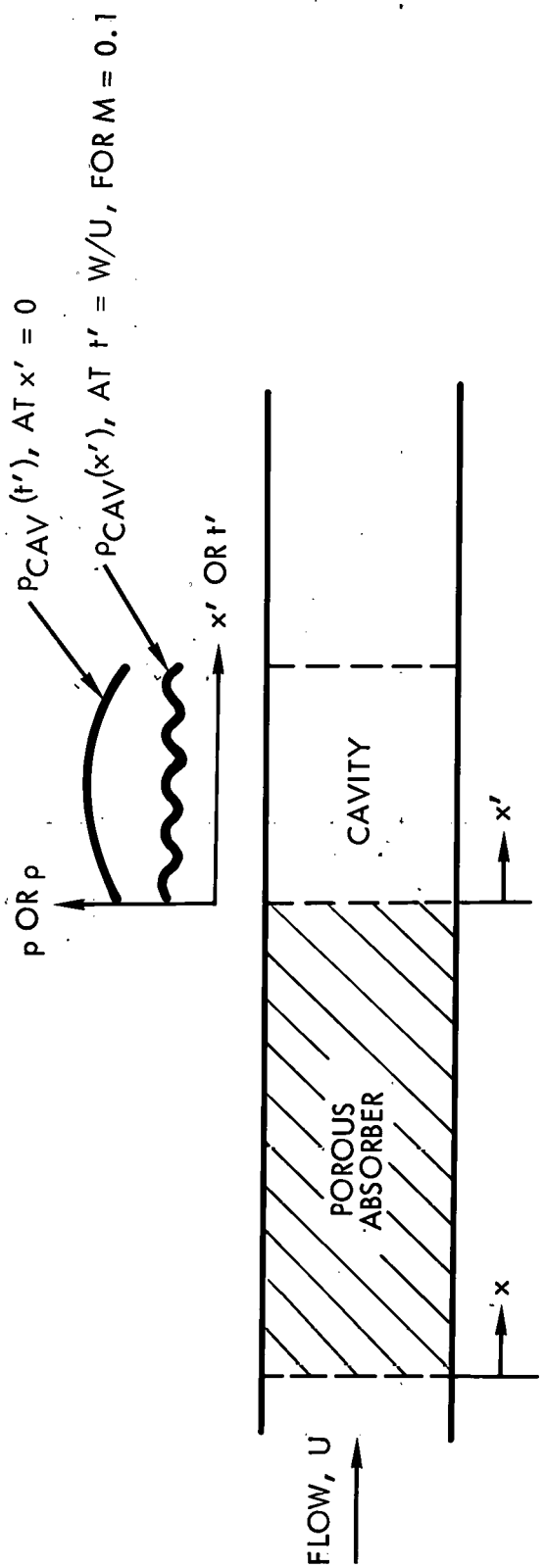

Figure 2-8. Schematic of an Upstream Porous Absorber.

DOCUMENT NO.
PAGE NO

Finally, the equation of state can be employed

$$\frac{1}{p}\frac{dp}{dx} = \frac{1}{\rho}\frac{d\rho}{dx} + \frac{1}{T}\frac{dT}{dx} \tag{42}$$

Simple manipulations of these four equations leads to

$$\frac{dp}{dx} = -k\left[\frac{1 + (\gamma-1)\,M^2}{1 - M^2}\right] \tag{43}$$

and

$$\frac{d\rho}{dx} = \frac{-k}{RT\,(1-M^2)} \tag{44}$$

where $M^2 = u^2/\gamma RT = u^2/(\gamma-1)\,C_pT$.

Thus

$$\frac{1}{\rho}\frac{d\rho}{dx} = \frac{1}{[1 + (\gamma-1)\,M^2]}\frac{1}{p}\frac{dp}{dx} \tag{45}$$

and

$$\frac{1}{T}\frac{dT}{dx} = \left[\frac{(\gamma-1)\,M^2}{1 + (\gamma-1)\,M^2}\right]\frac{1}{p}\frac{dp}{dx} \tag{46}$$

which implies that the changes in gas properties inside the absorber are neither isentropic nor isothermal. Note that Eqs. (45) and (46) do not apply to k = 0, in which case the trivial, constant property solution is obtained.

Two important conclusions can be derived from this analysis:

(a) Gas which is discharged from the absorber while the pressure in the cavity is still fluctuating will have a density variation "imprinted" on it, corresponding to the cavity pressure variations, according to Eq. (45). Even after these cavity pressure fluctuations decay, and assuming that the gas which is already in the cavity responds to this decay isentropically, there will be a residual density variation in the cavity given by

$$\frac{d\rho}{\rho} = \left[\frac{1}{1 + (\gamma-1)\,M^2} - \frac{1}{\gamma}\right]\frac{dp}{p} \tag{47}$$

BOTTOM OF PAGE

or

$$\frac{d\rho}{dx}\left(x', t' = \frac{W}{U}\right) = \left\{\frac{(\gamma-1)(1-M^2)}{\gamma\left[1+(\gamma-1)M^2\right]}\right\}\frac{dp}{p}(0,t') \qquad (48)$$

where x' refers to the width of the cavity, from x' = 0 to x' = w, and t' refers to the time interval during which the cavity was filled,* varying from t' = 0 to t' = W/U. This form of density variation imprinted on the incoming gas is often referred to as an "entropy wave."

(b) Gas which remains in the absorber after the pressure fluctuations in the cavity have subsided is not in a uniform state. The spatial (x) property variations will depend on the spatial and temporal form of the pressure fluctuations which existed in the absorber while pressure waves were interacting with it. A more detailed analysis will be required to determine the exact variations in the gas properties left behind in the absorber.

The above discussion indicates that an unchoked flow-through absorber may not be acceptable as an upstream absorber for any pulsed laser. Similar problems can be anticipated with passive absorbers, which interact with the gas in the flow duct (and cavity) whenever the pressure fluctuates there. Under the current program we have demonstrated (e.g., Section 3.1.3) that a vented duct absorber introduces disturbances into the gas which would be inadmissible for a high-beam-quality laser. More analysis and experimentation is clearly warranted for resolving this upstream pressure-wave suppression problem for fusion-type lasers. There is a need for innovative ideas and new techniques and devices.

3.1.3

innovative

* t' and x' are related through t' = (W-x')/U, where U is the mean-gas velocity and W/U is the cavity fill time.

2.1.3 Other Salient Problems of Fusion Laser Flow Systems

In this section we will identify and review some additional flow problems (other than pressure-wave suppression) which are relevant to the design of fusion laser flow systems. We will also attempt to grade these problems according to the level of technical effort which will be required to resolve them. The results of this exercise are presented in Table 2-5.

Temperature Uniformity

The need to maintain a temperature uniformity of the order of a few tenths or a few hundreths of a degree Kelvin in a large flow system represents a formidable task. It must be done within the allowable pressure drop constraints, imposed by the overall flow (and system) efficiency requirements. The outer environment of the flow system will require a close thermal control. Because of the temperature cycling which the gas undergoes, due to successive initiation and cooling, and its complex flow pattern, additional thermal conditioning stations may be required in the flow loop. If the temperature conditioning is performed with a combination of stream-wise heat exchangers and wall heat transfer (heating or cooling), a pressure drop penalty must be paid. Hence, the difficulty of achieving the required temperature uniformity depends to a large extent on the pressure drop "allocated" to suppress the (initiation) pressure waves. Since thermal conditioning also involves pressure drops (like flow and acoustic conditioning), it should be easier to achieve the desired temperature uniformity in low repetition rate and low Mach number lasers.

Interface and Flow Stability

Shortly after the initiation process in the laser cavity, there exists an interface with a temperature jump between the cold gas and the initiated (hot) gas. When this interface is accelerated by either the upstream- or the downstream-traveling shock wave, a Rayleigh-Taylor-type of instability can develop at the interface. Such an instability has been observed in combustion phenomena as well as in CO_2-electric discharge laser cavities. The instability will probably occur in all repetitively pulsed lasers with shock waves of sufficient strength. There are several

Table 2-5. Hierarchy of Technological Problems in Fusion Laser Flow System Design

PROBLEM	SOLUTION PROSPECTS
Pressure Wave Suppression	Difficult to Very Difficult
Temperature Uniformity	Difficult to Very Difficult
Flow and Interface Stability	Difficult
Large-Scale Vorticity	Easy to Difficult
Boundary-Layer Separation	Easy to Difficult
Unsteady Flow Phenomena	Easy to Difficult
Turbulence Velocity Fluctuations	Easy to Difficult to Very Difficult

problems associated with this instability: (a) it can cause a flow-reversal and thereby require larger flush factors, C; (b) it can generate flow nonuniformities and thereby degrade the beam; and (c) it can contribute to the generation of three-dimensional pressure waves, due to reflections from the curved interface. It is not clear at present how serious a problem this is. It will clearly require further analysis and experimentation.

Large-Scale Vorticity

In a closed-loop fusion laser flow system, large-scale vortices will be produced predominantly by the compressor (or fan) that drives the flow. Secondary sources of large-scale vorticity are the 90° bends in the flow loop. Flow conditioning devices such as screens, honeycombs, baffles, etc., can be employed to reduce the vorticity and smooth the flow. However, such devices will impose additional pressure drops on the flow system.

Boundary-Layer Separation

Unsteady boundary-layer separation is a potential problem in any closed-cycle laser. If it occurs, there is a possibility of large-scale random disturbances being fed into the laser cavity as the flow is convected around the flow loop. Separation can be avoided by distributing the momentum within the boundary layer more uniformly. This can be achieved by vortex generators which inject low momentum fluid from the bottom of the boundary layer into the outer part of the boundary layer and vice versa. It can likewise be achieved with active boundary-layer control techniques. Any boundary layer control technique employed will incur a flow power penalty and reduce the flow efficiency.

Unsteady Flow Phenomena

The appearance of alternate slugs of hot/cold gas in the flow loop and the repetitive nature of flow suggests that there is a possibility of periodic (large-scale) disturbances (thermal or vortical) propagating around the circuit. It may be necessary to design special elements of the flow system to eliminate these potential flow instabilities.

Turbulence Velocity Fluctuations

This could become a very difficult problem for flow systems with $M > 0.1$. If the flow Mach number becomes too large, then the required turbulence levels become very small ($\lesssim 10^{-3}$) and hard to achieve. A number of turbulence control elements (e.g., screens) will have to be employed and a substantial pressure drop will be incurred. This problem too becomes much easier for low Mach number flow systems.

2.2 FLOW SYSTEMS FOR CO_2 LASERS

2.2.1 Summary of the Relevant Laser Properties

As shown in the previous section (2.1), the laser properties which will affect the flow system design and performance are:

(a) the laser gas mixture, pressure and temperature

(b) the cavity shape and dimensions

(c) the initiation energy deposited in the cavity per pulse

(d) the laser energy extracted per pulse

(e) the pulse repetition frequency (PRF)

(f) the laser wavelength.

In the present study we have considered two CO_2 laser modules. The first is based on the demonstrated performance of a currently operating CO_2 laser; i.e., the HELIOS laser at LASL. The second is based on a hypothetical upgrade of the existing laser modules which could increase the total energy extracted per pulse by a factor of 10. The upgrade is essentially conservative, but would still require substantial technical development.

The flow-system-related properties of a demonstrated CO_2 laser module are presented in Table 2-6 (Ref. 2-14). This module operates with an E-beam sustained electric discharge. A 300 kV (peak), 1 A/cm^2 E-beam, with a pulse duration of 5 μsec is used. A DC field of 200 kV, with 8 A/cm^2 is applied for 3 μsec during the E-beam pulse. The combined energy deposition density is thus 250 J/liter (or about 100 J/lit-atm), average. The small-signal-gain of this device is 0.3%/cm and spontaneous emission is controlled by a bleachable absorber, placed at one end of the cavity, with an absorption thickness of $\alpha\ell = 9$. The extracted energy fluence is 0.8 J/cm^2, well within the damage threshold limit of the NaCℓ windows used.

The multi-line saturation fluence for the gas mixture and pressure listed in Table 2-6 is about 0.3 J/cm^2. The maximum extractable energy is thus

Table 2-6. Flow-Related Properties of a Demonstrated CO_2 Laser Module (The HELIOS System, at LASL).

Gas Mixture	$He/N_2/CO_2$ = 3/0.25/1
Gas Pressure	1800 Torr
Gas Temperature	Room Temperature
Cavity Volume	245 Liters
Optical Length, L	200 cm
Initiation Height, H	35 cm
Flow Width, W	35 cm
Deposited Energy Density	100 Joule/lit-atm
No. of Amplified Pulses	1 Pulse per Initiation
Extracted Energy Density	1.66 Joule/lit-atm
Pulse Repetition Frequency, PRF	Single Shot
Laser Wavelength	10.6 μ
Total Energy Extracted	1 K Joule
Initiation Efficiency	1.66%

$$S = (E_{ex} - E_{in}) = g_o J_s \text{ joule/liter (or 3.8 joule/lit-atm)}$$

where g_o is the small signal gain and J_s the saturation fluence. The extraction efficiency of this system is therefore η_{ex} = 1.66/3.8 = 44%.

The projected properties of a 10 kJ CO_2 laser module are presented in Table 2-7. The scale-up is based on a nearly 40% increase in the gas pressure (to 2500 Torr) and a similar increase in the cavity height and width, as compared to the demonstrated system. The optical length, L, is left unchanged so that amplified spontaneous emission (ASE) can be controlled. It is assumed that the E-beam and discharge voltages will be made proportional to the product of initiation height and gas pressure, so that optimal E/N values will be maintained. The E-beam and discharge current densities are assumed to remain the same as in the HELIOS system. The energy deposition density will thus remain essentially unchanged too, at 100 J/lit-atm. The gas mixture will be most likely a pure N_2/CO_2 mixture, at a ratio of 0.25/1, which should produce a higher laser efficiency. The specific effects of this gas mixture on the initiation requirements are not considered here. The small signal gain under these conditions should be g_o = 0.4%/cm and the saturation flux J_s = 0.4 J/cm^2. The extractable energy per pass should thus be 16 J/liter. Assuming no change in the extraction efficiency (η_{ex} = 44%), about 7 J/liter (or 2 J/lit-atm) should be extracted from this laser cavity per pulse. We assume finally that a multi-pulse power extraction scheme will be used in this laser (see e.g., Refs. 2-15 and 2-19), with three successive pulses going through the laser cavity, at 0.5 μsec intervals, and nearly 7 J/liter extracted by each pulse. The total energy extracted will thus be 20 J/liter (or 6 J/lit-atm), with an initiation efficiency of about 6%. If more than three to four pulses are passed through the amplifying medium, the energy extracted per pulse diminishes significantly compared to the first pulse.

The E-beams, PFN's and power supplies required for this scaled up CO_2 laser are within the current state of the art. Multipulse amplification is, however, a new concept which requires experimental verification and technological development. The increased cavity cross section will

Table 2-7. Projected Flow-Related Properties of an Advanced CO_2 Laser Module.

Gas Mixture	N_2/CO_2 = 0.25/1
Gas Pressure	2500 Torr
Gas Temperature	Room Temperature
Cavity Volume	500 Liters (or TBD)
Optical Length, L	200 cm
Initiation Height, H	50 cm
Flow Width, W	50 cm (or TBD) P)
Deposited Energy Density	100 Joule/lit-atm
No. of Amplified Pulses	3 Per Initiation
Extracted Energy Density	6 Joule/lit-atm
Pulse Repetition Frequency, PRF	TRD TBD
Total Energy Extracted	10 K Joule (or TBD) P)
Initiation Efficiency	6%

require correspondingly larger salt windows which must also withstand a 40% increase in pressure. No such windows are currently manufactured and this too may require a substantial technological development. Aerodynamic windows should be considered as a possible replacement for salt windows, particularly for repetitively pulsed laser operation.

2.2.2 Beam Quality Requirements

CO_2 fusion laser beams at λ = 10.6 μm are required to have a good BQ due to their relatively long wavelength. This statement is made for a situation where the focal length of the "last mirror" is 15 m and the laser aperture is 0.5 m (largest envisioned initiation dimension). A 15 m safety distance has been used in previous system studies, and the 1/2 m dimension is based upon a modest increase of the 35 cm initiation dimension used in the HELIOS Laser System. Equation (1) then implies that the focussable spot size is related to the beam quality by

$$d(mm) = 0.636\ BQ \tag{49}$$

This relationship implies that the smallest spot size which can be obtained (BQ = 1) is 0.636 mm; it also implies for a spot size of 1 mm the maximum allowable BQ = 1.57. The required beam quality range is thus bounded by $1 < BQ \leq 1.57$. For this range of BQ the permissible phase aberrations are small and the exponential expression can be used for estimating the required media homogeneity.

Equations (1) and (4) were used to compute the required medium homogeneity of an advanced CO_2 laser (Table 2-7). The results are shown in Figure 2-9. The maximum spot size boundary reveals that the medium homogeneity must be better than 6.4×10^{-4}. Note that for a near-perfect beam (BQ $\approx$ 1.01), the medium homogeneity has to be about an order of magnitude better than that corresponding to BQ = 1.57, even though the focussed spot size is only 1/3 smaller.

The requirements on the random density disturbances are calculated from Equations (5a) and (5b). These requirements can be written as

$$\left(\frac{\Delta\rho}{\rho_1}\right)^R_{rms} \leq \left(\frac{\Delta\rho}{\rho_1}\right)^0_{rms} \frac{\Lambda^{1/2} L^{1/2}}{D} \tag{50}$$

when the turbulence scale $\Lambda \geq D$, and

$$\left(\frac{\Delta\rho}{\rho_1}\right)^R_{rms} \leq \left(\frac{\Delta\rho}{\rho_1}\right)^0_{rms} \left(\frac{L}{\Lambda}\right)^{1/2} \tag{51}$$

when $\Lambda < D$. Superscripts "R" and "0" stand for random and ordered variations, respectively. $(\Delta\rho/\rho_1)^0_{rms}$ represents the ordered disturbances as discussed in the preceding paragraph and presented in Figure 2-9.

The cavity geometry selected in Section 2.2.1 above has an optical length of L = 2m and an initiation aperture dimension $D \approx H = 0.5m$. Thus we can determine the dependence of the allowable random $(\Delta\rho/\rho_1)^R_{rms}$ versus the inhomogeneity scale size, Λ. This is shown in Figure 2-10. Since we expect Λ to be relatively small compared to the aperture dimension, the random $(\Delta\rho/\rho_1)^R_{rms}$ can be at least an order of magnitude (or two) larger than the ordered $(\Delta\rho/\rho_1)^0_{rms}$. Hence, for the 1-mm spot size $(\Delta\rho/\rho_1)^0_{rms} \leq 6.4 \times 10^{-4}$ and the random $(\Delta\rho/\rho_1)^R_{rms} \lesssim 6.4 \times 10^{-3}$.

The pressure and temperature uniformity requirements and their relationship to the initiation overpressure are shown in Figure 2-11. The CO_2 laser gas mixture of interest for the advanced system is $CO_2:N_2 = 4:1$, with a $\gamma = 1.30$. For an energy deposition of 100 J/lit-atm at an initial temperature of $T_1 = 300°K$, we compute from (13), $(\Delta p/p_1)_{init} = (\Delta T/T_1)_{init} = 0.27$. The initial overpressure must thus be reduced by a factor of 325 if a focal spot size of 1 mm is to be achieved.

The requirements on the velocity uniformity are presented in Figure 2-12. Δu represents the ordered velocity fluctuations and u' the random, small-scale (turbulent) velocity fluctuations. U is the mean velocity. A range of Mach numbers, from M = 0.03 to M = 0.30, is considered. The velocity uniformity required to obtain a focal spot size of d = 1 mm is within the realm of conventional wind tunnel technology, for the range of Mach numbers considered here. For M = 0.3 or larger, the flow uniformity must be carefully controlled. Similar requirements have been met in the past in low noise and low turbulence wind tunnels (see, e.g., Reference 2-5).

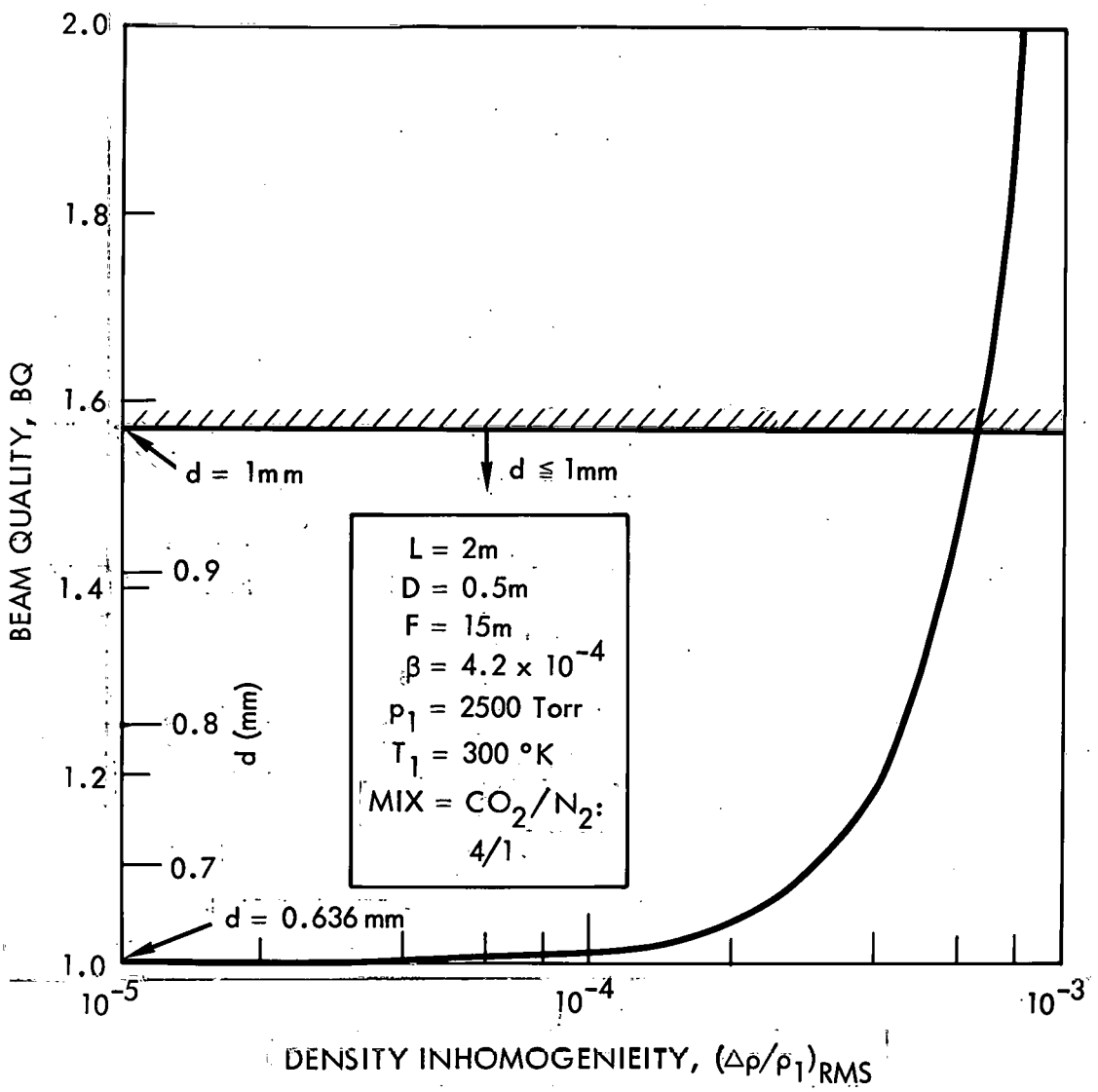

Figure 2-9. Beam Quality Requirements for a CO_2 Fusion Laser.

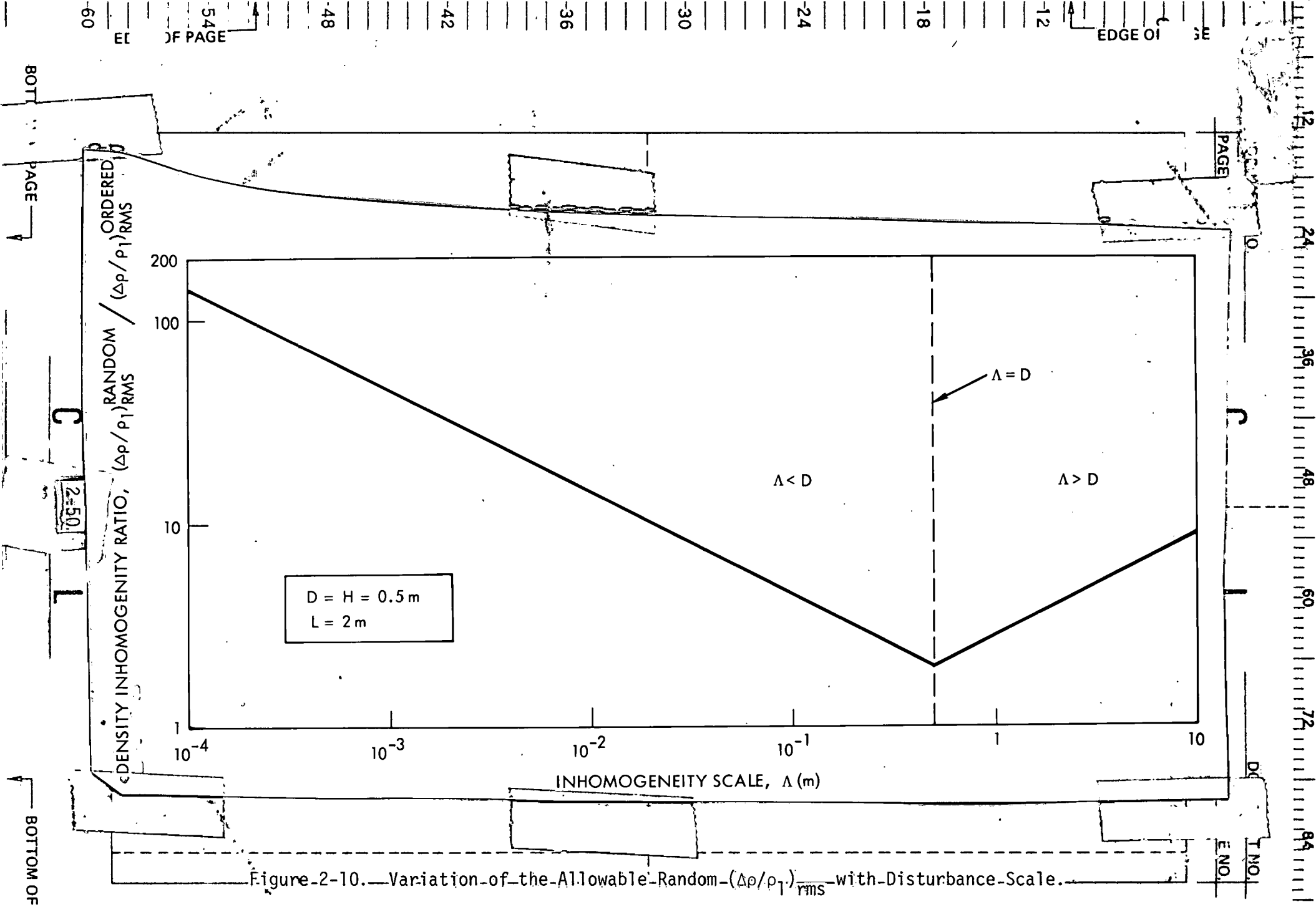

Figure 2-10.—Variation of the Allowable Random $(\Delta\rho/\rho_1)_{rms}$ with Disturbance Scale.

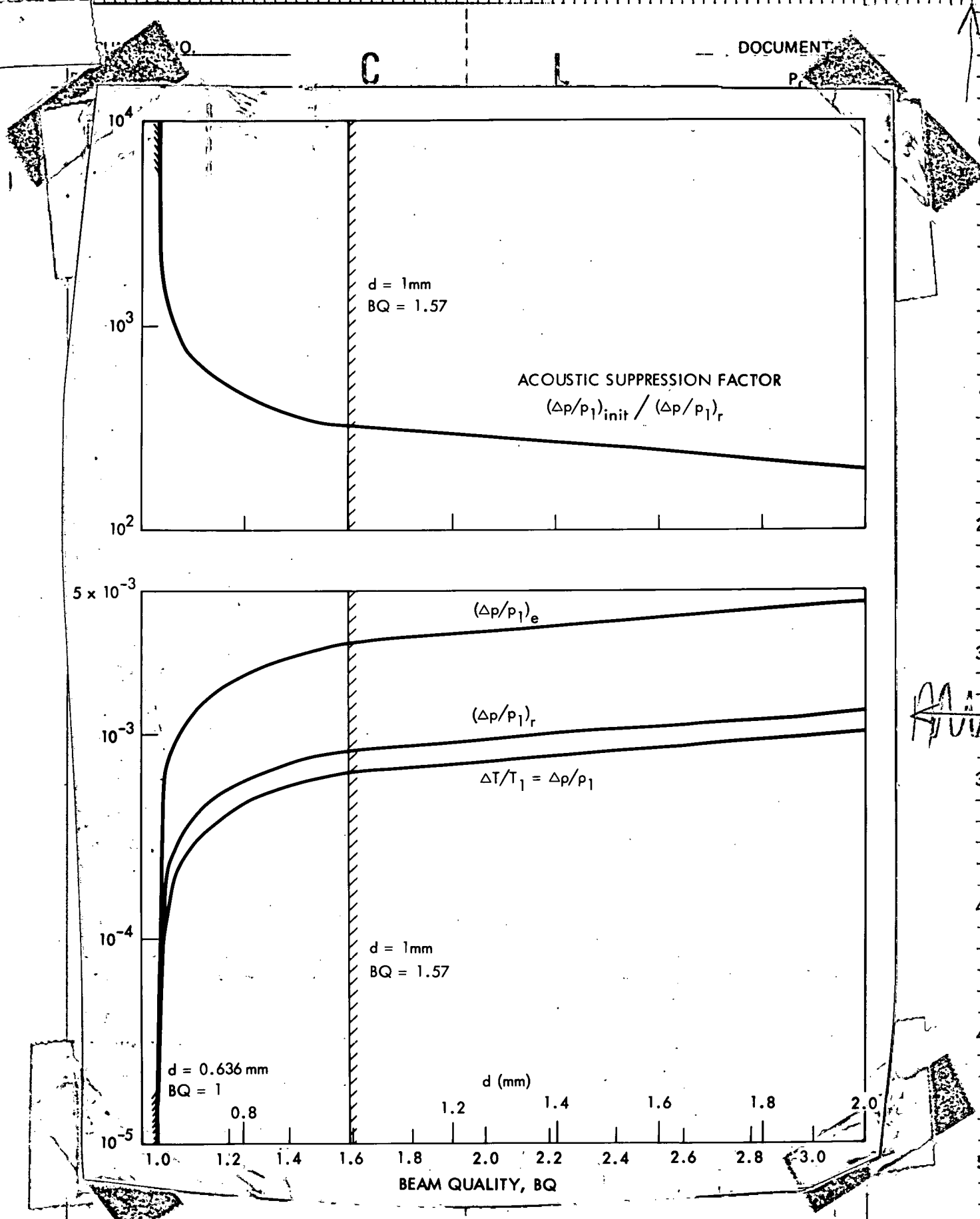

Figure 2-11. Pressure and Temperature Uniformity Requirements for a CO_2 Laser.

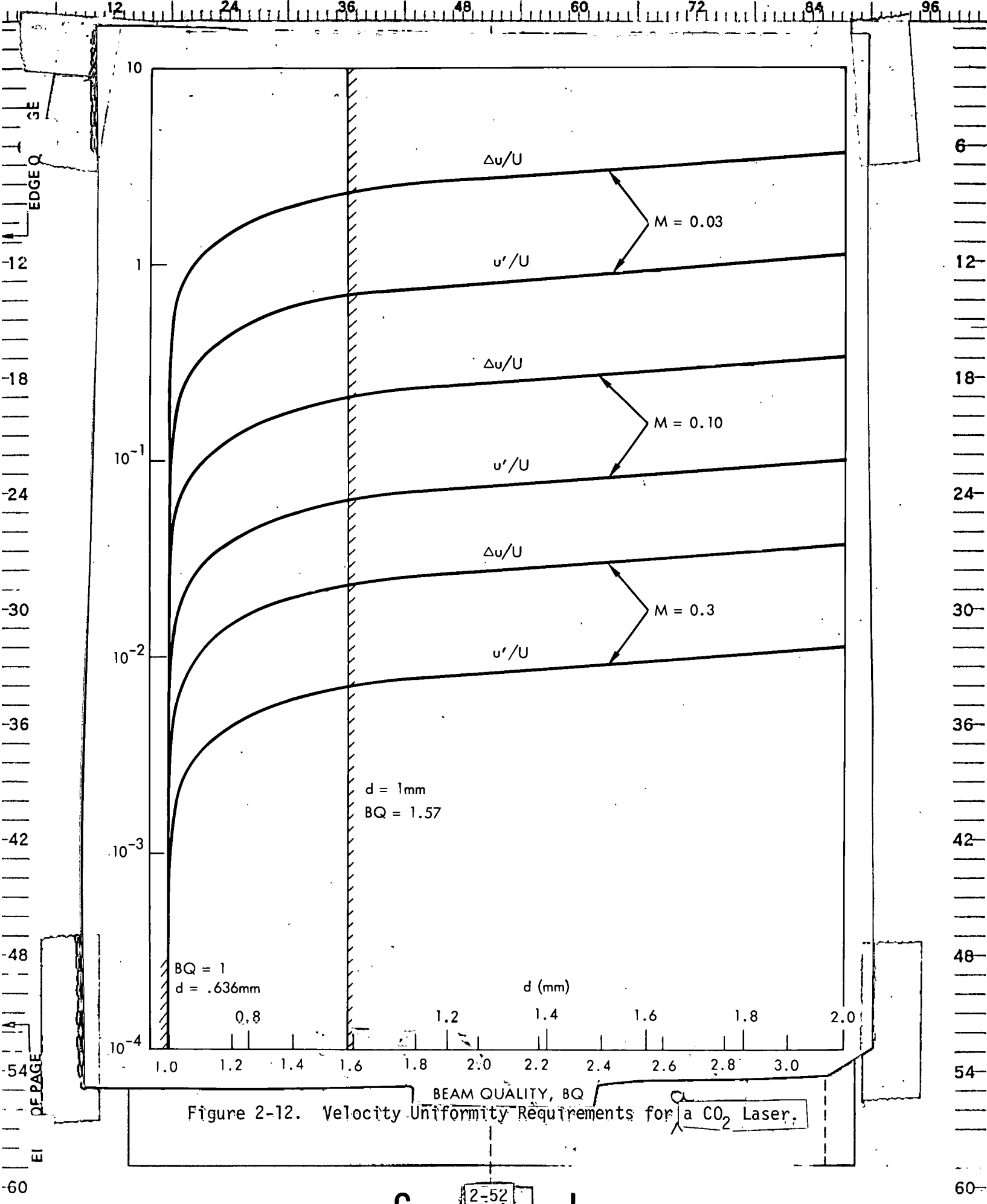

Figure 2-12. Velocity Uniformity Requirements for a CO_2 Laser.

2.2.3 Average Flow Requirements; Mach Number

The average (mean) flow velocity U depends on two other flow system parameters, W and PRF, as indicated by Equation (36). Division by the speed of sound provides the Mach number. The speed of sound for the 4:1 gas mixture with a molecular weight of 40.8 at T_1 = 300°K is 282 m/sec. Figure 2-13 shows the variation of the required mean velocity and Mach number, as a function of the cavity width, W, and the PRF, for a CO_2 laser. The range of W shown is probably the largest range one would want to consider, with the 0.5 m flow dimension giving a square cavity aperture and 5 m dimension yielding a slender flow channel with aspect ratio of 10. The PRF range indicated is also rather wide, but consistent with repetition rates considered for fusion lasers.

2.2.4 Flow Efficiency Requirements

The general discussion of flow efficiency in Section 2.1.1.2 is here made specific to the CO_2 system. In particular, Figure 2-3 is utilized to indicate a more limited range of efficiency parameters. The relationship between overall laser efficiency and the initiation and flow efficiencies is shown again in Figure 2-14. Three boundary lines have been drawn. The minimum required overall CO_2 laser system efficiency is assumed to be 5% (see Ref. 2-19). This immediately establishes a minimum initiation efficiency (5%). The maximum or "limiting" initiation efficiency has not been established analytically or experimentally. Long pulse (20 μsec) efficiencies of 30% have been quoted for CO_2 lasers. Twenty percent is the upper limit ever suggested for short pulse CO_2 lasers.[2-19] With $\eta_I \leq 20\%$, the minimum flow efficiency is 6.7%. Note how critically the minimum flow efficiency depends upon the (electrical) initiation efficiency. The flow system will have much stricter requirements (allowable pressure drop) if the initiation efficiency does not significantly exceed 5%. The flow efficiency range of 10-20% (indicated) is both realistic and achievable as described further below.

We recall that the flow efficiency is inversely proportional to the overall flow-system pressure drop, as shown in Figure 2-4. The above comments relating to flow efficiency can help to bound the allowable pressure drop for the CO_2 laser system. This is shown in Figure 2-15.

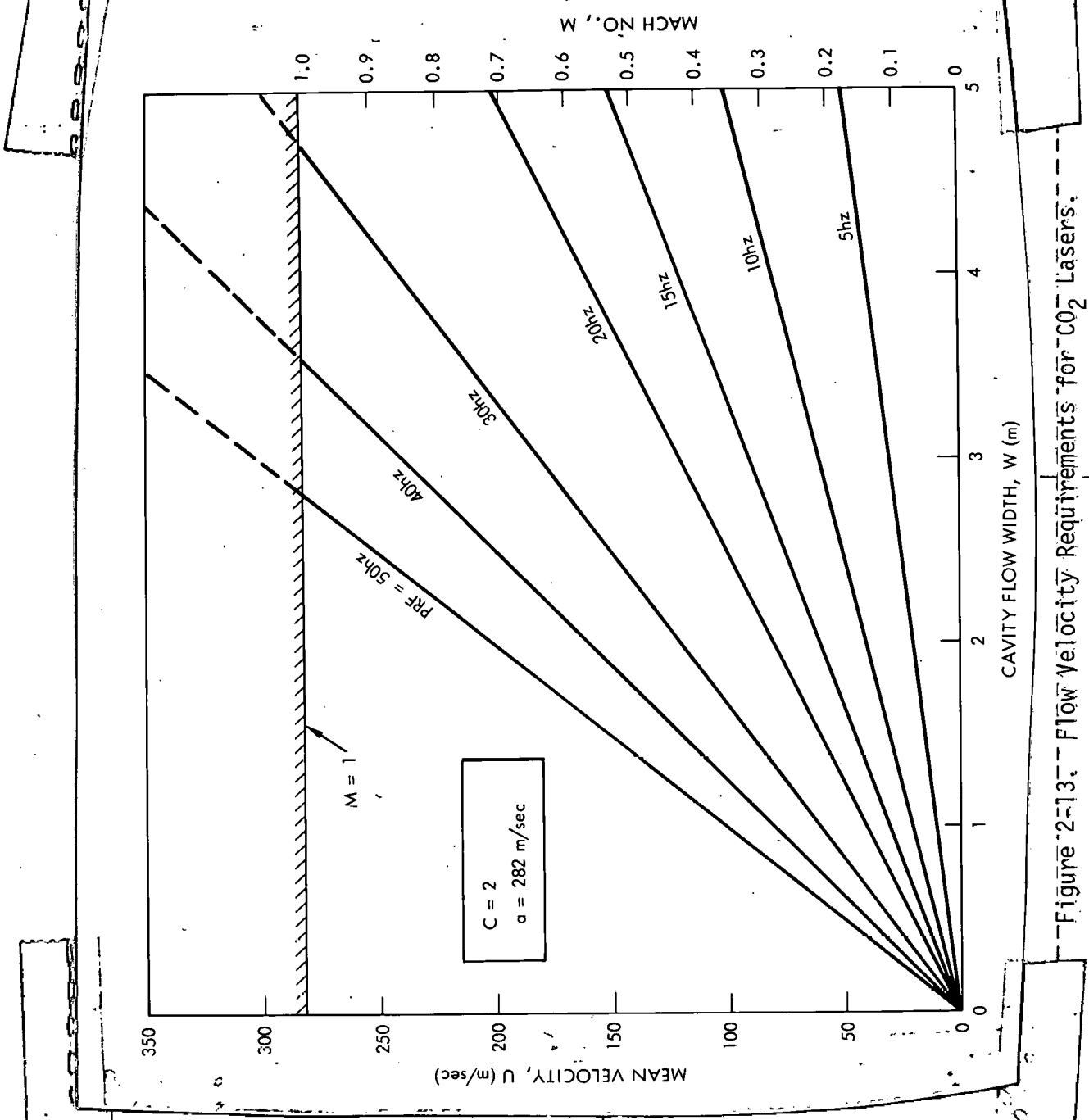

Figure 2-13. Flow Velocity Requirements for CO_2 Lasers.

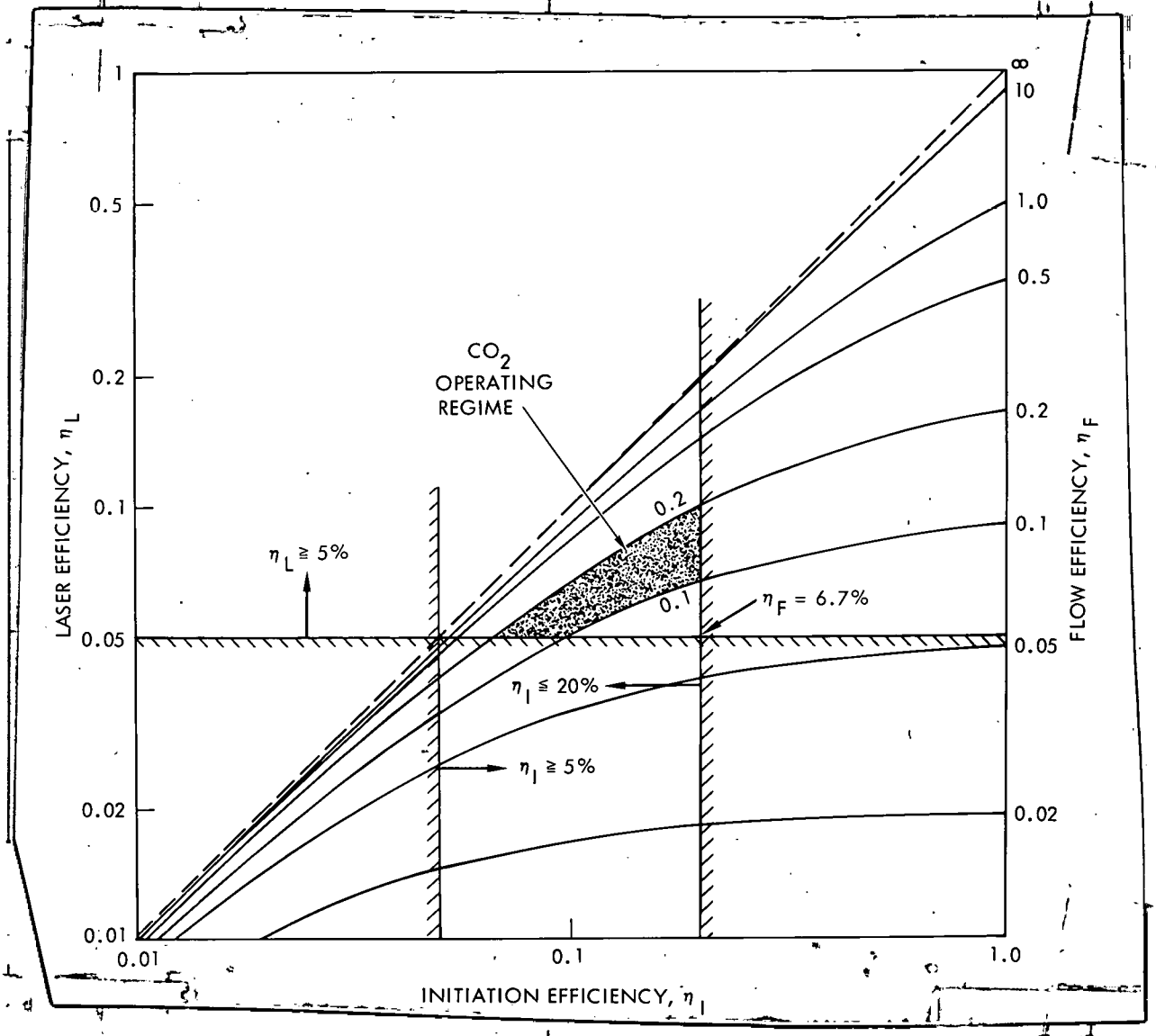

Figure 2-14. CO_2 Fusion Laser System Efficiencies.

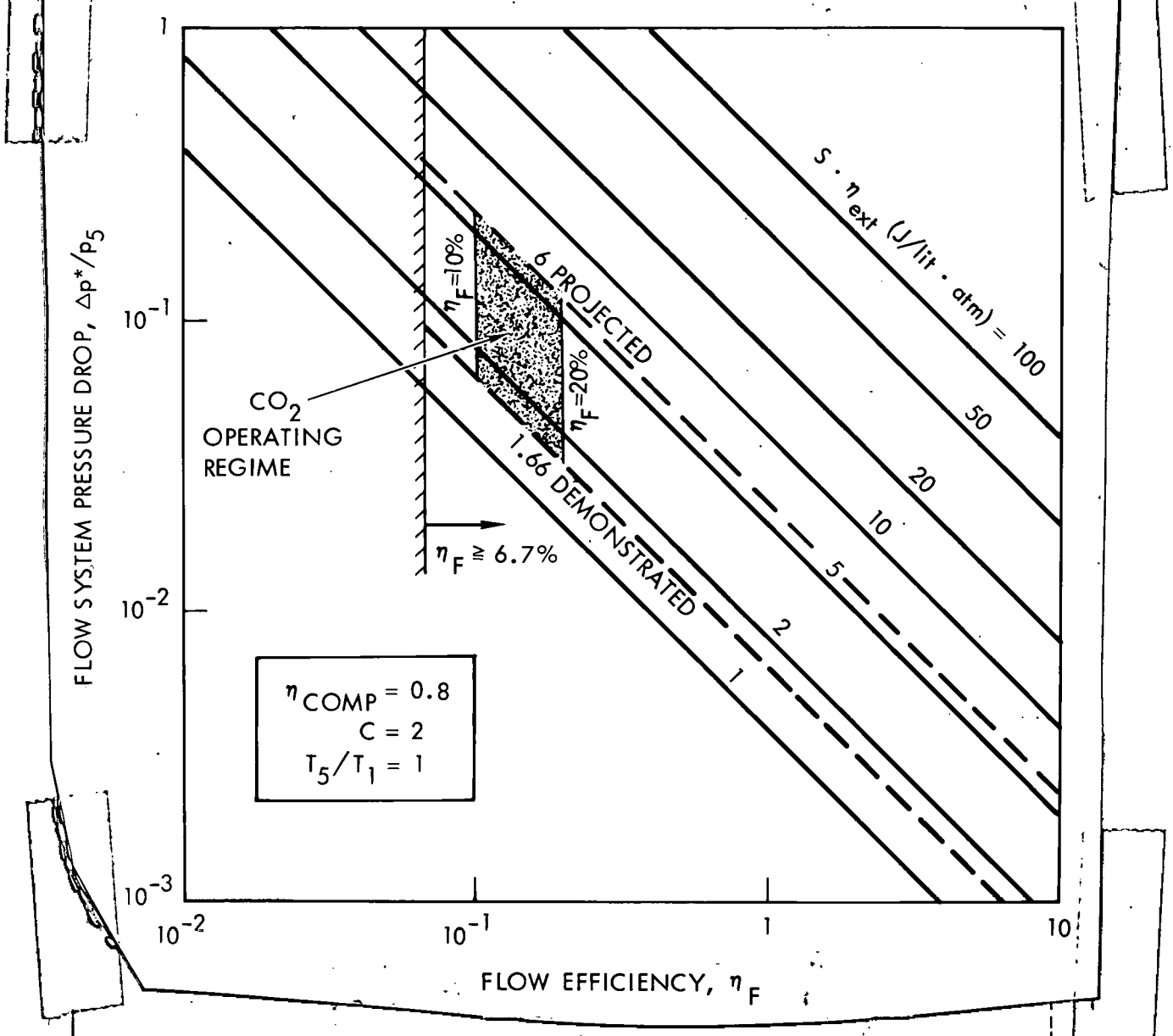

Figure 2-15. Permissible Pressure Drop Versus Required Flow Efficiency in a CO_2 Fusion Laser.

BOTTOM OF PAGE

The minimum flow efficiency of 6.7% is shown. The extracted energy density will determine the permissible pressure drop; the LASL HELIOS laser has demonstrated 1.66 J/lit-atm and we have projected a 6 J/lit-atm for an advanced high gain system. These $S \cdot \eta_{ext}$ lines are shown dashed in Figure 2-15. We have also added the realistic η_F range of 10-20% and indicated the CO_2 operating regime. For the projected extraction energy density of 6 J/lit-atm, the allowable pressure drop $\Delta p^*/p_5$ varies between 0.237 at $\eta_F = 0.10$, to 0.119 at $\eta_F = 0.20$. These values point to the need for meeting all the flow and beam quality requirements at the smallest $\Delta p^*/p_5$ possible. Note that a conventional low-speed wind tunnel with a test section velocity of 100 mph can operate with a pressure drop of approximately 4×10^{-3}, or about a factor of 50 or so smaller than the allowable numbers quoted here. Hence the flow system for the fusion laser has "excess" pressure drop available, which can be utilized for pressure suppression at the required $(PRF)^{-1}$ and other flow conditioning requirements. Quantitative estimates for the various contributions to the overall pressure drop in a CO_2 system are presented in the next subsection.

2.2.5 Estimation of Flow-Loop Pressure Drop

The rather general pressure drop relationships described in Section 2.1.1.2 are now made specific to the CO_2 laser system. We again consider the contributions listed in Table 2-3.

Cavity Heat Addition

The relatively small allowable pressure drop for fusion lasers will necessitate the use of relatively small flow Mach numbers ($\lesssim 0.3$). This implies that the previously derived expression for cavity heat addition pressure drop can be significantly simplified since M^2 (< 0.1) appears frequently in (27) and (29). To first order, $K_1 = M_2^2/M_1^2 - 1$, and also $T_{01}/T_{01} = M_2^2/M_1^2 - 1$. Hence, we obtain for Equation (28)

$$p_{01} - p_{02} = \frac{\rho_1 V_1^2}{2}\left(\frac{\Delta T_{01}}{T_{01}}\right) \tag{52}$$

and the pressure drop resulting from heat addition ($\Delta p_1^* \equiv p_{01} - p_{02}$) is given by

$$\Delta p_1^* = \left(\frac{\Delta T_{01}}{T_{01}}\right) q_1 \quad \text{and} \quad K_1 = \left(\frac{\Delta T_{01}}{T_{01}}\right) \tag{53}$$

For the advanced CO_2 laser system, the net energy deposition density is $\Delta Q = S \cdot \eta_{ext} = 94$ J/lit-atm. The other parameters needed to define $\Delta T_{01}/T_{01}$ are $\rho_1 = 5.45$ gm/lit, (at $p_1 = 3.29$ atm), $C_p = 0.87$ J/gm-°K, and $T_{01} = 300$°K. The result is $\Delta T_{01}/T_{01} = 0.217$. The resultant contributions to the pressure drop are tabulated in Table 2-8, with the cavity Mach number M as the parameter. We use the range 0.03 to 0.3. The calculated pressure drops for cavity heat addition range from 0.317 Torr to 31.7 Torr.

Subsonic Diffuser

The loss coefficient for the subsonic diffuser has a range $0.25 \lesssim K_3 \lesssim 0.40$. We use an intermediate value of $K_3 = 0.30$ in our pressure drop estimations. The resulting contributions to the pressure drop are shown in Table 2-8. This range of pressure drop varies from 0.438 Torr to 43.9 Torr.

Table 2-8. Pressure Drop Contributions for a CO_2 System at 2500 Torr Nominal Cavity Pressure. (Tabulated Values are in Torr).

		M = 0.03	0.1	0.3
Cavity Heat Addition	Δp_1^*	0.317	3.53	31.71
Subsonic Diffuser	Δp_3^*	0.439	4.88	43.9
Pressure Suppressors	$\Delta p_2^* + \Delta p_9^*$	$\Delta p_2^* + \Delta p_9^*$	$\Delta p_2^* + \Delta p_9^*$	$\Delta p_2^* + \Delta p_9^*$
Flow Turns	Δp_T^*	0.878	9.75	87.8
Flow Conditioning	Δp_{C1}^*	0.0051	0.052	0.234
	Δp_{C2}^*	2.93	32.5	292.5
	Δp_{C3}^*	0.366	4.06	36.6
Heat Exchangers	Δp_5^*	1.649	18.31	164.9
	Δp_7^*	0.729	8.10	72.9
Boundary-Layer Friction	Δp_F^*	0.0642	0.65	6.42
Totals (Excluding $\Delta p_2^* + \Delta p_9^*$)		7.38 Torr	81.8 Torr	737.0 Torr
$\overline{\Delta P^*/P_1}$ (Excluding $\Delta P_2^* + \Delta P_9^*$) for the Advanced CO_2 Laser (P_1 = 2500 Torr)		2.95×10^{-3}	3.27×10^{-2}	2.95×10^{-1}

Pressure Suppressors

The pressure drops of the downstream (Δp_2^*) and upstream (Δp_9^*) suppressors are not predetermined. Their permissible values will be shown in Section 2.2.6.

Flow Turns

Well-designed flow corners with turning vanes have loss coefficients of about $K_T = 0.15$. Since there are four corners in the flow system, the total loss coefficient is $4K_T = 0.60$. The resulting pressure drop contributions are given in Table 2-8 and their range is from 0.878 Torr to 87.8 Torr.

Flow Conditioning

A reasonable length for the contraction section is about 5H. Note that a carefully contoured contraction section could be designed with a length $\ell_c \approx H$; however, such a rapid contraction could produce excessive flow nonuniformities. If we utilize $\ell_c/H = 5$ and a turbulent skin friction coefficient, $C_f = 0.08\ Re^{-1/4}$, we obtain values of $K_{c1} = 0.0036$, 0.0026, 0.0012 at M = 0.03, 0.1, 0.3, respectively. Hence the values of p_{c1}^* can be calculated (Table 2-8). These contributions are generally negligible.

The screen loss coefficient was chosen to be 1. If we employ two such screens upstream of the laser cavity, the pressure drop contributions are as shown in Table 2-8. The range of Δp_{c2}^* varies from 2.92 to 292.5 Torr. We shall assume there is one honeycomb with $K_{c3} = 0.25$ and the contributions are listed in Table 2-8.

Heat Exchangers

The cavity heat addition increases the stagnation temperature from 304.5°K to 369.6°K at M = 0.3, from 300.5°K to 365.7°K at M =0.1, and from 300.0°K to 365.1°K at M = 0.03. Hence, with a coolant temperature T_5 of 250°K, $K_5 = 1.13$ (nearly independent of M). The contributions to Δp_5^* are as shown in Table 2-8.

In the preceding section we have observed that the allowable $\Delta p^*/p_5$ for the CO_2 fusion laser system is limited to be at most ≈ 0.24. For this value the compressor will heat the laser gas by about $\left(1 + \frac{(\gamma-1)}{\gamma} \frac{p^*}{p_5}\right)$ T_{01} or 16.6 °K. Hence, using a coolant temperature of T_7 ($\leq$ 250°K with T_{06} = 316.6 °K results in K_7 = 0.498, with the contributions to Δp_7^* as shown in Table 2-8.

Boundary-Layer Friction

The frictional losses depend on the "length" of the flow circuit relative to the cross section of the flow ducts. Even if we utilize a value of 20 for ℓ/D_h, due to the high Reynolds number of the flow the frictional effects will be quite small, as indicated in Table 2-8.

DOCUMENT NO.
PAGE NO.

2.2.6 Permissible Pressure Drops for the Acoustic Absorbers

The total pressure drop for the entire flow loop excluding the pressure suppressor contributions are given at the bottom of Table 2-8. We can obtain the permissible pressure drop for the acoustic absorbers once we know the overall allowable pressure drop based upon system efficiency considerations (Section 2.2.4). If we focus on the indicated CO_2 system operating range shown on Figure 2-15, we observe that for the projected 6 J/lit-atm extracted energy density the largest allowable $\Delta p^*/p_5$ is 0.237 (at η_F = 10%). The pressure p_5 is the pressure entering the compressor; its value is the laser cavity pressure p_1 (= 2500 Torr) minus the losses encountered up to the compressor station. From Table 2-8 we find (approximately) that p_5 = 2497 Torr at M = 0.03, p_5 = 2469 Torr at M = 0.1, and p_5 = 2214 at M = 0.3. Consequently the allowable pressure drops for the entire system are given in Table 2-9.

The permissible pressure drops for the acoustic absorbers are obtained by subtracting the total (excluding absorbers) pressure drop of Table 2-8 from the total allowable Δp^* of the entire system. The results are quite revealing. First of all, the losses at M = 0.3 are so large that one cannot meet the requirements independent of the acoustic absorber pressure drops. The pressure drops allowed for the acoustic absorbers at M = 0.03 and 0.1 are reasonable and offer enough room for satisfying the beam quality and flow uniformity requirements.

2.2.7 Preliminary Conceptual Flow System Design and Evaluation

In the preceding section, we concluded that the Mach number for the CO_2 fusion laser flow system must be less than 0.3. Values of M = 0.1 and 0.03 were acceptable since there appeared to be enough of a permissible pressure drop for the acoustic suppression. Utilizing this information, we propose here two specific flow systems that have significantly different geometries.

We first look at Figure 2-13 and observe that for our range of W $\sim$ 0.5 m to 5 m, the allowable pulse repetition frequencies can be anywhere from 5 Hz to 50 Hz if the maximum allowable $M_{max} \approx 0.2$. If we consider a large W cavity (3m) at M = 0.21 as one of our cases, then PRF = 10 Hz (with our typical flush factor C = 2). For this case, the total flow

DOCUMENT NO.
PAGE NO.

Table 2-9. Pressure Drop Summary for a CO_2 System. (Tabulated Values are in Torr)

	M = 0.03	0.1	0.3
Total Allowable Δp^*	591.8	585.2	524.7
Total Excluding Acoustic Absorbers	7.4	81.8	737.0
Permissible for Acoustic Absorbers $(\Delta p_2^* + \Delta p_9^*)$	584.4	503.4	(-)212.3

loop size becomes rather large as shown in Figure 2-16 (drawn to scale). The overall size of the entire flow loop is roughly 9 m x 21 m.

This laser amplifier module could produce 60 kJ of energy per pulse, assuming an advanced CO_2 laser design (Table 2-7). Due to the relatively high Mach number (from the pressure loss point of view), the flow system must be very carefully designed. Pressure must be conserved along the flow loop. The diffuser must be long and with a shallow opening angle. The flow turns must be carefully designed and the upstream flow conditioning will require careful contouring and several screens. Note that most of the flow loop cross section is five times larger in flow area than the laser cavity cross section, because this reduces the average flow velocity and minimizes the pressure losses.

Let us consider next a substantially smaller laser module and flow system. We return to Figure 2-13 and propose a system with a square (H x W = 0.5 m x 0.5 m) laser aperture. At W = 0.5 m, the range of pulse repetition frequencies (5 Hz to 50 Hz) implies $M \sim 0.018$ to 0.18. If we again select PRF = 10 Hz, then M = 0.035. At this low Mach number the flow-loop losses are very small and we do not have to be very fancy in designing the flow loop. We must still be careful in utilizing screens and other flow conditioners upstream of the cavity. The conceptual design is shown in Fgiure 2-17 (drawn to scale). We now have a constant area duct with a mean velocity of 10 m/sec in the entire laser flow system. The overall size of the flow loop (5 m x 3 m) is substantially smaller than for the large flow loop design (Figure 2-16). There is a factor of 12.6 reduction in the projected area of the entire system and it is only six times smaller in energy output per pulse.

The cost of the flow system will be roughly proportional to its volume. There will therefore be an incentive to decrease the flow loop volume required to generate a unit of extractable energy. In this sense the smaller (10 kJ) system is more cost-effective than the larger (60 kJ) system. In the smaller system (Figure 2-17), the flow loop volume is roughly 20 times larger than the cavity volume, whereas in the larger system (Figure 2-16) the flow loop volume is nearly 70 times larger than the cavity volume.

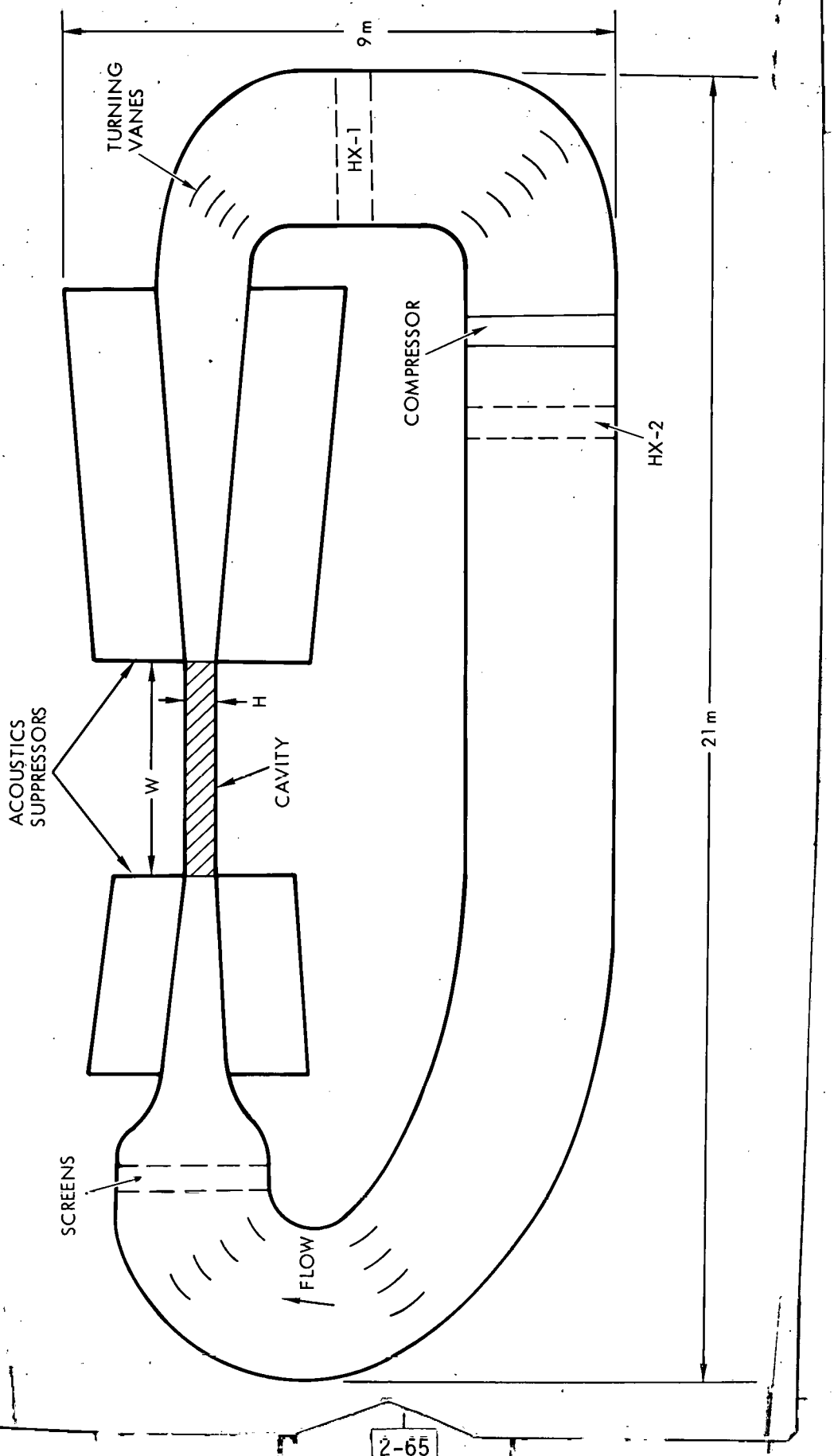

Figure-2-16:- Conceptual Design for a Large Scale CO_2 Laser Flow Loop (HXW = 0.5 m x 3 m, M = 0.21, PRF = 10 Hz).

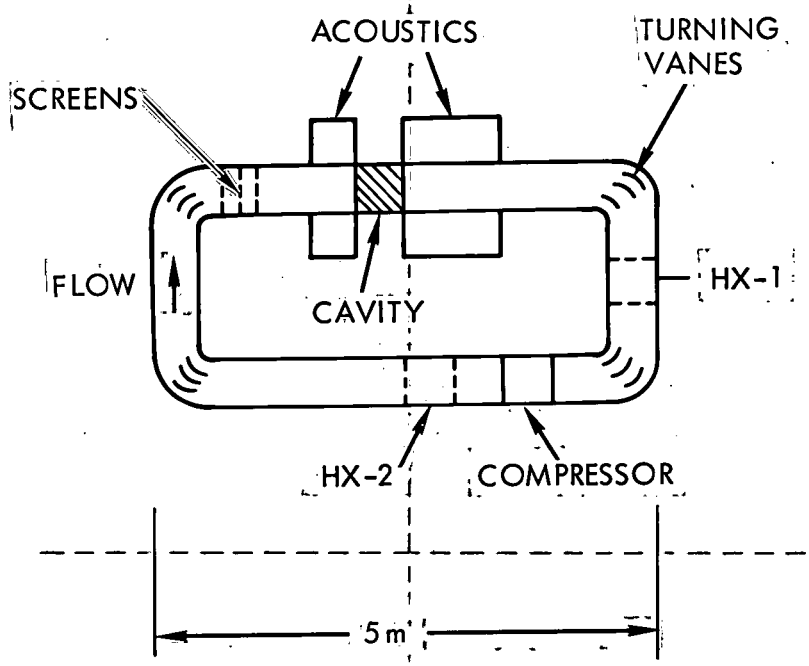

Figure 2-17. Conceptual Design for a Small Scale CO_2 Laser Flow Loop (HxW = 0.5 m x 0.5 m, M = 0.035, PRF = 10 hz).

Furthermore, the smaller module can be operated at lower Mach numbers, the pressure losses should be lower and it should also be easier to achieve the required media homogeneity conditions. It thus appears that flow-system considerations will drive the CO_2 laser power amplifier design toward moderately-sized modules -- of the order of 10-to-20 kJ, rather than 50-to-100 kJ per module.

2.3 FLOW SYSTEMS FOR KrF LASERS

2.3.1 Summary of the Relevant Laser Properties

The KrF laser has no "storage" capability and therefore it cannot produce the 1 to 10 nsec pulses which will be required for ICF. Multi-pulse amplification (in the form of angular optical multiplexing) and Raman pulse compression have been proposed as possible techniques for extracting short, intense pulses from the KrF medium (see Refs. 2-16 and 2-17). Neither one of these techniques was demonstrated to date on a large scale (namely, 1 kJ or larger).

It is therefore difficult at present to define a set of properties and operating conditions (such as listed in Section 2.2.1) for a short pulse laser system based on KrF. We nevertheless proceed and define three hypothetical laser drivers, based on KrF, so that a preliminary evaluation can be made of the flow system requirements of such drivers.

The first system to be considered here is based on using optical multiplexing alone as a means of obtaining short pulses from KrF. The final KrF amplifier is assumed to be pumped by an E-beam and to generate an excited gain media for 100 nsec. Ten consecutive 10-nsec pulses can then be sent through this amplifier, at slightly different angles, and combined (or stacked) after exiting the amplifier into one high-intensity beam.

Typical projected properties and operating conditions of such a laser are listed in Table 2-10, based on References 2-17 and 2-18. Only those properties which will affect the flow system design and performance are considered here. The justification for selecting this set of parameters can be found in the references cited.

Table 2-10. Projected Properties of a KrF Amplifier

Gas Mixture	$Ar/Kr/F_2$ = 0.937/0.060/0.003
Gas Pressure	1 Atm
Gas Temperature	Room temperature
Cavity Volume	250 liters (or TBD)
Optical Length, L	100 cm
Initiation Height, H	50 cm
Flow Width, W	50 cm (or TBD)
Deposited Energy Density	100 Joule/lit-atm
Extracted Energy Density	10 Joule/lit-atm
Pulse Repetition Frequency, PRF	TBD
Laser Wavelength	0.249 μm
Total Energy Extracted	2.5 kJ (or TBD)
Initiation Efficiency	10%

The operation of a KrF amplifier under the conditions listed in Table 2-10 will require an E-beam of about 500 kV, generating 100 A/cm^2 for 100 nsec. The saturation fluence under these conditions will be J_s = 0.1 $joule/cm^2$, with a small signal gain of g_o = 20%/cm and a non-saturable absorption coefficient of about α = 1%/cm. The maximum extractable energy density will approach 20 joule/lit. An extraction efficiency of 50% is assumed, yielding an extracted energy density of 10 joule/lit and a fluence of 1 $joule/cm^2$, well within the range of permissible power loadings for UV windows, such as quartz.

We consider next a system which uses a combination of angular multiplexing and Raman pulse compression. To specify the properties of such a system, as a basis for our flow studies, we assume that three 33-nsec pulses will be passed through a KrF amplifier, such as described in Table 2-10, and then stacked before entering the Raman cell. The Raman cell, filled with methane, is assumed to produce an additional compression by a factor of five to six.

We will first consider a low pressure (1 atm) CH_4-filled Raman cell (see, e.g., Ref. 2-17). The saturation fluence of the CH_4 cell at 1 atm is estimated to be 2 $joule/cm^2$. An input of 10 $joules/cm^2$ KrF laser pulse

will be required to obtain reasonably high (say, 50%) conversion to a compressed backward Stokes pulse. Ten KrF laser amplifiers, with an output fluence of 1 joule/cm^2, will be required for one Raman cell, if the cross section of the Raman cell is made equal to that of the KrF amplifiers. The length of the Raman cell is set at 5 meters, so that the beam propagation time through the cell is equal to half the multiplexed KrF pulse time.

It is further assumed that a Stokes input beam of 1 joule/cm^2 fluence will be used and that the Stokes output (with 50% conversion efficiency) will thus be 6 joule/cm^2.

The methane cell is irradiated by the KrF lasers with a deposited energy density of 20 joule/liter. 10 joule/liter will be converted into a backward Stokes pulse and can be considered as the cell's extracted energy density. Because of the difference between the Stokes and KrF wavelengths (268 vs. 249 nm), 0.7 joule/lit of the converted 10 joule/lit will be deposited in the Raman cell as sensible heat.

The flow-related properties of this Raman cell are summarized in Table 2-11.

One window of the 1-atm Raman cell will be subject to a fluence of 16 joule/cm^2. This is clearly beyond what present state-of-the-art solid UV windows would allow. One would have to consider the application of aerodynamic windows to a 1-atm Raman cell. An alternative is to operate the Raman cell at a considerably higher pressure, which would reduce its saturation fluence and correspondingly reduce the required KrF input fluence and the converted Stokes fluence. Properties of a 5-atm CH_4 cell are presented in Table 2-12, as an example. In this case, only two KrF amplifiers, of the type described in Table 2-10, will be required to feed one Raman cell. The fluence through the cell window will be only 3.2 joule/cm^2. The energy density which can now be extracted from the cell is however, significantly reduced, as shown in Table 2-12. Designing an efficient flow system for a high-pressure Methane cell could therefore be considerably more difficult.

Table 2-11. Flow-Related Properties of a 1-Atm Raman Cell

Gas Medium	CH_4
Gas Pressure	1 atm
Gas Temperature	Room Temperature
Cavity Volume	1250 liters (or TBD)
Length, L	500 cm
Height, H	50 cm
Width, W	50 cm (or TBD)
Deposited Energy Density (as heat)	0.7 joule/lit-atm
Extracted Energy Density	10 joule/lit-atm
Pulse Repetition Frequency, PRF	TBD
Laser Wavelength	0.268 μm
Total Energy Extracted	12.5 kjoule (or TBD)
Combined Initiation Efficiency (KrF+Raman)	5%

Table 2-12. Flow-Related Properties of a 5-Atm Raman Cell

Gas Medium	CH_4
Gas Pressure	5 Atm
Gas Temperature	Room Temperature
Cavity Volume	1250 liters (or TBD)
Length, L	500 cm
Height, H	50 cm
Width, W	50 cm
Deposited Energy Density (as heat)	0.15 joule/lit-atm
Extracted Energy Density	2 joule/lit-atm
Pulse Repetition Frequency (PRF)	TBD
Laser Wavelength	0.268 μm
Total Energy Extracted	2.5 kjoule
Combined Initiation Efficiency (KrF+Raman)	5%

2.3.2 Beam Quality and Media Homogeneity Requirements

If a KrF laser is to be used in conjunction with a Raman pulse compressor, the KrF laser beam does not have to be of high quality, since it is not aimed at the target.[2-18] Only its lengthwise integrated intensity distribution across the Raman cell must be fairly uniform, so that a sufficiently uniform backward Stokes beam can be extracted from the Raman cell and focused on the target.

We must, however, consider also the possibility of using a KrF laser with angular multiplexing alone, and without the Raman compressor. In that case the beam extracted from the KrF laser must be of sufficiently high quality, so that it can be focused directly on the target. We will therefore consider here, separately, the beam quality requirements for the KrF amplifier and Raman cell, assuming that each of them has to produce a beam which can be focused on a 1-mm target.

The beam quality, as defined in Eq. 1, can be larger by about a factor of 40 for KrF fusion lasers than the BQ required for CO_2 lasers, due to the wavelength ratio ($\lambda_{CO_2}/\lambda_{CH_4}$ = 10.6/0.268 = 39.6) of these two systems. We will assume that the beam aperture and the last mirror focal length is the same in the KrF system as in the CO_2 system; namely, F = 15 m and D = 0.5 m. Equation 1 then provides a direct relationship between the focusable spot size d and BQ for both the KrF laser and the Raman cell. These relations are

$$d(mm) = 0.0149\ BQ \quad \text{for} \quad KrF \tag{54a}$$

and

$$d(mm) = 0.0161\ BQ \quad \text{for} \quad CH_4\ \text{Raman Cell} \tag{54b}$$

The smallest possible spot sizes (BQ = 1) are 0.0149 mm and 0.0161 mm for the two beams, respectively. If we again require that the maximum allowable focal spot size be 1 mm, then the maximum permissible BQ are 67.1 and 62.1, respectively. The required BQ range is thus much larger than for CO_2.

The exponential relationships used earlier for relating the BQ to the density nonuniformities of the amplifying medium are probably not valid for BQ > 2. Using these expressions to estimate the permissible density variation, $\Delta\rho/\rho$, for a given BQ, will give a conservative estimate

when BQ > 2 and should then be viewed only as a lower bound of the allowed $\Delta\rho/\rho$. Another estimate of the permissible $\Delta\rho/\rho$, versus the BQ desired, can be obtained from the geometric optics arguments presented earlier. Consider, e.g., an ordered density distribution given by $\langle\Delta\rho/\rho\rangle = (\Delta\rho/\rho)\cos(5\pi X/W)$, with 2.5 cycles of density variation across the beam aperture ($\ell = W/2.5$). Such density variations can be induced by pressure fluctuations in the cavity (through entropy production), when the flow Mach number is M = 0.2. The corresponding BQ, based on Equation (9), is given by

$$BQ^2 \approx 1 + \left[10\,\frac{L}{\lambda}\,\beta\left(\frac{\rho}{\rho_a}\right)\left(\frac{\Delta\rho}{\rho}\right)\right]^2$$

This example will be designated here and in subsequent figures by "geometric-2.5 cycles." It should be viewed as a rather liberal estimate of the allowed $(\Delta\rho/\rho)$ for a specified BQ. For M < 0.2, which is expected in most fusion-type lasers, ℓ will be shorter, the number of $\Delta\rho/\rho$ cycles will be larger and the BQ worse.

In Figures 2-18 and 2-19 the upper and lower bounds of $\Delta\rho/\rho$, as a function of BQ, are given for the KrF laser gas mixture and the CH_4 Raman cell. The two bounds practically coincide at BQ = 2, but then they diverge and move apart rapidly. The difference between the KrF curve and the CH_4 curves is mainly due to the difference in the optical length L and the β of these two systems. The difference in the CH_4 curves is due to factor of 5 pressure difference. At 5 atm, the OPD variation is five times larger than it is at 1 atm for the same $(\Delta\rho/\rho)$.

In what follows we assume that a beam quality of the order of 2 will be required for the KrF and CH_4 systems, and use only the exponential expression (lower bound) to determine the media homogeneity requirements. Although the required spot size (1 mm) and the assumed focal length of the last mirror (15 m) would allow using a KrF laser with a large BQ, it is reasonable to require that the laser operate as close as possible to its ideal BQ. This would allow focusing the laser beam to a spot size which is much smaller than the target size, which may be desirable in terms of the laser/target interaction. It could also allow moving the last mirror a greater distance from the target, which will largely simplify the problem of mirror protection. Furthermore, optical multiplexing requires a large number of mirrors, each introducing it's own

DOCUMENT NO.
PAGE NO.

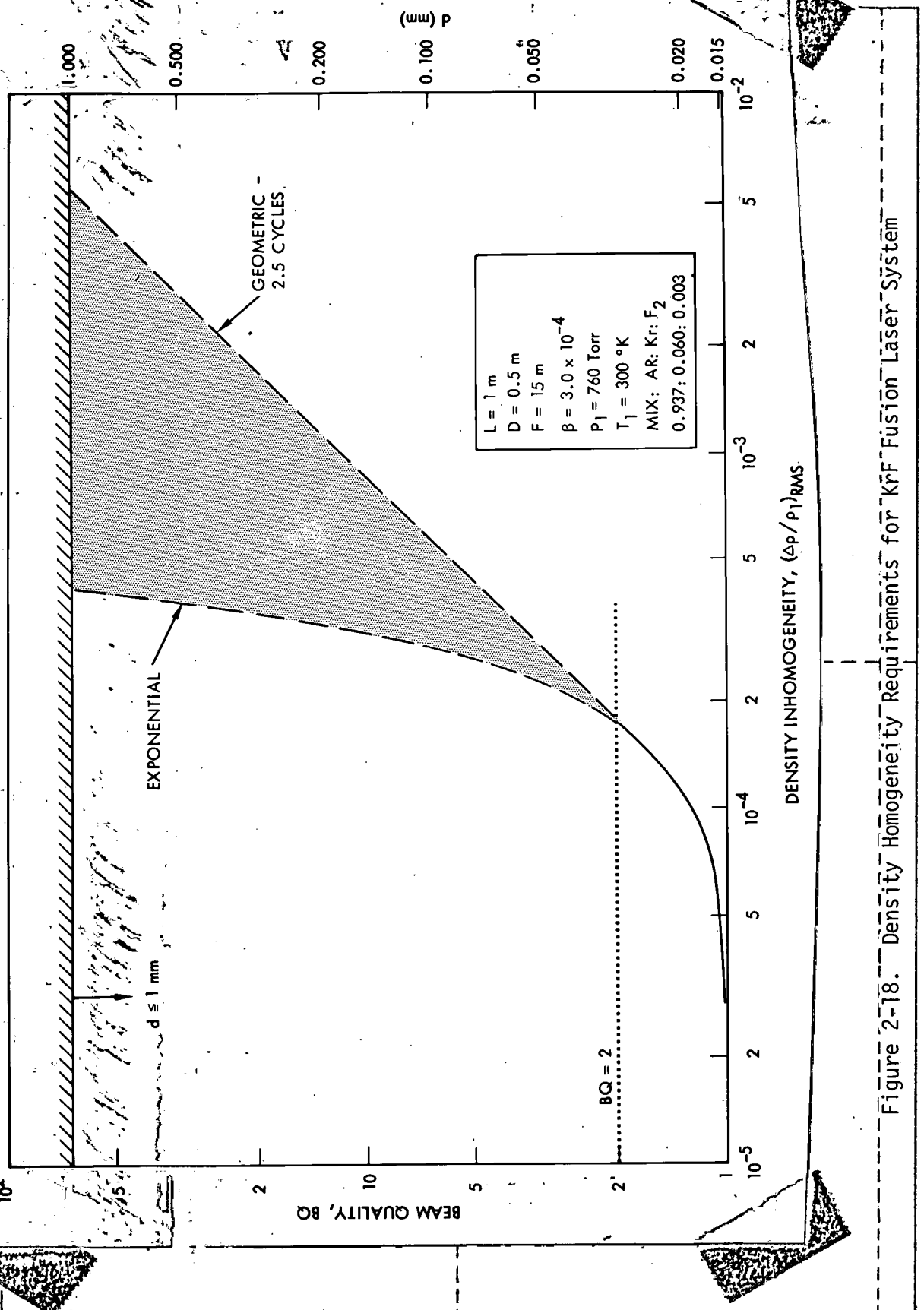

Figure 2-18. Density Homogeneity Requirements for KrF Fusion Laser System

BOTTOM OF PAGE

BOTTOM OF PAGE

DOCUMENT NO.
PAGE NO.

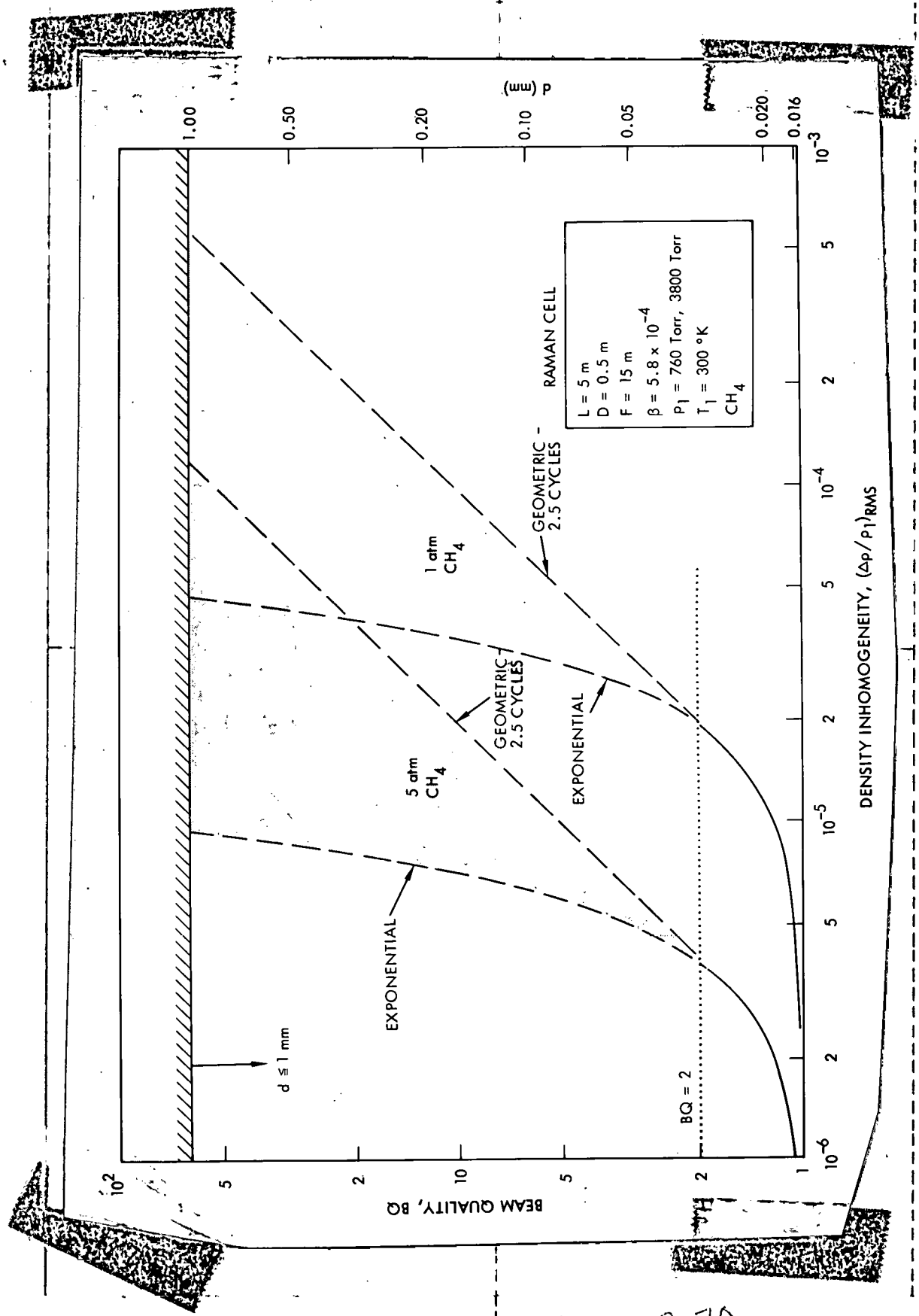

Figure 2-19. Density Homogeneity Requirements for CH_4 Raman Cell at 1 and 5 Atm

BOTTOM OF PAGE
BOTTOM OF PAGE

aberrations. There will be generally a strong motivation to make the lasing media as uniform as possible. However, when the media induced BQ approaches 2, large decreases in $\Delta\rho/\rho$ (or in OPD) will result in only moderate improvements in BQ and in the focused spot size. We will therefore require that the laser-media related BQ be in the range of 2 to 5 and large-scale ordered density nonuniformities be in the range of 1.6 to 4×10^{-4} for the KrF medium, 2 to 5×10^{-5} in the CH_4 medium at 1 atm and 4 to 10×10^{-6} in the CH_4 medium at 5 atm.

The requirements on the random density disturbances are presented in Figure 2-20. The indicated variations correspond to equations (50) and (51) of Section 2.2. Since we expect the turbulent inhomogeneity scale to be at least two orders of magnitude smaller than the aperture size, the permissible random $(\Delta\rho/\rho_1)_{rms}$ values are at least a factor of ten larger than the ordered $(\Delta\rho/\rho_1)_{rms}$ values given in Figs. 2-18 and 2-19. Hence, for the 1-mm spot size $(\Delta\rho/\rho_1)_{rms}$-random must be $\lesssim 4 \times 10^{-3}$ for the KrF laser and $\lesssim 5 \times 10^{-4}$ for the 1 atm CH_4 cell.

The pressure and temperature uniformity requirements are shown in Figure 2-21. The KrF laser gas mixture of interest is predominantly composed of Ar ($\sim$94%). Hence $\gamma = 1.67$, and $\gamma/\gamma-1 = 2.5$. The factors of γ and $\gamma/\gamma-1$ are needed to find the residual pressure fluctuations and the "entropy producing" pressure fluctuations. Specific values of these pressure and temperature uniformity requirements at a BQ = 2 and 5 are given in Table 2-13. There is approximately a factor of 50 difference between the KrF amplifier requirements and the Raman cell requirements at 5 atm. Representative acoustic suppression factors for the two systems are shown in Figure 2-22, using the conservative BQ estimate. We must first compute the initiation overpressures from Equation (13). For the KrF laser, with an energy deposition of 100 J/lit-atm at an initial temperature of $T_1 = 300^{\circ}K$, we obtain $(\Delta p/p_1)_{init} = (\Delta T/T_1)_{init} = 0.603$. The initiation overpressure is considerably smaller for the Raman Cell because the energy deposition is so much smaller, i.e., 0.7 J/lit-atm. For the CH_4 Raman Cell with $\gamma = 1.33$ and an initial temperature $T_1 = 300^{\circ}K$, we find $(\Delta p/p_1)_{init} = (\Delta T/T_1)_{init} = 2.08 \times 10^{-3}$. The minimum acoustic suppression factors (for d = 1mm) are 860 for the KrF laser and 33.3 for the 1 atm CH_4 cell.

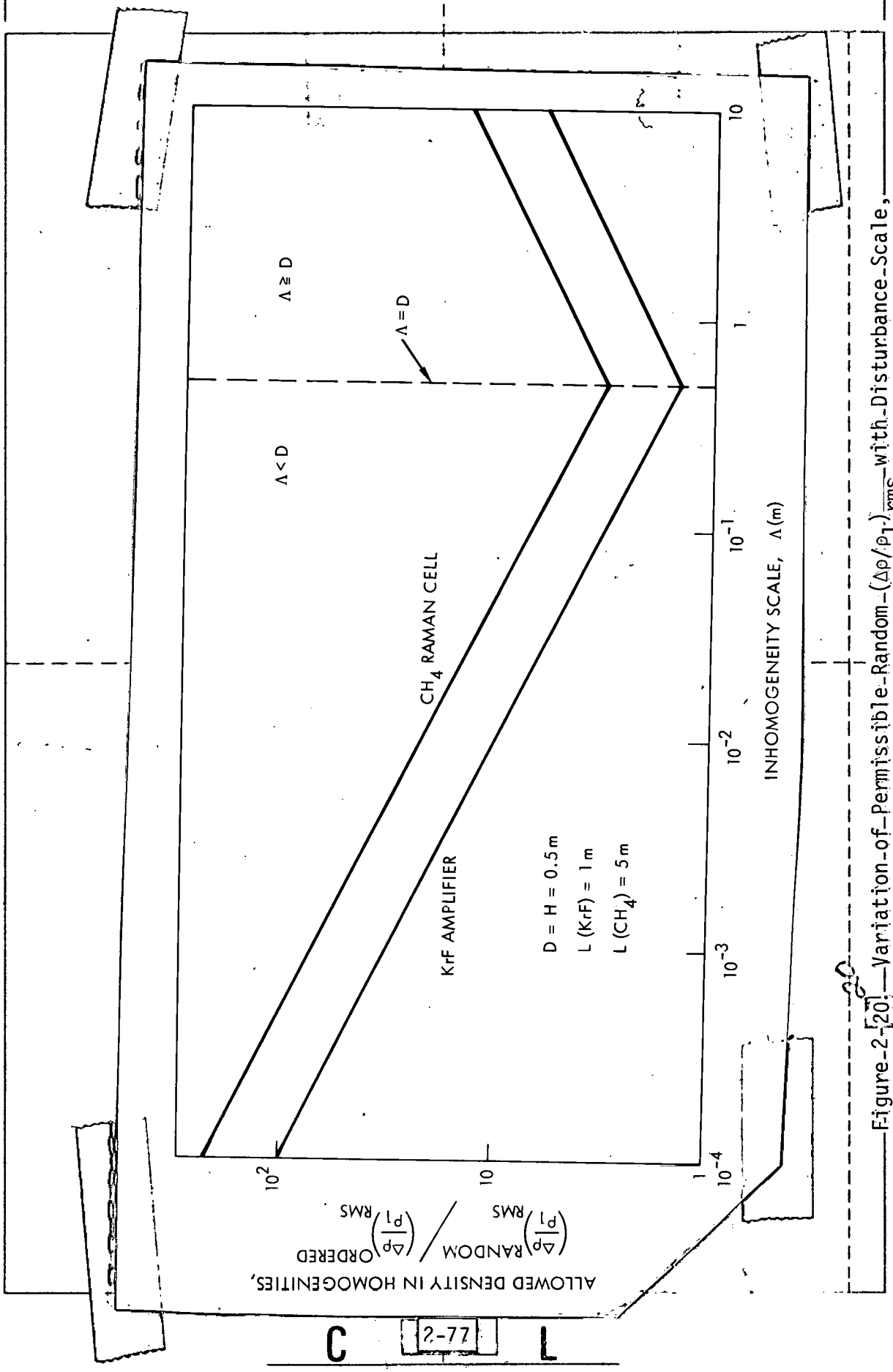

Figure 2-[20]. Variation of Permissible Random $(\Delta\rho/\rho_1)_{rms}$ with Disturbance Scale, for KrF Geometries.

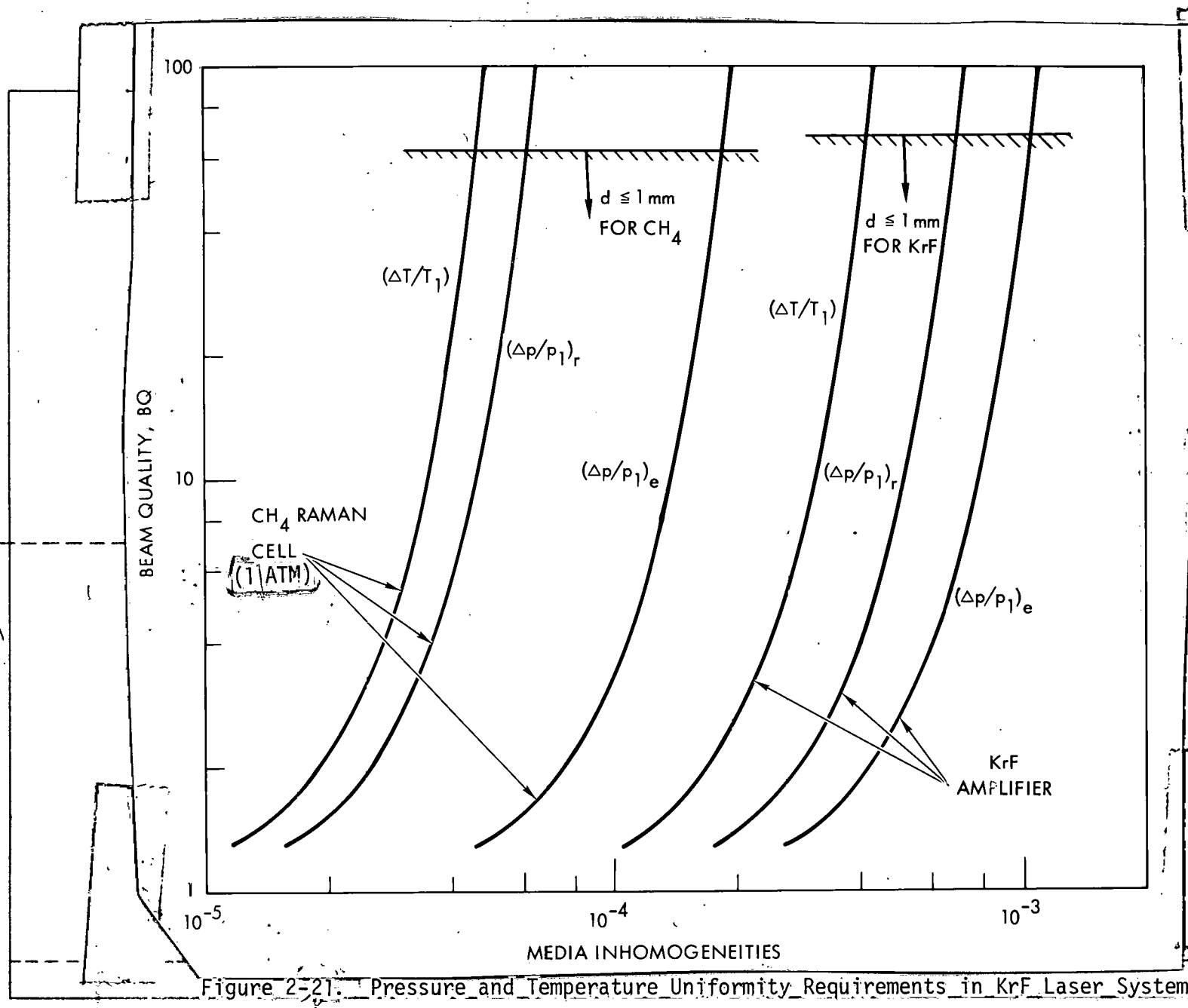

Figure 2-21. Pressure and Temperature Uniformity Requirements in KrF Laser Systems.

Table 2-13. Pressure and Temperature Uniformity Requirements for CH_4 Raman Cell and KrF Amplifier at BQ = 2 to 5

	1 Atm CH_4 Cell	5 Atm CH_4 Cell	KrF Amplifier
$\left(\frac{\Delta p}{p_1}\right)_r$	2.5 to 6.3 x 10^{-5}	5.0 to 12.5 x 10^{-6}	2.7 to 7.2 x 10^{-4}
$\left(\frac{\Delta p}{p_1}\right)_e$	7.6 to 19 x 10^{-5}	1.5 to 3.8 x 10^{-5}	4.3 to 10.8 x 10^{-4}
$\left(\frac{\Delta T}{T_1}\right)$	1.9 to 4.8 x 10^{-5}	3.8 to 9.5 x 10^{-6}	1.7 to 4.3 x 10^{-4}

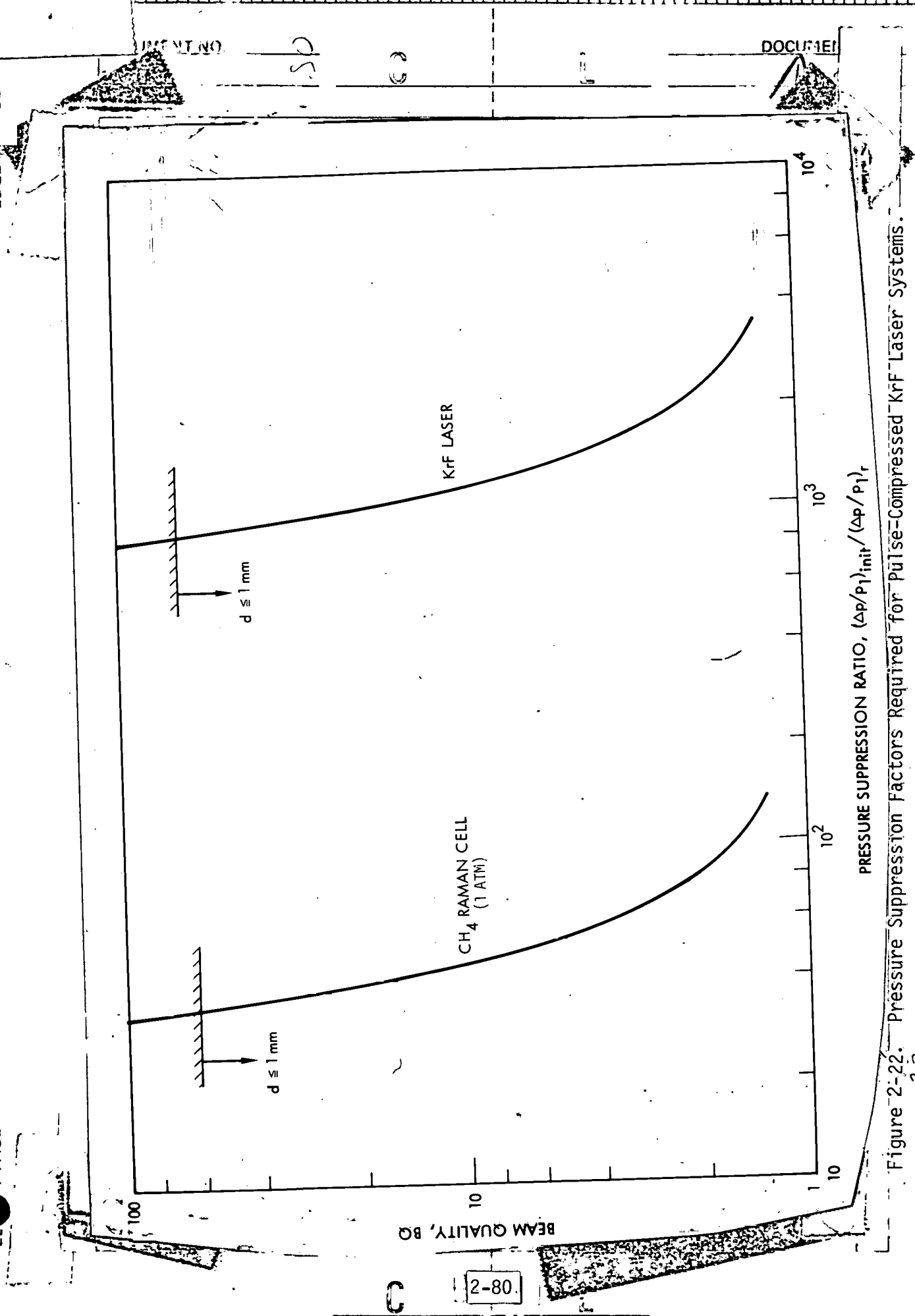

Figure 2-22. Pressure Suppression Factors Required for Pulse-Compressed KrF Laser Systems.

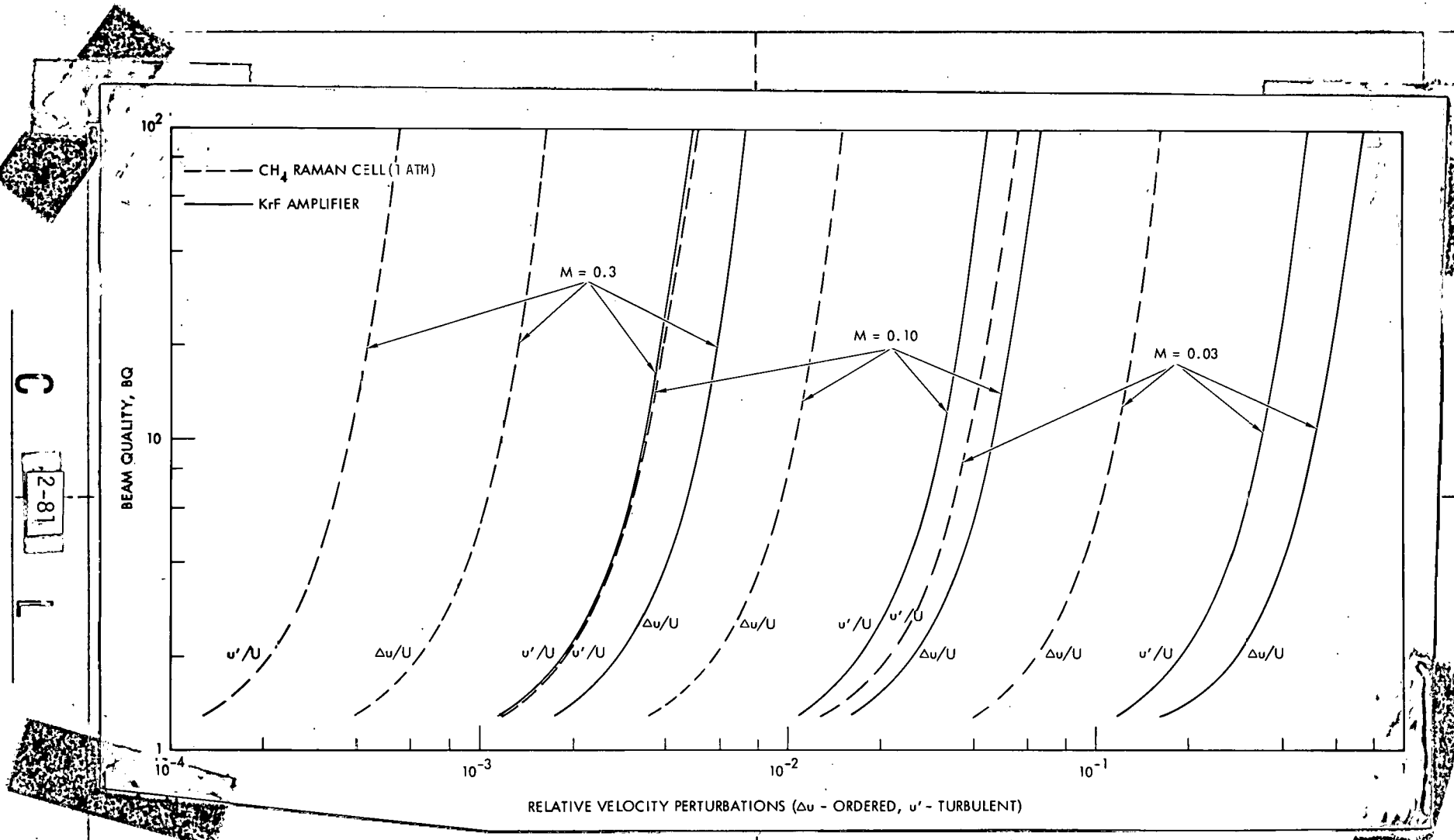

Figure 2-23. Velocity Uniformity Requirements for Pulse-Compressed KrF Laser Systems.

The next subject we discuss are the requirements on the velocity fluctuations -- both large-scale (Δu) and small-scale, turbulent (u'). The flow Mach number must now be factored into the requirements. It will be assumed henceforth that the aperture size (H x W) will be the same for the KrF laser and the Raman Cell. The PRF is naturally the same for both elements. This does not imply that the Mach number in the two flow cavities is the same because the flush factor C can be different and the speed of sound is different. The difference in Mach number will, however, be at most a factor of 2. We utilize the same range as before ($0.03 \leq M \leq 0.3$). The flow velocity requirements are illustrated in Figure 23. Even though the figure is somewhat busy, we immediately discern the fact that the Raman Cell under the highest Mach number (0.3) conditions must have a very small ($\lesssim 10^{-3}$) velocity inhomogeneity. We are dealing here with turbulence levels representative of low-turbulence wind tunnels used for studying boundary-layer stability rather than conventional wind tunnel turbulence (where $u'/U \sim 1\%$). At the lowest Mach number (0.03), it would be relatively easy to meet the flow uniformity requirements for both cavity flows.

The turbulence velocity, u'/U, homogeneity requirements for the various laser systems under study are given in Figure 2-24 at a specific BQ value. We have previously discussed the rationale for selecting a BQ = 2 for KrF and CH_4. The maximum allowable BQ of 1.6 is used in the CO_2 laser. The turbulence velocity requirements are plotted versus Mach number. Two shaded areas are shown at the top and at the bottom of the figure. The upper region ($u'/U \gtrsim 10^{-2}$) is relatively easy to achieve and does not necessitate any significant flow management; indeed, we shall make this assumption when we calculate allowable pressure drops. The lower region ($u'/U \lesssim 10^{-4}$) is very difficult to achieve. As will be shown later, a dynamic head loss of K = 40 (or 20 ρU^2) is required to achieve such low turbulence (see Figure 2-28). Hence, our concern will be with the range $10^{-2} \gtrsim u'/U \gtrsim 10^{-4}$. Note that it is only for the 5 atm Raman Cell that the turbulence velocity homogeneity falls below 10^{-4}.

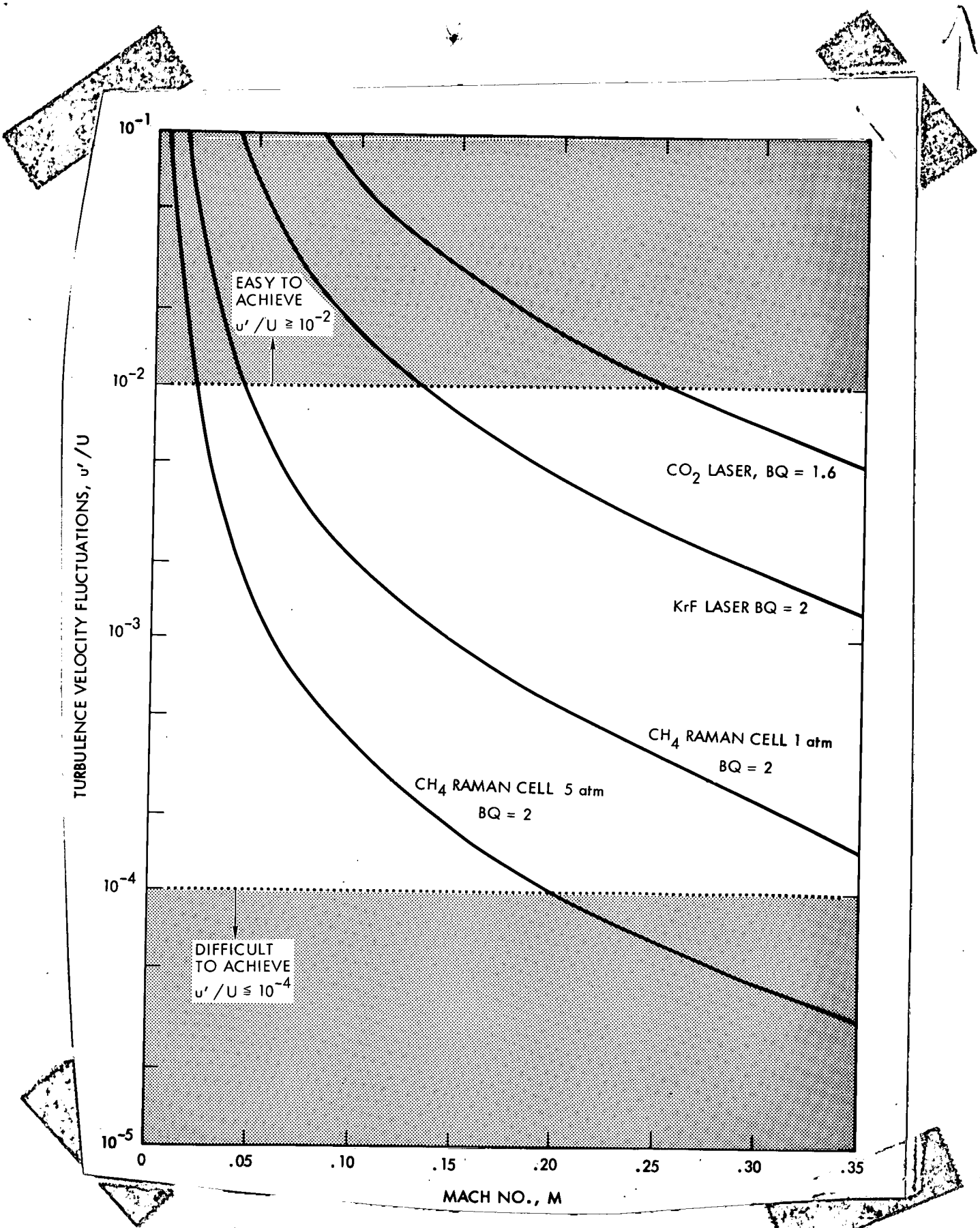

Figure 2-24. Maximum Allowable Turbulence Velocities as a Function of Mach Number

2.3.3 Mean Flow Requirement; Mach Number

The discussion in this subsection parallels the one of Section 2.2.3. However, we must consider two separate flow systems for the pulse-compressed KrF fusion laser system. The flow velocity requirements are similar to those of a CO_2 laser, but the Mach number scale has changed to reflect the different sound speeds for the two flows. Since we will continually be referring to the two systems, let us use the subscript A to refer to the KrF laser and subscript B to refer to the Raman Cell. Hence, in Figure 2-25 we show a M_A and a M_B scale. Note that we will continue to take a flush factor of $C_A = C_B = 2$. Because the KrF laser mixture is predominantly Ar with a molecular weight of 39.94, the speed of sound a_B is 455 m/sec. In the preceding subsection we have found that M_B should be less than 0.3 and probably as small or smaller than 0.1. This implies (from Figure 2-25) that in the 10-20 Hz range, the flow dimension length W is fixed in the range of 1 - 2 m. Note, however, that with $M_B = 0.1$, M_A is forced to be ~ 0.14 and could lead to flow uniformity and efficiency difficulties. There will generally be some interesting tradeoffs between systems A and B. This point is amplified in the next subsection.

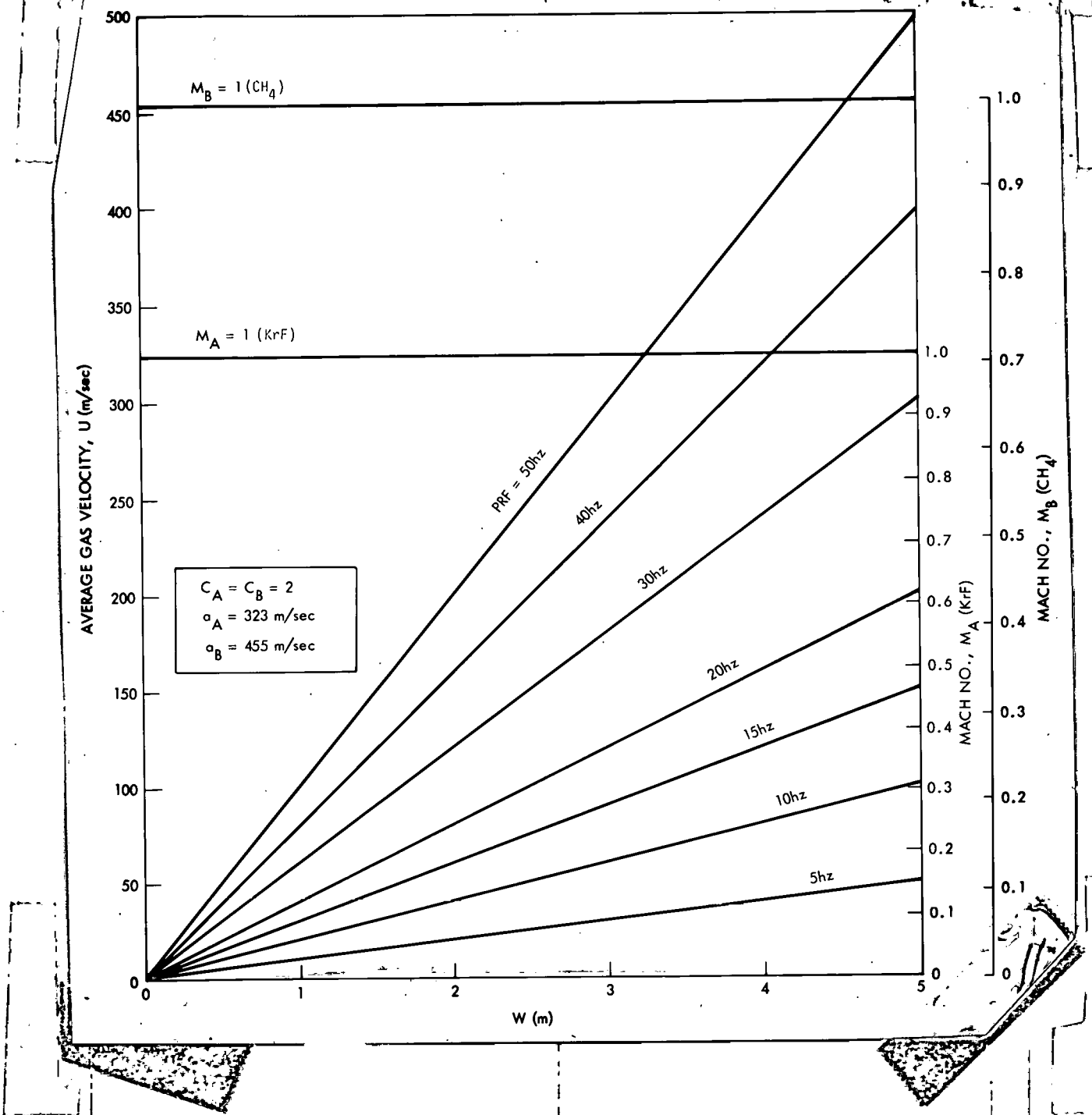

Figure 2-25. Flow Velocity Requirements for Pulse-Compressed KrF Average Gas Velocity, U(m/sec).

2.3.4 Flow Efficiency Requirements

The essence of the previous flow efficiency discussion in Section 1.1.2 remains unchanged, however in the application to KrF laser systems we must consider the KrF laser alone as well as the KrF laser/CH_4 cell combinations. For the KrF laser alone, we proceed as with the CO_2 laser analysis. There is a direct tradeoff between flow efficiency η_F and the total allowable system pressure drop $\Delta p^*/p_5$. If we use the projected properties of a KrF amplifier (Table 2-10), with $S \cdot \eta_{ext}$ = 10 joule/lit·atm, then we can directly use Figure 2-4 to find the allowable $\Delta p^*/p_5$. At η_F = 0.1, $\Delta p^*/p_5$ = 0.395 and at η_F = 0.2, $\Delta p^*/p_5$ = 0.197.

The subject of the pulse compressed KrF system is somewhat more complex since we now have to consider the different efficiencies for the KrF laser (A) and the CH_4 Raman Cell (B). We will find that there is a tradeoff between η_{FA} and η_{FB} which must be considered for evaluating the total flow efficiency $\eta_{F(A+B)}$. The discussion of Section 3.1 has defined one pulse-compressed KrF laser system consisting of 10 KrF lasers feeding a single Raman Cell. The output of the Raman Cell will be the ICF driver source. The overall laser efficiency can thus be written as

$$\eta_L = \frac{P_{LB}}{P_{I(A+B)} + P_{F(A+B)}} \tag{57}$$

where regeneration has been neglected. By definition

$$\frac{1}{\eta_{F(A+B)}} = \frac{P_{F(A+B)}}{P_{LB}} = \frac{10P_{FA} + P_{FB}}{P_{LB}} \tag{58}$$

where P_{FA} is the flow power for a single KrF laser. Upon utilizing relationships similar to (18) and (19), Equation (58) becomes

$$\frac{1}{\eta_{F(A+B)}} = 10\left(\frac{P_{1A}}{P_{1B}}\,\frac{V_{1A}}{V_{1B}}\right)\frac{1}{\eta_{FA}} + \frac{1}{\eta_{FB}} \tag{59}$$

where

$$\eta_{FA}\left(\frac{\Delta p^*}{p_5}\right)_A = \frac{(S\cdot\eta_{ext})_B\,\eta_{comp}}{101.3\,C_A(T_{5A}/T_{1A})} \tag{60}$$

and

$$\eta_{FB}\left(\frac{\Delta p^*}{p_5}\right)_B = \frac{(S\cdot\eta_{ext})_B\,\eta_{comp}}{101.3\,C_B(T_{5B}/T_{1B})} \tag{61}$$

Two KrF laser and Raman Cell combinations will be treated here. The KrF laser cavity is assumed to be at 1 atm in both cases. In the first case a 1 atm CH_4 cell is used whereas for the second a 5 atm CH_4 cell is assumed.

When the laser and CH_4 cavities are at the same pressure (1 atm), then $p_{1A} = p_{1B}$, and since $V_{1A} = V_{1B}/5$, Eq. (59) reduces to

$$\frac{1}{\eta_{F(A+B)}} = \frac{2}{\eta_{FA}} + \frac{1}{\eta_{FB}} \tag{62}$$

For the 5 atm CH_4 cell we have $p_{1A} = p_{1B}/5$ and since the cavity volume ratios remains unchanged, Eq. (59) reduces in this case to

$$\frac{1}{\eta_{F(A+B)}} = \frac{2}{5\eta_{FA}} + \frac{1}{\eta_{FB}} \tag{63}$$

Both relationships, Eqns. (62) and (63) are plotted in Figure 2-26.

Figure 2-26 can provide some guidance for selecting a design point and the operating conditions at a KrF/CH_4 system. On the one hand we would like to have the largest allowable $(\Delta p^*/p_5)_B$ for the Raman Cell because of the very stringent $(\Delta\rho/\rho)$ requirements there. On the other hand, the overpressure in the Raman Cell is very small and one might hope to achieve the required pressure suppression with very little pressure drop. An optimal tradeoff can be made only after the pressure suppression devices are better defined and understood. Some specific examples can illustrate this point.

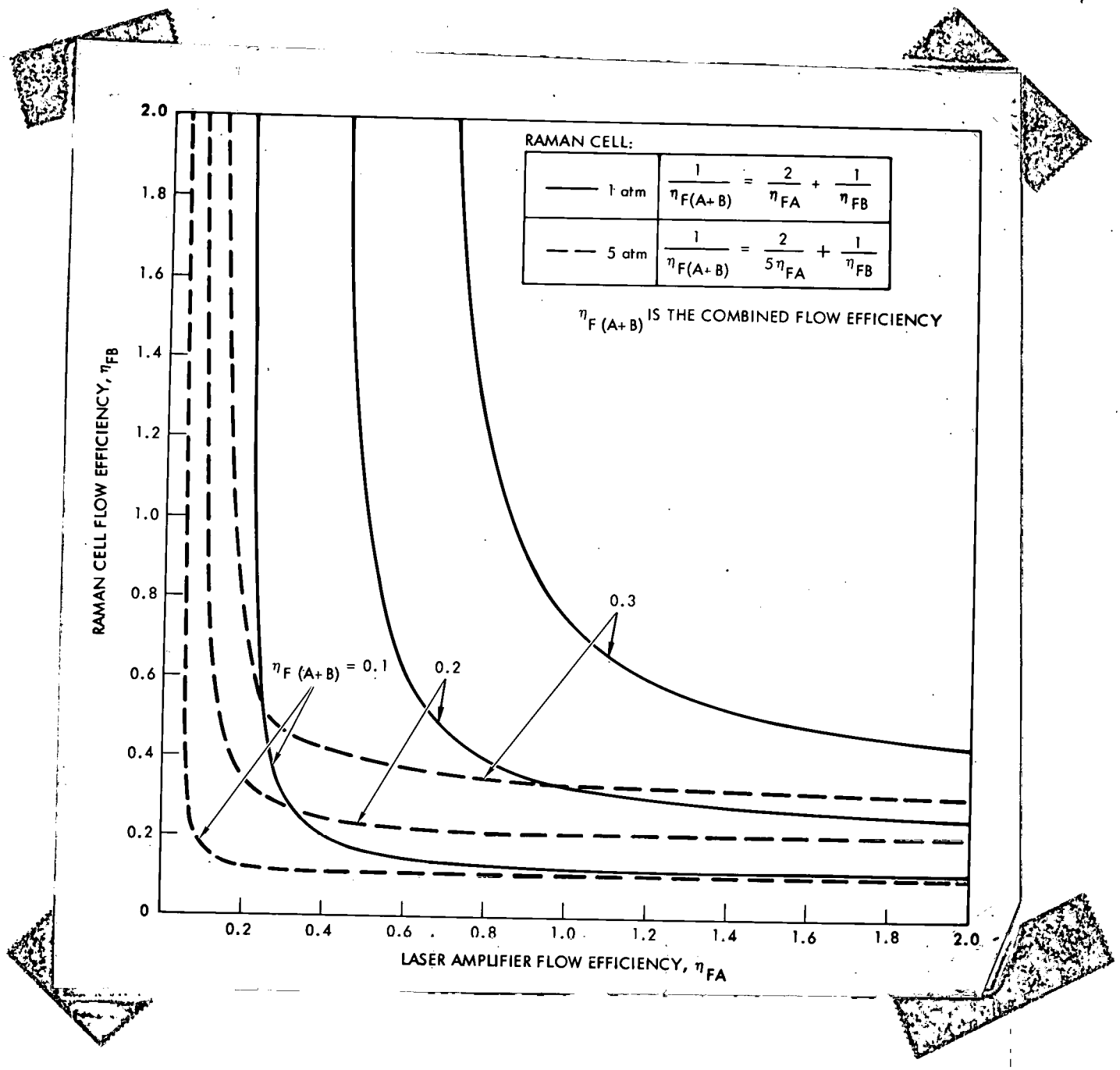

Figure 2-26. Flow Efficiency Tradeoff Between a KrF Laser Amplifier and its Raman Cell.

To proceed with such examples we must return to Figure 2-3 of Section 2.1.1.2 and isolate an operating regime for the pulse-compressed KrF system. We assume that the minimum acceptable combined initiation efficiency for a KrF laser amplifier and compressor is $\eta_{I(A+B)} \gtrsim 2.5\%$. This is a reasonable requirement since KrF systems alone have exhibited initiation efficiencies $\sim$ 10-12%. The maximum combined initiation efficiency is taken as $\eta_{I(A+B)} \leq 10\%$ (equivalent to $\eta_{IA} \leq 20\%$). It is also assumed that a minimum flow efficiency should be 10% and that the range of from 10% to 20% is realistic and potentially achievable. The shaded region in Figure 2-27 is the KrF operating regime. Let us now return to Figure 2-26 and examine three different points on a particular $\eta_{F(A+B)}$ curve (considering the 1 atm CH_4 only), i.e., $\eta_{F(A+B)} = 0.10$. The three cases are shown in Table 2-14 together with the allowable pressure drops. In order to compute the pressure drops, we use $(S \cdot \eta_{ext})_A = (S \cdot \eta_{ext})_B = 10$ J/lit-atm, $\eta_{comp} = 0.8$, $C_A = C_B = 2$, and $T_{5A}/T_{1A} = T_{5B}/T_{1B} = 1$, hence, from Equations (60) and (61)

$$\eta_{FA} \left(\frac{\Delta p^*}{p_5}\right)_A = \eta_{FB} \left(\frac{\Delta p^*}{p_5}\right)_B = 0.0395$$

There is therefore a range of choices for $(\Delta p^*/p_5)_{A \text{ or } B}$ as defined above and by the above selected constraint of $\eta_{F(A+B)} = 0.10$. Table 2-14 presents only a few possible choices. The best choice will depend on the pressure drop characteristics of these two systems, which will be discussed in the next subsection.

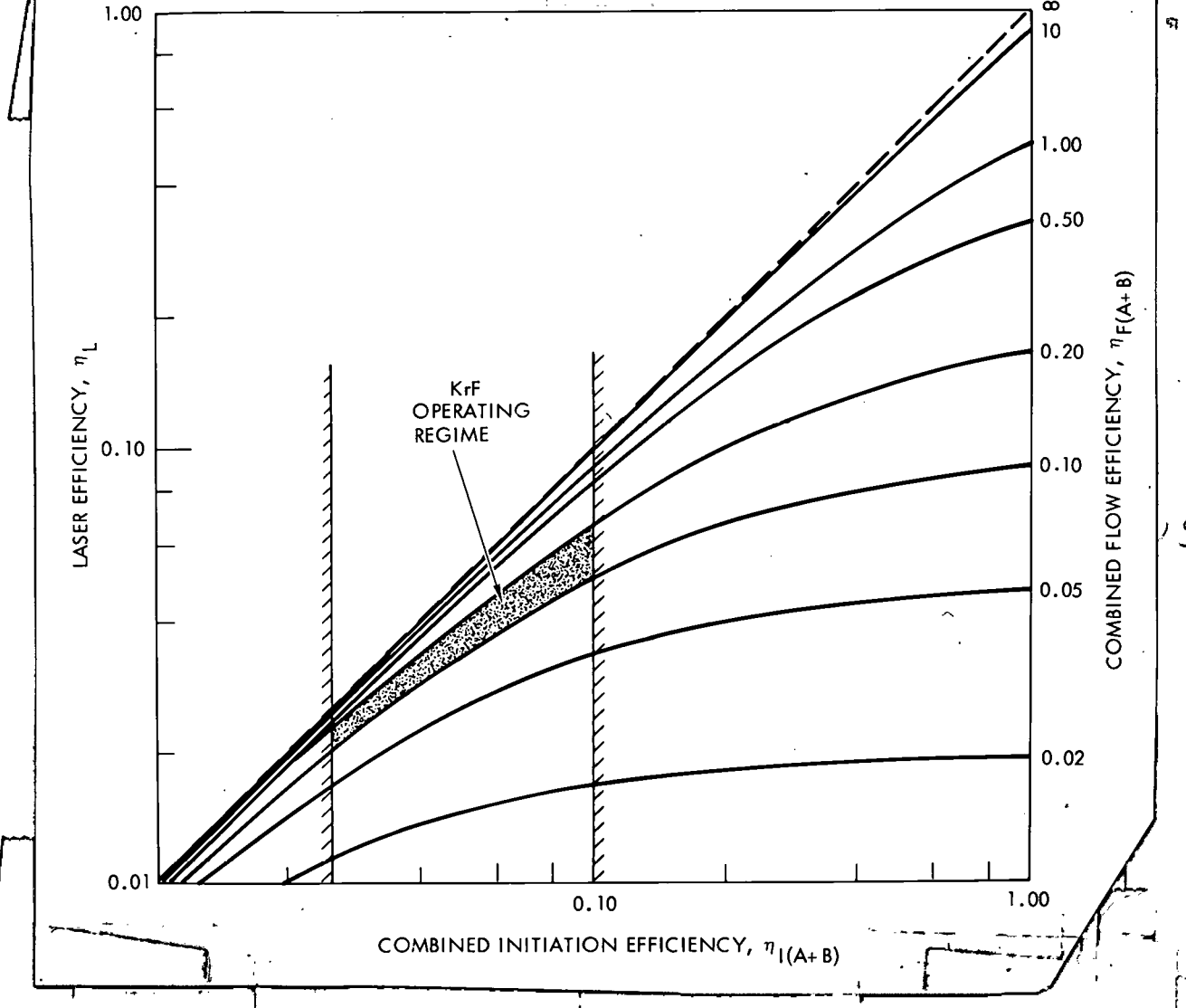

Figure 2-27. Laser Efficiency Versus Initiation and Flow Efficiencies for Pulse Compressed KrF.

DOCUMENT NO.
PAGE NO.

Table 2-14. Allowable Pressure Drops for the KrF Laser and the 1-Atm Raman Cell ($\eta_{F(A+B)} = 0.10$)

		η_{FB}	η_{FA}	$(\Delta p^*/p_5)_B$	$(\Delta p^*/p_5)_A$
CASE 1	Large $\left(\frac{\Delta p^*}{p_5}\right)_B$	0.15	0.60	0.263	0.0658
CASE 2	Intermediate $\left(\frac{\Delta p^*}{p_5}\right)_B$	0.3	0.3	0.132	0.132
CASE 3	Small $\left(\frac{\Delta p^*}{p_5}\right)_B$	1.1	0.22	0.0359	0.180

2-42

2.3.5 Estimation of the Flow-Loop Pressure Drops

The general pressure-drop relationships of Section 2.1.1.2 are made specific to the KrF laser alone and to the KrF/Raman Cell systems characterized by the properties listed in Tables 2-10, 2-11, and 2-12.

This subsection is divided into two parts. The first part describes the pressure drops required for flowing the laser gas around the circuit without regard to flow or thermal conditioning. The second part specifically discusses the pressure drops required for achieving the turbulence uniformity (u'/U) and the thermal uniformity requirements. These pressure drop estimates allow one to deduce the pressure drops available for the acoustic suppressors (see Section 2.3.6). Hence, we consider four pressure drops as outlined below:

1. Allowable overall flow system pressure drop deduced from efficiency requirements: $\left(\frac{\Delta p^*}{p_5}\right)_{TOTAL}$.
2. Pressure drop due to base flow (no flow management): $\left(\frac{\Delta p^*}{p_5}\right)_{FLOW}$.
3. Pressure drop due to flow and thermal management: $\left(\frac{\Delta p^*}{p_5}\right)_{FTM}$.
4. Pressure drop available for acoustic management (suppression): $\left(\frac{\Delta p^*}{p_5}\right)_{AM}$.

The overall $(\Delta p^*/p_5)_{TOTAL}$ has been described in section 2.3.4. $(\Delta p^*/p_5)_{FLOW}$ and $(\Delta p^*/p_5)_{FTM}$ are described below and $(\Delta p^*/p_5)_{AM}$ is summarized in section 2.3.6.

2.3.5.1 Base Flow Pressure Drop, $(\Delta p^*/p_5)_{FLOW}$

Cavity Heat Addition

As found in Section 2.2.5, the pressure loss coefficient for the cavity heat addition is $K_1 = \Delta T_{01}/T_{01}$. For the KrF laser with $\rho_A = 1.62$ gm/lit $P_A = 1$ atm, $C_{P_A} = 0.528$ J/gm^{0}K, and $T_{01} = 300^0$K the result is $(\Delta T_{01}/T_{01}) = 0.351$. Likewise for the CH_4 Raman cell with $\rho_B = 0.651$ gm/lit, $P_B = 1$ atm, $C_{P_B} = 2.22$ J/gm^{0}K, and $T_{01} = 300^0$K the result is $(\Delta T_{01}/T_{01})_B = 1.61 \times 10^{-3}$. At $p_B = 5$ atm, $\rho_B = 3.26$ gm/lit but $(\Delta T_{01}/T_{01})_B$ remains unchanges at 1.61×10^{-3}.

Subsonic Diffuser

A reasonable value of $K_3 = 0.30$ is used as the pressure drop coefficient.

Flow Turns

If we again utilize well-designed turning vanes in the flow corners with a $K_T = 0.15$, then the total loss coefficient is $4\ K_T = 0.60$.

Flow Contraction

We can utilize the same loss coefficients for the contraction section as used in Section 2.2.5, i.e., $K_{C1} = 0.0036, 0.0026, 0.0012$ at M = 0.03, 0.1, 0.3 respectively.

Heat Exchangers

Note that for the Raman cell there is no need for the first heat exchanger ($K_5 = 0$) since the temperature excess is rather small. One heat exchanger, downstream of the compressor, can bring the temperature back to the pre-initiation value. The KrF laser stagnation temperature increases to approximately 481°K (nearly independent of M) due to heat addition. Thus, if we use a coolant temperature of 250°K, $K_5 = 1.57$. If we use the maximum $\Delta p^*/p_5$ of Table 2-14 to estimate the temperature increase due to the compression, then $(T_{06})_A \approx 331°K$ and using the 250°K coolant, $K_7 = 0.77$. For the Raman cell, if we use a comparable $(T_{06})_B \approx 331°K$, then $K_7 = 0.77$.

Boundary-Layer Friction

We again choose a value of $\ell/D_h = 20$ for the extent of the straight sections in the wind tunnel. Due to the high Reynolds numbers of our flow systems (10^6 - 10^7), the skin-friction coefficient is quite small and K_F varies from 0.044 at M = 0.03 to 0.025 at M = 0.3.

The flow-only pressure drops are immediately obtained by multiplying the loss coefficients, K, by the dynamic pressure of the flow - $q = 1/2\rho U^2 = \gamma/2pM^2$. For the KrF amplifier with $\gamma = 1.67$, $q_A(\text{Torr}) = 634.6\ M^2$. In the 1 atm CH_4 cell with $\gamma = 1.33$, $q_B(\text{Torr}) = 505.4\ M^2$ and in the 5 atm cell, $q_B(\text{Torr}) = 2527.\ M^2$.

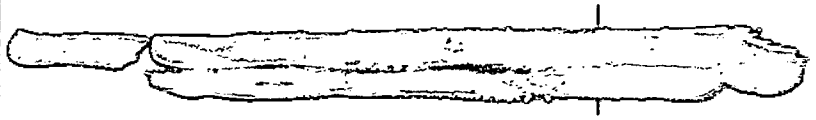

BOTTOM OF PAGE
BOTTOM OF PAGE

2.3.5.2 Flow and Thermal Management $(\Delta p^*/p_5)_{FTM}$

The flow uniformity requirements and the thermal homogeneity requirements are dictated by the density homogeneity and beam quality requirements, as indicated in Figures 2-24 and 2-23. The flow uniformity requirements are also a strong function of the flow Mach No. (see Fig. 2-24).

Turbulence quieting experiments have been undertaken in the past to determine the pressure drops (or resistance coefficients) needed to achieve a specific low turbulence level in wind tunnels and similar devices. In reference 2-20, experimental data taken at the National Bureau of Standards relates the measured u'/U to the total resistance coefficient K_{TOTAL} required to achieve the low turbulence levels. This data is given in Figure 2-28. The number of screens needed to achieve the uniformity levels is also indicated. The data of Figure 2-28 together with Figure 2-24 can be utilized to determine the required pressure drop versus Mach number. This is given in Figure 2-29 for the fusion laser systems of current interest. Note that the curves are drawn for a specific beam quality. The "translation" from Figure 2-24 to Figure 2-29 proceeds as follows. For $u'/U > 10^{-2}$, no extra pressure drop is needed $(\Delta p^*/p_5)_{FM} = 0$ $(K = 0)$; for $2\times10^{-3} \lesssim u'/U \lesssim 10^{-2}$ $K = 1$; and for $u'/U \lesssim 2\times10^{-3}$, K is given by the multiple-screen curve of Figure 2-28. Since rather scant experimental information is available on how to achieve the severe thermal uniformity requirements of fusion lasers, we make here the approximation that the pressure drop needed for thermal management is equal to that needed for turbulence management, $(\Delta p^*/p_5)_{TM} = (\Delta p^*/p_5)_{FM}$. Hence, the total pressure drop for flow and thermal management is given by $(\Delta p^*/p_5)_{FTM} = 2(\Delta p^*/p_5)_{FM}$. The results of Figure 2-29 will be used to determine the pressure drop available for acoustic management.

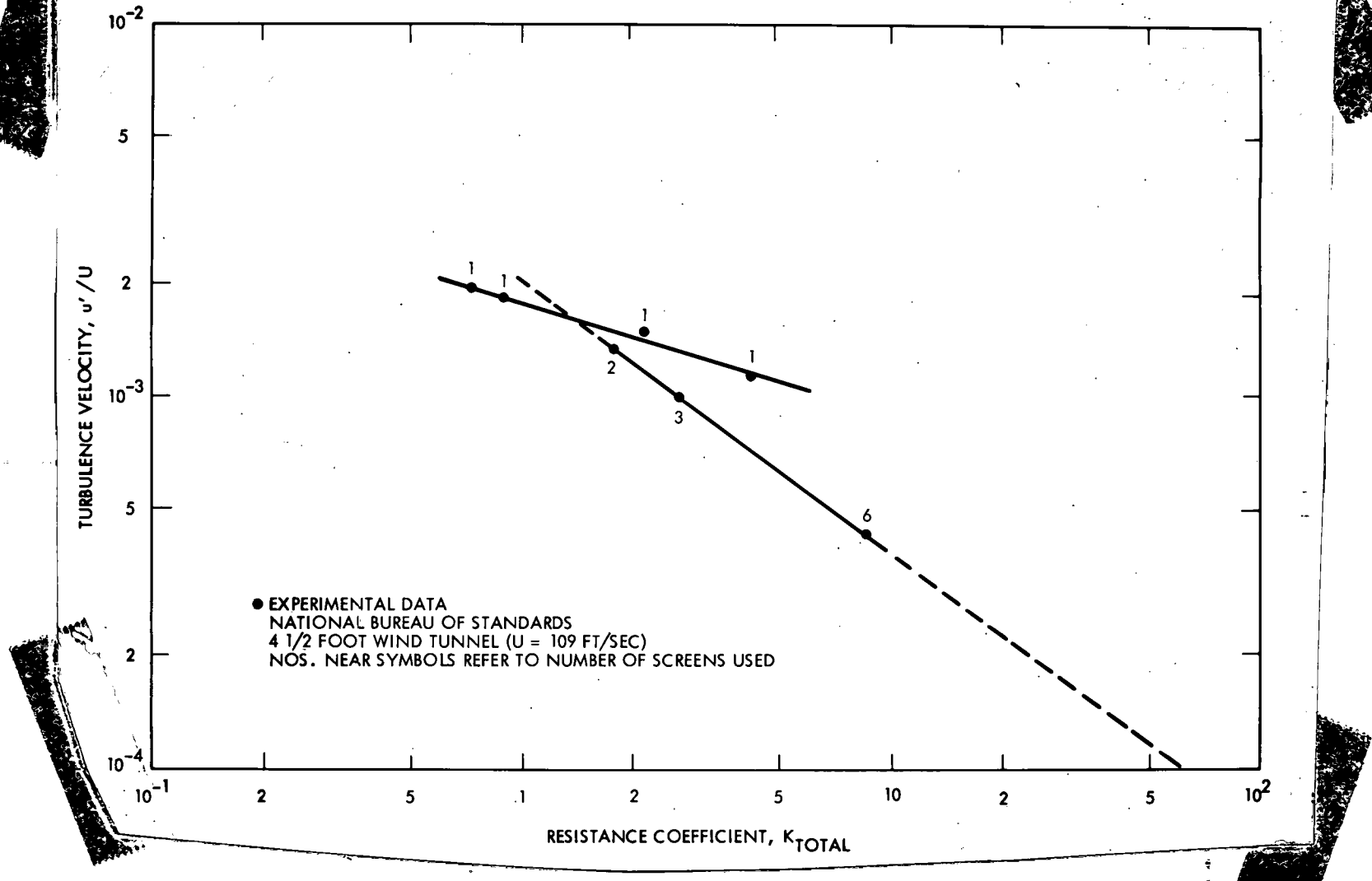

Figure 2-28. Resistance Required to Achieve Low Turbulence Velocity Levels

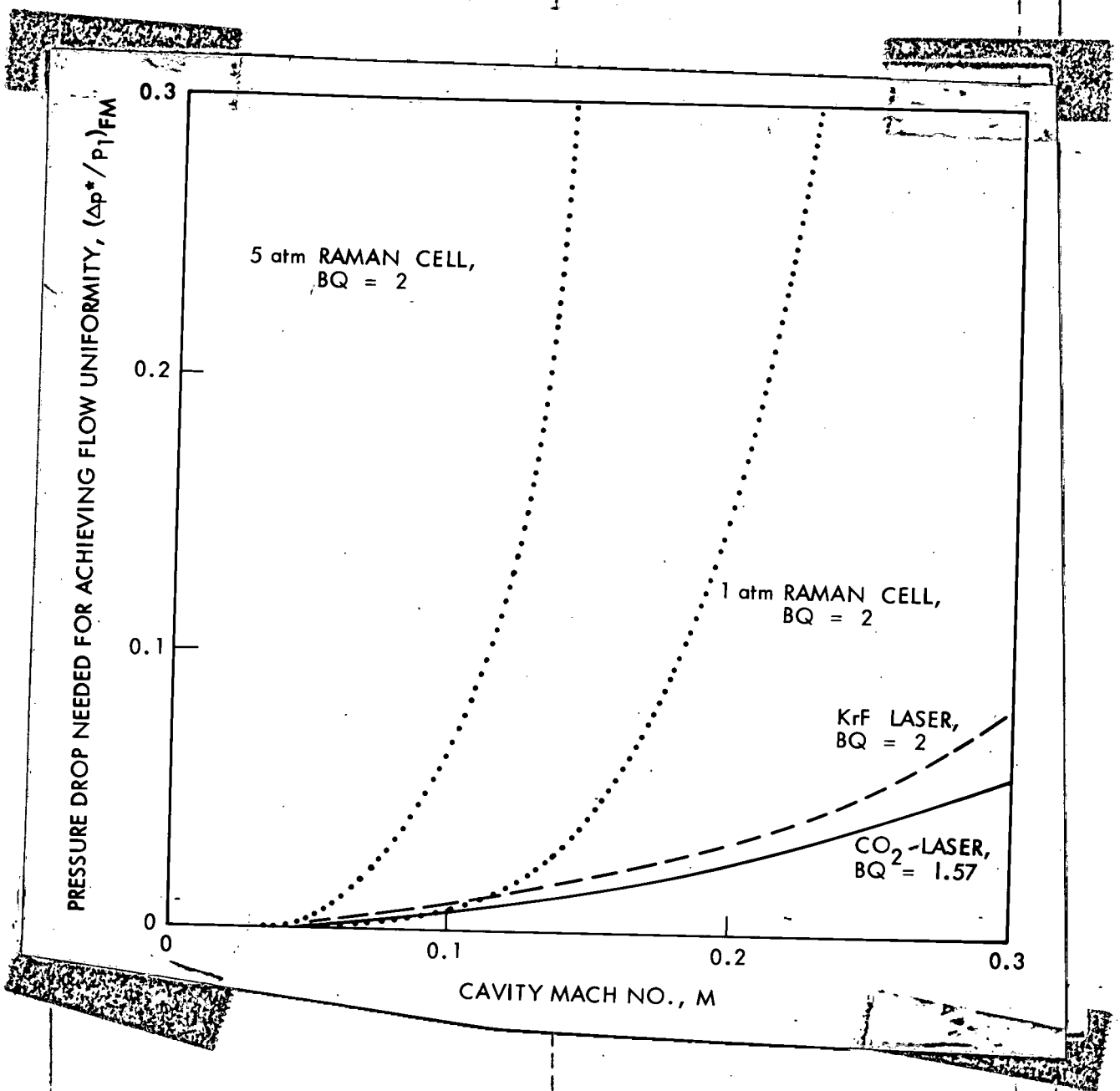

Figure 2-29. Pressure Drop Through Screens Required for Flow Management (u'/U)

2.3.6 Permissible Pressure Drops for the Acoustic Absorbers

The permissible pressure drop for acoustic suppression purposes is determined in this section. The quantity of interest is $(\Delta p^*/p_5)_{AM}$ which is defined as follows

$$\left(\Delta p^*/p_5\right)_{AM} = \left(\Delta p^*/p_5\right)_{TOTAL} - \left(\Delta p^*/p_5\right)_{FLOW} - \left(\Delta p^*/p_5\right)_{FTM}$$

The first two terms on the right hand side of this relation were discussed earlier and can be evaluated quite accurately. The third term which represents flow and thermal management is more difficult to determine - particularly the pressure drop required for achieving the stringent temperature controls required for fusion lasers. Hence, the definition of $(\Delta p^*/p_5)_{AM}$ is influenced by the uncertainty in the characterization of the thermal management problem. It is difficult to determine whether or not our supposition that $(\Delta p^*/p_5)_{TM}$ (thermal management) = $(\Delta p^*/p_5)_{FM}$ (flow management) is a conservative approximation. We shall assume that it is a reasonable supposition and proceed to define the allowable pressure drop for acoustics.

In Figure 2-30, the quantity $(\Delta p^*/p_5)_{AM}$ is given versus cavity flow Mach number M for a KrF laser operated with optical multiplexing alone (no pulse compression). Two reasonable values of flow efficiency (0.10, 0.20), required for a projected KrF laser with an extraction energy density of 10 J/lit-atm, are used. At M = 0 when there are no flow-related losses, $(\Delta p^*/p_5)_{AM} = (\Delta p^*/p_5)_{TOTAL}$. This value is inversely proportional to the flow efficiency. As the M increases the flow-related losses increase as M^2, however the separation between the efficiency curves remains the same. The results indicate that at $\eta_F = 0.10$, the maximum M is 0.272 whereas at $\eta_F = 0.20$, the maximum M is reduced to 0.194. Note that these maximum values correspond to a situation where the acoustic suppression is accomplished without pressure drop. This is certainly a desired goal, and it may even be approached with a porous wall/muffler type absorber. It is our feeling, however, that the stringet pressure suppression required for KrF lasers will not be achieved with side-wall (passive) absorbers alone. Some flow-through (active) absorbers will be required as well. The

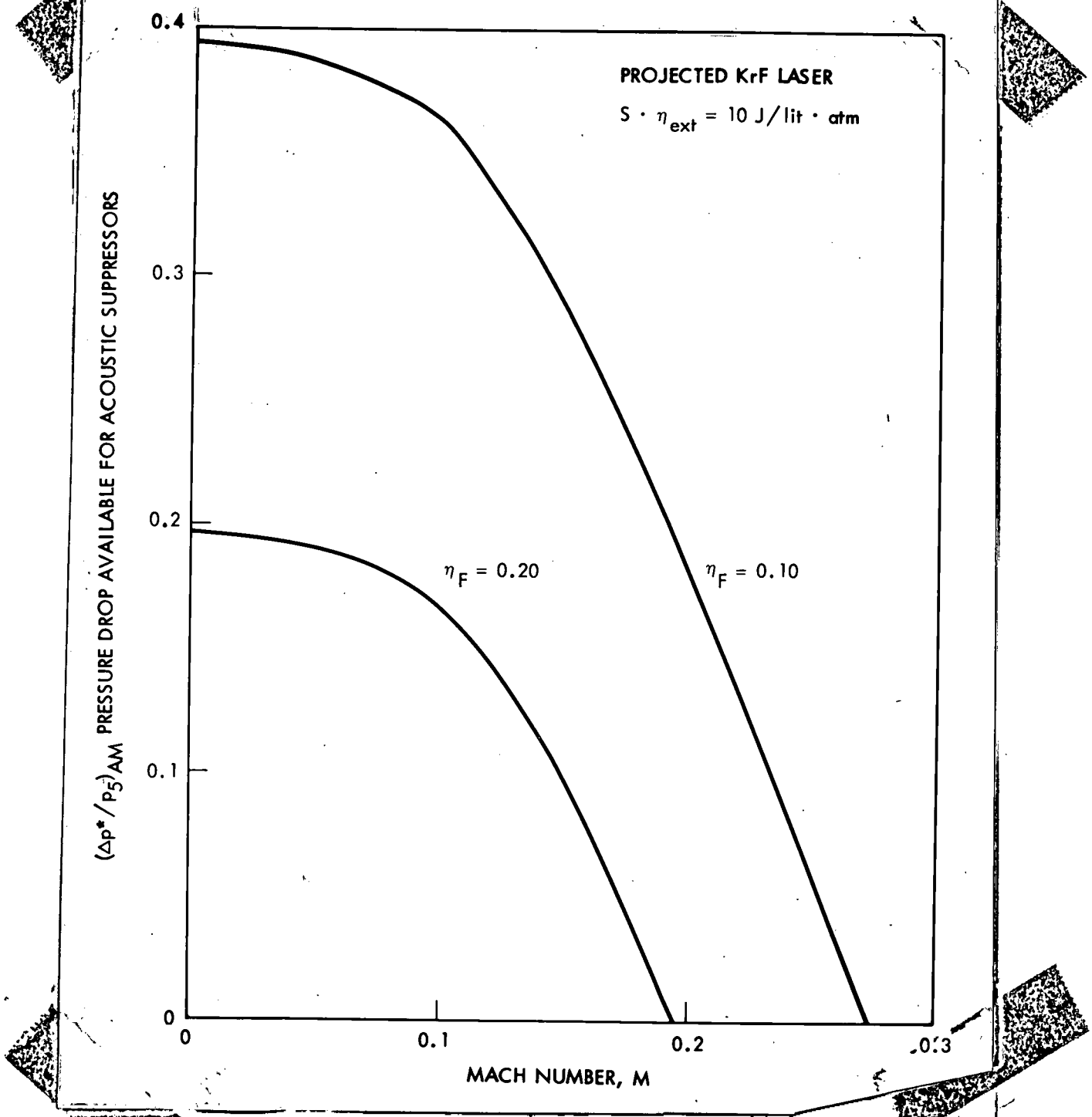

Figure 2-30. Pressure Drop Available for Acoustic Suppression Versus Mach Number for a KrF Laser with Optical Multiplexing.

permissible pressure drop for acoustic suppression, as indicated in Figure 2-30, can be well utilized and the maximum permissible M will be less than that which corresponds to $(\Delta p^*/p_5)_{AM} = 0$ on that figure.

The available pressure drop for pulse-compressed KrF/CH_4 systems is shown in Figure 2-31. Two pulse-compression cells are considered, one at 1 atm CH_4 and the other at 5 atm CH_4. In these calculations it has been assumed that there are no BQ requirements on the medium within the KrF laser cavity. Namely, it is assumed that the KrF laser itself requires no flow management, $(\Delta P^*_A)_{FTM} = 0$, and that the acoustic suppression which may be required for its cavity can be achieved without any pressure loss. We again show curves for two reasonable values of the combined flow efficiency, $\eta_{F(A+B)} = 0.10$ and 0.20. The individual curves fall off more rapidly with M, as compared to the case shown in Figure 2-30, because of the stricter media homogeneity requirements in the CH_4 cell.

Figures 2-30 and 2-31 illustrate what is the available pressure drop for pressure wave suppression, as a function of cavity flow Mach numbers, for the different KrF/CH_4 systems considered here. Note that for a system which employees a 5 atm CH_4 cell, the pressure drop is limited to $(\Delta P^*)_{AM} \leq 0.08\ P_5$, even at very low flow rates and M (which implies small flow width, W, and low PRF). We cannot estimate at this point how difficult a task this may be. The results obtained so far only establish the requirements on the acoustic suppressors which are yet to be developed.

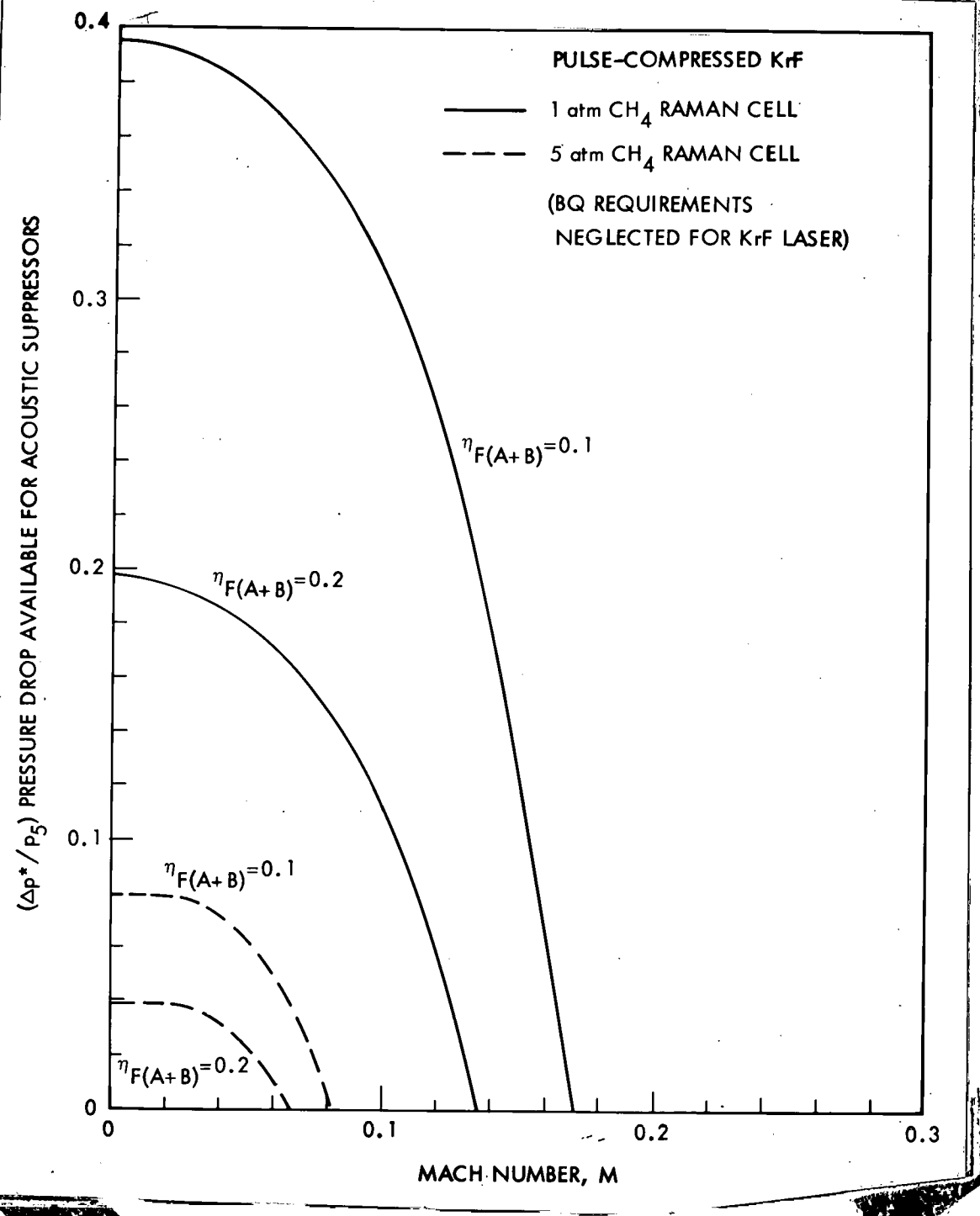

Figure 2-31. Pressure Drop Available for Acoustic Suppression in the Raman Cell Versus Mach Number for a Pulse-Compressed KrF System.

2.3.7 Comparison With the CO_2 System

It would be interesting to compare at this point the results for the KrF and CO_2 systems, using the same format. We have estimated the pressure drop required for flow management of the CO_2 laser, $(\Delta P^*)_{FTM}$, using the procedure outlined in 2.3.5.2. This value of ΔP^* was then subtracted from the overall permissible pressure drop to give the fraction available for acoustic suppression. The results are shown in Figure 2-32 for the range of flow efficiencies which is of interest; namely, between η_F = 0.1 and 0.2. The maximum pressure drop available is somewhat smaller in CO_2 than in KrF, but the fall-off with increasing M is also smaller. Operation at high M values seems to be permissible.

Other than determining the pressure drop available for acoustic suppression, Figures 2-30 and 2-31 can be used to determine the upper limit on the flow Mach number, which can be used only if pressure wave suppression requires no pressure drop. This maximum M determines also the maximum value of the product WxPRF. Using these limiting values of M, the inverse relationship of W and PRF is shown in Figure 2-23 for the different systems considered here. This figure seems to indicate that if the pressure drop associated with acoustic suppression is indeed zero, there is no serious limitation on either the flow length, W, or the pulse repetition frequency, PRF, of these laser systems. These curves should be viewed as the upper limit of W x PRF when η_F = 0.1. If higher flow efficiencies are required, the maximum M and W x PRF product will be smaller than shown here by a factor proportional to the square root of η_F.

Additional work on laser flow systems, including other candidates such as HF and Gr VI, is now in progress and will be reported on in our final report.

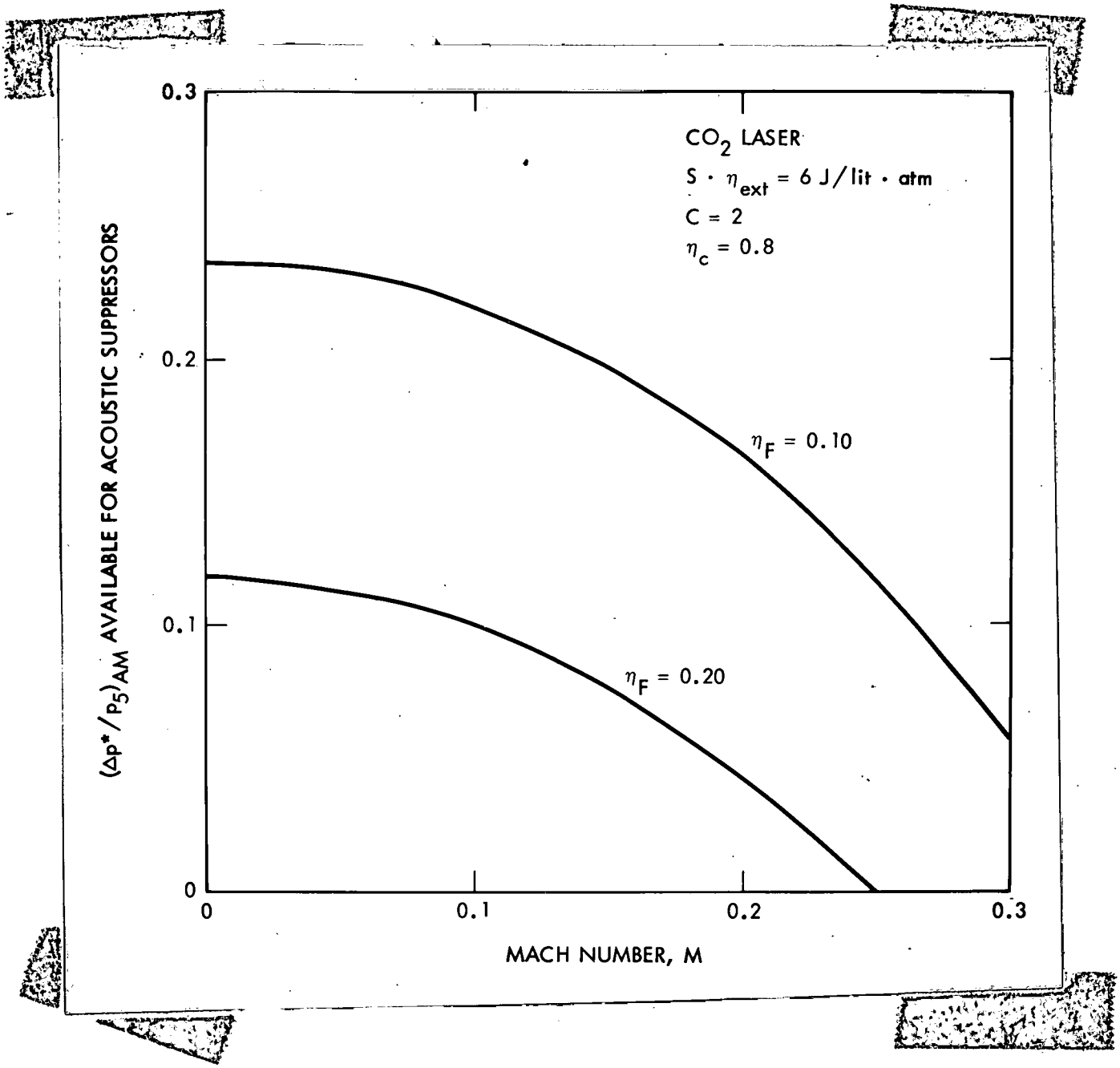

Figure 2-32. Pressure Drop Available for Acoustic Suppression Versus Mach Number for an Advanced CO_2 Laser Module.

DOCUMENT NO.
PAGE NO.

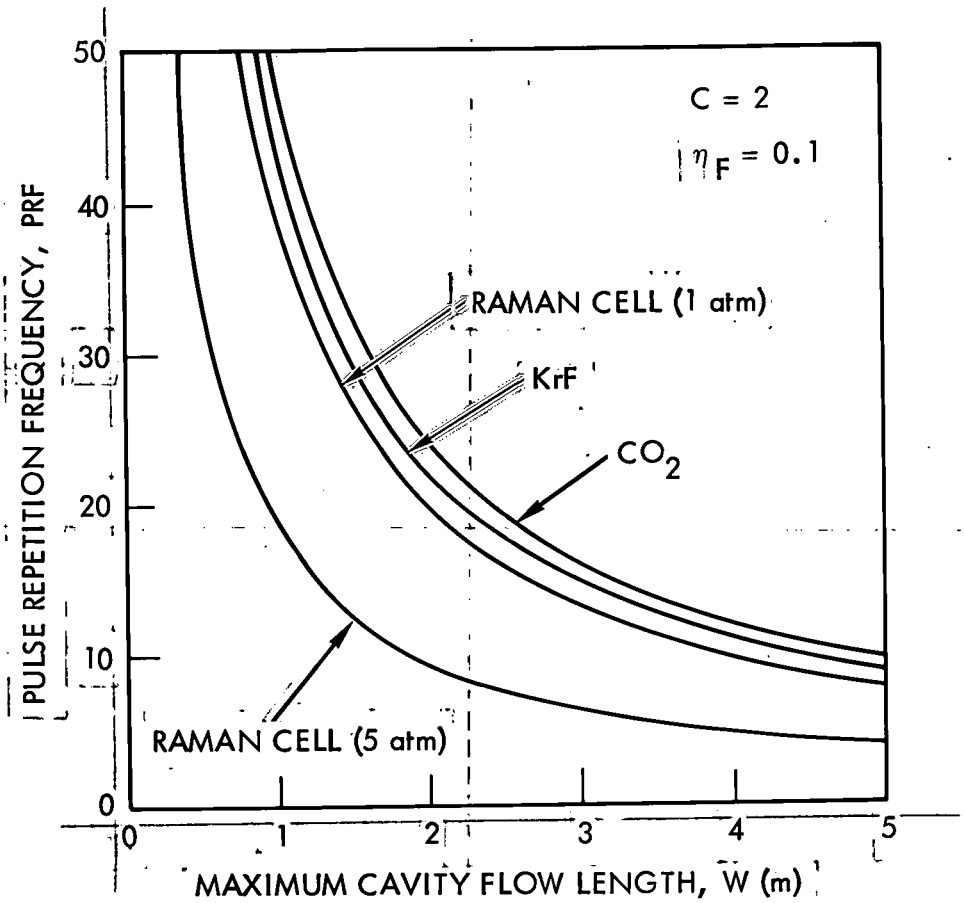

Figure 2-33. Maximum Flow Length W Versus PRF Allowed for η_F = 0.1, with Pressure Drop due to Acoustic Suppression Neglected.

3. PRESSURE WAVE SUPPRESSION STUDIES

3.1 EXPERIMENTS

3.1.1 Objectives and Approach

Gas-phase lasers, when initiated, retain within the cavity gas a large fraction of the total instantaneous energy released. This residual energy leads to substantial heating and overpressure in the cavity, and generates pressure waves which then reverberate in the flow system. Interaction of the waves with the various acoustic suppression devices and flow control and conditioning elements is complicated and produces inhomogeneities in the gas. Since such deterioration of the medium degrades the beam quality of the succeeding pulses, it is mandatory that these pressure waves be attenuated in a time which is compatible with the pulse repetition frequency of the laser. We must first try to understand and quantify these effects and then proceed to develop pressure wave attenuation devices which have a low pressure drop and can be incorporated into the closed-loop flow system of a fusion laser.

Although the physical basis of these effects is well understood in principle, the tremendous detail of complicated multidimensional and non-linear phenomena which occur through interactions between the pressure waves, the flow and the geometry of the various devices is not amenable to analysis or computation. However, experimental investigation and empirical modeling is invaluable in identifying the important issues and in evaluating the influence of various parameters. The models can then be incorporated into the existing approximate predictive methods, such as one-dimensional computer codes. A shock tube provides a simple, inexpensive laboratory tool to produce and measure such pressure wave-flow interactions in laser-like geometries and is used here to simulate a single pulse of such lasers. This approach serves the following objectives:

- Validate existing approximate analytical/computational prediction techniques (e.g., the 1-D FACTS Code)

- Develop diagnostic capabilities to measure attenuation of pressure waves and the effects of these waves on the medium homogeneity and beam quality.

- Identify, investigate and model the important issues that are not well understood, in order to improve the capabilities of the above prediction techniques.

- Develop and test new pressure suppression concepts and build up a data base of performance characteristics for alternate configurations and designs with improved performance.

3.1.2 Shock Tube Test Facility

3.1.2.1 Description of the Shock Tube

The shock tube is made of aluminum (0.25" thick) and has a rectangular cross section (3.5" square internally). It has two 8" and one 24" driver sections, which together with some filler blocks allow variation of driver length from 2" to 40" in 2" steps. There are two sections for the driven tube, 30" and 48" long. Normally, the tube is operated at ambient conditions with compressed air for driving waves (Figure 3-1). Different thicknesses of Mylar and soft aluminum are used as diaphragms, which bulge from the driver pressure and press against a set of crossed knife blades, at a distance which can be set so the diaphragm bursts at a predetermined overpressure (Figure 3-2). The driver pressure is measured by direct reading just before the diaphragm bursts. Transducer ports are provided at various locations for measuring the transient waves. A 9.5"-long optical section with two opposite walls replaced by 6.5"-diameter Schlieren windows allows measurement of the optical quality of the gas within and immediately outside the tube. The third wall of this section is 0.375" thick and is replaceable, so the behavior of a variety of acoustically suppressing or absorbing walls can be observed (Figure 3-3).

F 3-1
F 3-2
F 3-3

Besides the regular driven section, a vented driven section is also used. This has the same cross section, except that the top wall has perforations (7.2% open, 23/64" diameter holes in a symmetric, rectangular, three-in-a-row pattern). This configuration corresponds to acoustic suppressors that have been found to be very effective in pulsed lasers. (Here the unvented walls of the tube represent surfaces of symmetry.)

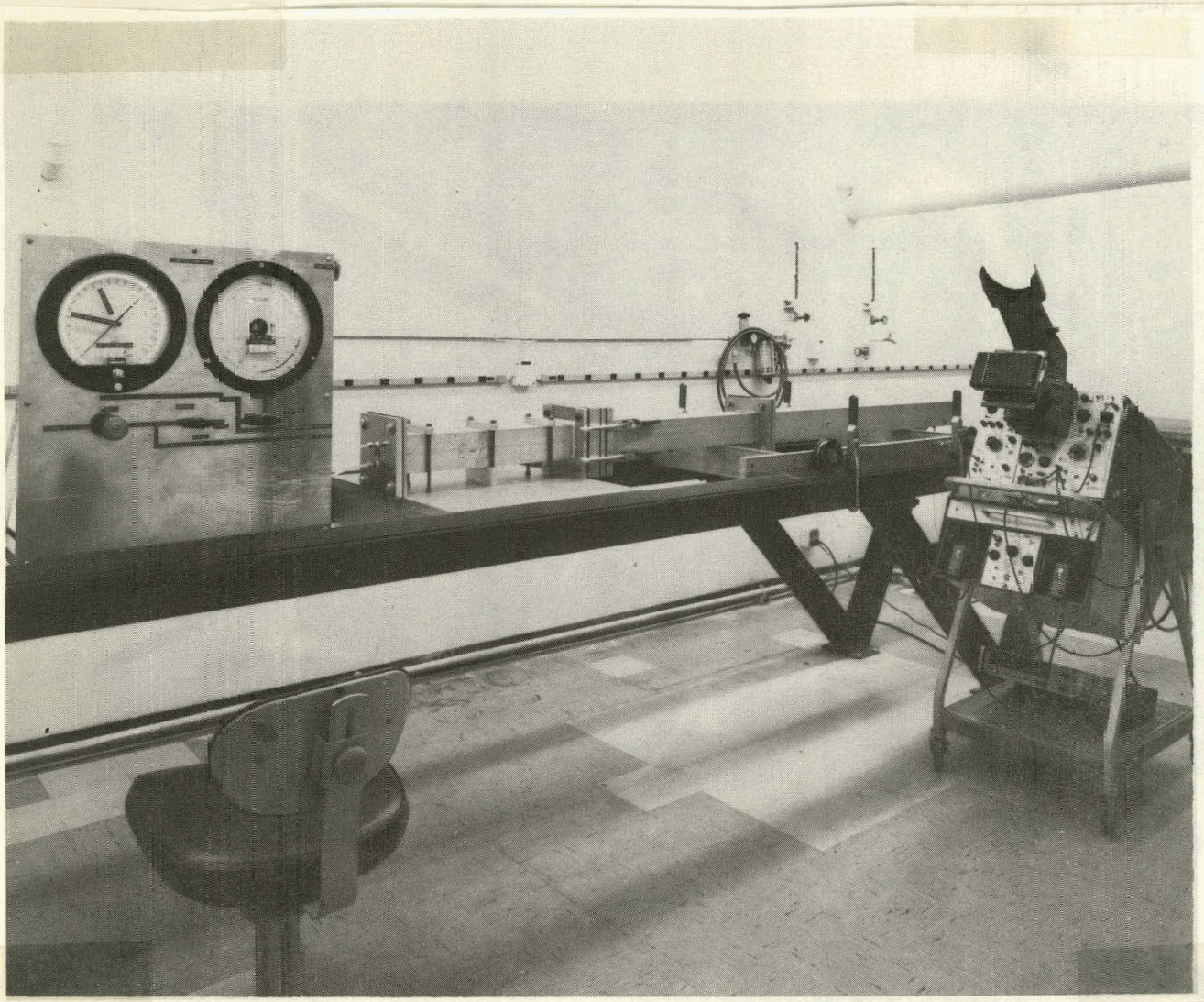

Figure 3-1. The Shock Tube Test Facility (24" Driver)

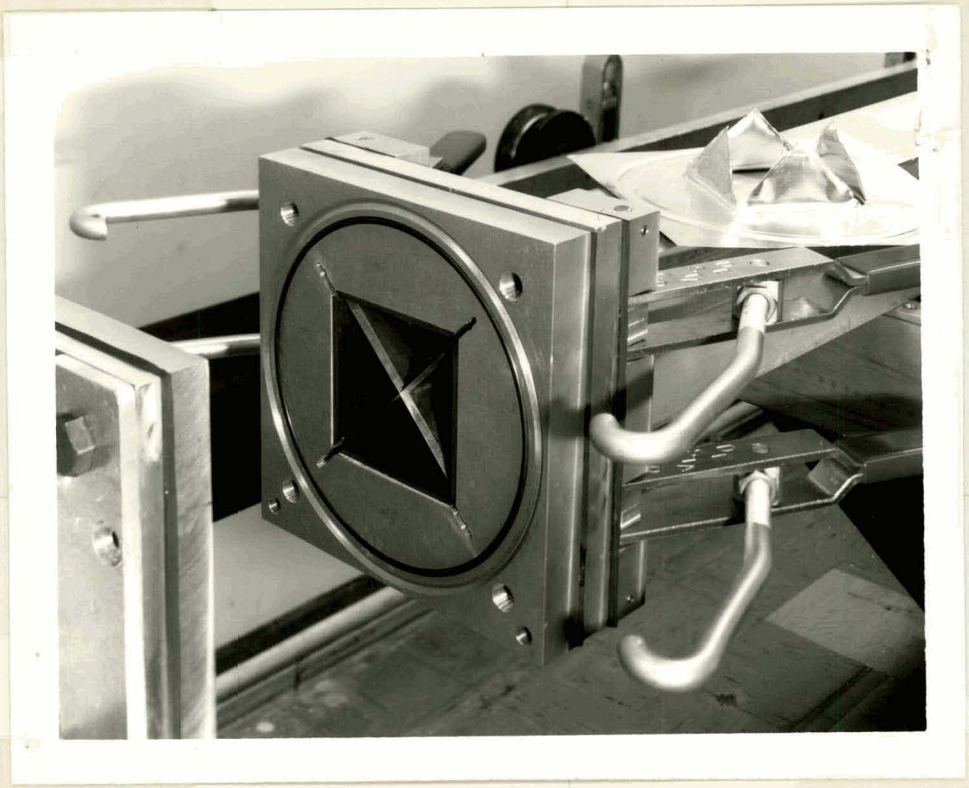

Figure 3-2. Diaphragm Station: Clamps, Knife Blades and a Burst Diaphragm

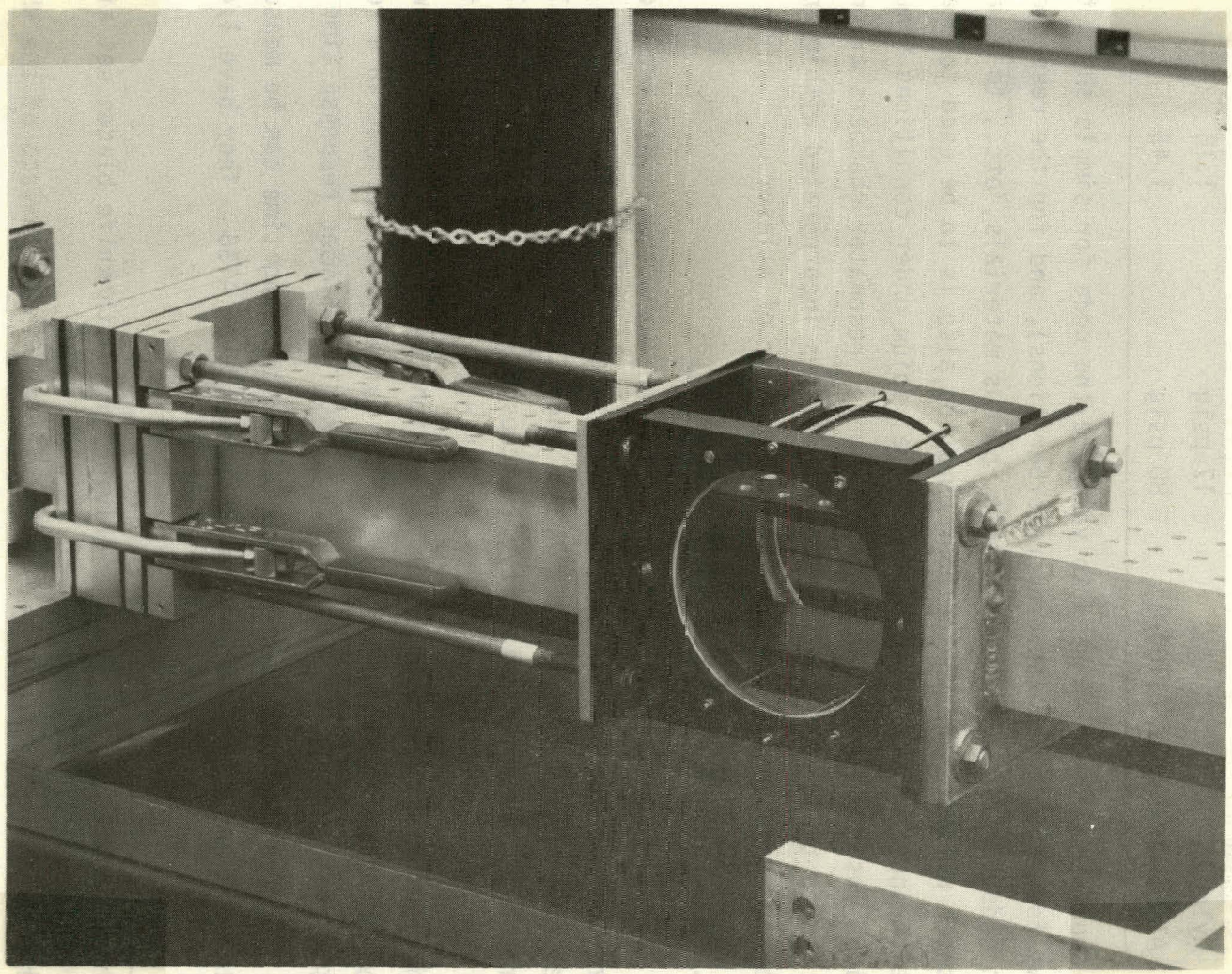

Figure 3-3. Optical Section and Vented Duct

Section lengths of 8", 16", 39" and 48" allow positioning of the optical section at different locations in the vented tube, to examine the quality of the local medium (Figure 3-3).

The nominal running conditions for the tests described later are tabulated below:*

DIAPHRAGM	BURST PRESSURE	SHOCK MACH NO.
Mylar 0.00025"	6 psig	1.08
Mylar 0.001"	17 psig	1.18
Aluminum 0.012" (1100-0)	80 psig	1.43

The shock tube is to be used to validate the code for simple shock tube flows for large times (several reverberations), and for the response of open ends, orifices, nozzles, vents, porous materials, etc., to a variety of shock pulses. The vented configuration also is to be used to measure wave attenuation and degradation of the medium under conditions simulating various lasers, some of which involve outer resonator chambers around the vented tube, or flow conditioning devices incorporated within an absorber representing the upstream attenuator of a laser.

3.1.2.2 Pressure Diagnostics and Instrumentation

The pressure measurements of the strong wave transients are made with piezoelectric gauges with built-in integrated circuit preamplifiers. Two types of gauges are used: PCB 113A21 and PCB 106b. The first has 1/4" diameter, 20 mV/psi sensitivity, 1 microsec risetime, 0.05 psi resolution, and 100 psi range. The latter has 1/2" diameter, 300 mV/psi sensitivity, 5 microsec risetime, 0.0003 psi resolution, and 15 psi range.** However, only for a few tests, as mentioned, the latter gage was used in a recessed adapter with 0.03" opening and approximately 0.3 msec response time.

The residual acoustic fluctuations after long time can be measured with Bruel and Kjaer condenser microphones type 4136. They have 1/4"

* These conditions are for air driving air, with knife blades set at 0.2" from the diaphragm.

** The gages are normally used flush with the inner surface of the shock tube.

diameter, 10 V/psi sensitivity, 5 microsec risetime, 10^{-5} psi resolution and 1.5 psi range. The amplitudes of the initial transients in the experiments are far beyond the range of the microphones and some automatic shuttering is required to protect them.

Preliminary measurements have been made with piezoelectric gauges and are recorded photographically from a Tektronix 556 oscilloscope with 1A6 preamplifiers (1 mV resolution). Future measurements will be acquired, stored, processed and reproduced digitally with a Norland 3001 (Figure 3-4). This device has four transient recording channels (1024 points at 200 kHz each, or two channels of 2048 points at 500 kHz each) with 10-bit resolution, coupled with a programmable microprocessor which controls a cathode ray tube display and a flexible disk magnetic mass storage device. It can also drive a printer and analog plotter. The built-in software is extensive and sophisticated, and handles Fast Fourier Transforms, Correlations, Convolutions, etc., with simple keystroke operations, as well as performs algebraic operations, integrations, differentiations, etc., on arrays of data, with simple user programs.

3.1.2.3 Optical Diagnostics

The optical changes caused in the medium by the waves are initially strong and contain sharp gradients, which decay to weaker and smoother fluctuations in time. Therefore it is advantageous to first use shadowgraphy to visualize the initial nature and extent of the degradation of homogeneity in the medium, and then Schlieren technique for the later stages. Both methods use a spark light for a point source (0.03" pin hole, submicrosecond flash) and a 100" focal length spherical mirror for collimating the beam. In the shadowgraph, Polaroid black and white film type 667 and type 57 (ASA 3000) are used for recording the image directly behind the optical section. The Schlieren enhances the sensitivity by reflecting back the collimated beam through the optical section, and utilizing the same spherical mirror to refocus the beam onto a pinhole or a dot which eliminates the undesireable portion of light from the beam. The filtered beam is then used to image the optical section onto the film.

Both of the techniques above, although excellent in investigating the nature of the optical deterioration of the medium, are not sufficiently

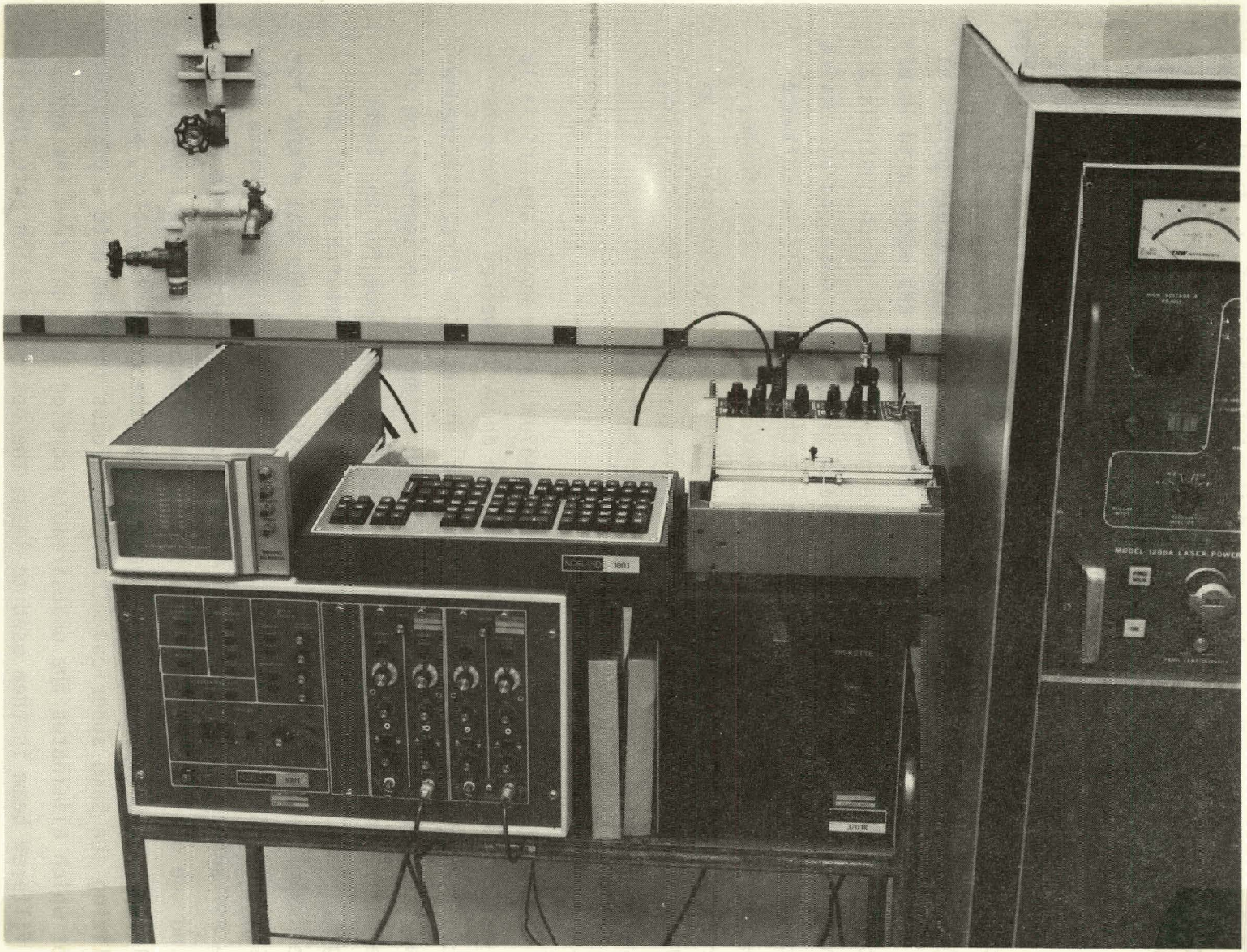

Figure 3-4. Digital Processing Oscilloscope: Norland 3001

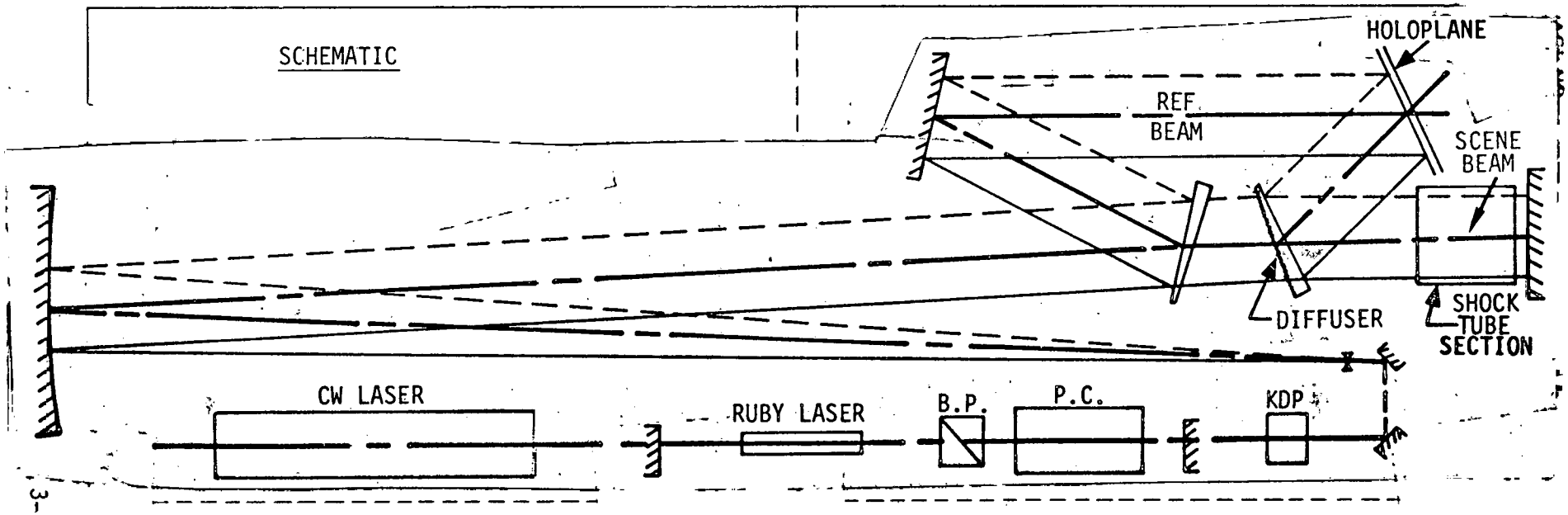

- TECHNIQUES FOR ENHANCING THE SENSITIVITY OF THE HOLOGRAPHIC INTERFEROMETER
  - DOUBLE PASS SYSTEM
  - FREQUENCY DOJBLING FROM RUBY OR He-Ne LASERS
  - DARK BACKGROUND INTERFEROMETRY BY PHASE SHIFTING
  - INCREASE OPTICAL PATH: WIDER SECTIONS, HEAVY GASES (SF_6 OR FREONS), HIGHER PRESSURES
  - DENSITOMETRIC READING OR INTERFEROGRAM
  - STORED BEAM HOLOGRAPHIC INTERFEROMETRY WITH DIRECT READOUT OF LIGHT INTENSITY AND PHASE VARIATIONS.

Figure 3-5. Plan for Holographic Interferometry

quantitative to measure phase perturbations to a coherent beam of light. This can be done with holographic interferometry. Figure 3-5 shows a schematic of the holocamera which is to be used in this program. Here, basically, the monochromatic, coherent collimated beam of a Q-switched ruby laser is split into a reference beam and a scene beam. The scene beam is double-passed through the optical section and is then combined with the reference beam to form a fine fringe interference pattern, a hologram, on the film. This pattern contains the information of the phase perturbations caused by the optical train. The development of inhomogeneities in the medium produces a changed pattern on the same film during a second exposure. The Moire fringes formed by the two patterns correspond to the fringes of a Mach-Zehnder interferometer, and can be used to measure the optical path differences caused by the inhomogeneities.

3.1.3 Shock Tube Experimental Results

3.1.3.1 Closed-Tube Tests

Simple shock tube tests were performed first to obtain pressure wave data for comparison with the computations, i.e., to ensure good agreement for the short time when the flow in the shock tube is well understood and to examine the development of differences over much longer periods. This was done with the strongest and the weakest diaphragms. The results for a 24"-long driver, with 78"-long driven section at ambient pressure are presented below (Figure 3-6).

Two pressure gages (PCB113A21) were located in the driven section, one near the midpoint and one near the far closed end (respectively, 33" and 76" from the diaphragm). Figure 3-7 and 3-8 show oscilloscope records, respectively for 0.00025" Mylar (6 psig) and 0.012" soft aluminum (80 psig) diaphragms. In each figure, the top picture shows the short time (10-20 ms) transients, and the bottom picture, the long time (100 ms) oscillations. The top trace in each picture is the signal from the gage near the midpoint of the tube, and the bottom trace is that of the gage at the far end of the driven section.

As is well known in normal shock tube operation, the pressure difference across the diaphragm is divided between two waves when the diaphragm bursts: a compression wave, which steepens into a shock as it travels into the driven section, and a rarefaction, which spreads as it travels into the driver. The rarefaction reflects from the closed end of the driver and then travels into the driven section, following the shock. The two waves together form a compression pulse, approximately twice the length of the driver, which then bounces back and forth between the two closed ends of the whole tube.

In Figure 3-7, the gage near the midpoint (top picture, top trace) shows the first pass of this compression pulse, its second pass after reflection from the closed end of the driven section and its third pass after its reflection from the closed end of the driver. Thus, near the midpoint of the tube, each pass of the compression pulse can be observed separately. For the gage near the closed end (top picture, bottom trace),

BOTTOM OF PAGE — How many pages? — BOTTOM OF PAGE

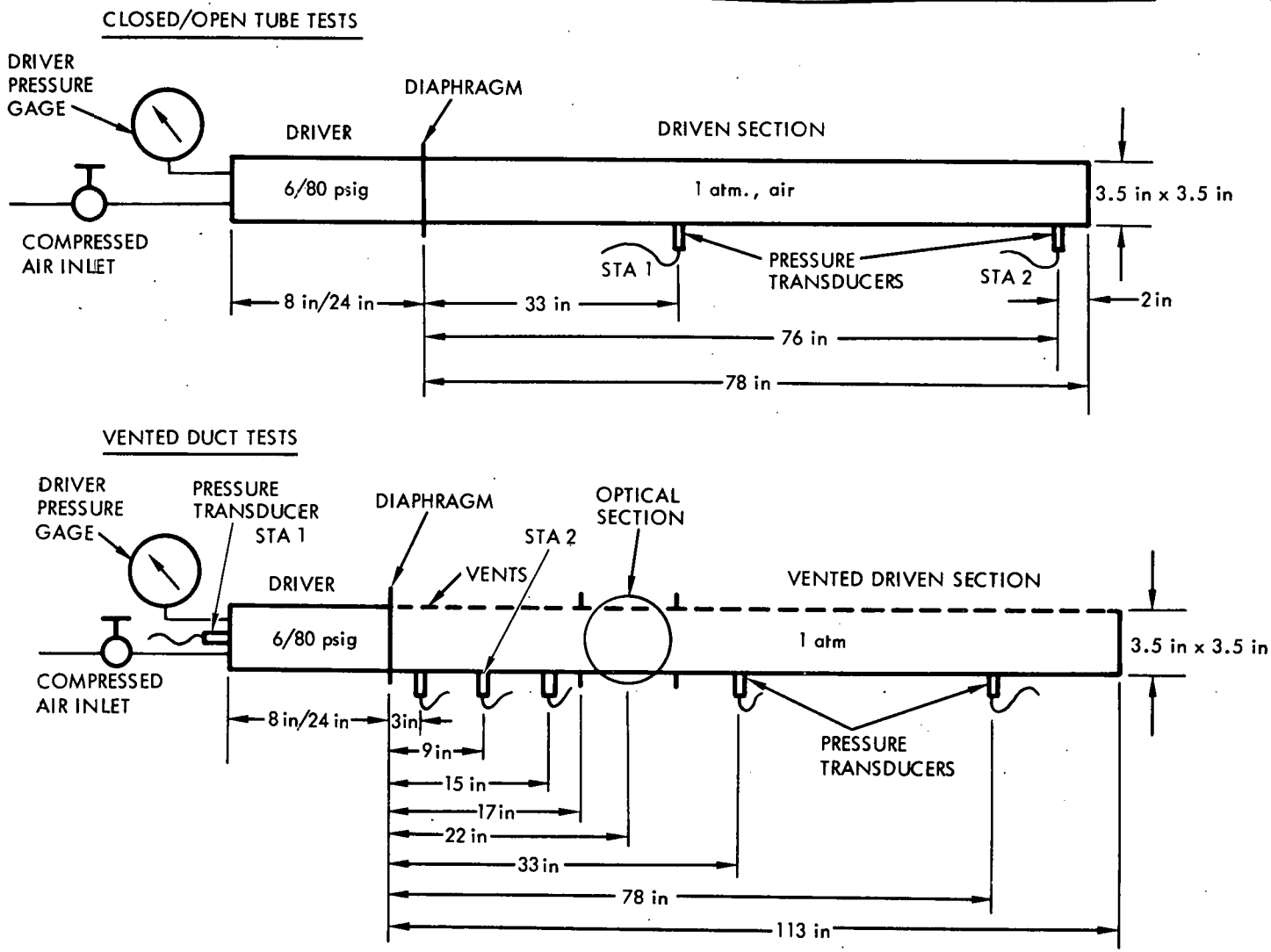

Figure 3-6. Test Configurations of Shock Tube

24" DRIVER, 78" DRIVEN SECTION, 6 PSIG OVERPRESSURE

2 ms/DIV

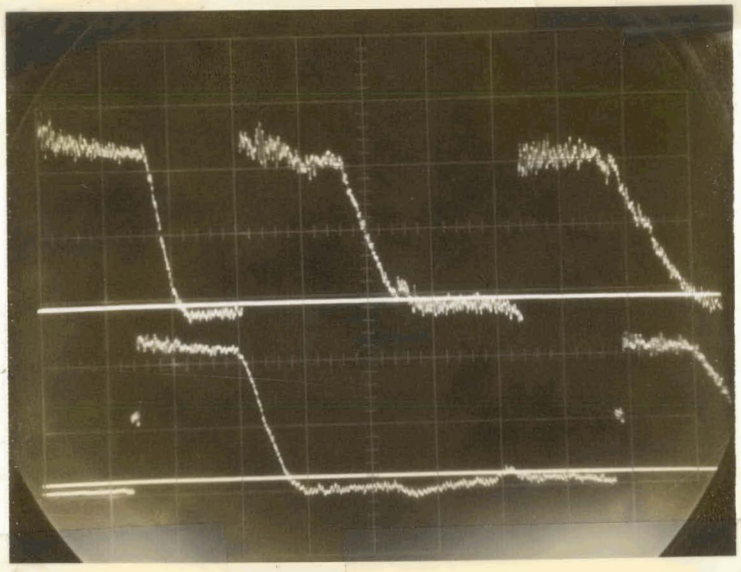

GAGES PCB 113A21 AT

0.075 ATM/DIV — 33" FROM DIAPHRAGM

0.17 ATM/DIV — 76" FROM DIAPHRAGM

SHORT-TERM TRANSIENTS

10 ms/DIV

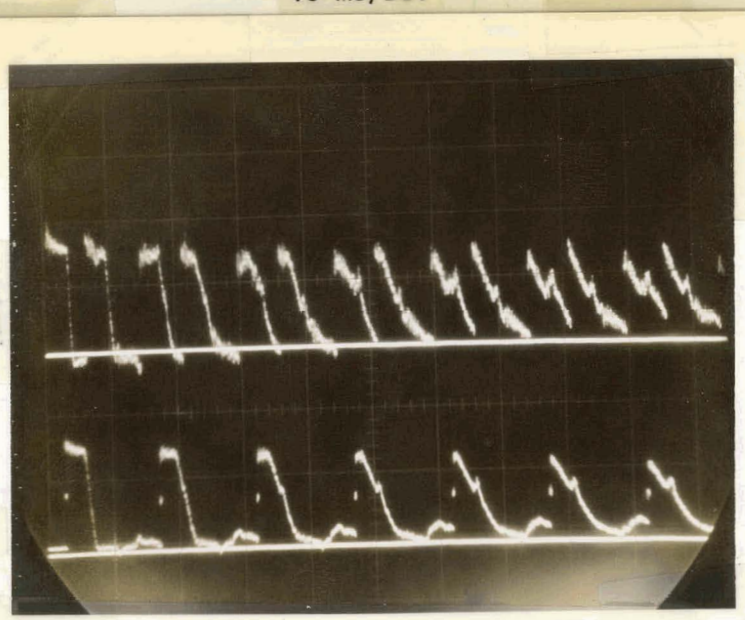

GAGES PCB 113A21 AT

0.078 ATM/DIV — 33" FROM DIAPHRAGM

0.184 ATM/DIV — 76" FROM DIAPHRAGM

LONG-TERM OSCILLATIONS

Figure 3-7. Closed Tube Tests, Weak Waves

24" DRIVER, 78" DRIVEN SECTION, 80 PSIG OVERPRESSURE

1 ms/DIV

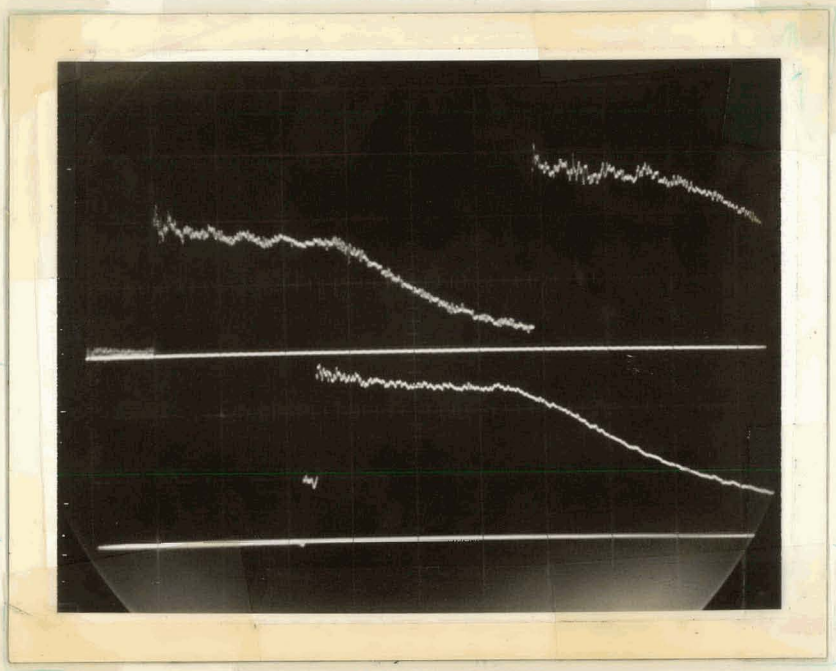

.70 ATM/DIV

1.55 ATM/DIV

GAGES PCB113A21 AT

33" FROM DIAPHRAGM

76" FROM DIAPHRAGM

SHORT-TERM TRANSIENTS

10 ms/DIV

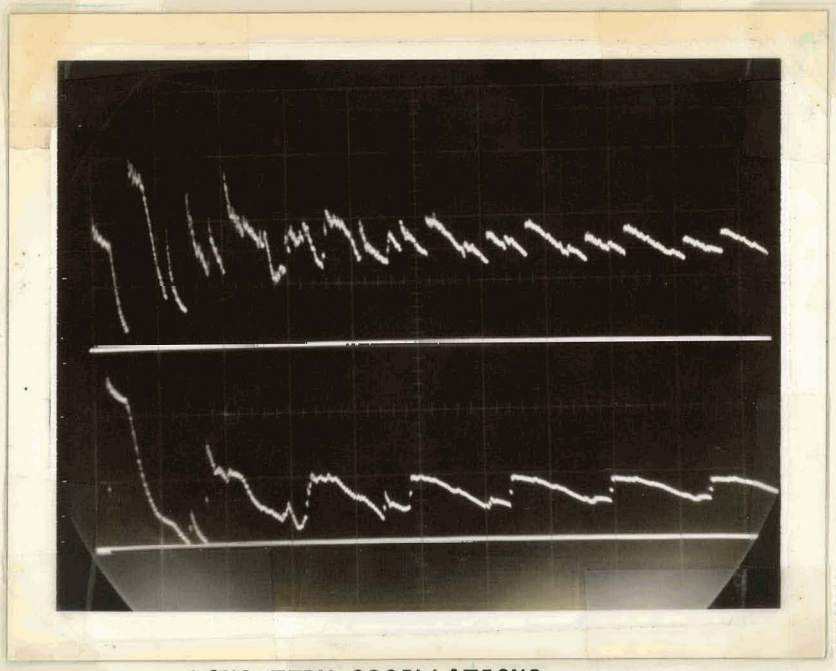

.61 ATM/DIV

1.55 ATM/DIV

GAGES PCB113A21 AT

33" FROM DIAPHRAGM

76" FROM DIAPHRAGM

LONG-TERM OSCILLATIONS

Figure 3-8. Closed Tube Tests, Strong Waves

the incident pulse and its reflection are superposed. The overpressure in this case is small, and the waves exhibit almost a linear (acoustic) behavior, i.e., the superposition results in approximately twice the amplitude. Thus the gage near the closed end observes twice as large a pulse, half as often, in contrast to the other gage. This behavior persists for many reflections (bottom picture), with very little decay in the amplitude of the oscillation, as may be expected of waves which are almost linear.

In comparison, Figure 3-8 shows the waves produced by a strong overpressure which are quite nonlinear. Although qualitatively the behavior is quite similar, it is easy to see that the rarefaction spreads far more and the shock reflection from the closed end more than doubles the pressure (top picture). Here the traces end before the second pass of the compression pulse is completed. In this case, the amplitude of the waves decays rapidly due to the strongly nonlinear behavior (bottom picture), as the rarefaction catches up with and eats into the shock wave and the mean pressure settles to a value above the initial pressure in the driven section. Some additional weaker waves can also be seen in this picture, as well as in the previous figure, where they are much weaker. Such waves may be caused by reflections from contact surfaces (entropy discontinuities caused by the nonlinearities), or from experimental non-idealizations like diaphragm petals or area constrictions (25%) at the knife edge station.

3.1.3.2 Open-Tube Tests

The flow ducts for the fusion lasers may often have to be open ended, so a smooth mean flow can be maintained with a minimum pressure drop. Also, understanding of the impulsive jet flows generated by wave interactions with nozzles and orifices is a key issue in effective acoustic wave suppression and control of medium homogeneity. Therefore, pressure-wave data was obtained in the simple situation of an open-ended shock tube, for comparison with model computations of wave reflection and subsequent long-time oscillation. This is done for the weak and strong waves, as in the previous case of a closed shock tube. The shock tube configuration, instruments and their locations, etc., are also identical to that case, except that the far end of the driven section (which has no flange) is left open to the atmosphere.

In this case also, a compression pulse traveling towards the open end develops in the same fashion as for the closed tube. However, at the open end very complicated processes occur. The waves diffract and diverge into the atmosphere, and the pressure at the open end tends back to atmospheric pressure within times of the order of a few acoustic travel times across the cross section of the tube. The wave diffraction is a complicated multidimensional process, and sets up transverse oscillations near the open end. Nevertheless, from a larger distance inside the tube, it still appears almost one-dimensional and results in a negative reflection coefficient, i.e., a compression reflects as a rarefaction and vice versa. This is a direct result of the condition that the pressure at the open end returns quickly to atmospheric pressure.

This phenomenon of pulse inversion during reflection from an open end can be seen in Figure 3-9, for weak waves (top picture, top trace). Here, the gage near the midpoint of the tube clearly shows the incident compression pulse coming from the driver and then its inversion due to reflection, i.e., a rarefaction pulse returning from the open end. The gage near the open end (top picture, bottom trace) shows only minor deviations from the ambient pressure as expected. This can be interpreted as the simultaneous occurrence (superposition) of the compression and the rarefaction pulse at that location. However, the real process is quite complex as evidenced by the sharp deviations from ambient pressure and the high frequency fluctuation which appears to be a transverse oscillation in the tube.

The reflection of the rarefaction pulse from the end of the driver, and again its reflection from the open end as a compression pulse, etc., can be seen clearly at the gage near the midpoint (bottom picture, top trace). An inversion occurs at each reflection from the open end, and after each inversion the pulse makes two passes over the gage, on its way to the driver and back. In contrast to the corresponding closed tube case (Figure 3-7, bottom picture, top trace), the decay of oscillation in the open tube is substantially rapid. This is attributable to the radiation of acoustic energy to the atmosphere from the open end, and to the kinetic energy transmitted to fluid when separation and vortex formation occurs at the mouth of the open tube during each reflection process.

24" DRIVER, 78" DRIVEN SECTION, 6 PSIG OVERPRESSURE

2 ms/DIV

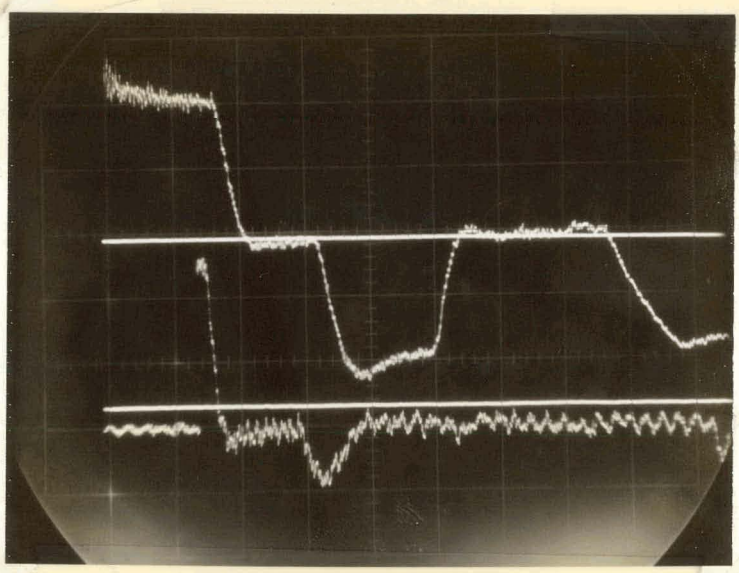

.067 ATM/DIV

.072 ATM/DIV

GAGES PCB113A21 AT

33" FROM DIAPHRAGM

76" FROM DIAPHRAGM

SHORT-TERM TRANSIENTS

10 ms/DIV

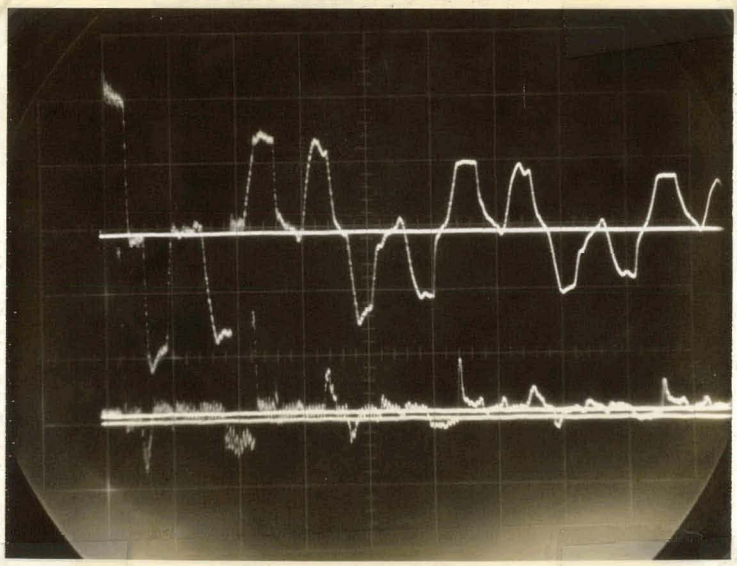

.071 ATM/DIV

.108 ATM/DIV

GAGES PCB113A21 AT

33" FROM DIAPHRAGM

76" FROM DIAPHRAGM

LONG-TERM OSCILLATIONS

Figure 3-9. Open Tube Tests, Weak Waves

The energy in these jet-like impulsive out-flows and in-flows is not recoverable, but is dissipated by turbulence and eventually by viscosity. In this context, it is interesting that the reflection from the open end, the rarefaction pulse (top picture, top trace), is substantially smaller in amplitude than the incident compression pulse, even though the pressure at the open end (bottom trace) returns very closely to ambient pressure during the reflection.

For the stronger waves, although qualitatively the same phenomenon of inversion occurs upon reflection from the open end (Figure 3-10, top picture), the real process can be even more complicated and can make gross changes in the overall picture. For example, the reflections seem to decay so strongly that it is hardly possible to trace a clear sequence of pulses being inverted and reflected between the two ends of the tube (bottom picture). Only a mean long wave oscillation is observed which seems to correspond to the organpipe mode of the whole tube. It is also important to note that the pressure at the open end is unable to return to ambient pressure during reflection (top picture, bottom trace), in contrast to the weak wave case (Figure 3-9, top picture, bottom trace). It is very likely that the flow out of the mouth of the open tube is supersonic during the reflection, and supports expansion waves in the flow. This is similar to the oblique expansion waves found in over-expanded jets, in which case the pressure in the nozzle is maintained above ambient pressure.

F3-10

F3-9

3.1.3.3 Vented Duct Tests

Acoustic suppressors using the vented duct concept are known to be quite effective in repetitively pulsed gas-phase lasers. Here, short and long shock tube drivers were fired into a vented driven section (open to the atmosphere, but with a closed end), and attenuation of pressure oscillations was measured for strong and weak waves. Further, spark shadowgraphy was used to visualize and understand various phases of the flow through vents, and the nature and extent of medium contamination produced by the flow into the tube during the negative phase of pressure oscillation, even at a station far away from the driver.

24" DRIVER, 78" DRIVEN SECTION, 80 PSIG OVERPRESSURE

2 ms/DIV

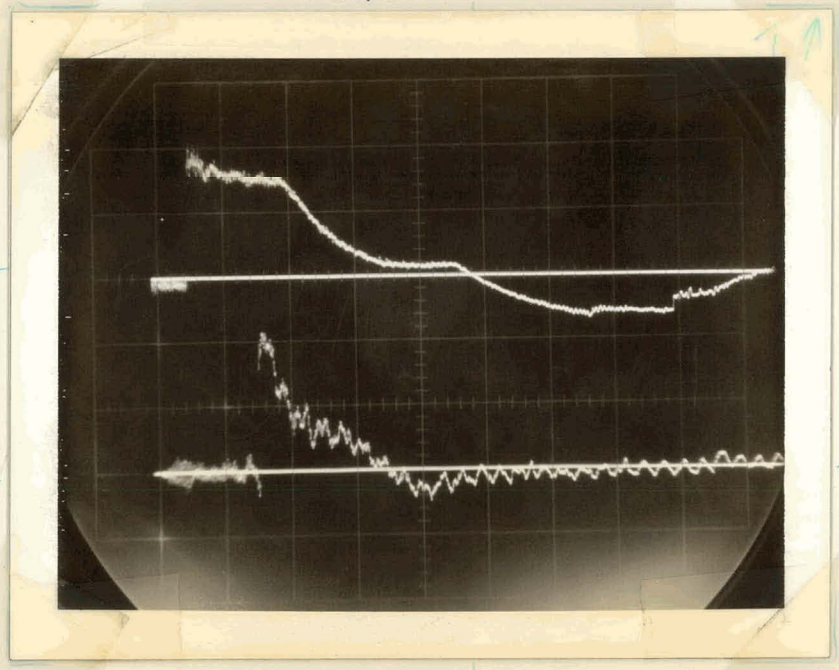

0.86 ATM/DIV

0.63 ATM/DIV

GAGES PCB113A21 AT

33" FROM DIAPHRAGM

76" FROM DIAPHRAGM

SHORT-TERM TRANSIENTS

10 ms/DIV

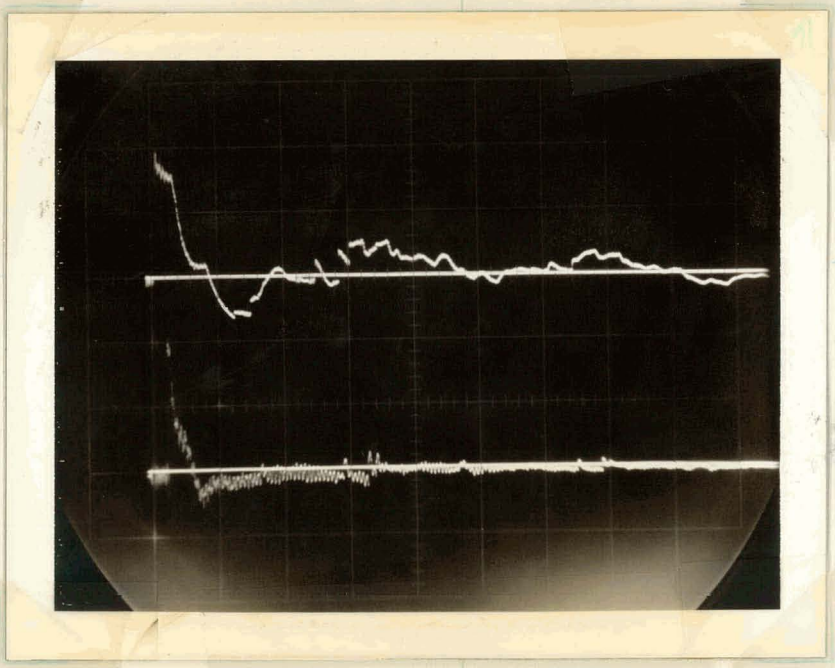

0.77 ATM/DIV

0.67 ATM/DIV

GAGES PCB113A21 AT

33" FROM DIAPHRAGM

76" FROM DIAPHRAGM

LONG-TERM OSCILLATIONS

Figure 3-10. Open Tube Tests, Strong Waves

The correspondence between the geometries of a typical laser flow duct and the vented configuration of the shock tube is shown in Figure 3-11. The bottom wall of the shock tube (opposite the vented wall on top) and the closed end wall of the driver represent surfaces of symmetry across which very little flow is expected to occur. There is almost no variation in the wave and flowfields of the laser in the direction of the beam, and the narrowness of the shock tube in this direction is of no consequence. The upstream suppressor of the laser may be different and, again, it is possible to test independently that configuration in the shock tube.

For the experiments described below, the vented driven section was 113" long, with the 9.5" optical section placed at 17" from the diaphragm (Figure 3-6). For these tests it was found more useful to locate one gage at 9" from the diaphragm into the driven section and the other gage at the center of the driver endwall, although a few tests were made with the gages at 33" and 78" from the diaphragm for comparison with the previous tests. Generally, the piezoelectric transducers were used flush with the shock tube wall. Only special tests PCB106B's were used in recessed mounts as mentioned above. Two different driver lengths were used, 8" and 24", with two types of diaphragms giving driver overpressures of 80 psig and 6 psig. Pressure variations were observed also for long times (0.1 sec) and at high amplifications. The far end of the vented tube was normally closed, except for a few tests as mentioned below.

Figure 3-12 shows the behavior of the strong waves in the vented duct with an 8" driver. The top picture shows the pressure changes at the familiar locations (33" and 78" from the diaphragm) in the driven section. Clearly, unlike the previous cases, a repeating pattern of pulses does not develop. The compression pulse from the driver is weakened substantially as it travels down the tube, by the expansion waves generated from the outflow through the vents, which catch up with the leading shock. The reflection from the closed end becomes even weaker and is too small to be identified at the 33" location (bottom trace).

The lower picture in this figure shows the pressure variations inside and close to the driver. At 9" from the driver (top trace), very strong rapid fluctuations are observed immediately behind the shock, and the venting appears to result in a substantial period of underpressure in this

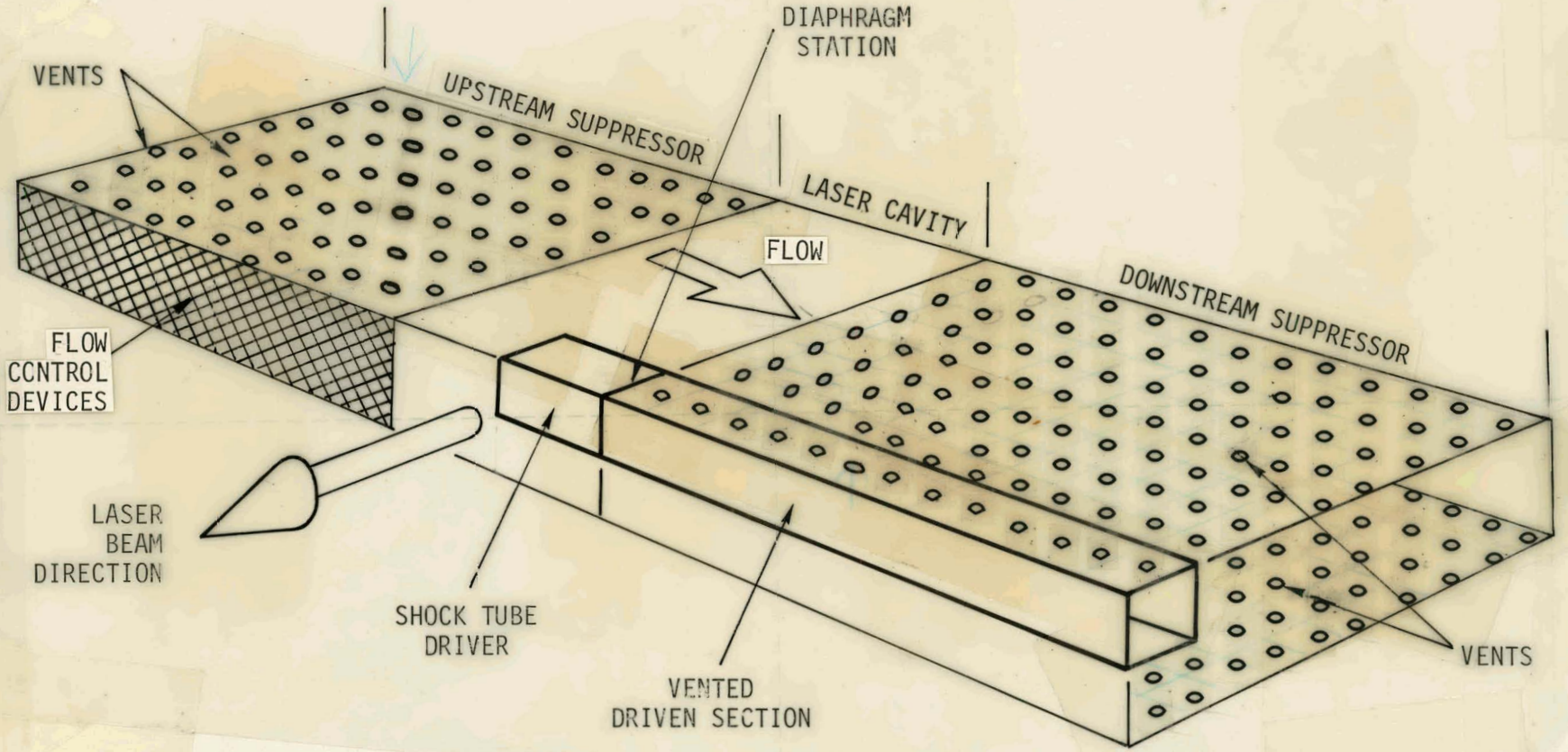

LASER AND SHOCK TUBE: GEOMETRICAL CORRESPONDENCE

8" DRIVER, 113" VENTED TUBE, 7.2% OPEN, 80 PSIG OVERPRESSURE

2 ms/DIV

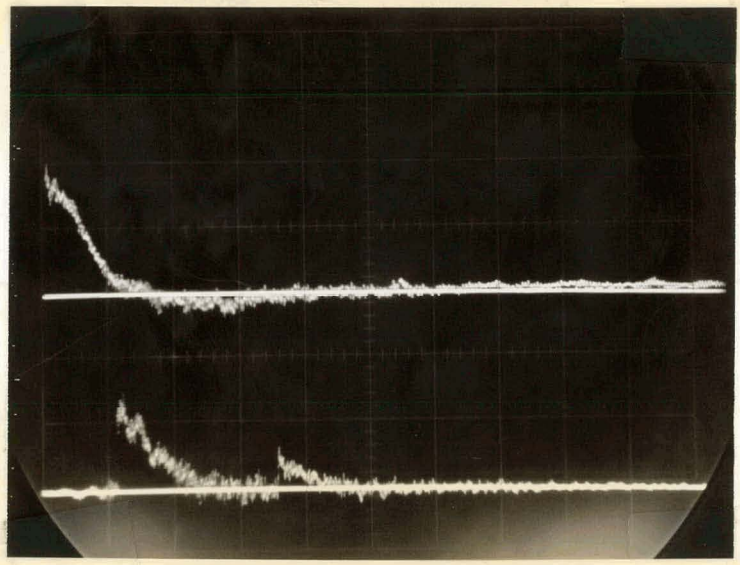

GAGES PCB113A21 AT

.73 ATM/DIV

33" FROM DIAPHRAGM

.73 ATM/DIV

78" FROM DIAPHRAGM

TRANSIENTS IN TUBE

2 ms/DIV

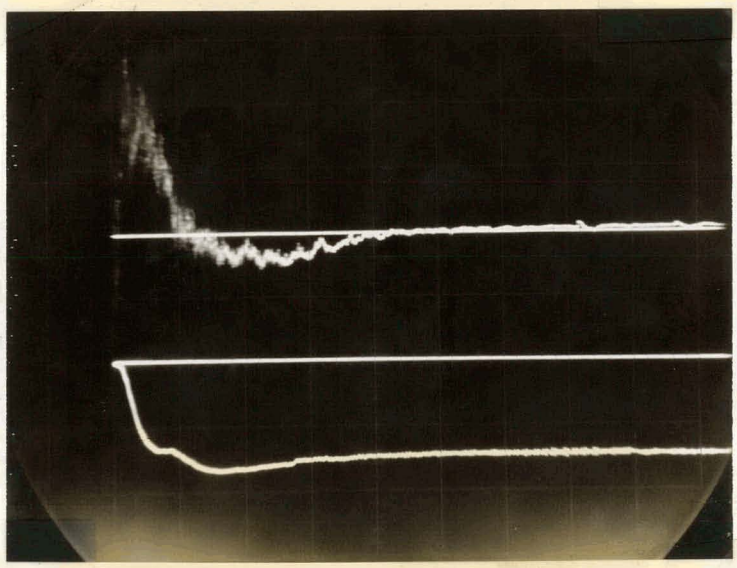

GAGES PCB113A21 AT

.73 ATM/DIV

9" FROM DIAPHRAGM

3.65 ATM/DIV

CENTER OF DRIVER ENDWALL

TRANSIENTS NEAR DRIVER

Figure 3-12. Vented Tube Tests, Strong Waves, Short Driver

area after the compression pulse has passed. At the closed end of the driver (bottom trace), a significant undershoot is also seen as the gage settles to ambient pressure from its zero at the driver overpressure. Again, the undershoot implies a pressure substantially below the ambient pressure.

In the next figure (3-13), the signals from the same four pressure gages are shown in the same sequence, amplified ten times to exhibit the fine-scale oscillations and the details of undershoot. The high frequency fluctuations in the tube (top picture) probably result from the multitude of three-dimensional diffraction waves, each being radiated from a different vent hole, as the shock passes over it. This must lead to a certain amount of transverse oscillation, and perhaps other complicated wave modes. The high frequency oscillation also occurs at the 9" location (bottom picture, top trace), although it appears to have decayed strongly in about 10-15 msec. The arrival of the reflected shock and its re-reflection from the driver can be seen clearly on this amplified scale. Although observed on a less sensitive scale, the pressure at the driver endwall seems to show much less high frequency oscillation. Its distance from the vent holes, nonlinear spreading of expansion waves, and gage location on the tube centerline (which is a node for transverse pressure oscillations) are possible reasons. The pressure in the driver and its vicinity seems to recover from the undershoot fairly monotonically in this case.

The pressure variations for the same 8" driver in the case of weak waves are shown in Figure 3-14. The top picture shows the pressure at 9" from the driver (top trace) and on the driver end wall (bottom trace). Qualitative features of the traces are quite similar, such as the occurrence of expansion waves behind the shock, high frequency fluctuations, pressure undershoot and the occurrence of the reflected shock. The high frequency fluctuation seems relatively smaller and the reflected shock larger, indicating that the venting is less effetive at attenuating weak waves. This is to be expected since strong waves produce strong jet-like flows through the vent holes which cause more energy dissipation. The bottom picture shows the above pressure variations on amplified scales (top trace: X4; bottom trace: X5, bottom trace is shifted to the right by 1 division). Clearly, the relative undershoot is larger in this case

8" DRIVER, 113" VENTED TUBE, 7.2% OPEN, 80 PSIG OVERPRESSURE

2 ms/DIV

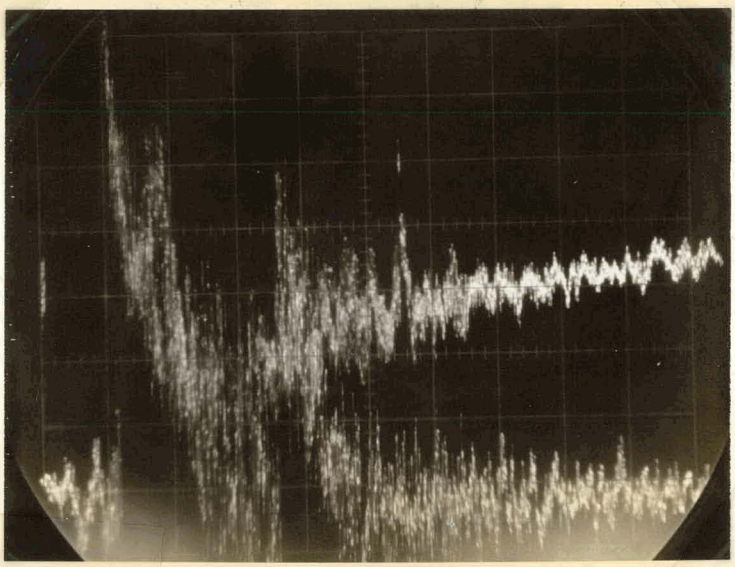

.073 ATM/DIV

.073 ATM/DIV

GAGES PCB113A21 AT

33" FROM DIAPHRAGM

78" FROM DIAPHRAGM

RAPID OSCILLATIONS IN TUBE

2 ms/DIV

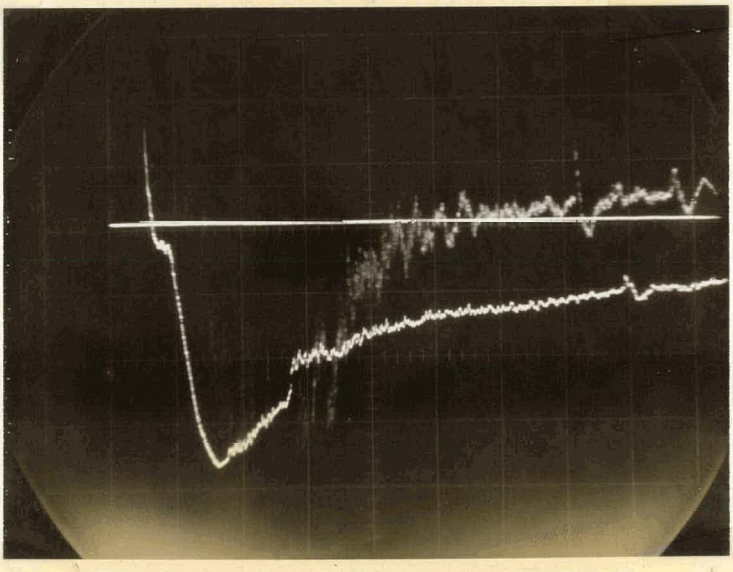

.073 ATM/DIV

.365 ATM/DIV

GAGES PCB113A21 AT

9" FROM DIAPHRAGM

DRIVER ENDWALL

OSCILLATIONS NEAR DRIVER

Figure 3-13. Vented Tube Tests, Strong Waves at High Amplifications

8" DRIVER, 113" VENTED TUBE, 7.2% OPEN, 6 PSIG OVERPRESSURE

2 ms/DIV

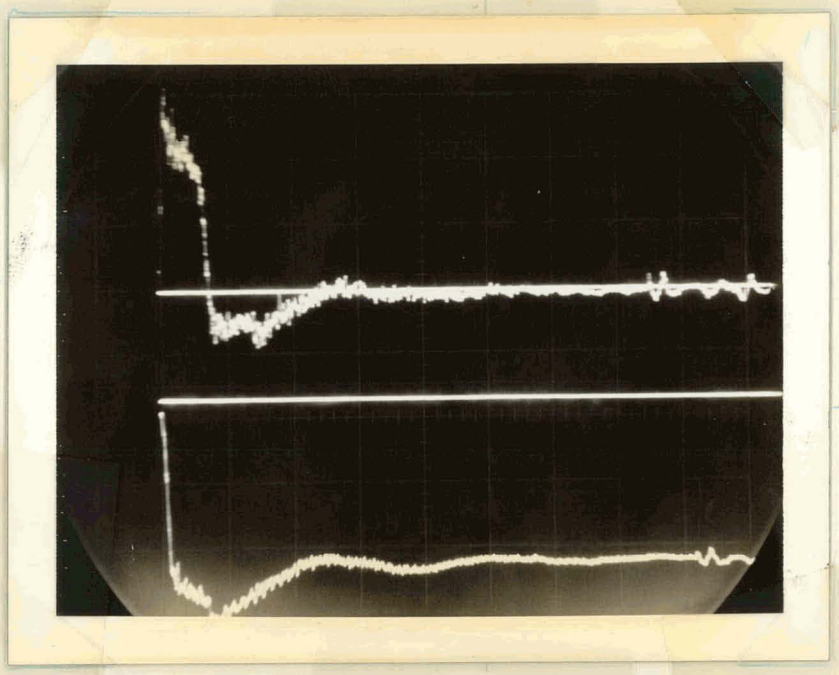

.06 ATM/DIV

.185 ATM/DIV

GAGES PCB113A21 AT 9" FROM DIAPHRAGM

DRIVER ENDWALL

TRANSIENTS NEAR DRIVER

2 ms/DIV

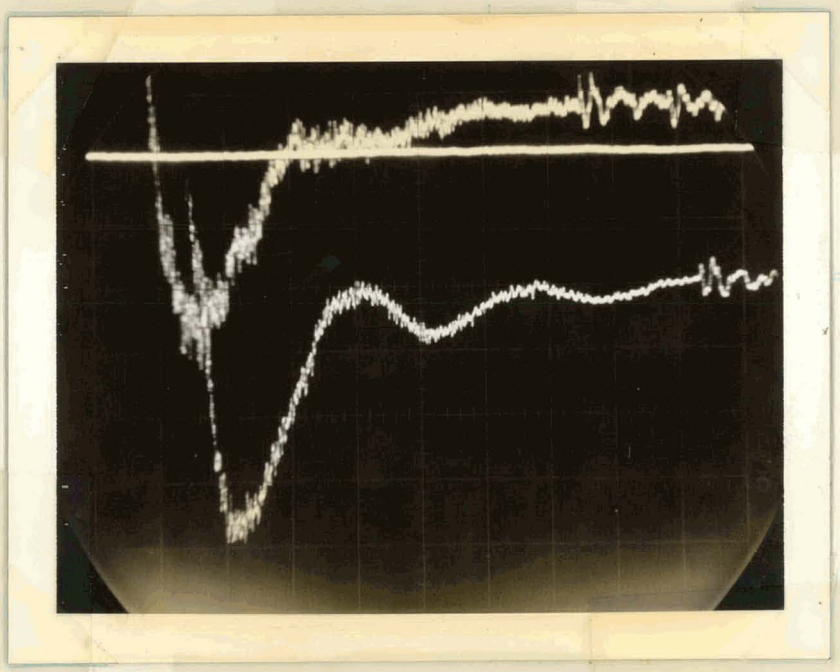

.015 ATM/DIV

.037 ATM/DIV

GAGES PCB113A21 AT 9" FROM DIAPHRAGM

DRIVER ENDWALL

AMPLIFIED TRANSIENTS

Figure 3-14. Vented Tube Tests, Weak Waves, Short Driver

and the pressure undulates as it returns to ambient conditions, which substantiates the fact that vents are less effective for weaker waves.

The magnitude of the undershoot in the duct pressure varies along the duct. It is maximum within the driver and gets smaller at larger distances from the driver. This is shown in Figure 3-15, with the PCB106B gages at driver endwall (top picture, bottom trace), and at the following distances from the diaphragm: 3" (bottom picture, top trace), 9" (top picture, top trace), 15" (bottom picture, bottom trace). Qualitatively, this seems similar to a quarter-wave oscillation of a open tube which in this case is the driver. However, there is no clear indication of the existence of a definite pressure node corresponding to the open end.

Figures 3-16 and 3-17 show the pressure variations at the driver endwall and at the 9" location as recorded with PCB113A21 gages, respectively, for the strong waves and the weak waves. Again, the same qualitative features are seen: expansion following the shock, high frequency fluctuations, undershoot and the reflected shock. However, the overall process occurs correspondingly slower for the longer driver. The lower pictures in each figure show the pressure signals at high amplifications; for strong waves, X10; for weak waves, X4 top trace, X2.5 bottom trace. Again, it is clear that for weak waves the undershoot is larger and there is pronounced undulation, indicating that the venting is less effective for these waves. It is interesting that for the long driver, even the strong waves show some undulation. On comparison of the relative undershoots and the undulation for the two drivers, both for strong and weak waves, it appears that, for a given venting, longer drivers produce more undulation and perhaps bigger undershoots. The effect seems stronger for the weaker waves.

The behavior of the residual pressure fluctuations for a period as long as 0.1 sec is shown in Figure 3-18, for the case of weak waves. The top picture corresponds to the 8" driver, the top trace is the pressure at 9" from the diaphragm and the bottom trace is that on the driver endwall. The fluctuations and undulations are seen to attenuate strongly. The linear rise in the signal from the driver endwall gage is a spurious effect. The gage is zeroed at the initial driver overpressure, and when

8" DRIVER, 113" VENTED TUBE, 7.2% OPEN, 6 PSIG OVERPRESSURE

2 ms/DIV

.015 ATM/DIV

.037 ATM/DIV

GAGES PCB106B AT

9" FROM DRIVER

DRIVER ENDWALL

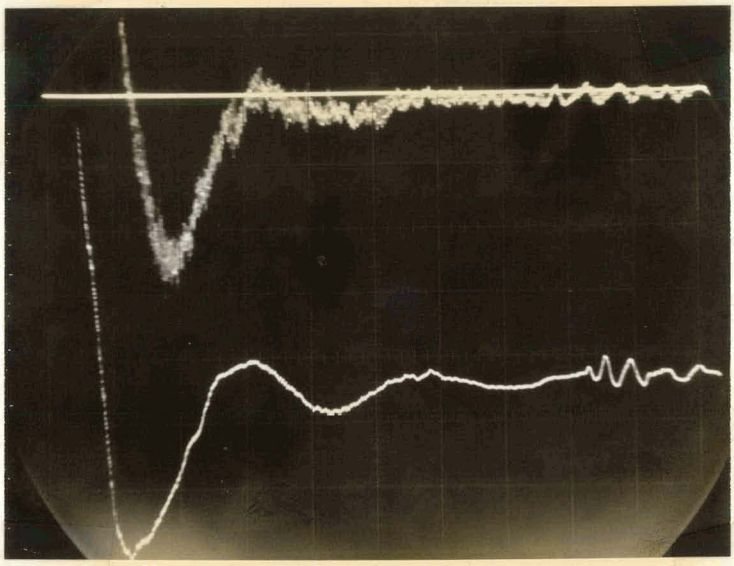

2 ms/DIV

.0185 ATM/DIV

.015 ATM/DIV

GAGES PCB106B AT

3" FROM DRIVER

15" FROM DRIVER

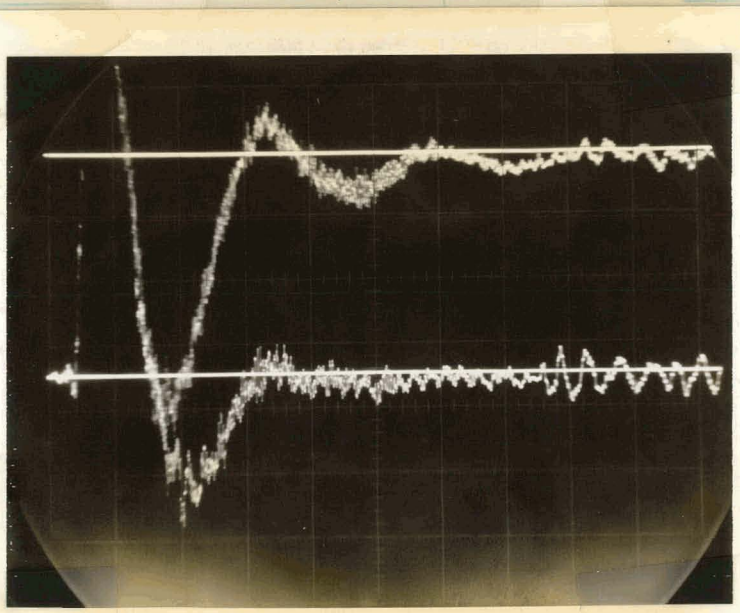

Figure 3-15. Quarter-Wave Oscillation of Vented Tube, Weak Waves, Short Driver

24" DRIVER, 113" VENTED TUBE, 7.2% OPEN, 80 PSIG OVERPRESSURE

2 ms/DIV

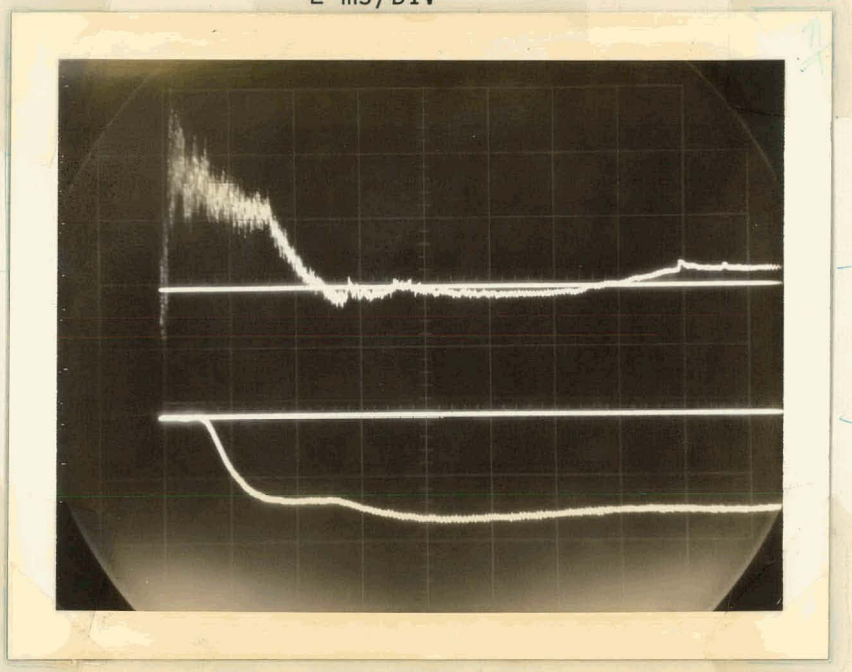

.73 ATM/DIV

3.65 ATM/DIV

GAGES PCB113A21 AT

9" FROM DIAPHRAGM

DRIVER ENDWALL

TRANSIENTS NEAR DIRVER

2 ms/DIV

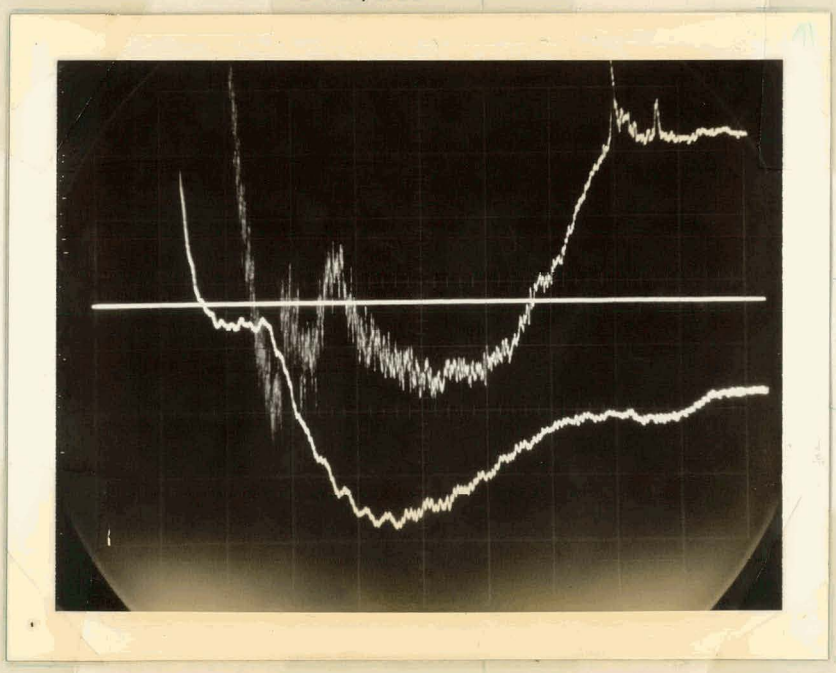

.073 ATM/DIV

.365 ATM/DIV

GAGES PCB113A21 AT

9" FROM DIAPHRAGM

DRIVER ENDWALL

AMPLIFIED TRANSIENTS

Figure 3-16. Vented Tube Tests: Strong Waves, Long Driver

24" DRIVER, 113" VENTED TUBE, 7.2% OPEN, 6 PSIG OVERPRESSURE

2 ms/DIV

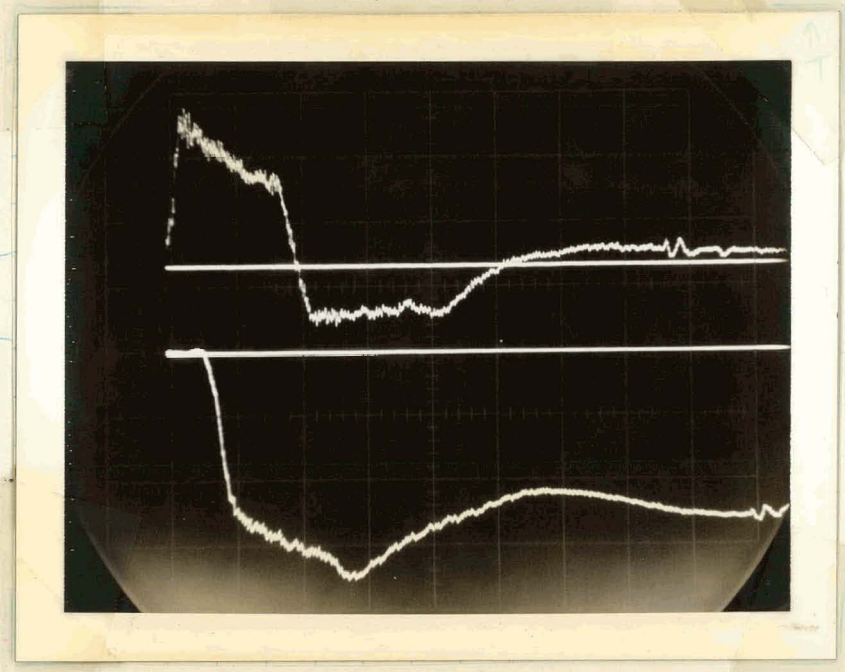

.06 ATM/DIV

.185 ATM/DIV

GAGES PCB113A21 AT 9" FROM DIAPHRAGM

DRIVER ENDWALL

TRANSIENTS NEAR DRIVER

2 ms/DIV

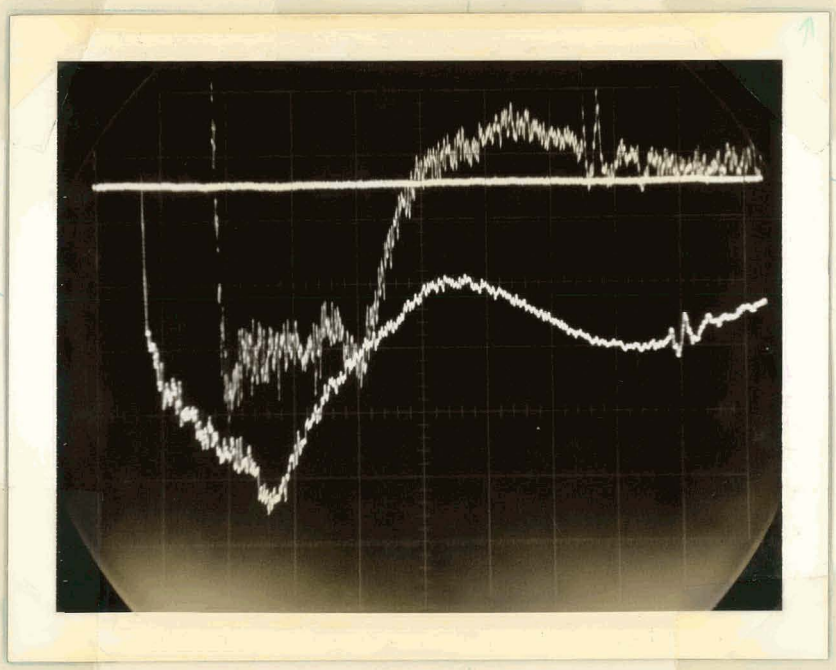

.015 ATM/DIV

.074 ATM/DIV

GAGES PCB113A21 AT 9" FROM DIAPHRAGM

DRIVER ENDWALL

AMPLIFIED TRANSIENTS

Figure 3-17. Vented Tube Tests: Weak Waves, Long Driver

10 ms/DIV, 6 PSIG OVERPRESSURE, 113" VENTED TUBE, 7.2% OPEN

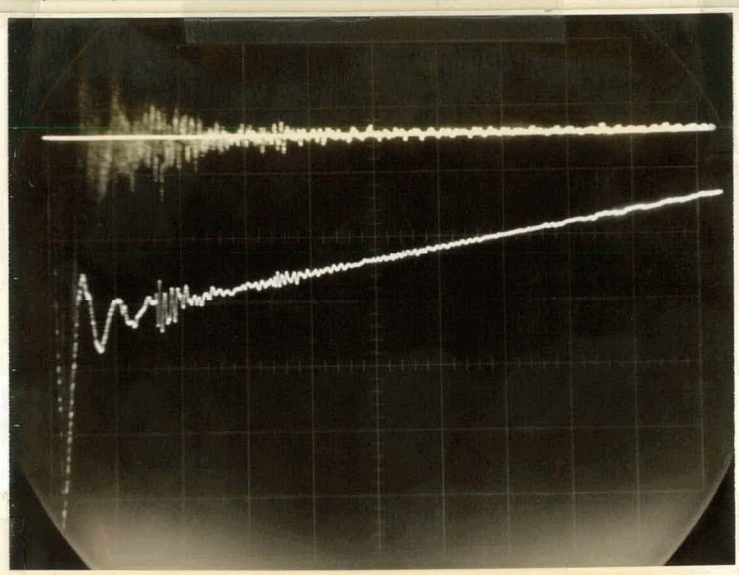

.006 ATM/DIV

GAGES PCB106B AT 9" FROM DIAPHRAGM

DRIVER ENDWALL

.037 ATM/DIV

8" DRIVER

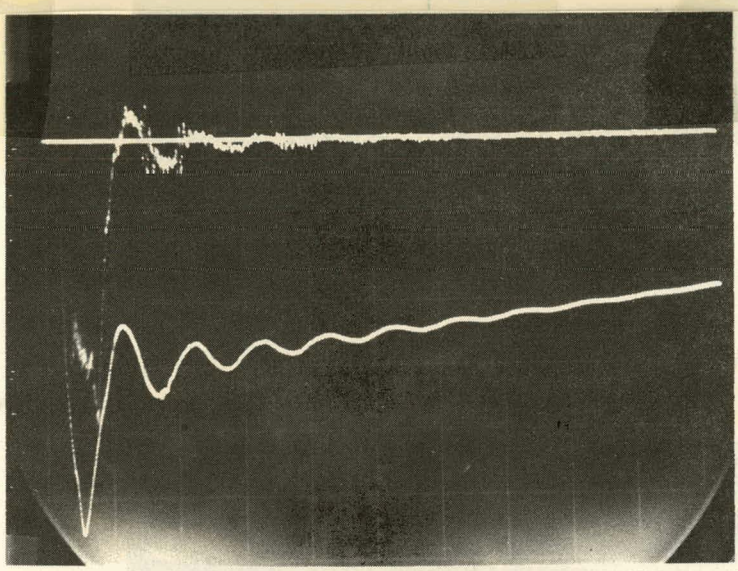

.015 ATM/DIV

GAGES PCB106B AT 9" FROM DIAPHRAGM

DRIVER ENDWALL

.074 ATM/DIV

24" DRIVER

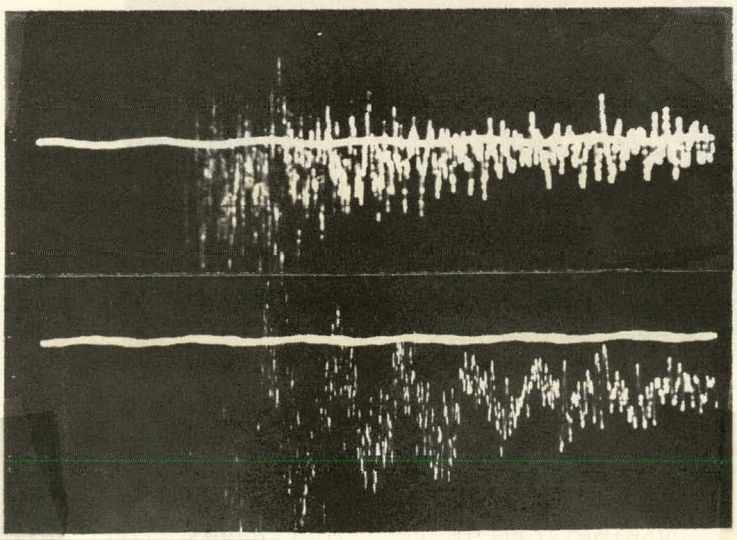

.0006 ATM/DIV

GAGE PCB106B AT 9" FROM DIAPHRAGM

8" DRIVER

.0006 ATM/DIV

24" DRIVER

Figure 3-18. Long-Term Oscillations in Vented Tube: Weak Waves

the pressure jumps down to ambient conditions the gage output swings negative, but then slowly decays back to zero in an exponential fashion (time constant $\sim$ 1 sec). The beginning of this exponential decay becomes very noticable at the high amplification used in these pictures. The next lower picture shows the corresponding pressure traces for the 24" driver. Here, as expected, the undulations last longer. The two traces at the bottom of the figure are the two top traces of the two pictures, observed at much higher amplification: top trace, X10 (8" driver); bottom trace, X25 (24" driver). The timescale is unchanged. In order to obtain good resolution of the small signals, the more sensitive PCB106B gages were used for the measurements in this figure. Residual pressure fluctuations as large as 0.01 psi are seen to persist for times as long as 0.1 sec for both drivers. For the longer driver, even the slow undulation is still quite noticeable at this time.

Further tests were made with the PCB 106B gages flush with the shock tube wall, to confirm the nature of these residual oscillations. Only weak waves were fired from a 8" driver and the far end of the vented section was left open. These pressure traces shown in figure 3-19 and 3-20 are comparable to those in Figure 3-14. The diaphragm material for these tests is the .00025" mylar which is not very uniform and results in substantial variation from run to run as seen from the differences in Figures 3-19 and 3-20. The wave reflected from the open end shows rapid oscillation behind it similar to the reflection from a closed end. The amplitude and frequency of these oscillations suggests that they may correspond to an oscillatory flow in the vents. This is perhaps an indication that the effectiveness of the attenuation provided by the coarse venting is substantially reduced for the small amplitude residual fluctuations. The long time behavior of these fluctuations is shown in the top picture in Figure 3-21, at a high amplification. The typical frequency of these residual high frequency fluctuations also appears to correspond with a transverse quarter wave (organ pipe oscillation) across the vented tube again implying oscillatory flow in the vents.

In order to ensure that the observed signal is not a spurious result of stress waves or structural vibrations in the shock tube, the above test was repeated with a sealed cap over the pressure sensitive face of the transducer located at 9" from the diaphragm. This isolated it from the

8" DRIVER, 113" VENTED TUBE, 7.2% OPEN, 9 PSIG OVERPRESSURE

2 ms/DIV

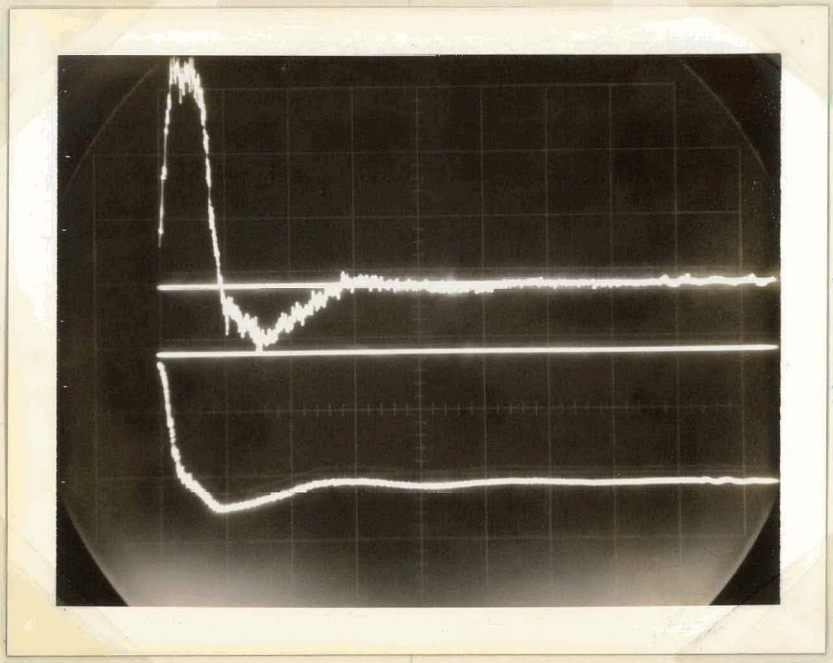

.06 ATM/DIV

.37 ATM/DIV

GAGES 106B (FLUSH) AT

9" FROM DIAPHRAGM

DRIVER ENDWALL

TRANSIENTS NEAR DRIVER

2 ms/DIV

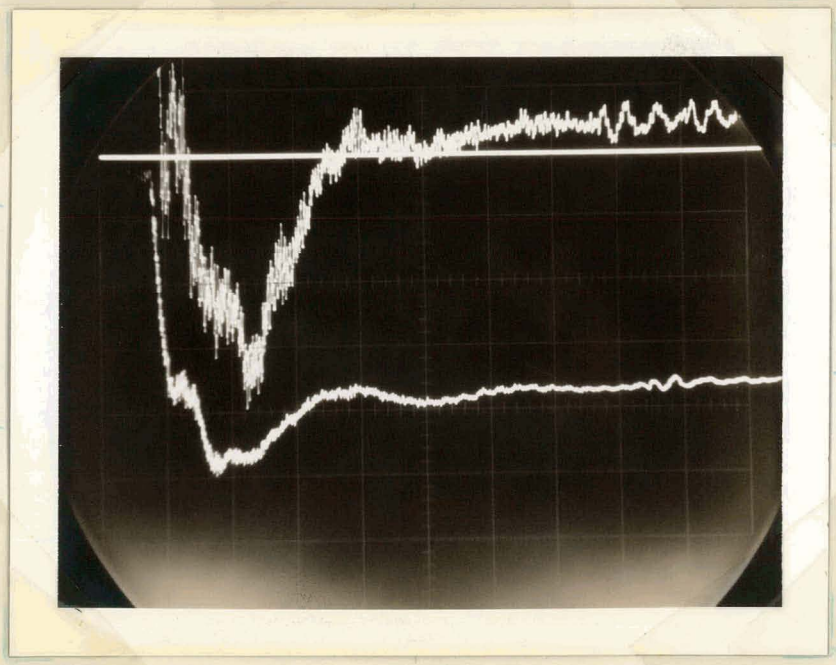

.015 ATM/DIV

.074 ATM/DIV

GAGES 106B (FLUSH) AT

9" FROM DIAPHRAGM

DRIVER ENDWALL

AMPLIFIED TRANSIENTS

Figure 3-19. Vented Tube Tests, Weak Waves, Short Driver

8" DRIVER, 113" VENTED TUBE, 7.2% OPEN, 9 PSIG OVERPRESSURE

2 ms/DIV

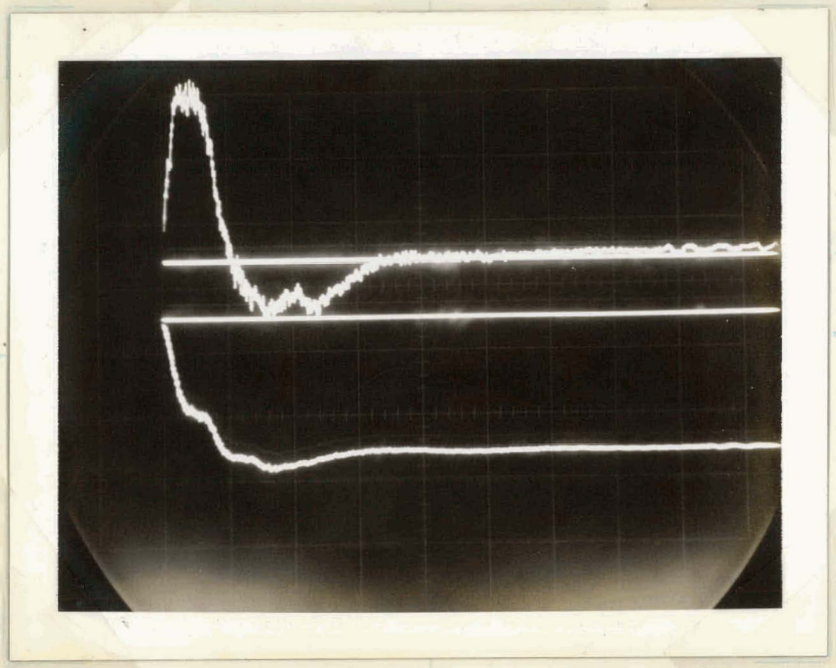

.06 ATM/DIV

.37 ATM/DIV

GAGES 106B (FLUSH) AT

9" FROM DIAPHRAGM

DRIVER ENDWALL

TRANSIENTS NEAR DRIVER

2 ms/DIV

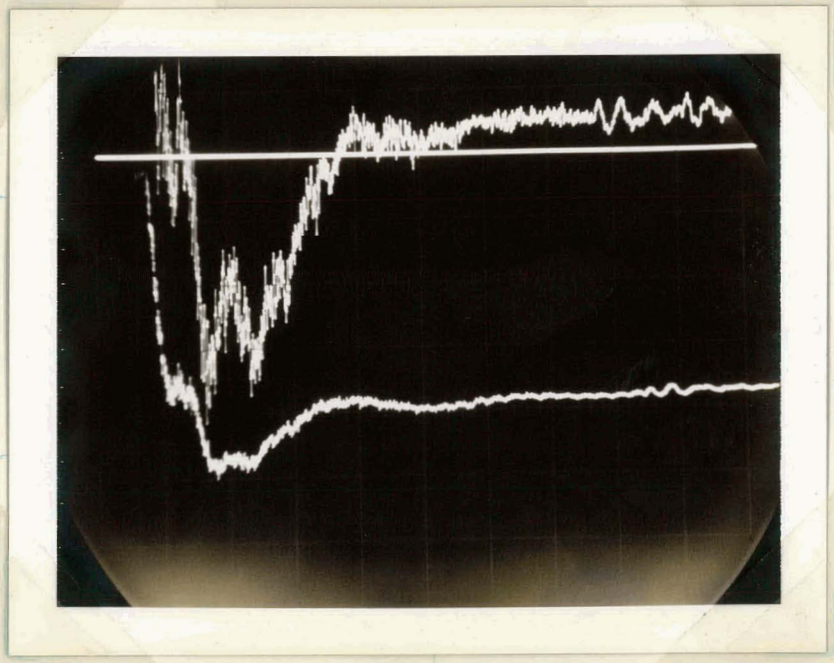

.015 ATM/DIV

.074 ATM/DIV

GAGES 106B (FLUSH) AT

9" FROM DIAPHRAGM

DRIVER ENDWALL

AMPLIFIED TRANSIENTS

Figure 3-20. Vented Tube Tests, Weak Waves, Short Driver

8" DRIVER, 113" VENTED TUBE, 7.2% OPEN, 9 PSIG OVERPRESSURE

10 ms/DIV

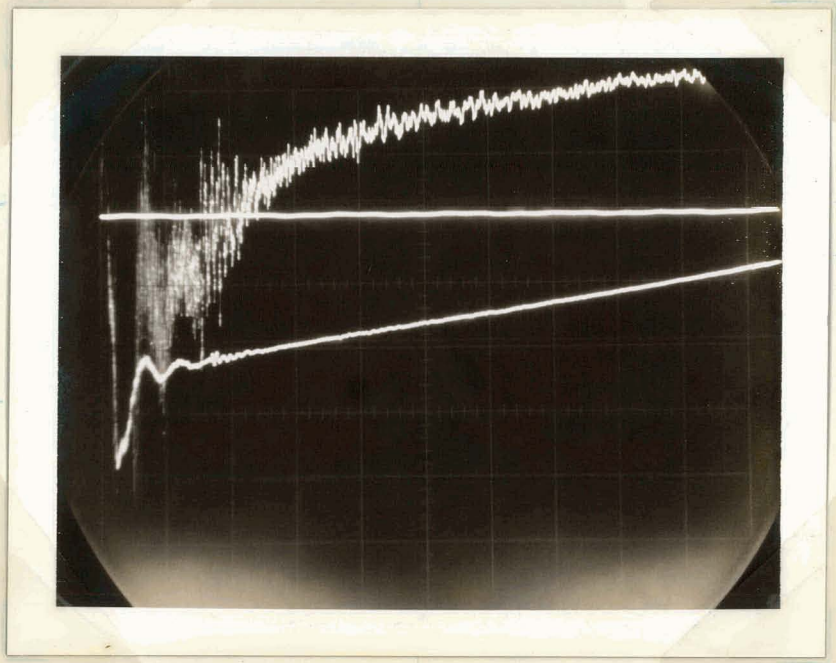

GAGES
106B (FLUSH)
AT

9" FROM DIAPHRAGM

DRIVER ENDWALL

.003
ATM/DIV

.074
ATM/DIV

LONG TERM OSCILLATIONS

Figure 3-21. Vented Tube Tests, Weak Waves, Short Driver

10 ms/DIV

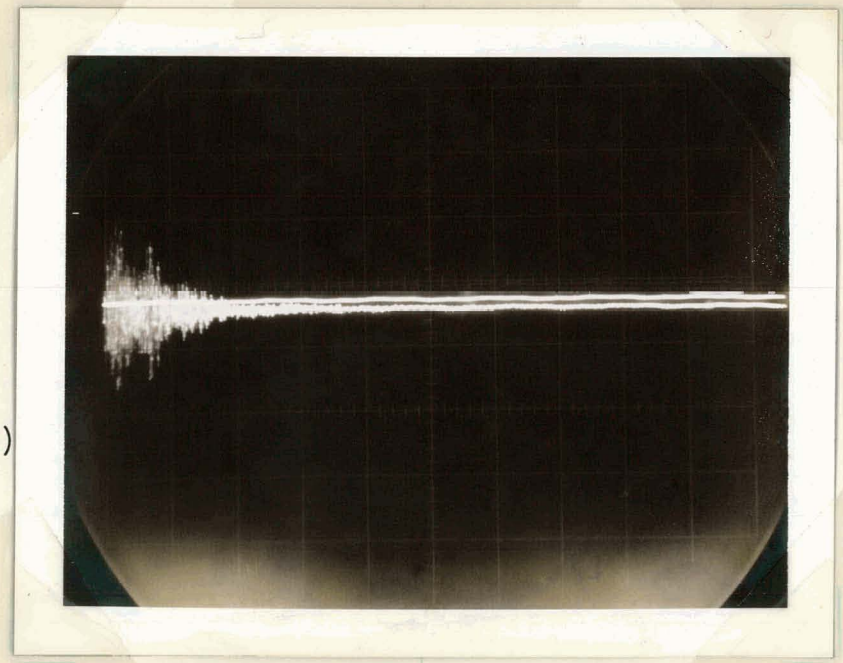

GAGE 106B

(FLUSH, BUT CAPPED
TO SEAL FROM PRESSURE)

9" FROM DIAPHRAGM

.003
ATM/DIV
(EFFECTIVE)

STRESS WAVE AND VIBRATION NOISE

Figure 3-22. Vented Tube Tests, Weak Waves, Short Driver

the pressure waves. The resulting signal is shown in Figure 3-22. The relatively insignificant noise level demonstrates the insensitivity of the gauge to spurious effects and confirms the observation of the residual high frequency acoustic fluctuations at long times (> 20 ms).

3.1.3.4 Flow Through Vents

Visualization of the wave field inside the vented duct and the flow through the holes at various stages of the attenuation are shown in a sequence of spark shadowgraphs in Figures 3-23, -24, -25. The case shown is a 24" driver with a .001" mylar diaphragm firing nominally at 17 psig into the vented tube. The center of the shadowgraph pictures is 22" from the diaphragm, and the view shows the flow through the horizontal vented top plate of the optical section which is 3/8" thick. The window radius is 3.25". The black shadow at the bottom of the picture is not the bottom wall of the tube. This region is masked off to avoid spurious reflections.

The first picture shows the shock wave - sharp, black, vertical, straight line on the left - travelling in the duct from right to left. Behind the shock wave, as well as outside the vented plate a number of weak wave fronts can be seen. These result from the diffraction of the shock wave at the vent holes. The diffraction also produces an impulsive jet flow through the hole which generates a vortex ring, seen in the sideview as a horizontal dumbel shaped dark object, just above the vented plate in the right half of the picture. In the second picture the shock has just left the picture, after diffracting from another row of holes. A fresh vortex ring is seen emerging, while the previously formed ring is continuing to develop and move up. It should be noted that there are three holes in each row which produce three vortex rings, but their shadows coalesce to show only one ring. However, multiple diffraction fronts can be seen due to slight misalignment of the light beam from the row direction. The next two pictures show later stages of the rings where they become unstable and break up leaving behind a turbulent jet. The cores of the vortex rings become visible, since the gas in the center of the core dilates in response to the decompression caused by the centrifugal action as the gas spins around the core. On the other hand, the jet becomes visible because it is formed from the boundary

24" DRIVER, 113" VENTED SECTION, 17 PSIG OVERPRESSURE

1. 1350 MICROSEC.

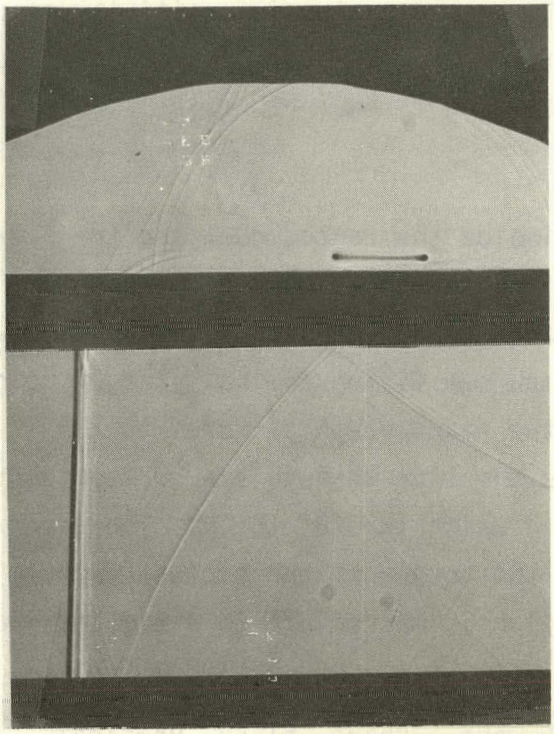

2. 1380 MICROSEC

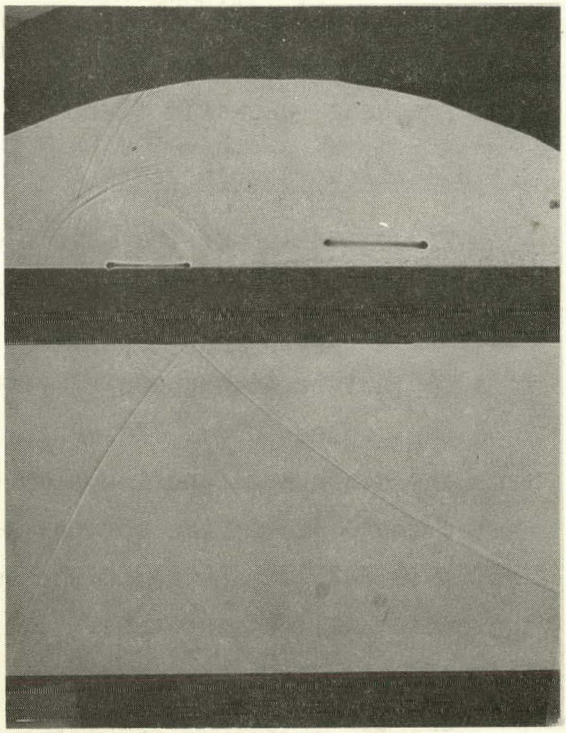

3. 1.5 MILLISEC.

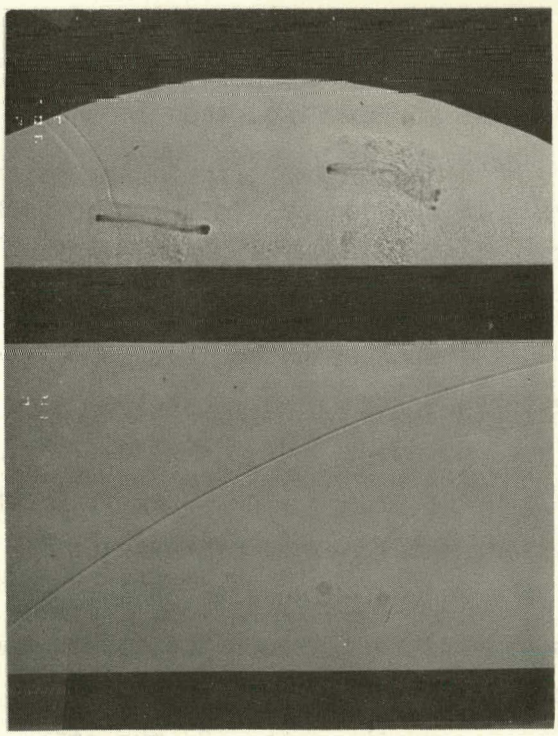

4. 2.0 MILLISEC.

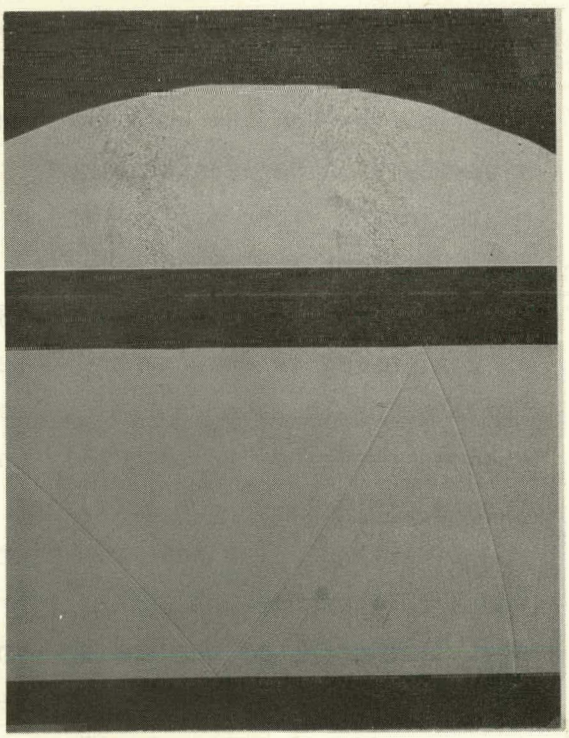

Figure 3-23. Shock Interaction With Vents

24" DRIVER, 113" VENTED TUBE, 17 PSIG OVERPRESSURE

5. 2.5 MILLISEC.

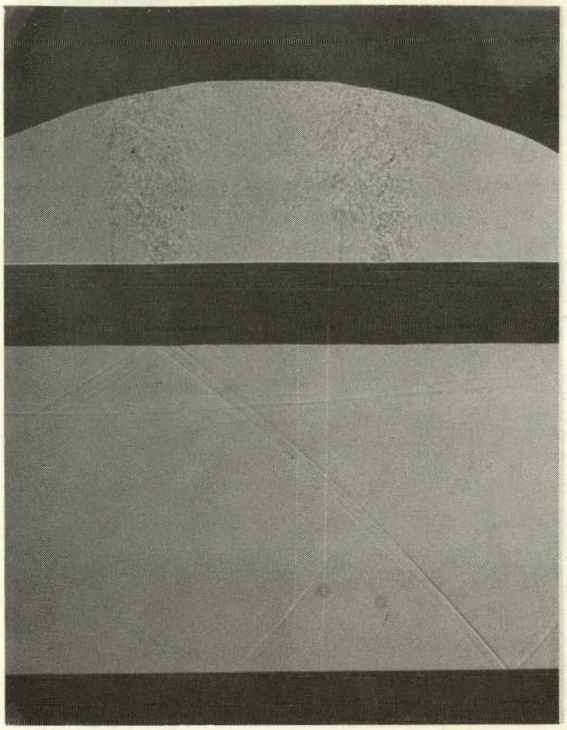

6. 3.7 MILLISEC.

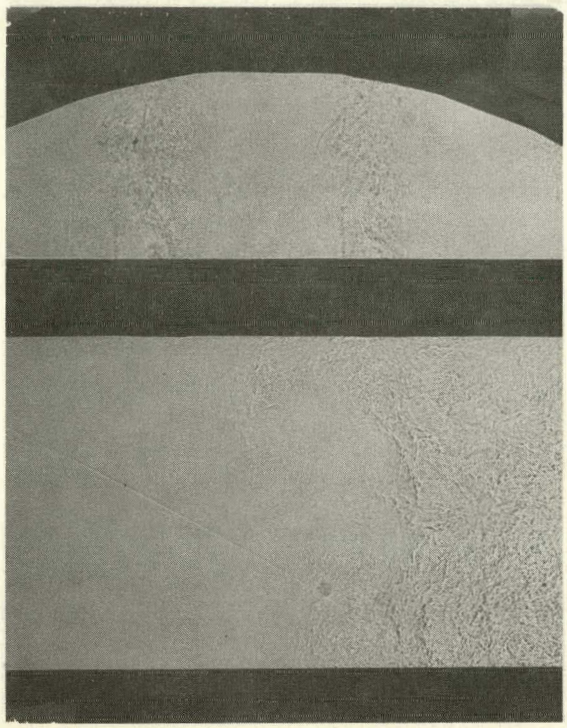

7. 4.0 MILLISEC.

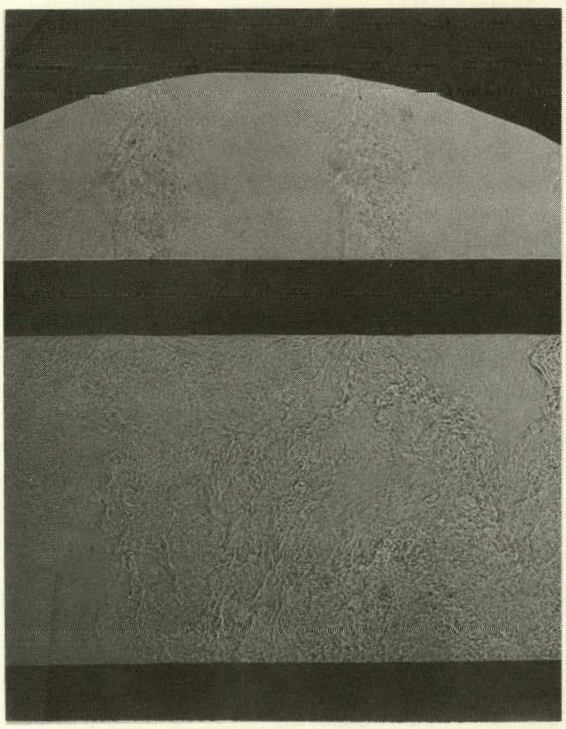

8. 4.5 MILLISEC.

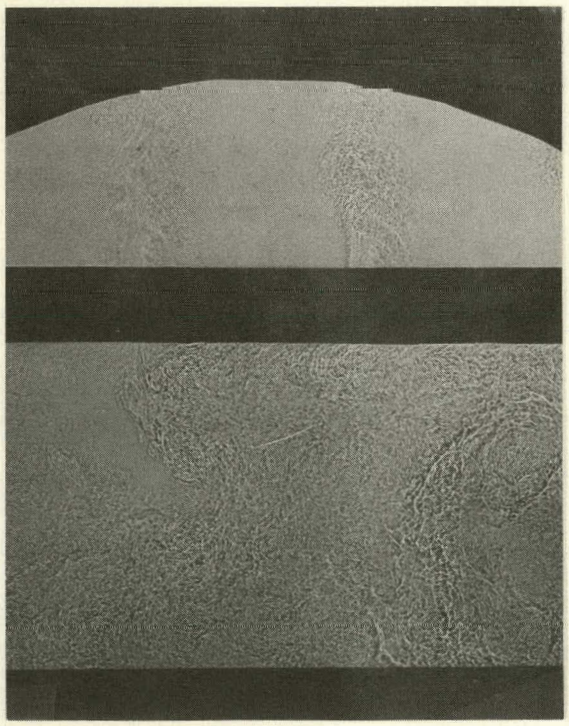

Figure 3-24. Flow in Vented Tube

24" DRIVER, 113" VENTED TUBE, 17 PSIG OVERPRESSURE

9. 5.5 MILLISEC.

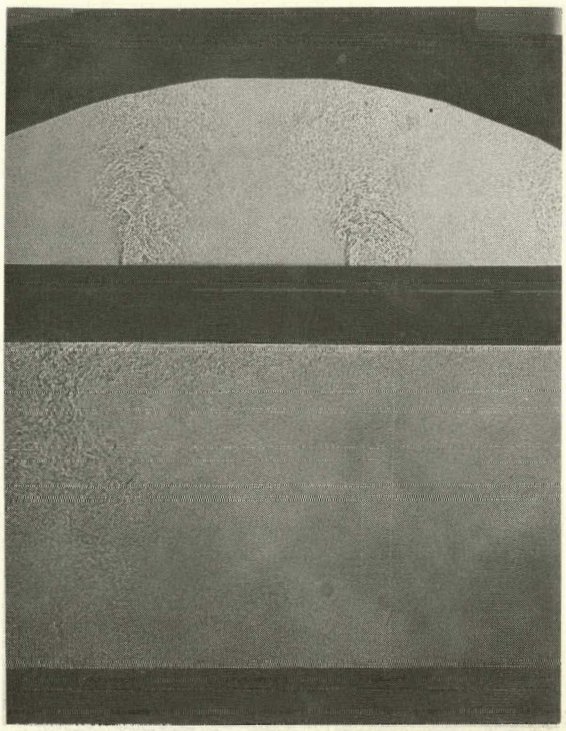

10. 6.5 MILLISEC.

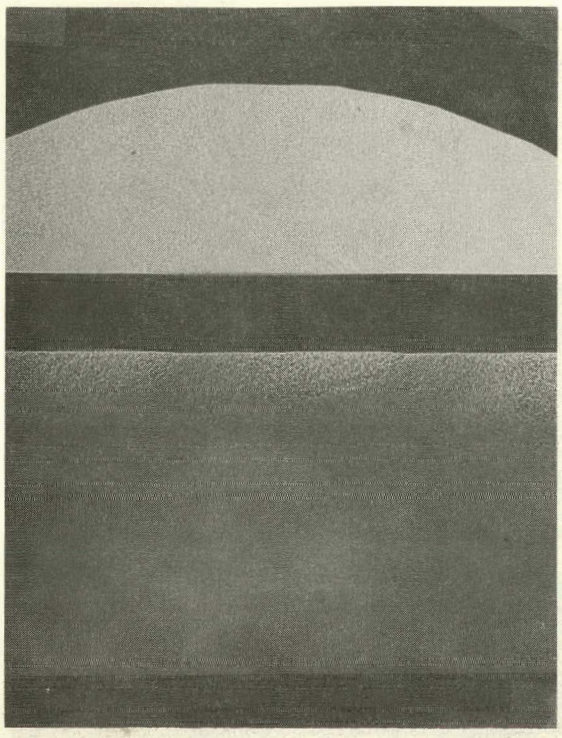

11. 7.5 MILLISEC.

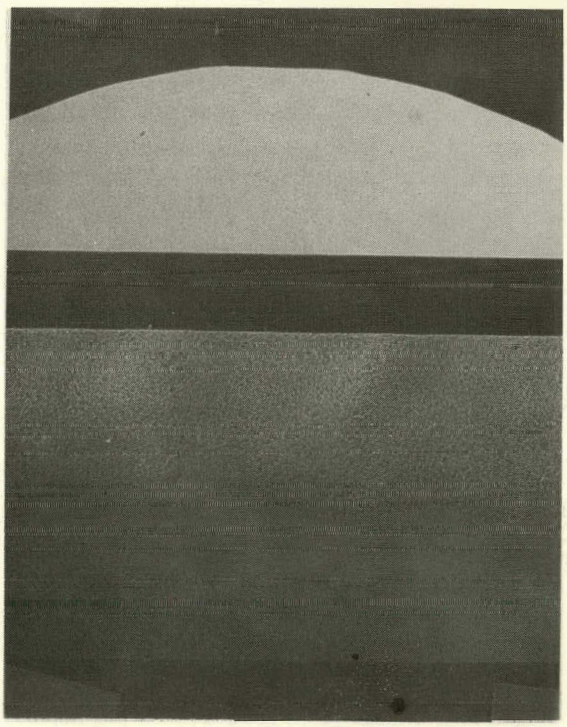

12. 8.5 MILLISEC.

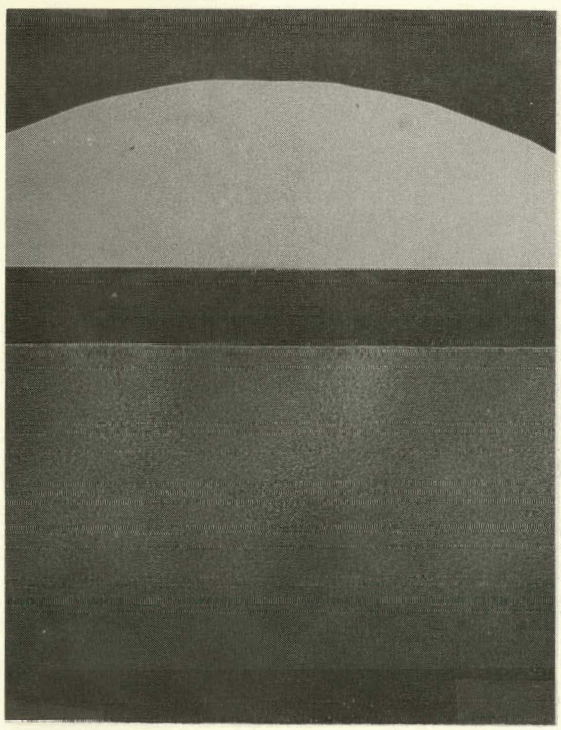

Figure 3-25. Back-Flow Through Vents

layers separating from the vented plate. The boundary layers carry a temperature difference across them, since the gas which was originally at the temperature of the tube has been irreversibly heated by the shock wave. The temperature gradients across the boundary layer cause sufficient refraction to produce visualization of the turbulence.

The next four pictures in this sequence show how the diffraction wave fronts continue to persist in the region even after many reflections. They also show the arrival of the turbulent contact surface between the shock heated gas on the driven side of the tube and the cold driver gas (-33°C, cooled by isentropic expansion). In the rest of the sequence, the contact surface flows past the view as the driver gas comes in. The driver gas, which is room air, appears darker at the low temperature due to scattering from particles of condensed water vapor. These last four pictures also correspond to the period of the pressure undershoot in the duct. The jets shooting out of the vents can be seen decelerating and dissipating, leaving uniform turbulence outside the duct. Then the outer gas, which appears lighter, begins to flow back into the dark gas within the tube. The jets formed by this inflow can be seen to penetrate and contaminate the gas deep inside the tube. Also, because of the inflow, the driver gas is pushed along the tube far beyond 25", which is much greater than 18", the distance predicted by isentropic expansion.

This process of contamination by inflow during the pressure undershoot extends many driver lengths as shown in Figure 3-26. In this case, the 8" driver is used, the film is larger and the sensitivity of the shadowgraph has been highly enhanced. The same diaphragm and overpressure is used as before, however due to the short length of the driver, the expanded driver gas does not extend into the field of view during the period of inflow. The three pictures here show weak but sharp wave fronts inside the tube, uniform turbulence outside after the jets have decayed and the development of the inflow jets which fully contaminate the field of view during this period. Clearly, the region where such contamination occurs is much longer than 3 lengths of the driver.

8" DRIVER, 113" VENTED TUBE, 17 PSIG OVERPRESSURE

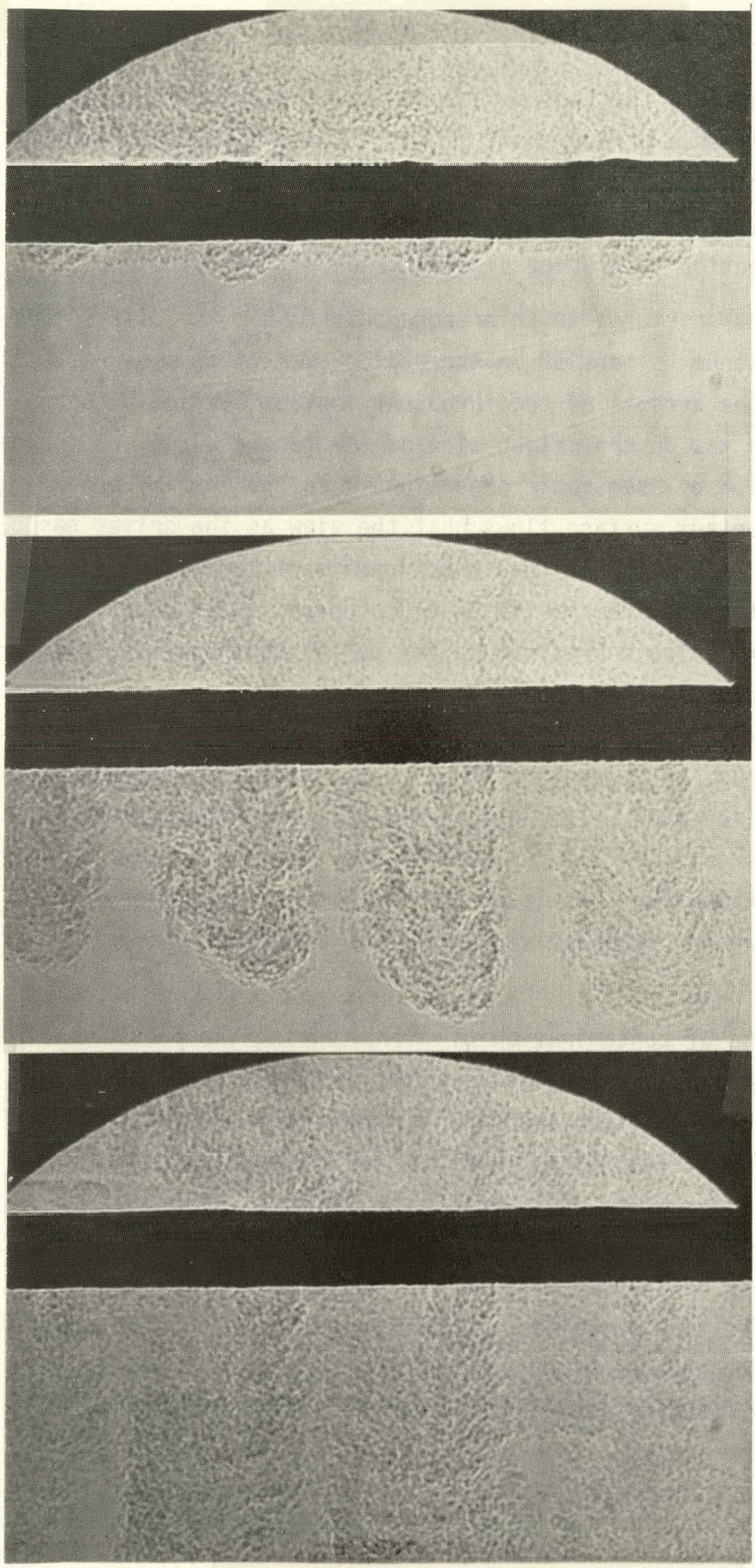

1. 4.5 MS

2. 5.5 MS

3. 6.5 MS

Figure 3-26. Backflow Through Vents Far From Driver

Thus, the above flow visualization has already identified some critical issues. For fusion lasers, where it is not possible to protect the upstream fluid from the waves by choked orifice plates and acoustic suppression devices are necessary upstream of the cavity, two major contamination problems exist; contamination with the cavity gas and contamination from boundaries by inflow through vents. Expansion of the cavity gas into the upstream duct is unavoidable, however the region contaminated by this gas is greatly increased by the mixing and jet inflow from side-wall vents which occur during the period of the pressure undershoot. Even when this effect is minimized, no cleanup process seems possible for this contamination, other than maintaining a high mean flow rate to flush this fluid past the cavity. The second problem of contamination results from the wall boundary layers, which separate and mix with the upstream medium during the vent inflow phase. This causes turbulent density fluctuations over a region much larger than that contaminated by the cavity gas. However, the magnitude of these fluctuations is of the order of the irreversible entropy change produced by the shock waves (since the fluid in the boundary layers tries to return to original state by diffusion of heat into the walls), and they decay in time by turbulent and diffusive dissipation. It may be possible to enhance this decay artificially to some extent (e.g. by use of screens) as the gas flows into the cavity. It is not clear, however, whether this is likely to be adequate (especially when boundary flows of different fluids are involved), considering the extremely high medium homogeneity required for some laser systems. For both problems, use of high mean flow rates (high flush factors) can always provide a fresh, homogeneous medium in the cavity, but the pumping work required for this severely impairs the overall laser efficiency, which is already critically low.

Although here the upstream contamination problem is demonstrated only for a vented duct, the problem is more general and fundamental in character. It must be resolved to allow the development of low-pressure-drop absorbers for the region upstream of the laser cavity. Production of turbulent flows is a mechanism basic to most devices which adequately dissipate the wave energy released from the laser

cavity. Consequently, irreversible entropy fluctuations are an inherent part of the problem and solutions have to be found to sufficiently diminish their magnitude or their effects on the laser medium, without adversely affecting the flow system efficiency.

BOTTOM OF PAGE
BOTTOM OF PAGE

3.2 ANALYSIS

3.2.1 FACTS Code Description

The analytical modeling of acoustic suppressors for Pulsed Fusion Laser is performed with the aid of a numerical code (the FACTS code) previously developed at TRW. The FACTS code solves the following set of equations which describe the unsteady, quasi one-dimensional flow of gas in a duct of slowly varying cross-sectional area:

conservation of mass

$$\frac{\partial}{\partial t}(\rho A) = -\frac{\partial}{\partial x}(\rho A u) - S_1; \tag{64}$$

conservation of momentum

$$\frac{\partial}{\partial t}(\rho A u) = -\frac{\partial}{\partial x}(\rho A u^2) - A\frac{\partial}{\partial x}(P) - S_2; \tag{65}$$

conservation of energy

$$\frac{\partial}{\partial t}\left[\rho A(e+u^2/2)\right] = -\frac{\partial}{\partial x}\left[\rho A(e+u^2/2 + P/\rho)u\right] - S_3; \tag{66}$$

ideal gas equation of state

$$P = \rho RT = (\gamma - 1)\rho e; \tag{67}$$

and for a perfect gas

$$e = C_v T = \frac{R}{\gamma - 1} T. \tag{68}$$

S_1, S_2, and S_3 are source-sink terms with units of mass, momentum and energy flux per unit length of duct respectively. These source-sink terms are used to account for a perforated duct wall vented to the atmosphere and to account for sections of duct filled with a permeable sound absorbing material.

A Lax-Wendroff differencing scheme with Flux-Corrected Transport (Reference 3-6, 3-7) was used to generate the time-dependent solutions to Equations 64, 65, and 66. The Lax-Wendroff differencing technique intentionally diffuses the solution in order to treat problems with strong gradients or shocks. The Flux-Corrected Transport technique is a method of removing the diffusion added to assure numerical stability. Shock waves that take five or six mesh spaces to describe with the Lax-Wendroff method alone are described in two mesh spaces when the FCT technique is used. For more information on the FACTS code see examples of its use in solving pressure wave suppression problems in Reference 2-10.

This code was modified and upgraded under the current program to improve its predictive capabilities and make it more suitable to deal with pressure wave attenuation problems in fusion-type, pulsed lasers. In some of these lasers, notably in the KrF system, pressure attenuation levels to better than 10^{-4} are required. To follow the attenuation process to these low overpressure levels one must pay careful attention to the detailed ingredients of the code and make sure that they properly model the relevant physical processes. Also, in fusion-type lasers, the pressure wave attenuation must be accomplished with low pressure drop absorbers. Past work on pressure suppression modeling did not sufficiently emphasize this point. Recent code modifications and extensions are described in the following subsections.

3.2.2 Recent Code Modifications

3.2.2.1 Model for Side-Wall Vents

3.2.2.1.1 General Requirements

The quasi one-dimensional approach used in the numerical model requires that the side-wall venting be expressed in the form of source-sink terms in the conservation equations. These source-sink terms represent the rate of increase or decrease of mass, momentum and energy due to side-wall venting. If σ is the rate of mass flowing out through the vents of the duct per unit length, then the general forms of the source-sink terms as defined in Equations 64 to 68 are given by

$$S_1 = \sigma \tag{69}$$

$$S_2 = \sigma\, u_{sx} \tag{70}$$

$$S_3 = \sigma\, (e_s + P_s/\rho_s + u_s^2/2) \tag{71}$$

where the subscript s denotes average conditions of the fluid as it leaves or enters the duct, and where u_{sx} is the x-component (the component parallel to the flow in the duct) of the average velocity of the fluid as it leaves or enters the duct. S_1 represents the rate of mass entering or leaving the duct per unit length, S_2 represents the rate at which momentum is transferred into or out of the duct per unit length, and S_3 is a combination of the rates at which energy in the form of internal energy, e_s, kinetic energy, $u_s^2/2$, and work, P_s/ρ_s, is transferred into or out of the duct per unit length. The line flux of mass, σ, can be expressed in general as:

$$\sigma = \rho_s\, u_{sy}\, a_s \tag{72}$$

where a_s is the vent area per unit length of the duct, and u_{sy} is the y-component (perpendicular to the flow in the duct) of the average velocity of the fluid as it enters or leaves the duct. In other words, $\rho_s\, u_{sy}$ represents the actual mass flux of the fluid leaving (σ positive) or entering (σ negative) the duct.

3.2.2.1.2 Static Pressure, Isentropic Flow Model with Constant Discharge Coefficient

The specific form of the source terms for side-wall venting will depend on the shape and size of the vent holes, on the mean flow and Mach No. in the duct and on the volume into which the vents exhaust.

The first case considered was that of an infinite volume into which the side-walls vent. The gas in this infinite volume was assumed to be stagnant with fixed (constant) properties. Under these conditions, the properties of the gas as it enters or leaves the duct were determined by using quasi-steady, isentropic compressible flow relations for flow through an orifice. The static pressure in the duct was assumed to be

the driving pressure in this first model, rather than the total or stagnation pressure. With this assumption, when the static pressure in the duct equals the static pressure outside of the duct, there will be no flow through the vents. Also, when there is no flow in the main duct, the static pressure is equal to the total pressure there and the flow model reduces to ideal flow through an orifice. It should be emphasized that this model gives the maximum ideal flow through the vents.

If the static pressure inside the duct is less than the pressure in the chamber surrounding the vented duct, ($P < P_c$), then the flow will be into the duct and the inflow conditions are given by

$$M_s = \min \left[\left[\left\{ \left(\frac{2}{\gamma-1} \right) \left[\left(\frac{P_c}{P} \right)^{\left(\frac{\gamma-1}{\gamma} \right)} - 1 \right] \right\}^{1/2} ; 1.0 \right] \right] \quad (73)$$

$$\rho_s = \rho_c \Big/ \left(1 + \frac{\gamma-1}{2} M_s^2 \right)^{\left(\frac{1}{\gamma-1} \right)} \quad (74)$$

$$P_s = P_c \Big/ \left(1 + \frac{\gamma-1}{2} M_s^2 \right)^{\left(\frac{\gamma}{\gamma-1} \right)} \quad (75)$$

$$e_s = P_s / \left[\rho_s (\gamma-1) \right] \quad (76)$$

$$u_{sy} = -M_s \sqrt{\gamma P_s / \rho_s} \quad (77)$$

$$u_{sx} = 0.0 \quad (78)$$

Equation 73 gives the Mach number of the fluid as it enters the duct and accounts for the fact that the flow may be choked as it enters the duct if the pressure ratio is high enough. Equations 74 and 75 are used to evaluate the density and pressure once the Mach number is known. The internal energy and the y-component of the velocity are given by Equation 76 and 77. In this case, when the flow is into the duct, the x-component of the velocity is zero as it enters the duct.

When the static pressure in the duct is greater than the outer chamber pressure ($P > P_c$), the outflow conditions are given by

$$M_s = \min \left[\left[\left\{ \left(\frac{2}{\gamma-1} \right) \left[\left(\frac{P}{P_c} \right)^{\left(\frac{\gamma-1}{\gamma} \right)} - 1 \right] \right\}^{1/2}, 1.0 \right] \right] \quad (79)$$

$$\rho_s = \rho \Big/ \left(1 + \frac{\gamma-1}{2} M_s^2 \right)^{\left(\frac{1}{\gamma-1} \right)} \quad (80)$$

$$P_s = P \Big/ \left(1 + \frac{\gamma-1}{2} M_s^2 \right)^{\left(\frac{\gamma}{\gamma-1} \right)} \quad (81)$$

$$e_s = P_s / \left[\rho_s (\gamma-1) \right] \quad (82)$$

$$u_{sy} = M_s \sqrt{\gamma P_s / \rho_s} \quad (83)$$

$$u_{sx} = u \quad (84)$$

These equations are similar to the ones for inflow. Note that Equation 84 implies that all of the x-momentum of a gas particle in the duct is carried out of the duct with the vented gas. Experiments which measure the direction of the gas flow after leaving the vents can be used to modify this assumption.

Recognizing that the venting flow properties given by Equations 74 through 84 represent ideal maximums, a discharge coefficient was added to Equation 72 so that the expression for line flux of mass becomes

$$\sigma = C_D \rho_s u_{sy} a_s \quad (85)$$

The evaluation of this discharge coefficient to account for the effects of grazing flow and other effects is considered in subsequent sections.

3.2.2.1.3 Non-Ideal Effects

The constant discharge coefficient model presented in the previous section does not account for the effects of grazing flow on the flow through a side-wall orifice or an array of orifices. A literature search was made to find experimental values of discharge coefficients for flow through an orifice plate with grazing flow parallel to the plate.

Szumowski (Reference 3-8) has measured values of the discharge coefficient for air in terms of the duct Mach number and the ratio of ambient to stagnation pressure. Subsonic and supersonic flows were tested. These results were obtained specifically for the problem of shock wave decay in a perforated duct (Reference 3-9). The discharge coefficient data obtained by Szumowski were for flow out of the main duct only. No inflow data were included.

Another source of discharge coefficient data was from investigators of sound-absorbent linings consisting of cavity-backed perforated lining material used for inlet and exhaust ducting of jet engines. Rogers and Hersh (Reference 3-10) have obtained steady-flow resistance ($\Delta P/V$) and discharge coefficient data for incompressible flow through perforated side-walls for both inflow and outflow. Stokes, Davis, and Sellers (Reference 3-11) have performed similar experiments for outflow only (flow out of the main duct through the perforated side-walls).

An attempt was made to find a set of flow parameters which would collapse the outflow data onto a single curve. The results of this effort are summarized in Figure 3-35 where the discharge coefficient based on total (stagnation) pressure is plotted as a function of the ratio of the flow velocity in the duct to the maximum theoretical jet velocity based on the total pressure in the duct. Initial attempts to correlate the data using a discharge coefficient based on the static pressure in the duct, as defined by Equation 75, failed to collapse the data. This may indicate that the total pressure in the duct is recovered and provides the main driving force in the venting process. The discharge coefficient as used here is defined by

$$C_D = \frac{\dot{m}_{actual}}{\dot{m}_{ideal}} \tag{86}$$

$\dot{m}_{ideal}$ is given by

$$\dot{m}_{ideal} = \begin{cases} \dfrac{A\gamma P_t}{C_t}\sqrt{\left(\dfrac{2}{\gamma-1}\right)\left[\left(\dfrac{P_c}{P_t}\right)^{\frac{2}{\gamma}} - \left(\dfrac{P_c}{P_t}\right)^{\frac{\gamma+1}{\gamma}}\right]} \\ \text{if } \dfrac{P_c}{P_t} > \left(\dfrac{2}{\gamma+1}\right)^{\frac{\gamma}{\gamma-1}} \quad \text{subcritical flow} \\ \dfrac{A\gamma P_t}{C_t}\left(\left(\dfrac{2}{\gamma-1}\right)\right)^{\frac{\gamma+1}{2(\gamma-1)}} \\ \text{if } \dfrac{P_c}{P_t} \leq \dfrac{2}{\gamma-1}^{\frac{\gamma}{\gamma-1}} \quad \text{critical flow} \end{cases} \tag{87}$$

where c, P, γ, are sound speed, pressure, and ratio of specific heats, respectively; and where the subscripts t and c denote total conditions inside the duct and ambient conditions outside the duct, respectively. The ratio of duct flow velocity to the maximum theoretical jet velocity is given by the expression

$$\left(\frac{U}{V_j}\right)^2 = \frac{\frac{\gamma-1}{2} + \frac{1}{M_j^2}}{\frac{\gamma-1}{2} + \frac{1}{M^2}}, \tag{88}$$

where M is the duct flow Mach number and M_j is the theoretical maximum jet flow Mach number. M_j depends on the ratio of the total pressure in the duct to the static ambient pressure and is given by the expression

$$M_j^2 = \left[\left(\frac{P_t}{P_c}\right)^{\frac{\gamma-1}{\gamma}} - 1\right] \Big/ \left(\frac{\gamma-1}{2}\right) \tag{89}$$

3.2.2.1.4 Variable Discharge Coefficient Model Based on Correlation of Experimental Results

A strictly empirical model of the discharge coefficient for outflow was developed from the data on Figure 3-35 and from Perry's data on the variation of discharge coefficient with pressure ratio for a sharp edged orifice (Reference 3-12). Figure 3-36 shows the correlation curves which were used. The upper curve is a fit to the upper envelope of the data of Figure 3-35 and the lower curve is a fit to the lower envelope of the data of Figure 3-35. A fit to Perry's data (Reference 3-12) which is strictly applicable only for zero grazing flow was used to interpolate between the envelopes. The complete fit is given by

$$C_{D_o} = f_2 - \left(\frac{C_{D_o} - .6}{.843 - .6}\right)\left(f_2 - f_1\right), \quad (90)$$

where f_2 and f_1 are functions of the ratio of the duct velocity to the theoretical jet velocity, and where C_{D_o} is the discharge coefficient for a sharp edged orifice as given by Perry (Reference 3-12). The theoretical jet velocity, V_j, is determined by an isentropic expansion from the total pressure in the duct to ambient pressure outside of the duct.

The functions f_1 and f_2 depend on U/V_j as follows:

$$f_1 = 0.843+(U/V_j)^2\left\{-1.3221+(U/V_j)\left[1.4349-0.94847(U/V_j)\right]\right\} ; \quad (91)$$

$$f_2 = 0.6+(U/V_j)^2\left\{-0.16088+(U/V_j)\left[-1.20578+0.76154(U/V_j)\right]\right\} . \quad (92)$$

The sharp edged discharge coefficient C_{D_o} depends on the ratio of the static pressure in the duct to the ambient pressure outside of the duct. The following curve fit to Perry's data (Reference 3-12) was used to evaluate C_{D_o}:

$$C_{D_o} = 0.843+(P/Pa)^2\left\{-0.21527+(P/Pa)\left[-0.56085+0.53446(P/Pa)\right]\right\} \quad (93)$$

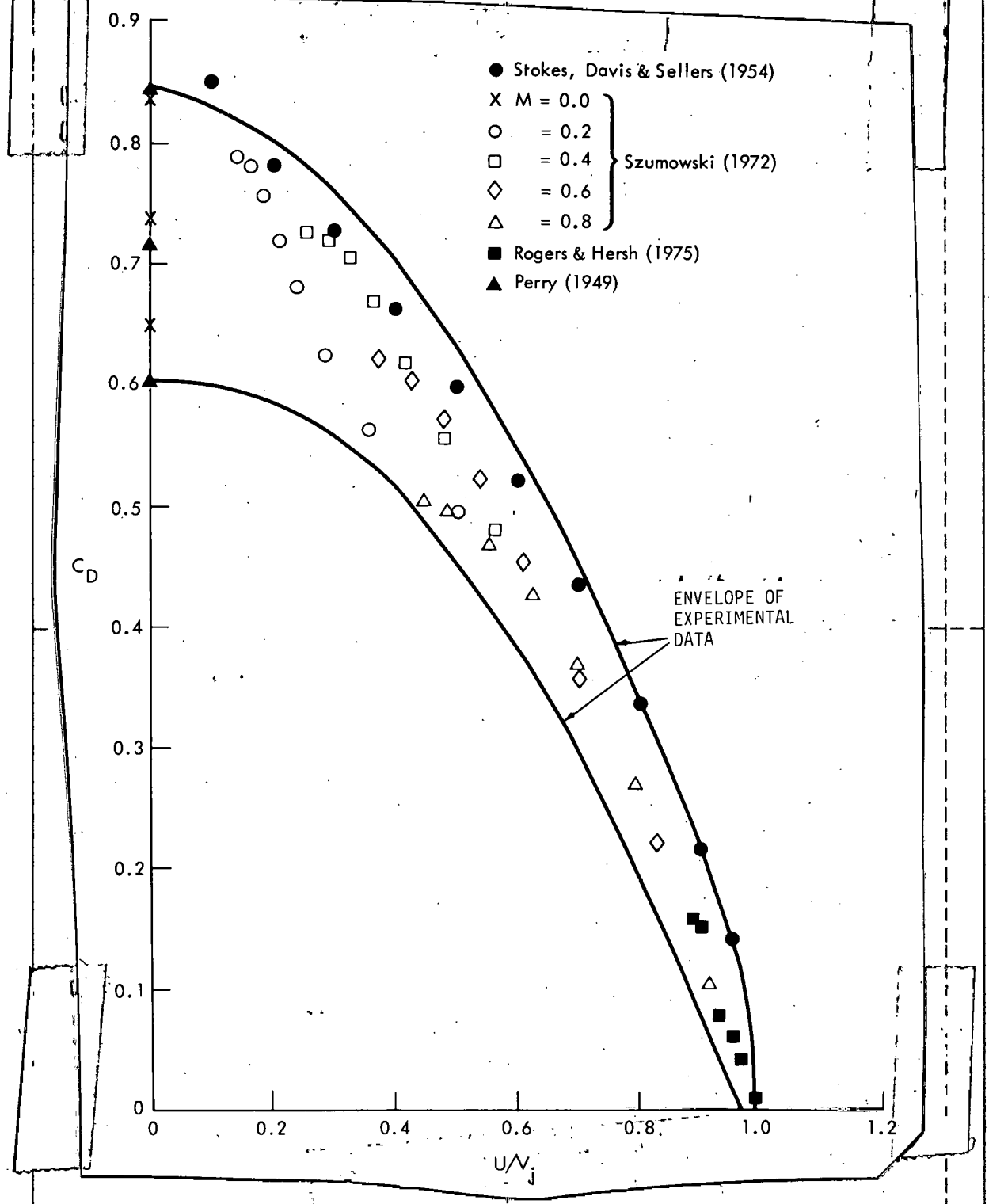

Figure 3-35. An Experimental Discharge Coefficient as a Function of the Ratio of Grazing Velocity to Theoretical Jet Velocity for the Flow Out of the Duct.

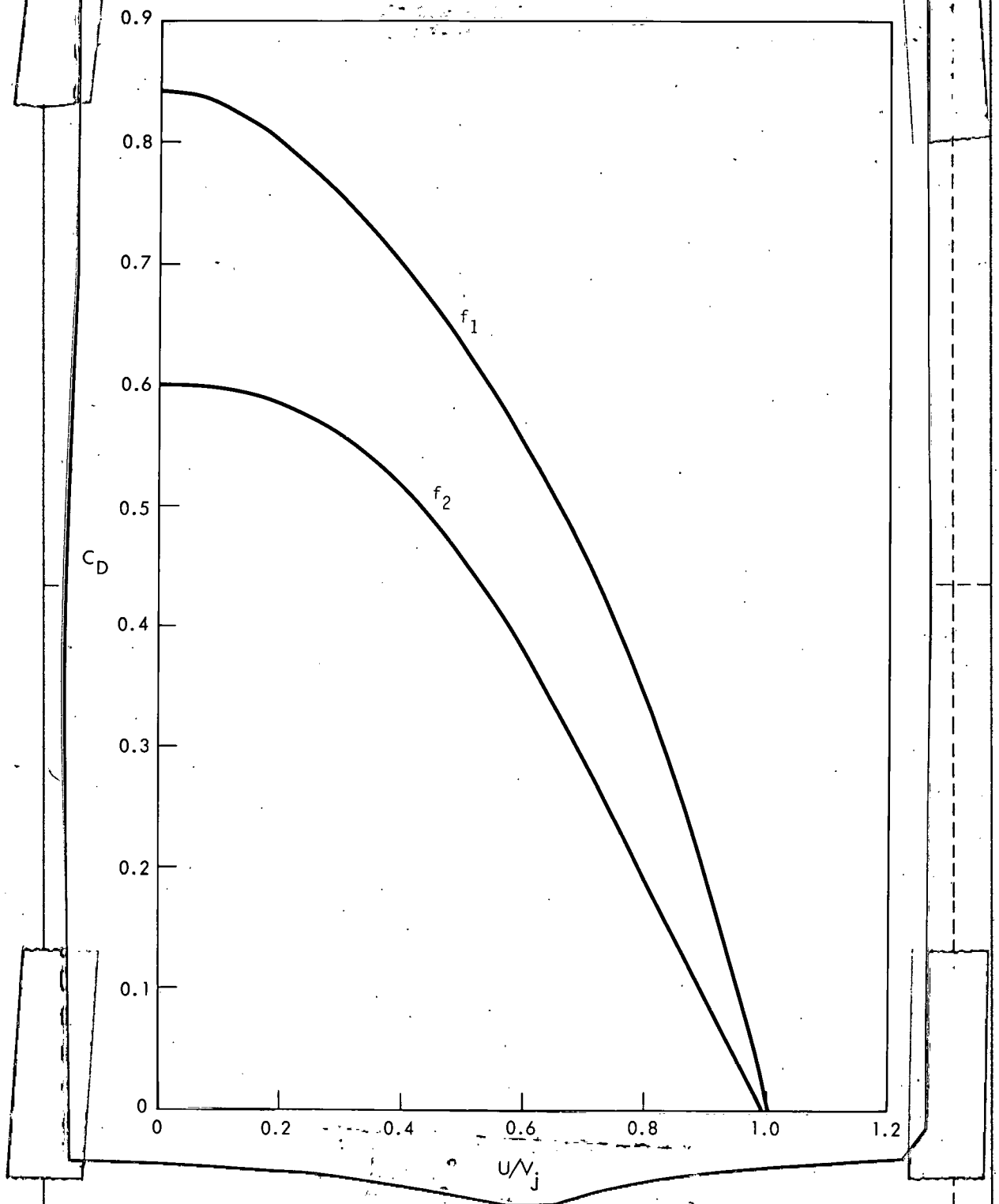

Figure 3-36. Curve Fit to Discharge Coefficient Data from Fig. 3-35.

For inflow, pressure ratio P/Pa is replaced by the ratio of the pressure outside of the duct to the static pressure inside the duct. Inflow is allowed only if the static pressure inside of the duct is less than the pressure outside the duct. The ideal flow to which the discharge coefficient is applied is based on the isentropic expansion from conditions outside the duct to static conditions inside the duct or to choked flow conditions if the pressure ratio is high enough. It is assumed above that there is no mean flow in the region outside the duct, so static and total pressures are always equal there.

3.2.2.1.5 Potential Flow Model for Variable Vent Discharge Coefficients in the Presence of Grazing Flow

In this subsection we describe a conceptual model which was designed to provide an analytical structure for correlating the behavior of the discharge coefficients for efflux from an orifice in the presence of grazing flow. The purpose is to derive an empirical formula for the discharge coefficient which is valid over the entire range of operating conditions and which does not suffer from the exclusion of certain limiting cases (in particular, the no-grazing-flow case) as do previous treatments (e.g., Rogers and Hersh, Reference 3-10). To this end, an effort is made to accurately represent the flow field in the duct far away from the orifice by treating it as the superposition of a uniform flow of velocity U and the flow due to a source or sink of strength m. This composite flow changes smoothly in the limit as, for example, the source strength (orifice flux) or the uniform flow velocity go to zero. Results describing the behavior of the "far field" flow are then used to determine the discharge coefficient from the conservation laws of fluid mechanics, under the assumption that the presence of the finite-size orifice introduces negligible effects on the forces exerted on the fluid approaching the orifice. In this report, for simplicity, we explicitly treat only the case of outflow from the duct through the orifice into an external plenum of pressure P_j, but the resulting correlation formula is also applied to the inflow case. Also, the analytical formulation is restricted to incompressible flow, but the result is applied to the case of choked flow as well.

Asymptotic Geometry of the Duct Flow Field

The duct is represented by the superposition of a sink and a uniform flow (see sketch). This flow field is often used to represent the flow

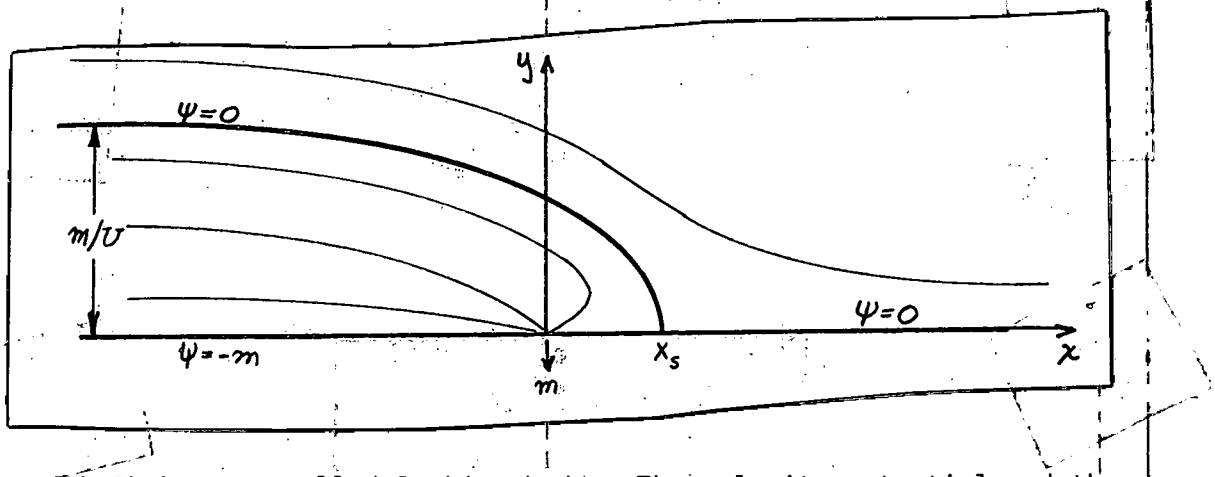

over an infinite, so-called Rankine body. The velocity potnetial and the stream function are given by

$$\phi = -Ux - \frac{m}{\pi} \ln r \tag{94}$$

$$\psi = Uy - \frac{m}{\pi}\theta \tag{95}$$

and the velocity components are

$$u_x = U - \frac{m}{\pi}\frac{x}{r^2} \tag{96}$$

$$u_y = -\frac{m}{\pi}\frac{y}{r^2} \tag{97}$$

The shape of the dividing streamline is given by

$$x = \frac{y}{\tan \frac{y}{x_s}} ; \tag{98}$$

it hits the plane of the orifice, y = 0, at a stagnation point

$$x_s = \frac{m}{\pi U} \tag{99}$$

We use this composite model to deduce an expression for the net vertical force on the fluid contained between the zero streamline and the wall. This force affects the momentum of the orifice flow and so acts to determine the angle α and mass flow of the jet emerging from the orifice. Therefore, it is particularly important to accurately represent the behavior of the net force in the limit of zero grazing flow or vanishing orifice flow. It turns out that the essential behavior of the net vertical force can be deduced by considering only the normal force on the wall. The pressure acting on the wall is given by Bernoulli's equation

$$p - p_\infty = \frac{\rho}{2}(U^2 - u^2). \tag{100}$$

Since on the wall ($y = 0$)

$$u = U - \frac{m}{\pi x}, \tag{101}$$

$$p - p_\infty = \frac{\rho U^2}{2}\left[2\frac{x_s}{x} - \left(\frac{x_s}{x}\right)^2\right]. \tag{102}$$

The total force in the y direction acting on the wall is given by

$$F_{y\ wall} = x_s \int (p - p_\infty)\, d\frac{x}{x_s}. \tag{103}$$

We estimate this force for the actual case in which an orifice of finite diameter d_o lies in the wall by integrating Equation 103 between the following limits; a) from $x = -L$ a long distance to the left of the origin to $x = -d_o/2$ at the left side of the orifice and b) from $x = d_o/2$ at the right side of the orifice to the stagnation point x_s, where eventually the limit $L \to \infty$ will be taken. Thus,

$$F_{y\ wall} = \frac{\rho U^2 x_s}{2}\left\{1 - \frac{4x_s}{d_o} + \left(\frac{x_s}{L} - \ell n\,\frac{L}{x_s}\right)\right\}. \tag{104}$$

The terms in the parentheses must be balanced by equivalent terms in the expression for the net force in the y direction on the dividing streamline, because the total net force must be independent of L, as $L \to \infty$. It can be

shown that the pressure on the dividing streamline depends only on the polar angle from the origin, θ, and therefore when integrating the pressure from $\theta = 0$ to $\theta = \tan^{-1}(-\pi x_s/L)$ the resultant contribution to the vertical force after subtracting off the terms matching (104) will simply be a constant. Thus,

$$F_y = \frac{\rho U^2 x_s}{2}\left\{1 - \frac{4x_s}{d_o} + \text{const}\right\} . \qquad (105)$$

Since we intend to develop an empirical correlation formula using experimental data, we "generalize" the above result by introducing two empirical constants

$$F_y = \frac{\rho U^2 x_s}{2}\left\{K_1 - K_2 \frac{x_s}{d_o}\right\} \qquad (106)$$

The Momentum Balance

In order to calculate the flux m through the orifice and the angle α of the emerging jet we consider the momentum balance on the control volume indicated in the sketch. As described above we represent the net force in

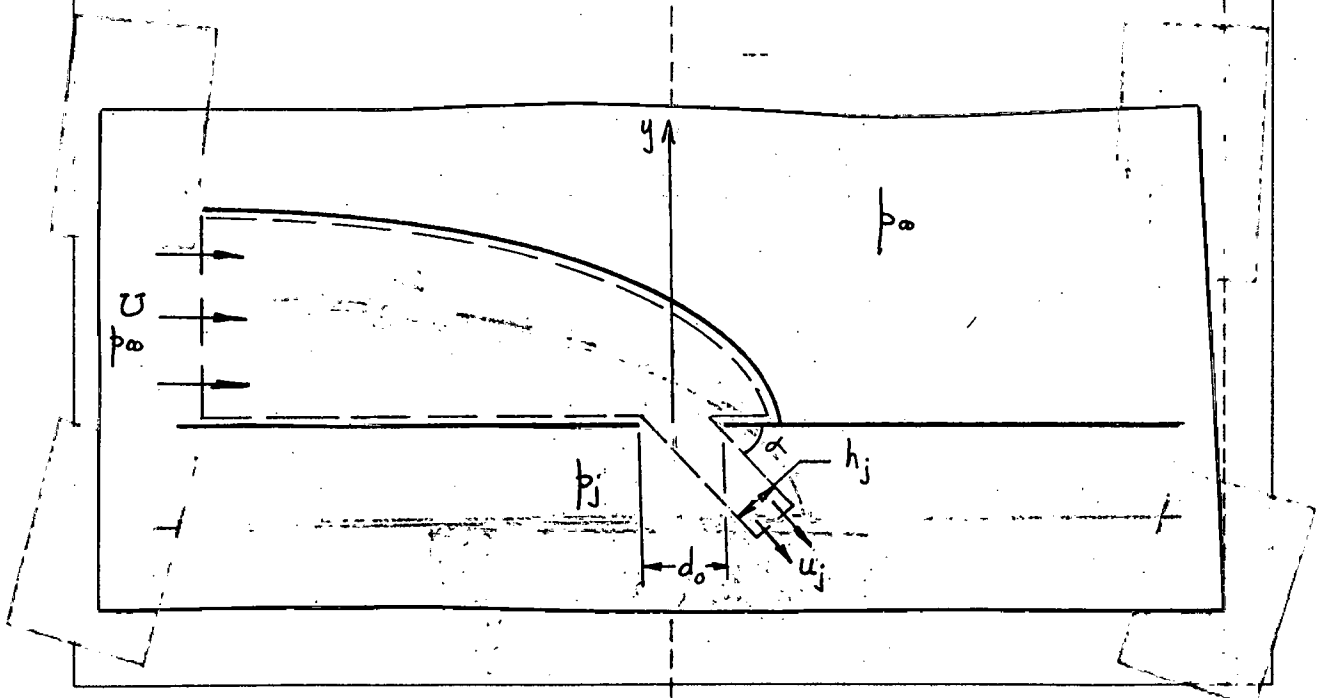

the vertical direction acting on the control volume above the plane y = 0 by Equation 106. An additional vertical force is exerted on the volume by the (uniform) pressure p_j in the plenum. In addition to the force in the x direction exerted by the pressure p_∞ against the left hand face of the control volume, which is balanced by the x-force on the dividing streamline (by d'Alemberts' paradox) there may also be x-forces developed near the corners of the orifice. These forces (F_x) are allowed for in this analysis but cannot be estimated by simple considerations. The equations conserving mass and momentum in the control volume are:

$$\text{Continuity} \qquad m = u_j h_j \tag{107}$$

$$\text{x-momentum} \qquad \rho(u_j \cos\alpha) u_j h_j - \rho U \frac{2m}{U} = F_x \tag{108}$$

$$\text{y-momentum} \qquad \rho(u_j \sin\alpha) u_j h_j = - F_y - (p_j - p_\infty) d_o \tag{109}$$

To determine the mass flux we need use only Equations (107) and (109). From (109)

$$u_j^2 \sin\alpha \; h_j = - \frac{F_y}{\rho} + \frac{p_\infty - p_j}{\rho} d \,, \tag{110}$$

$$\therefore \quad u_j h_j = \frac{U d_o}{\sqrt{2}} (C_p - C_y)^{1/2} \tag{111}$$

where

$$C_p \equiv 2 \frac{p_\infty - p_j}{\rho U^2}$$

$$C_y \equiv 2 \frac{F_y}{\rho U^2 d_o} \,. \tag{112}$$

Furthermore, solving for x_s

$$x_s = \frac{u_j h_j}{\pi U} = \frac{1}{\pi} \frac{d_o}{\sqrt{2}} (C_p - C_y)^{1/2} \tag{113}$$

$$X_s \equiv \frac{x_s}{d_o} = \frac{d_o}{\pi\sqrt{2}} (C_p - C_y)^{1/2} \tag{114}$$

Equations (111) and (114) are not independent. They are related by Equations (99) and (107). The functional behavior of F_y (and also F_x) are deduced from the arguments preceding Equation (105),

$$C_y = X_s(K_1 - K_2 X_s)$$

$$C_p = -K_3 x_s \ . \tag{115}$$

Subsituting (115) and (114) and solving for X_s,

$$X_s = - K_1' + \sqrt{K_1'^2 + K_2' C_p} \tag{116}$$

where

$$K_1' = \frac{K_1}{2} K_2'$$

$$K_2' = \frac{1}{2\pi^2 - K_2} \ . \tag{117}$$

Furthermore, the jet mass flow is given by

$$u_j h_j = \pi U d_o X_s = \pi U d_o \left[- K_1' + \sqrt{K_1'^2 + K_2' |C_p|} \right]. \tag{118}$$

Thus, we have arrived at a functional form for the orifice discharge coefficient C_D in terms of the duct grazing velocity U and the driving pressure force C_p which behaves properly in the limit $U \to 0$ and $C_p \to 0$. C_D is defined as follows:

$$C_D \equiv \frac{u_j h_j}{V_j d_o} \tag{119}$$

where

$$V_j = \left(2\,\frac{p_t - p_j}{\rho}\right)^{1/2} = U\left(C_p + 1\right)^{1/2} \qquad (120)$$

$$p_t \equiv p_\infty + \frac{\rho U^2}{2}$$

We evaluate K_2' in (118) by requiring that in the limit of zero grazing velocity the discharge coefficient reduce to the well-known classical value C_{D_o},

$$u_{jo} \equiv C_{D_o}\, U \sqrt{C_p} \qquad (121)$$

where the subscript $()_o$ refers to U = 0. Expressed in terms of V_j instead of C_p the final expression for the discharge coefficient becomes

$$C_D = -K\,\frac{U}{V_j} + \sqrt{\left(K\,\frac{U}{V_j}\right)^2 + C_{D_o}{}^2\left[1 - \left(\frac{U}{V_j}\right)^2\right]} \qquad (122)$$

where $K = \pi K_1'$ is to be determined by comparison with experiment.

In applying (122) we take

$$C_{D_o} = \text{fnc}\left(\frac{p_t}{p_j}\right) \qquad (123)$$

and specifically use Equation 93 to fit Perry's experimental data.

The constant K was selected so as to best fit the experimental data presented in Figure 3-35. The best fit was obtained with K = 0.21. The agreement between the model and the experimental data is quite remarkable, as shown in Figure 3-37. Equation 122 can now be directly incorporated into the FACTS code to provide the needed vent discharge coefficient as a function of the pressure ratio inside and outside of the vented duct, p_t/p_j, and the duct mean flow, U. Equation (122) is equally valid for outflow and inflow. For inflow p_t is the total pressure outside the vented duct and p_j the static pressure inside the duct. C_D as derived from Eq. (122) is then used in Eqns. (86) and (87) to determine the actual mass flow through the vents.

Eq 3-55

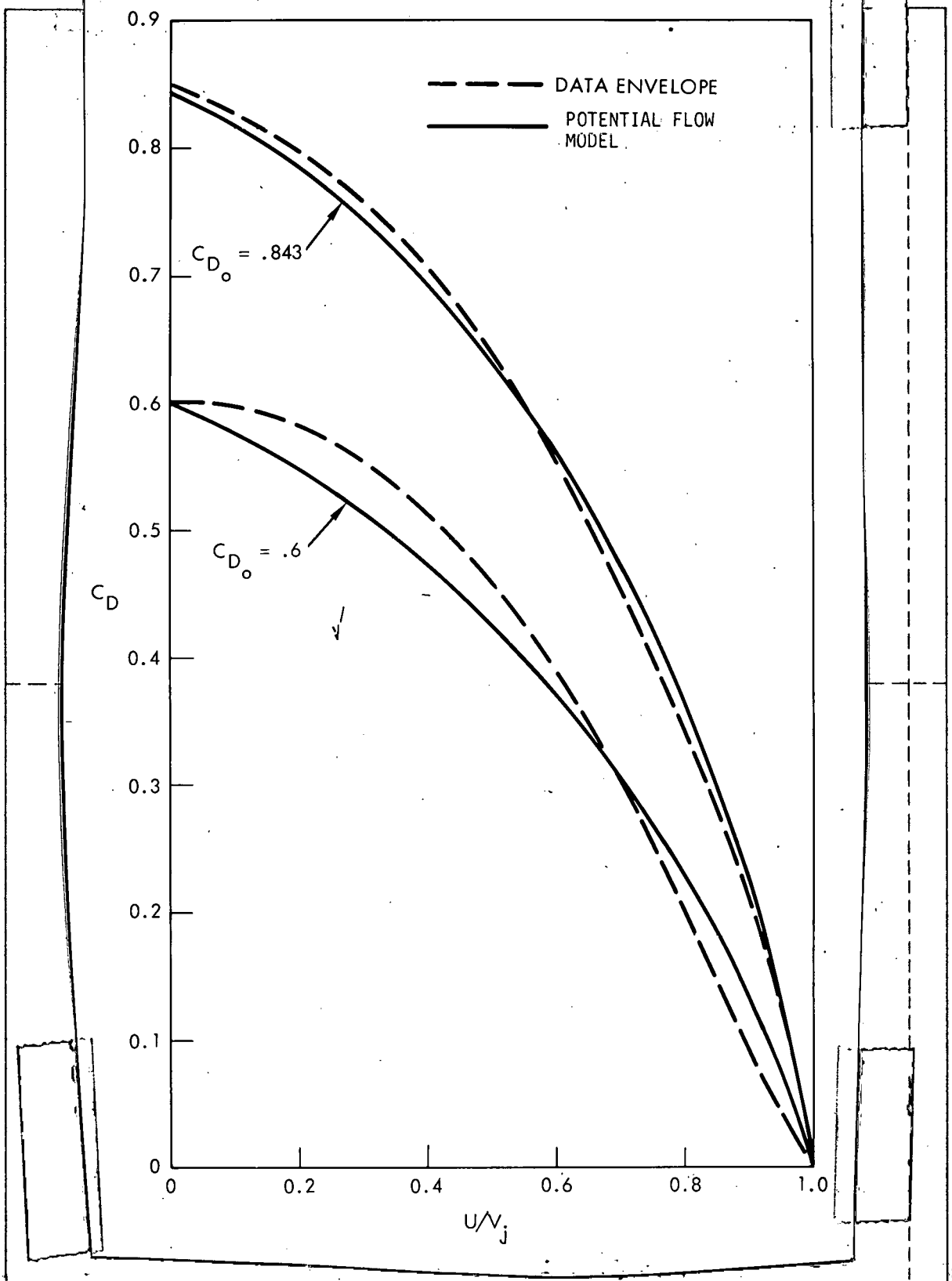

Figure 3-37. Comparison of Potential Flow Model for Discharge Coefficient (with K = 0.21) and the Envelopes of the Experimental Data.

3.2.2.2 Model for Open Ended Ducts

Side wall absorbers, if they are to be used in fusion-type lasers, will most likely have open-ended ducts, to reduce their flow resistance. The interaction of the shock waves generated in the laser cavity with the open downstream end of the acoustic duct must therefore be modeled and incorporated into the FACTS code.

When a shock wave or other pressure disturbance propagates through a duct and out of an open end, a very complicated three-dimensional unsteady flow situation results. A simple one-dimensional model cannot accurately predict the flow behavior near such an exit. However, it is possible to develop a quasi-one-dimensional flow model which will accurately predict the effects of an open end at least to some time after the initial shock exits the open end of the duct.

Previous researchers who have looked at this problem have been concerned with developing a model of the open ended duct for use with method of characteristics solutions (see References [3-13] and [3-14]). The approaches we use makes use of the same finite difference technique which was applied to solving the equations of motion.

Variable Area Model of an Open End

In our first attempt to model the open duct, we used the code capability of solving for flow in ducts with varying cross-sectional areas. When a shock propagates out of an open ended duct it forms a "shock bubble" which completely surrounds the exit of the duct. At distances from the exit which are large compared to the diameter of the duct, the flow is nearly one-dimensional and is in the direction in which the shock is propagating (see Figure [3-38]). By letting the cross-sectional area of the duct vary with distance from the exit in the same manner as the surface area of the shock bubble varies, the gross behavior of the exit flow will be approximated. The added variable area section of the duct is made long enough so that reflections from its termination do not propagate back into the main duct during times of interest.

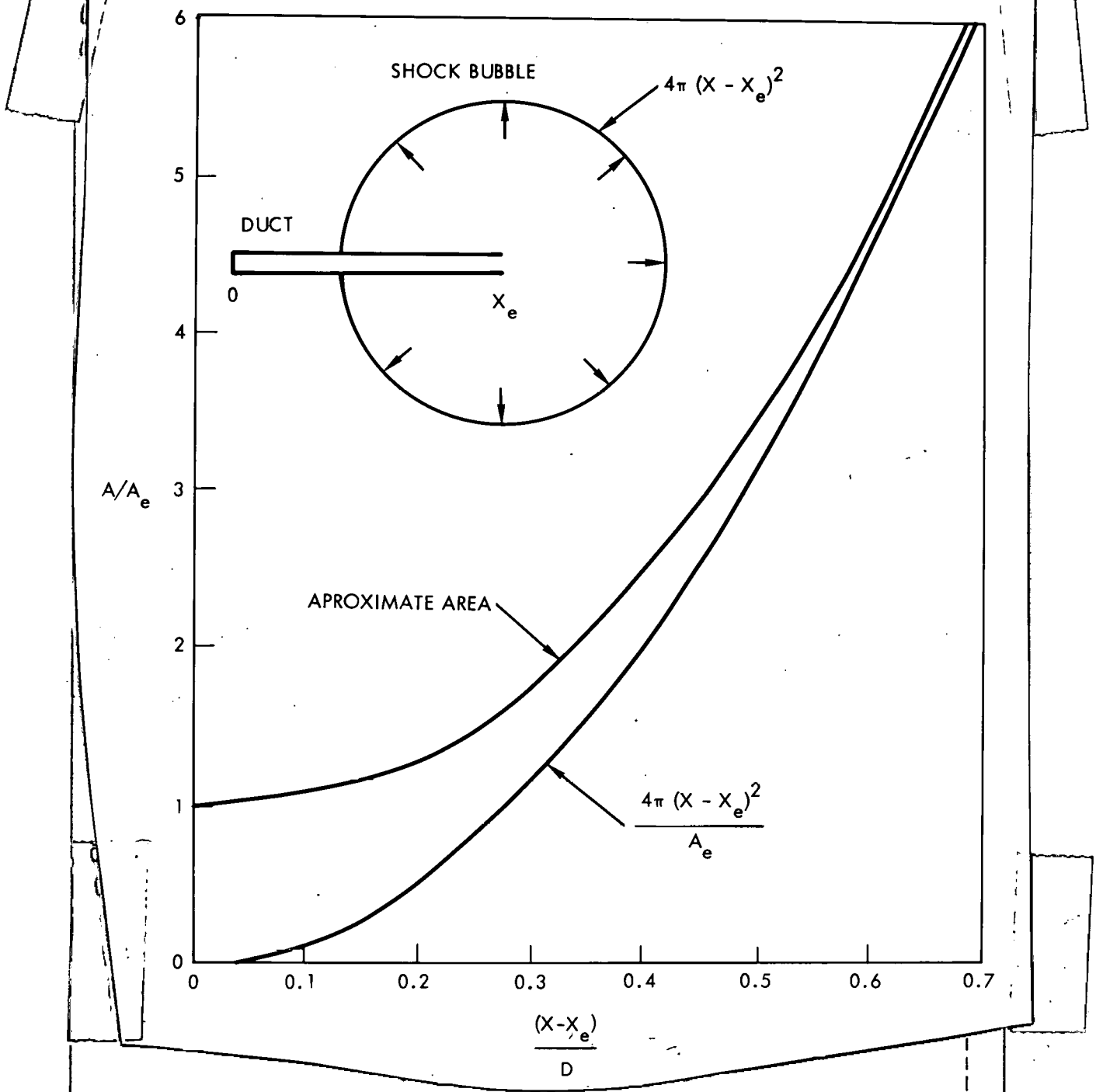

Figure 3-38. Variable Cross-Sectional Area Simulating of the Open End of a Duct.

Vented Duct Model of an Open End

In this second approach we use the vented duct capability of the finite difference code to simulate the open end of a duct. During previous studies (Reference 2-10), involving the vented duct concept of pressure wave suppression, it was noted that when a vented section of duct with large open area joined a non-vented section, the non-vented section behaved very much like an open-ended duct. Here we deliberately use this behavior to simulate the open-end of a duct. The side-wall vent area per unit length was chosen so that in each hydraulic diameter of vented duct the vent area was equal to the cross-sectional area of duct. This amount of venting was found to simulate the open end quite well. The length of the highly vented region is chosen so that disturbances which reflect from the closed end of this "added-on" vented duct do not return to the non-vented or moderately-vented section of duct. Because of the large amount of venting required to match the open end pressure decay, the length required can be kept to a minimum. This represents an advantage over the variable area model in that the required number of additional nodes and the additional computing costs can be kept to a minimum.

3.2.2.3 Modeling of Viscous and Heat Transfer Effects

To further improve and refine the predictive capabilities of the code, wall friction and heat transfer effects were incorporated in the code.

Viscous Effects

The actual effects of the finite viscosity will be to develop two- and three-dimensional boundary layers along the walls of the duct. These effects may be approximated in a gross sense by assuming that the effect of the boundary layers may be treated in an integral manner which acts in a uniform way across the whole cross-sectional area of the duct. Likewise, heat transfer from the walls is assumed to affect the overall flow in a one-dimensional gross sense. With these assumptions, the general form of the source terms which account for viscous and heat transfer in the equations of motion can be written as:

$$S_1 = 0 \quad (124)$$

$$S_2 = FA \quad (125)$$

$$S_3 = QA \quad (126)$$

where F is the wall shear force per unit volume acting on the fluid (F > 0 if u > 0, F < 0 if u < 0) and where Q is the heat transfer form the fluid to the walls of the duct. A is the cross-sectional area of the duct.

The wall shear force is determined from the wall shear stress for steady fully developed flow. Under these conditions, the wall shear stress, τ_w, is related to the flow friction factor by the definition:

$$\tau_w \equiv \frac{1}{2} \rho u|u| \, f(Re, \varepsilon/D_H) \quad (127)$$

where f is the friction factor, Re the Reynolds number, ε the effective wall roughness height, and D_H is the hydraulic diameter of the duct. The hydraulic diameter is defined by:

$$D_H \equiv 4A/C \quad (128)$$

where A is the cross-sectional area of the duct and C is the perimeter. The Reynolds number is based on the hydraulic diameter:

$$Re = \frac{\rho u D_H}{\mu} \quad (129)$$

where μ is the viscosity of the fluid. The friction factor is determined by the following equations taken from Reference (3-15):

$$f = \begin{cases} .0625\left[\phi + \log_{10}(Re/5.02) - \log_{10} w\right]^{-2}, \\ \quad \text{for } Re \geq 4\times10^3 \\ 16/Re, \\ \quad \text{for } Re < 4\times10^3 \end{cases} \tag{130}$$

and

$$w = \frac{\varepsilon\, Re}{D_H\ 18.57} + \log_{10}\frac{Re}{5.02} \tag{131}$$

where ϕ is found by interpolation from the following table:

w	$\phi(w)$
2	.057
10	.044
20	.029
40	.018
10^2	.0087
10^3	.0013
10^5	8×10^{-5}

The F in equation (125) is determined from:

$$F = \frac{\tau_w C dx}{dx A} = \tau_w \frac{C}{A} = \frac{4}{D_H}\ \tau_w \tag{132}$$

Heat Transfer Effects

For the heat transfer model we assume a constant wall temperature and fully developed flow. The heat flux from the fluid to the wall can be expressed as

$$\dot{q} = \frac{kNu}{D_H} (T_m - T_w) \quad (133)$$

where T_w is the wall temperature, T_m is the mixed mean fluid temperature, Nu is the Nusselt number, k is the thermal conductivity of the fluid, and D_H is the hydraulic diameter. The Nusselt number is given by the following equations which were taken from Reference (3-16):

$$Nu \begin{cases} = 0.21\ Pr^{0.6}\ Re^{0.8} \\ \quad \text{for } Re \geq 827 \\ = 3.658 \\ \quad \text{for } Re < 827 \end{cases} \quad (134)$$

Where Pr is the Prandtl number. The Q in equation (126) is given by:

$$Q = \frac{4\ k\ Nu\ (T_m - T_w)}{D_H^2} \quad (135)$$

3.2.2.4 Construction of Wave Diagrams

Wave diagrams or x-t diagrams are plots of the propagation of waves and particle paths in space and time. They originated with the method of characteristics solution to the equation of unsteady flow in gas dynamics. When using the method of characteristics, wave diagrams are produced practically as a by-product of that method of solution. Wave diagrams are a useful aid in understanding and visualizing complex unsteady flow phenomena. When finite difference methods are used to solve the equations of unsteady flow, wave diagrams are not automatically produced. It is necessary to construct them from the numerical solution, if they are desired. We have modified the FACTS code to facilitate the construction of wave diagrams by computer. This added capability of the FACTS code can be very helpful particularly when one must look for the details of the interactions of pressure waves with hot/cold interfaces in the pressure attenuator ducts.

As the code is running, we create a file which contains the fluid velocity, u, and the sound speed, c, at each node and at each time step. At a later time, if a wave diagram is desired, a post processing program can use the (u, c) file to create a wave diagram. The post processor creates a wave diagram by intergrating for particle paths, and characteristics:

particle paths

$$x_u = x_o + \int_o^t u\,dt$$

+ characteristics

$$x_{u+c} = x_o + \int_o^t (u+c)\,dt$$

- characteristics

$$x_{u-c} = x_o + \int_o^t (u-c)\,dt$$

The paths are stored and later machine plotted. The user can specify at which locations in the flow he wants to trace particles and characteristics. The characteristic tracers follow the particle paths in the x-t domain until the particles begin motion in the x-direction indicating that a pressure signal has arrived. When a characteristic crosses a boundary such as an end wall or an open end, the sign on the sound speed is changed so that the reflected characteristic is followed.

An example of the wave diagrams produced by this method is shown in Figure 3-39, which is for a shock tube with a 24 inch driver and a 78 inch driven section which was closed at the downstream end. The air in the driver was initially at 80 psig and the air in the driven section was initially at 1 atmosphere.

In Figure 3-38, particle paths are shown as dotted lines and characteristic paths as solid lines. The leading right running characteristic

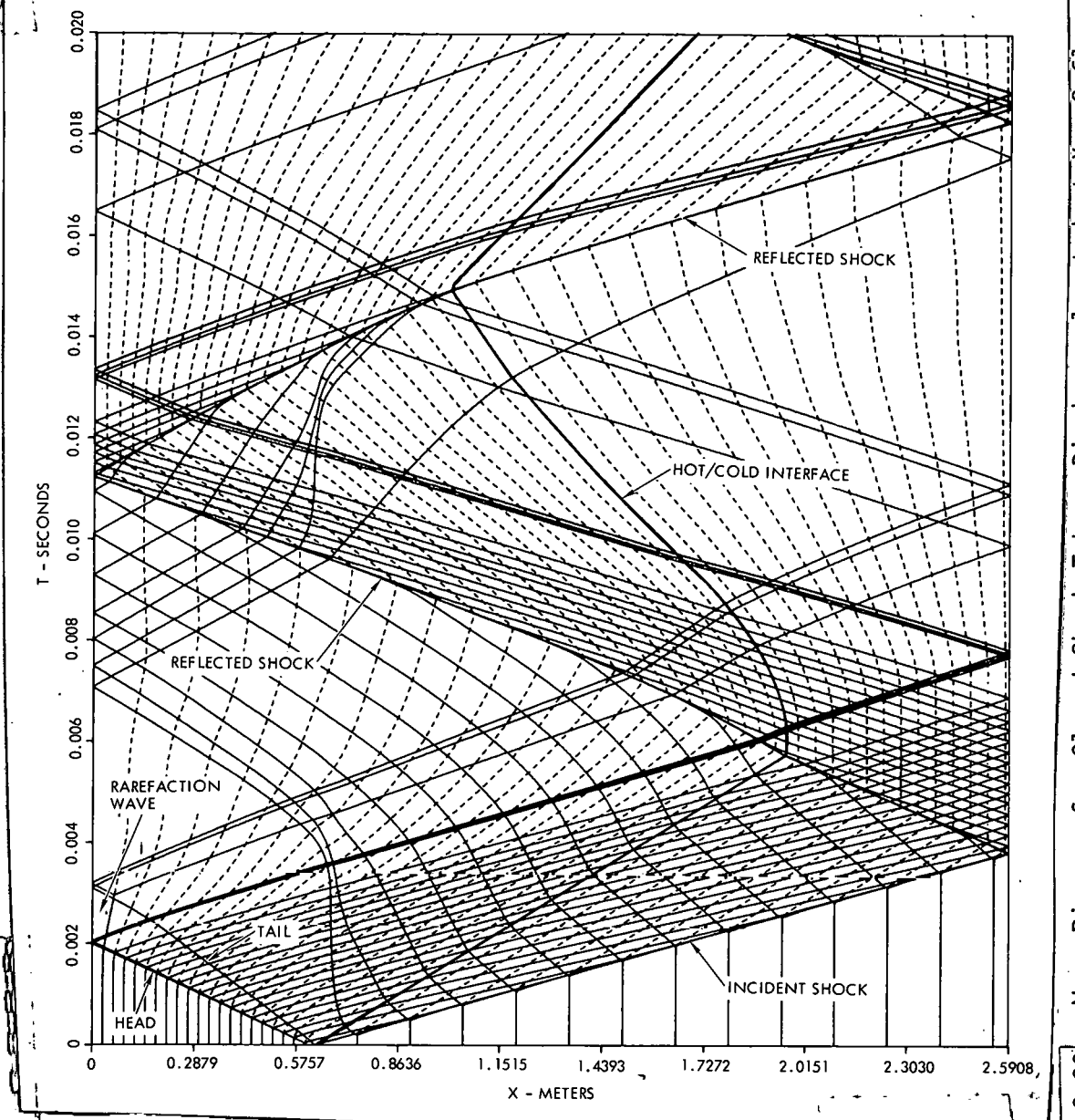

Figure 3-39. Wave Diagram for Closed Shock Tube. Diaphragm located at X = 0.61 meters. Dashed lines are particle paths and solid lines are characteristics. Driver pressure ratio is 5.4.

labeled "incident shock", traces the path of the right running shock wave. As the shock moves along, characteristics from behind begin to catch up and coalesce with the shock. The particle path which was originally at the diaphragm marks the interface between the driver gas which cooled upon expansion from the driver and the shock heated gas which was initially at ambient conditions. The particle path marking this interface is emphasized and shown as a solid line in Figure 3-38. The lateral spacing of the dotted (particle) lines indicate the local gas density. There was a 25% reduction in cross-sectional area located just downstream of the driver in order to simulate the broken diaphram which constricts the flow in this location. The flow through this region becomes nearly sonic. Under these conditions signals carried by characteristics propagating against the flow will be delayed. When these choked conditions occur. The characteristic paths become nearly vertical lines on the x-t diagram. Figure 3-38 indicates that choked conditions at the diaphragm occurred twice during the 20 millisecond period shown on this figure. The approximate location of the head and tail of the rarefaction wave which propagates into the driver are also picked up by the characteristic paths on the wave diagram.

Other options can be programmed into the post processer. Characteristics or particle paths of special interest can be specified, additional ones added at specified times and locations, or non-essential ones dropped from the plot. This wave diagram plotting capabilities will be utilized, as needed, to clarify details of wave interactions with slugs of gas of varying properties, such as will be produced in repetitively pulsed laser.

3.2.3 Comparisons of Code Predictions and Experimental Results

3.2.3.1 Closed Tube Tests

Pressure histories taken at two locations in the shock tube were compared with model predictions. A 24 inch long driver section was fired into a 78-inch long driven section which was closed at the downstream end and initially at 1 atm. pressure. Pressure histories were recorded at Station 1 located 33 inches from the driver and Station 2 located 76 inches from the driver (2 inches from the closed end). Data was recorded at low overpressures (~ 5 psi in the driver) and high overpressures (~ 80 psi in the

driver). The data was recorded for short durations (∿ 10 to 20 ms) and long durations (∿ 100 ms).

Low Overpressure Comparison

The short duration results for the low overpressure case are shown in Figure 3-40 and the long duration results for the low overpressure case are shown in Figure 3-41. The pressure pulse generated by the breaking of the diaphragm propagates down the tube and arrives at Station 1, 33 inches from the driver. The pulse is roughly trapezoidal in shape, the vertical leading edge of the pulse indicating the presence of a shock wave. This pulse reflects from the closed end as another similarly shaped pulsed, as indicated by the lower trace of Figure 3-40 (Station 2). The pulse then travels upstream and passes Station 1 with a nearly identical shape as when it passed the first time. The pulse continues upstream to the closed end of the driver where it reflects and returns to Station 1 and begins another cycle.

The two step pressure rise in the leading edge of the experimental data for the pulse arriving at Station 2 is due to the incident wave arriving at Station 2 (the first step), traveling two inches to the closed end, reflecting as a jump in pressure, and returning to Station 2 (the second step). The model did not distinctly show this second step because the two inch zone spacing used in the model was too coarse to resolve the difference in arrival times between the two waves.

Referring to Figure 3-41, as time progresses the trapezoidal wave shape becomes triangular as rarefaction waves catch up with the shock front. The same cycle of two pulses at Station 1 for each pulse at Station 2 continues with very little decay in shock strength. The agreement between model and experimental results is quite good.

High Overpressure Comparison

The comparison between experimental and model results are shown in Figure 3-42 (0 to 10 ms) and Figure 3-43 (0 to 100 ms). The early time results are much the same as those for low overpressure. The wave shapes are similar to the low overpressure waveforms and the agreement between code and experimental results is good.

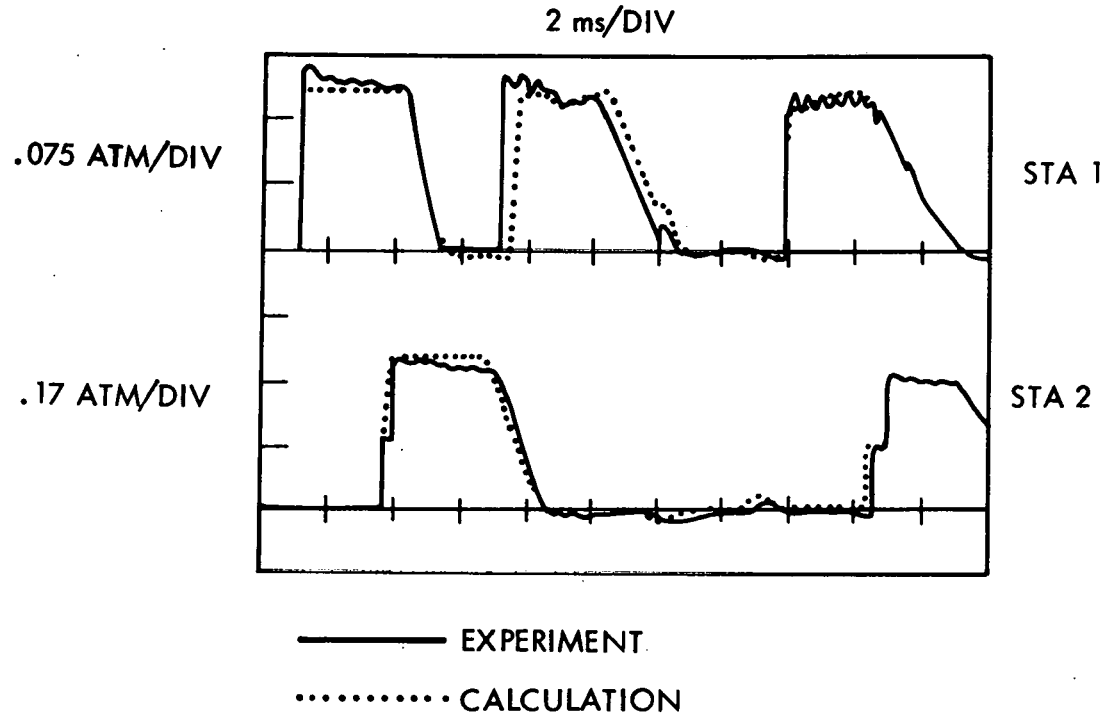

Figure 3-40. Pressure Histories for the Closed Tube with a 24" Driver at an Overpressure of 6 psi (test shown in Fig. 3-7).

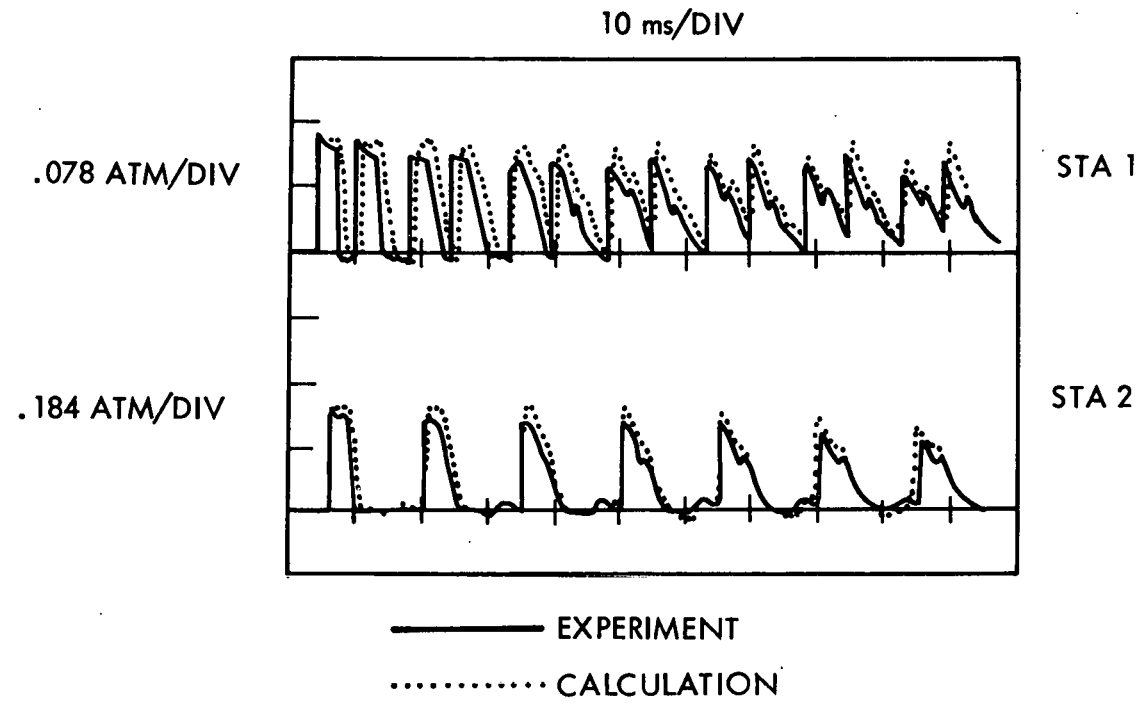

Figure 3-41. Pressure Histories for Closed Tube with 24" Driver at an Overpressure of 4.3 psi (test shown in Fig. 3-7).

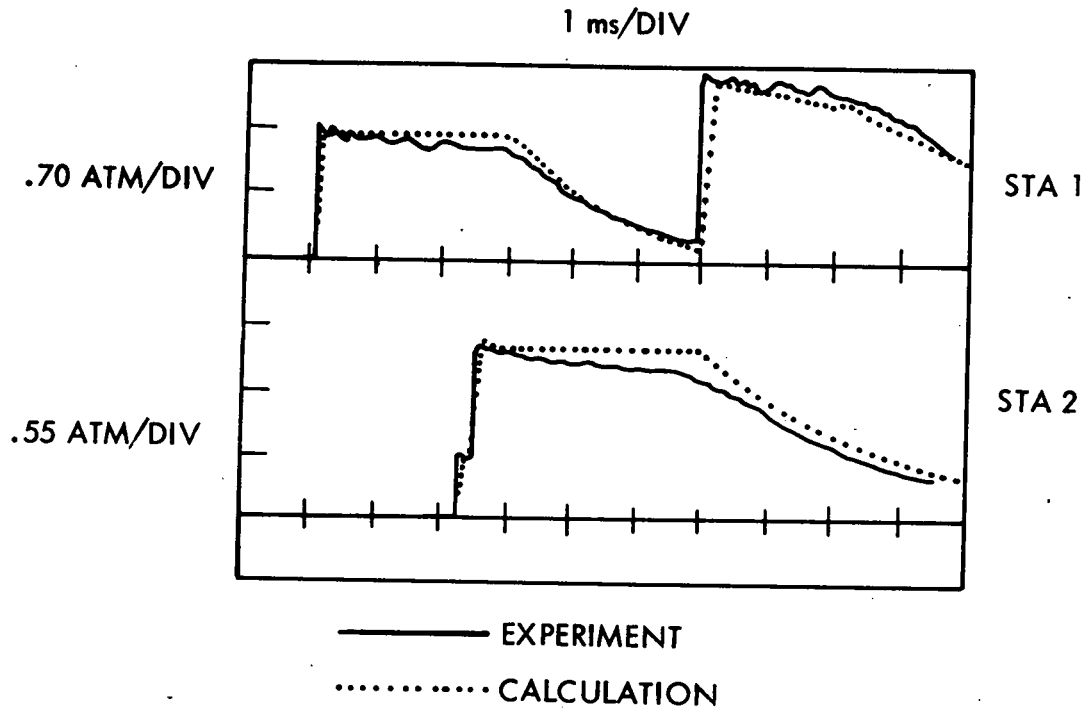

Figure 3-42. Pressure Histories for Closed Tube with 24" Driver at an Overpressure of 80 psi (test shown in Figure 3-8).

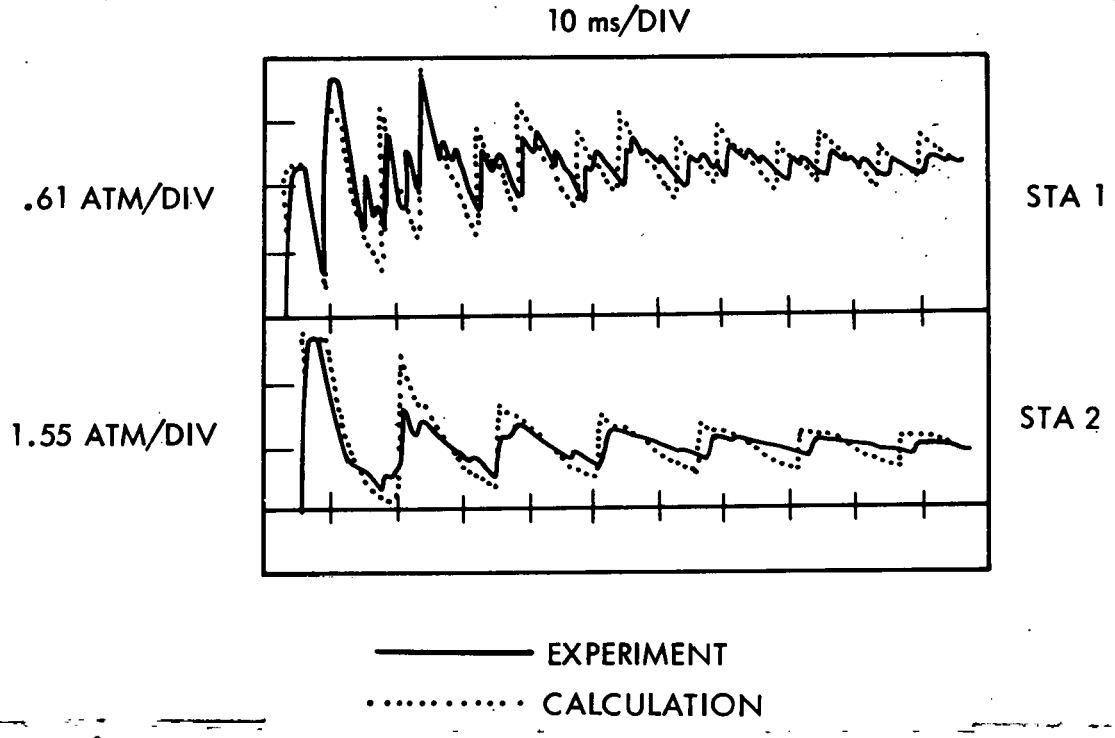

Figure 3-43. Pressure Histories for the Closed Tube with a 24" Driver at an Overpressure of 77 psi (test shown in Fig. 3-8; no friction in the code run).

At longer times the model and experimental results begin to show some differences; See Figure 3-42. Note on Figure 3-42 that at Station 1, between the second and third (code-predicted) pulses, the experimental data shows secondary pressure pulses. These secondary shock waves/pressure pulses first appear at Station 1 after the main pulse has passed this location on its way back to the driver. These secondary waves appear to be reflections from the thick aluminum diaphragm petals. This being a non-ideal process peculiar only to a shock tube, no attempt is made to model it in the code.

The pulse decay rates shown by the high pressure experimental results is faster than predicted by the code. Frictional and heat transfer at the walls, the diaphragm interactions, and turbulence at the contact surface and in the boundary layers can all contribute to the observed decay of the pressure pulse. Of these, only frictional and heat transfer effects were put into the code. As discussed elsewhere, the frictional and heat transfer effects were modeled using a quasi-steady approach which uses incompressible steady state empirical models for skin friction and heat transfer. This model includes a parameter (the surface roughness) which can be varied to increase the effects of friction. Increasing the parameter increases the momentum removed via the source-sink term in the momentum equation. Figure 3-44 shows a comparison for the long duration high overpressure experimental results with the code results when an unusually high amount of friction (effective roughness to hydraulic diameter ratio of $\sim .15$) is introduced to obtain decay rates comparable to those measured experimentally. This friction represents an equivalent measure of the total damping produced by the various processes listed earlier.

3.2.3.2 Open Tube Tests

The same experimental setup and transducer locations were used in the open ended duct tests as in the closed duct tests shown earlier. Station 1 was located 33 inches from the driver and Station 2 was located 76 inches from the driver (2 inches from the open end). Again tests were made with high ($\sim$ 80 psi) and low (7 psi) driver overpressures, and data was recorded for 20 ms and 100 ms intervals.

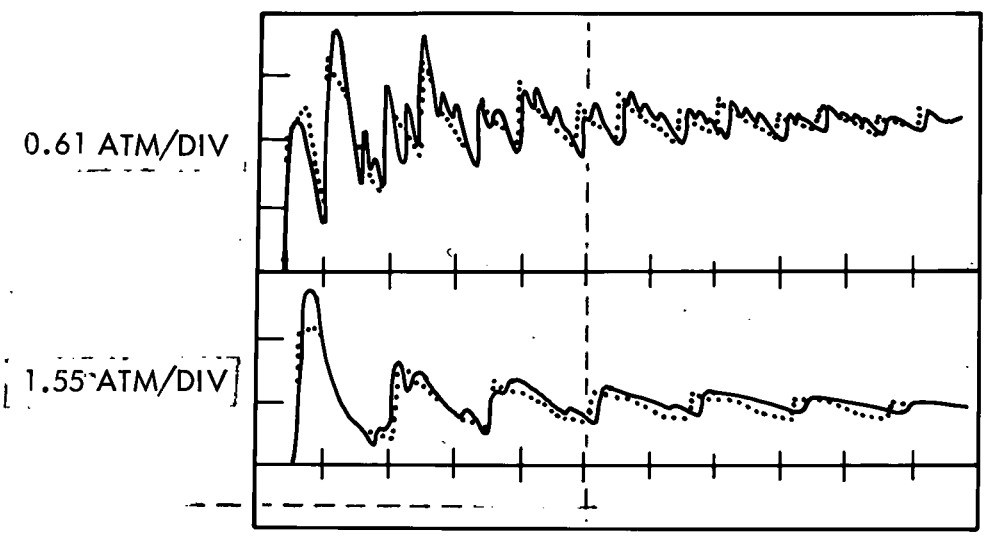

Figure 3-44. Pressure Histories for the Closed Tube with a 24" Driver at an Overpressure of 77 psi; with Friction and Heat Transfer ($\varepsilon/D_H = 0.137$) in the Code Run.

Low Pressure Results

The overall picture of what happens when the closed end is replaced with an open end is that now waves arriving at the open end are inverted upon reflecting. That is to say, compression or shock waves are reflected as rarefaction waves, and rarefaction waves at the open end are reflected as compression waves. This is illustrated by the results shown in Figure 3-45 for Station 1. First wave to arrive at Station 1 is a square wave headed by a shock wave. This reflects from the open end and is seen again at Station 1 as a square pulse led by a rarefaction. The negative reflection coefficient of an open end results from the quick return of the pressure there to ambient conditions, as illustrated by the measurements at Station 2. The reflected expansion pulse again reflects from the closed end of the driver and passes Station 1 again as an expansion pulse seen in the Station 1 data shown in Fgiure 3-46, which shows the results out to 100 ms.

The code correctly predicts the wave arrival times at Station 1, but overpredicts the amplitude of the reflection and shows negligible decay. This result is in contrast to the low overpressure closed end comparison where the model results matched the data fairly well. An examination of the open end experimental data at Station 2 (near the open end) can shed some light on the differences between the experiment and the model predictions. The experimental data taken near the open end (Figures 3-45 and 3-46 - lower traces) show the presence of high frequency transverse pressure oscillations due to multi-dimensional wave diffraction effects which the code does not model. Even more significant is the code prediction of the open end pressure being below ambient during pulse reflection (Figure 3-46). Clearly, this implies a stronger negative reflection and consequently a slower decay. It is believed that separation and vortex formation leading to a jet like dissipative flow, which occur in the real process of reflection from the open end, but are not modeled in the code, are responsible for these differences.

High Overpressure Results

The short term and long term results for the open-duct high pressure (~ 80 psi driver overpressure) cases are shown in Figure 3-47 and 3-48. These results are quite different from the low pressure open end results in that a distinct repeating sequence of sharp pulses fails to develop. One reason for this different behavior lies in the fact that the flow velocity at the open end of the duct reaches the speed of sound (choked flow) just after the first shock arrives. As long as the flow remains choked at the exit, pressure disturbance, which propagate with the speed of sound relative to the fluid, cannot propagate upstream. That is why there was an apparent delay in the arrival of the rarefaction wave expected to be formed when the main shock reached the open end. Sonic flow speed near the exit does not prevent disturbances from propagating towards the exit from upstream. When the rarefaction wave following the shock wave arrives at the exit, the flow velocity drops below sonic and disturbances can once again propagate upstream. In the high pressure case, differences in wave speeds alter the periodic nature of the waves observed in the low pressure case.

The pressure histories predicted by the code for the high pressure open ended duct agree fairly well in an overall sense, but some of the details of the wave structure were not predicted by the code. These differences between code and experimental data are due to two-dimensional effects which were not modeled in the code. In particular, wave interactions with the petals of the diaphragm as well as the area constriction which occurs at the diaphragm station are not included in the model. Further, the simple one-dimensional model of an open end does not account for the real jet-like multi-dimensional dissipative flow processes occurring at the open end. In applying the code to typical pressure wave suppression problems in pulsed lasers, it won't be necessary to model the first two effects. The model for open end of the duct however, may require some improvements so that the effects of an open end on the pressure-wave can be better predicted.

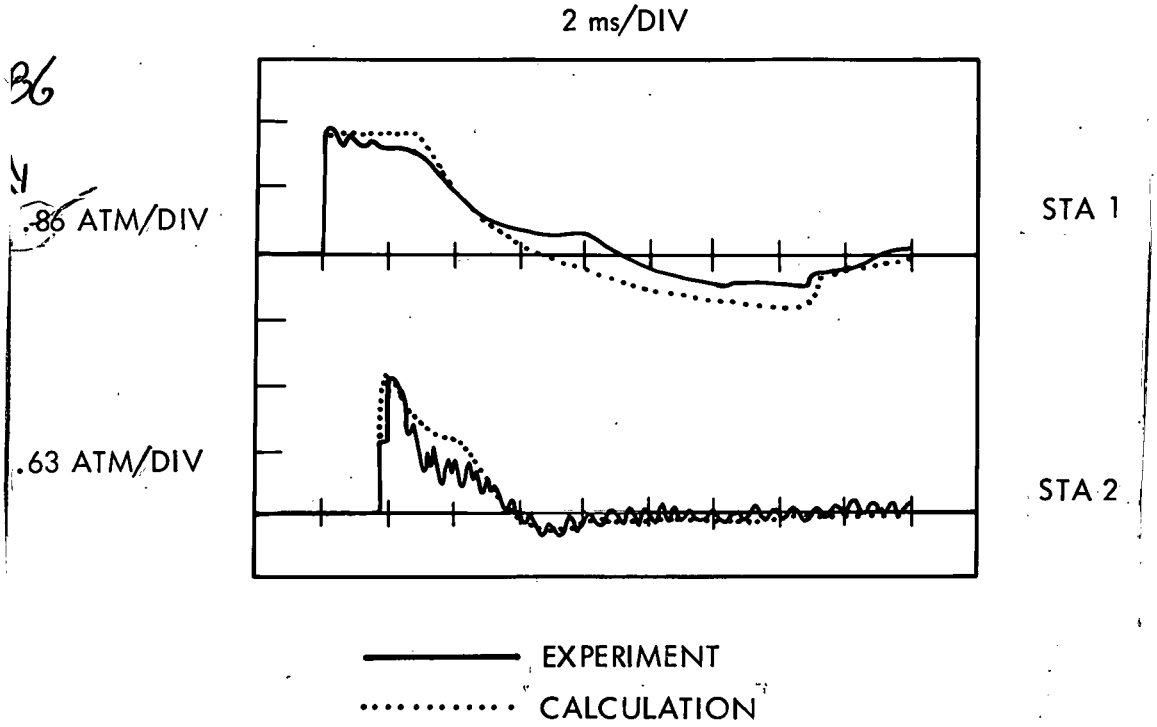

Figure 3-47. Pressure Histories for Open-Ended Duct with 24" Driver at an Overpressure of 75 psi (test shown in Fig. 3-10).

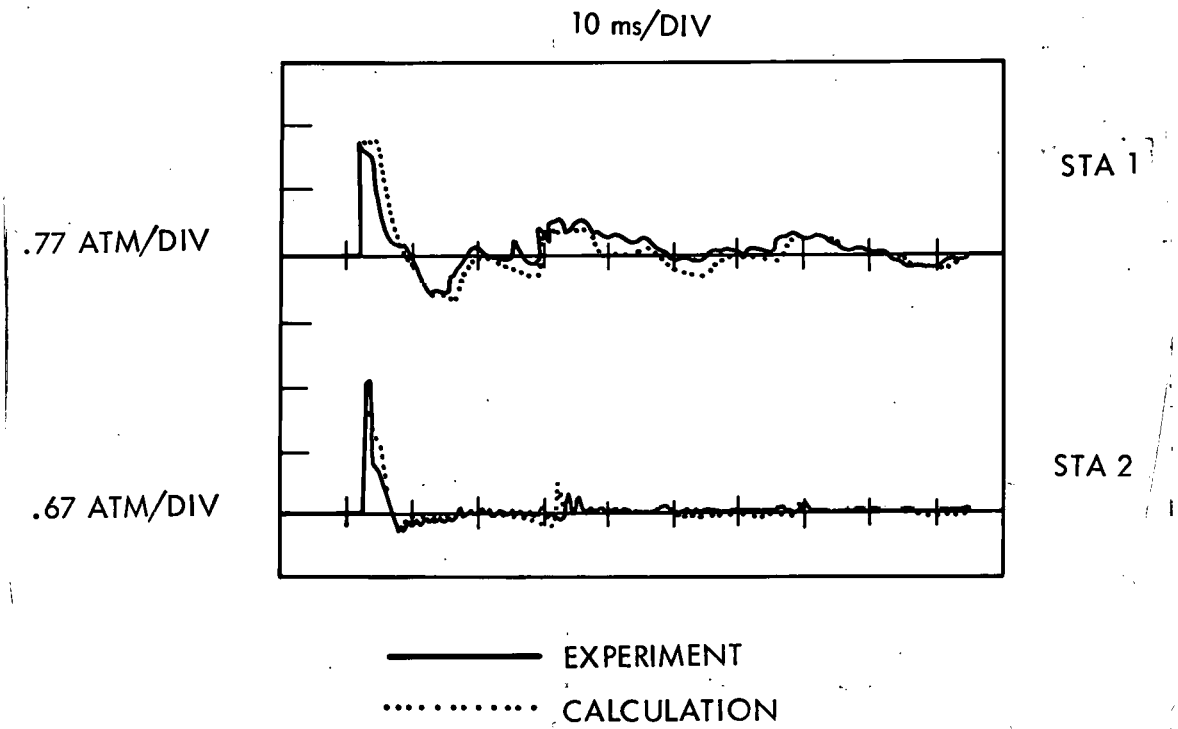

Figure 3-48. Pressure Histories for Open-Ended Duct with a 24" Driver at an Overpressure of 78 psi (test shown in Fig. 3-10).

3.2.3.3 Vented Duct Tests

8" Driver

The shock tube configuration and test conditions for which code calculations have been obtained are as follows: The shock tube driver was 8 inches long and the driven section was 111 inches long. The venting began 2 inches from the diaphragm and continued for the remaining length of the driven section, which was closed on the downstream end. The venting produced a 7.2% open area in one wall, which according to our code calculations should give a nearly optional rate of pressure wave attenuation. All test comparisons were made for a nominal driver overpressure of 7 psi.

Calculations were made using two venting models, the constant C_D model and the variable C_D model, which were discussed in Section 3.2.2.1. Two runs were made with the constant C_D, with C_D values of .6 and .9, and one with the variable C_D. As it turned out the results for the variable C_D model were nearly identical to the results obtained with the constant C_D model using a value of .6 for C_D. This result is not too surprising in view of the relatively low overpressure cases considered here, since the variable C_D model gives a discharge coefficient nearly .6 for low overpressures. Because the C_D = .6 and the variable C_D results are nearly identical, only the constant C_D results will be compared with the experimental data. The variable C_D in code results are expected to depart from the C_D = .6 results when higher driver overpressures are considered.

Experimental pressure histories were obtained from the upstream end (closed end) of the driver and 9 inches downstream of the diaphragm, at the beginning of the vented section. These two pressure histories are shown in Figure 3-49 compared with the computed results for a constant discharge coefficient of 0.9 and in Figure 3-50 compared with the computed results for a discharge coefficient of 0.6.

The upper trace gives the pressure history 9 inches downstream of the diaphragm. What is observed at the downstream station is a sudden rise in pressure followed by a slight drop in pressure, followed again by a sudden drop in pressure to a value below ambient, i.e., a pressure pulse followed by a rarefaction. The positive pulse is due to the shock generated by the diaphragm and the negative pulse or rarefaction is caused

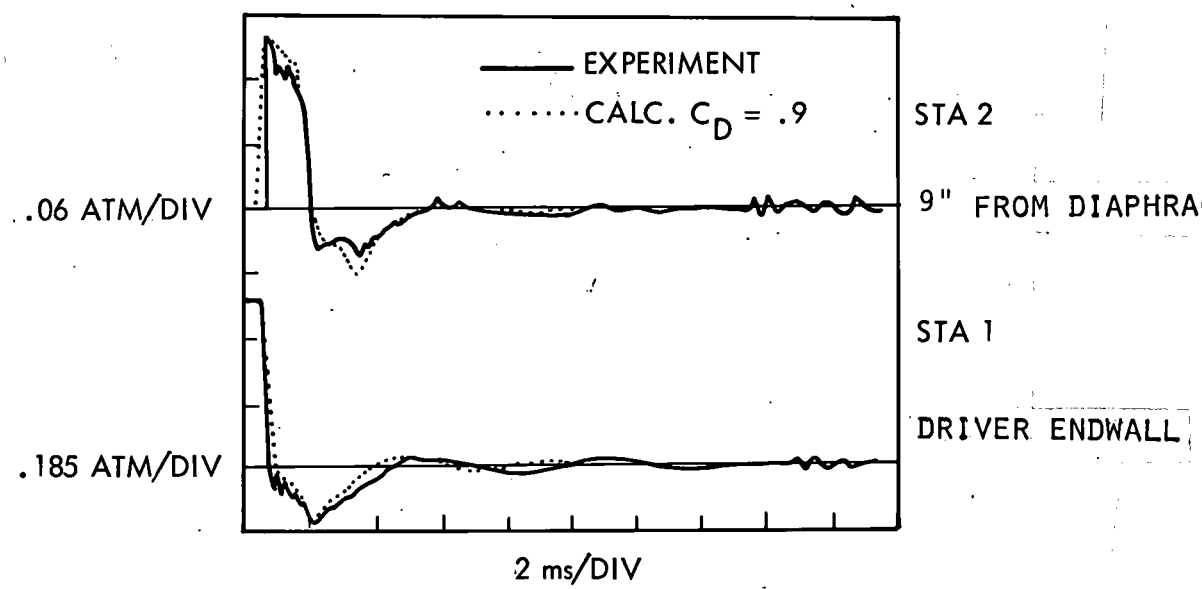

Figure 3-49. Vented Tube Test (7.2% Open) Closed-End Duct With 8" Driver and 6 psi Overpressure Test Shown in Figure 3-14.

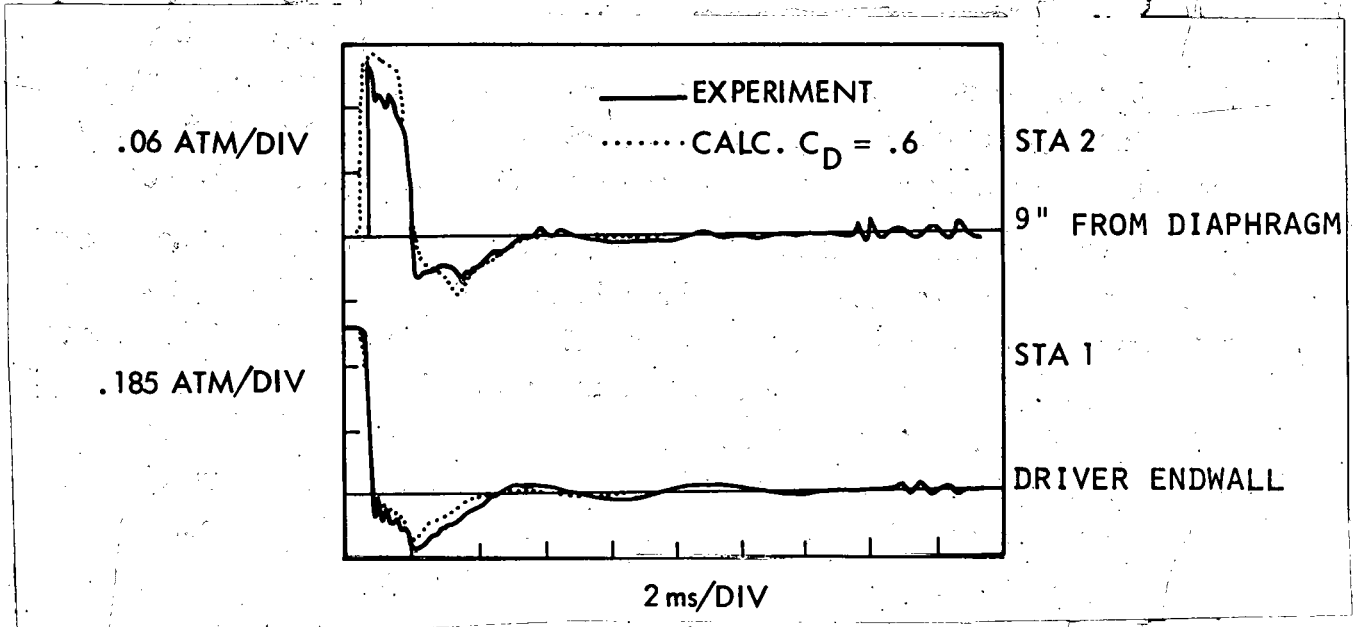

Figure 3-50. Pressure Histories for Open-Ended Duct with 24" Driver at an Overpressure of 5 psi (test shown in Fig. 3-14).

by the shock interacting with the vented region to produce a rarefaction wave which is reflected back to the driver where it reflects from the rigid wall and returns to the vented region.

The lower trace in Figure 3-49 gives the pressure history at the closed (upstream) end of the driver. At this station the high pressure driver gas encounters first a rarefaction wave generated by the bursting diaphragm followed by a rarefaction wave reflected from the vented region of the duct as the shock passes through the vented region. The pressure at this station returns to near ambient about 4 milliseconds after the diaphragm burst.

A third feature to note in Figure 3-49 and 3-50 are the presence of relatively late time disturbance at around 16 milliseconds. This disturbance is due to the return of the main shock after reflecting from the closed end of the vented duct. The finite difference (FACTS) code did not predict the return of this shock for either value of C_D. The oscillating nature of this signal which appears at a time when the first shock would be reflected from the closed end of the vented duct, is also unexpected. If at all, the code would predict a reflected shock followed by a rarefaction, so that pressure would jump up, and then decay back to ambient conditions. It may be that in this case, transverse oscillations or 2-D wave patterns develop behind the reflected shock to give the wavy pattern which was measured. This effect remains, so far, unexplained.

Another instance in which the code predictions do not match the experimental results occurs just after the main shock arrives at Station 2. At this point in time (just after the arrival of the main shock) the measured pressure jumps to the level behind the shock and then oscillates about this value for nearly 2 milliseconds. This is again believed to be due to two-dimensional waves generated by interactions between the shock wave and the vent holes, which the code is unable to handle at present. These disturbances were apparently propagated into the driver as well, as indicated by the presence of similar oscillations occurring at Station 1 at the closed end of the driver.

These secondary disturbances do not seem to affect the overall shape of the pressure histories. The overall shape is predicted well by the quasi one-dimensional model.

A more detailed look at these data comparisons is presented in Figure 3-51 where the pressure history at Station 1 (closed end of driver) is shown with an expanded pressure scale. On this scale one can see the pressure oscillations which are set up in the unvented region of the duct. When a pressure wave hits the closed end of the driver, it reflects with the same sign. When a pressure wave passes from the unvented region into the vented region a pressure wave of opposite sign is reflected back into the unvented region of the duct in much the same manner as pressure waves are reflected from an open end of a duct. The result of these waves traveling back and forth in the driver is a "quarter-wave" oscillation. The name quarter-wave is derived from the fact that the length of the unvented region is nearly equal to one-quarter of the wave-length of the oscillation which is set up.

The ½" gages with the recessed mounts, used to obtain the data shown in Figures 3-51 and 3-52, tend to round-off any pressure spike which they see. This is the reason for the discrepancy between the code and test results near the minima of the pressure trace. These gages have been used mainly to detect the small pressure "quarter-wave" fluctuations after the pressure in the tube has returned to nearly ambient conditions.

This quarter-wave oscillation is clearly seen in both the experimental data and the calculated results in Figure 3-51. The start of the first positive pulse of the calculated quarter-wave oscillation begins slightly before that of the experiment for both values of C_D. The calculated period is somewhat shorter than that shown by the experimental data, but it is the same for both values of C_D used in obtaining the calculated results. The amplitude predicted by the calculations with $C_D = 0.9$ was closest to that measured in the experiments. The rate of decay predicted by the code is faster than that measured.

The data near the beginning of the vented section (Station 2) is shown with an expanded pressure scale in Figure 3-52. The arrival of the main

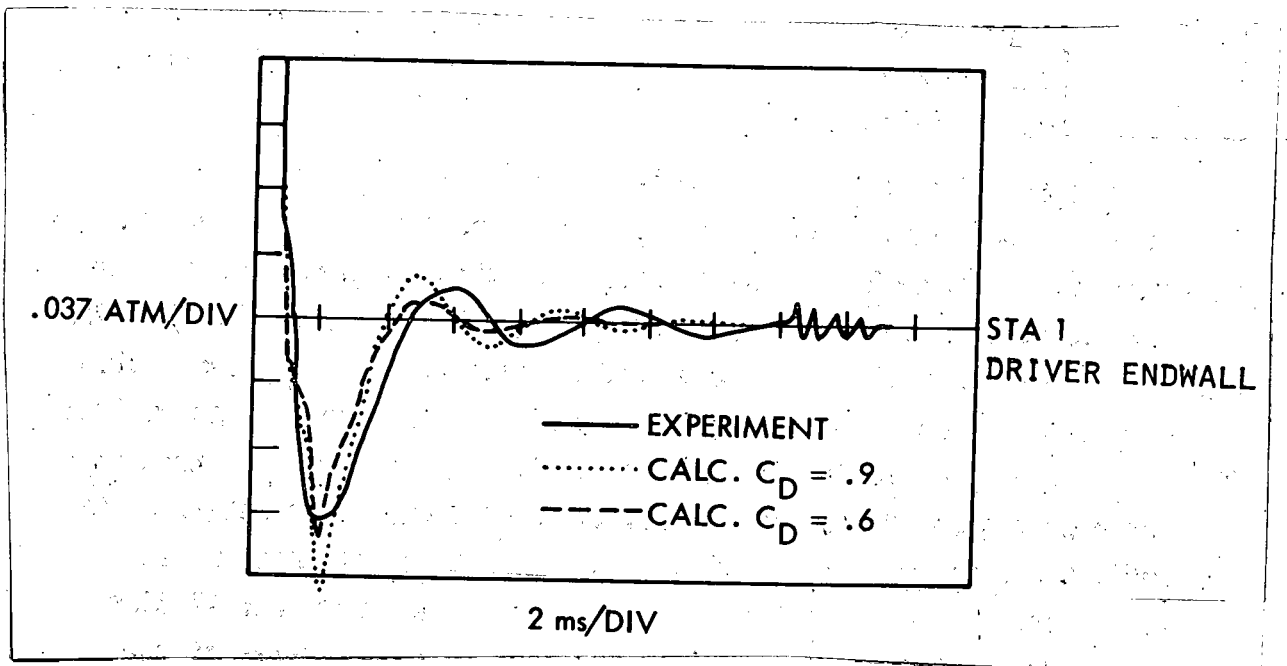

Figure 3-51. Vented Tube Test (7.2% Open) Closed-End Duct With 8" Driver and 7 psi Overpressure (Test Shown in Figure 3-14).

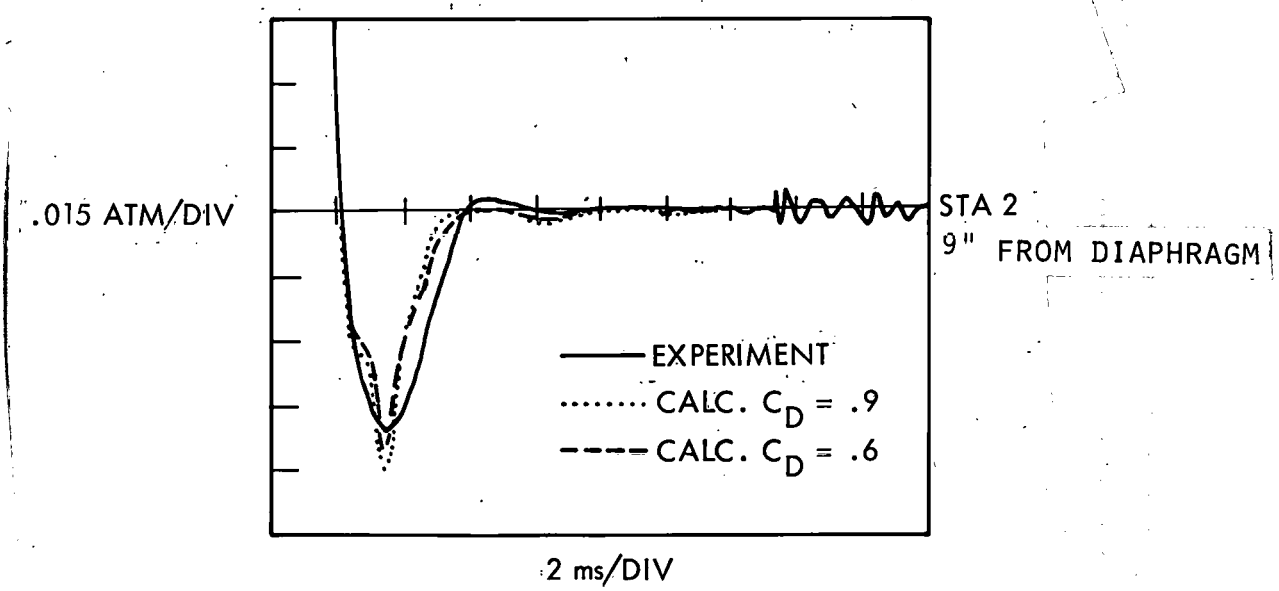

Figure 3-52. Vented Tube Test (7.2% Open) Closed-End Duct With 8" Driver and 7 psi Overpressure (Test Shown in Figure 3-14).

shock was deleted from Figure 3-52; only the process of recovery to ambient pressure is shown. The predicted pressure returned to ambient faster than the measured pressure did. The reason for this difference is not clear. Again, the experiments show the return of the main shock after being reflected from the closed end of the vented duct, but the computation does not.

24" Driver

Comparisons between code calculations and experimental measurements for the 24 inch driver were made for a driver overpressure of 6 psi. The driven section was 113 inches long and was vented on the top side beginning 2 inches from the diaphragm and continuing for the remaining length of the driven section. The venting produced a 7.2% open area in one wall. The end of the driven section farthest from the diaphragm was closed.

C_D was determined by using the potential flow model, Eq. (122), for both inflow and outflow. The calculations were carried out for 20 milliseconds from the diaphragm burst time.

Experimental pressure histories for the 6 psi overpressure cases were obtained from the upstream end of the driver (the closed end) and 9 inches downstream of the diaphragm in the vented section. These two pressure histories are shown in Figure 3-53 compared with the computed results obtained with the venting model. The overall behavior of the pressure is similar to that obtained for the 8 inch driver at the lower pressures; the main difference being that the duration of the pulses is longer with the 24 inch driver. We again have the presence of a late time disturbance at around 16 milliseconds. This disturbance is due to the return of the main shock after reflecting from the closed end of the vented duct. This reflected shock was not predicted earlier, when a constant C_D was used, nor was it predicted in the present calculations where a variable C_D model was used. Nor did the code predict many of the smaller oscillations that appear superimposed on the overall wave form. These small pressure oscillations are believed to be due to two-dimensional effects originating from the vents which are not currently modeled in the code. Aside from the high frequency oscillations the code results are in excellent agreement with the experimental measurement.

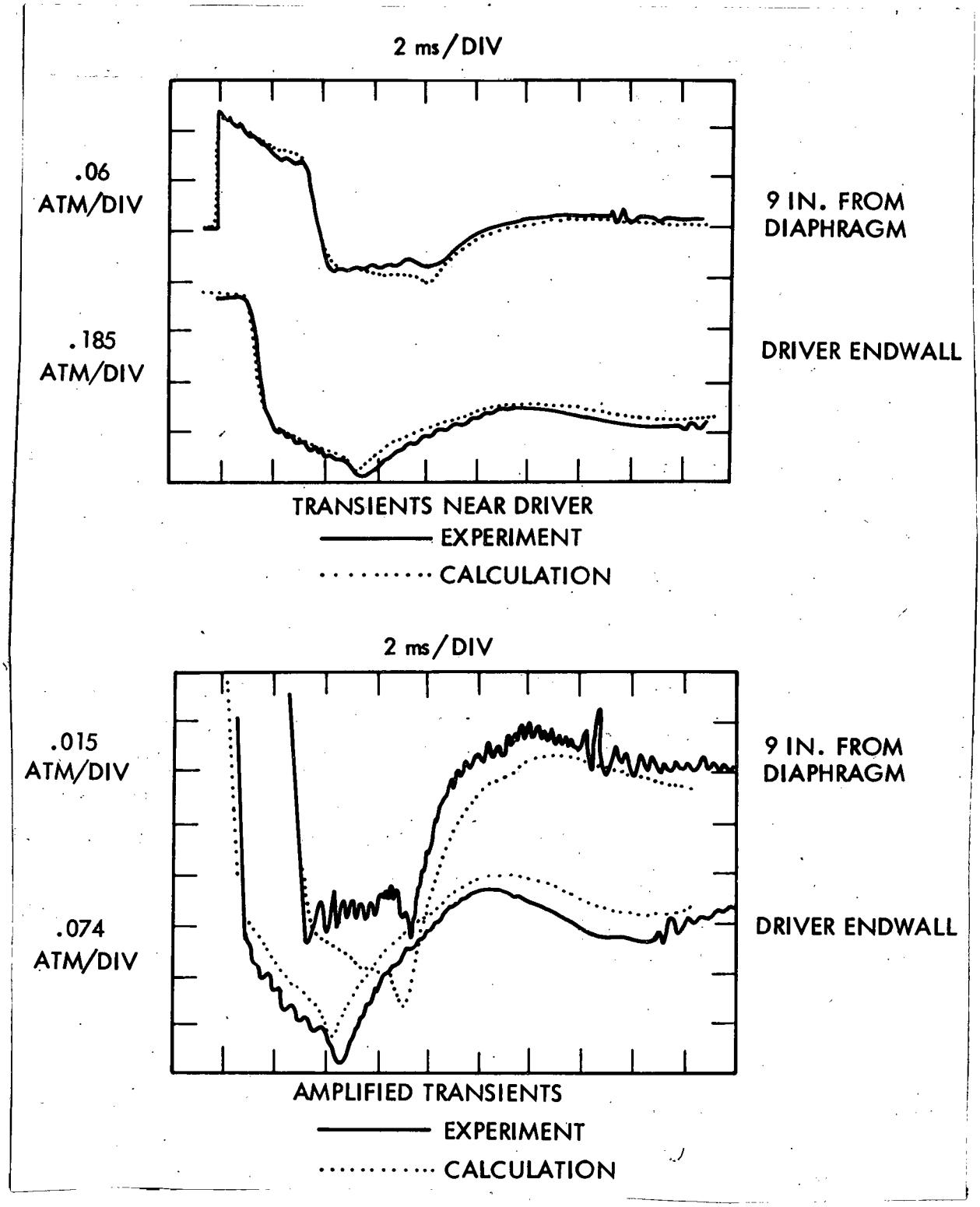

Figure 3-53. Pressure Histories for the Vented Duct (7.2% Open) With the 24" Driver at 6 psi Overpressure (Test Results Shown in Figure 3-17)

DOCUMENT NO.
PAGE NO.

We concluded from these comparisons that the quasi one-dimensional model gave reasonably good overall agreement with experiment and that using first a one-dimensional approach to the analysis was justified. In certain instances, two-dimensional phenomena were shown to have effects that could not be accounted for by the one-dimensional model. These effects are now better understood and will be accounted for in future modeling work. The venting model is adequate for predicting general trends, but it needs some improvement if the details of the return to ambient conditions are to be accurately predicted. There are some definite discrepancies between the code predictions and the test results. The two major ones are: (a) the code does not properly predict the nature of the low pressure oscillation (at the level of 10^{-2} to 10^{-3} atm) in and near the driver (which simulates the laser cavity), and (b) the pressure disturbances which show up at about 16 msec after the diaphragm burst are not predicted by the code. These disturbances can have a detrimental effect on the beam quality of the next pulse.

DOCUMENT NO.
PAGE NO.

3.3 PERFORMANCE CHARACTERISTICS OF VENTED DUCT SUPPRESSORS

3.3.1 Evaluation of Suppressor Performance

The method adopted for performance evaluation was predominantly experimental, with some test case comparisons with the FACTS Code. Basically, pressure transients were measured in the vented duct shock tube facility, simulating the single-pulse situation in a laser, without mean flow and driver gas heating. The data was quantified, stored and processed using improved instrumentation and a digital recorder with microprocessor and magnetic disk storage capability. The important common features of the pressure transients were evaluated from the data for a test matrix of operating and design parameter values (Tables 3-1 and 3-2). Also, data was obtained on the effect of an outer duct filled with porous materials.

In addition, the optical degradation of the medium caused by reversed vent-flow during the undershoot phase of the pressure transients was measured using double exposure holographic interferometry for the test case of Figure 3-26. At 6.7 msec, the average peak to peak fringeshift was .73 at .6948 μm wavelength, which corresponds to a refractive index variation of 2.8×10^{-6} and a relative density variation of about 10^{-2}. The scale length for the variations was approximately 2.5 cm, which corresponds to the spacing of the vents in the flow direction.

3.3.2 Pressure Transients

The decaying pressure oscillations were measured with modified PCB 106B piezoelectric transducers at locations shown in Figure 3-54. The outer duct with fiberglass packing was used only for a few final runs. Generally, the duct vented into the room for all other runs. Also shown are the typical wave interactions depicted on a X-t wave diagram. The diaphragm burst initiates a shock wave S traveling into the vented duct and an expansion wave E into the driver. The contact surface is the material boundary between the driver gas and the driven gas. Its trajectory is shown dotted. A typical interaction with a vent weakens the shockwave and reflects a weak expansion wave e. The trajectory of a fluid particle at the vent is shown dotted. All the weak expansion waves further interact with the vents generating a complex

situation with many more smaller waves which are not shown. The expansion E reflects from the end wall of the driver and follows the shock wave down the vented duct. Its interaction with the vented region reflects the small compression waves C. The expansion waves and the compression waves reflect back and forth between the driver end wall and the beginning of the vented region in a manner similar to an organpipe oscillation. This situation is further complicated by the various wave reflections from the contact surface, which is a discontinuity of density and temperature, but in reality is a diffuse, turbulent region of inhomogeneous gas.

The different waves S, E, e and C and their occurrence at the three pressure sensor locations correlates well with the observed pressure variations at these locations, as seen in Figure 3-55. Basically, the shockwave and the reflected expansion form a 'top hat' pressure pulse, which travels down the vented duct and decays. The small reflections from the pulse interacting with the vents produce pressure undulations of only the driver (or the laser cavity) which then decay due to the reciprocating dissipative flow through the vents near the driver. It is interesting to note that e is the major wave component responsible for the pressure undershoot causing the reversed ventflow.

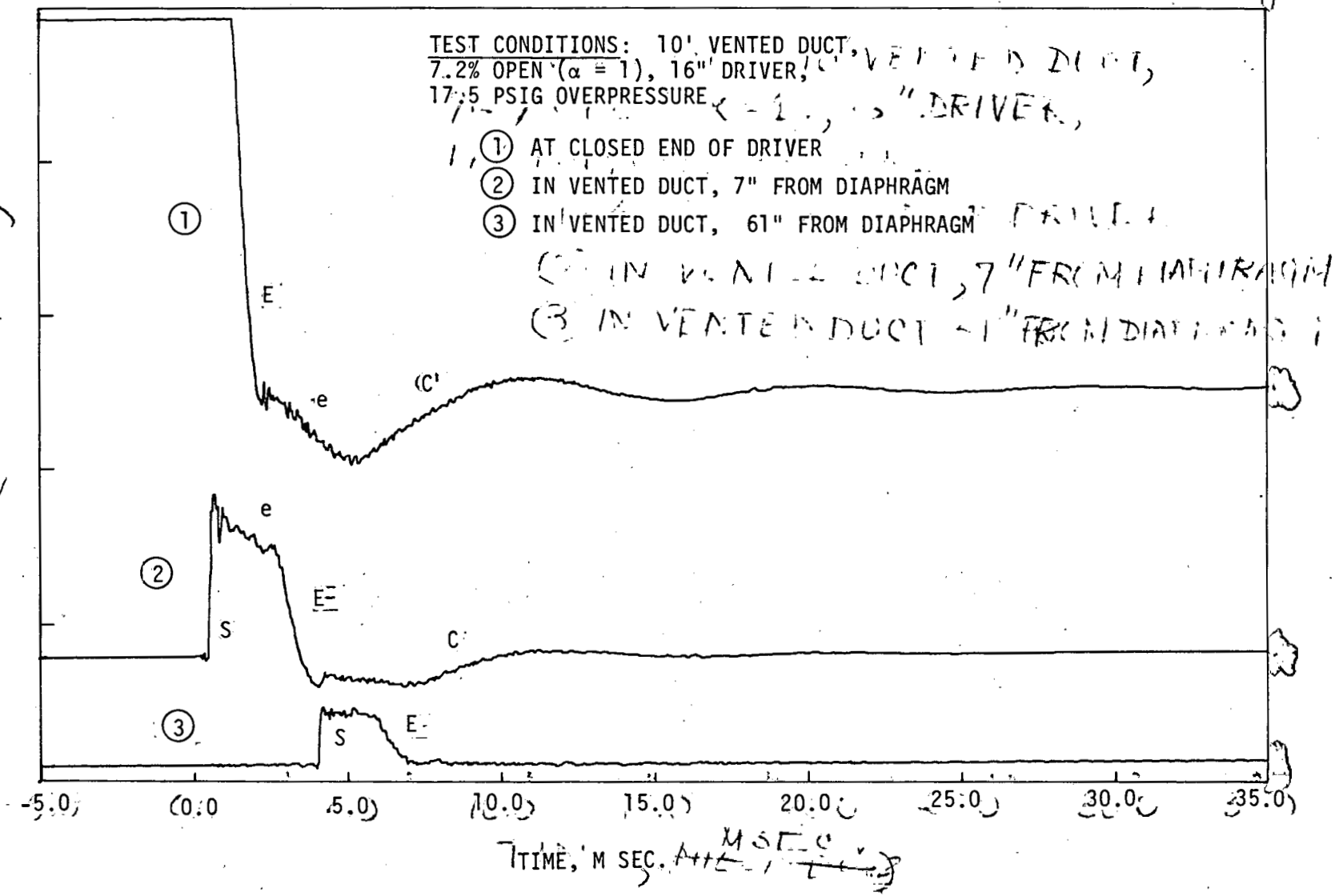

Figure 3-55. DIGITALLY RECORDED PRESSURE WAVE TRANSIENTS

3.3.3 Comparisons of Measurements and Computer Predictions

The three pressure traces of Figure 3-55 are shown again in Figure 3-56 on more suitable scales for comparison with the results of the FACTS code, which are shown dotted where distinguishable. In general, the agreement on this scale is excellent. It should be emphasized that there is no parameter matching involved. However the real test of the prediction scheme is its accuracy at predicting the residual weak disturbances after a long time. For this purpose Figures 3-57, 3-58 and 3-59 show such comparisons on a magnified scale for the residual driver oscillation observed at location 1 , respectively for two driver overpressures, two driver lengths and two vent fractions.

Although the comparisons on fine scale appear to support the general agreement between the experiment and the computations, several discrepancies become noticable. The agreement is only approximate for the amplitude, the period and the phase of the residual organpipe oscillation of the driver. The rates of decay of the oscillations also differ between the experiments and the computations, and the agreement becomes poorer as the oscillation amplitudes become smaller for larger times and must then be compared on even finer scales.

At very large times some different phenomena appear to dominate the acoustic perturbations as mentioned before in Section 3.1. The experiments show wideband high frequency fluctuations that seem rather random. The computationsshow no such fluctuations. These fluctuations are probably caused by multidimensional effects such as cross modes of the duct which the one dimensional code does not model. The amplitudes of such oscillation, however, can well exceed the acceptable pressure levels, as seen from the example in Figure 3-60. Here, for comparison, the noise level of the sensor is also shown. This was obtained by preventing the pressure fluctuations from reaching the sensor with a sealed cap. Also shown are the Fourier spectra of the two signature to emphasize their wideband character.

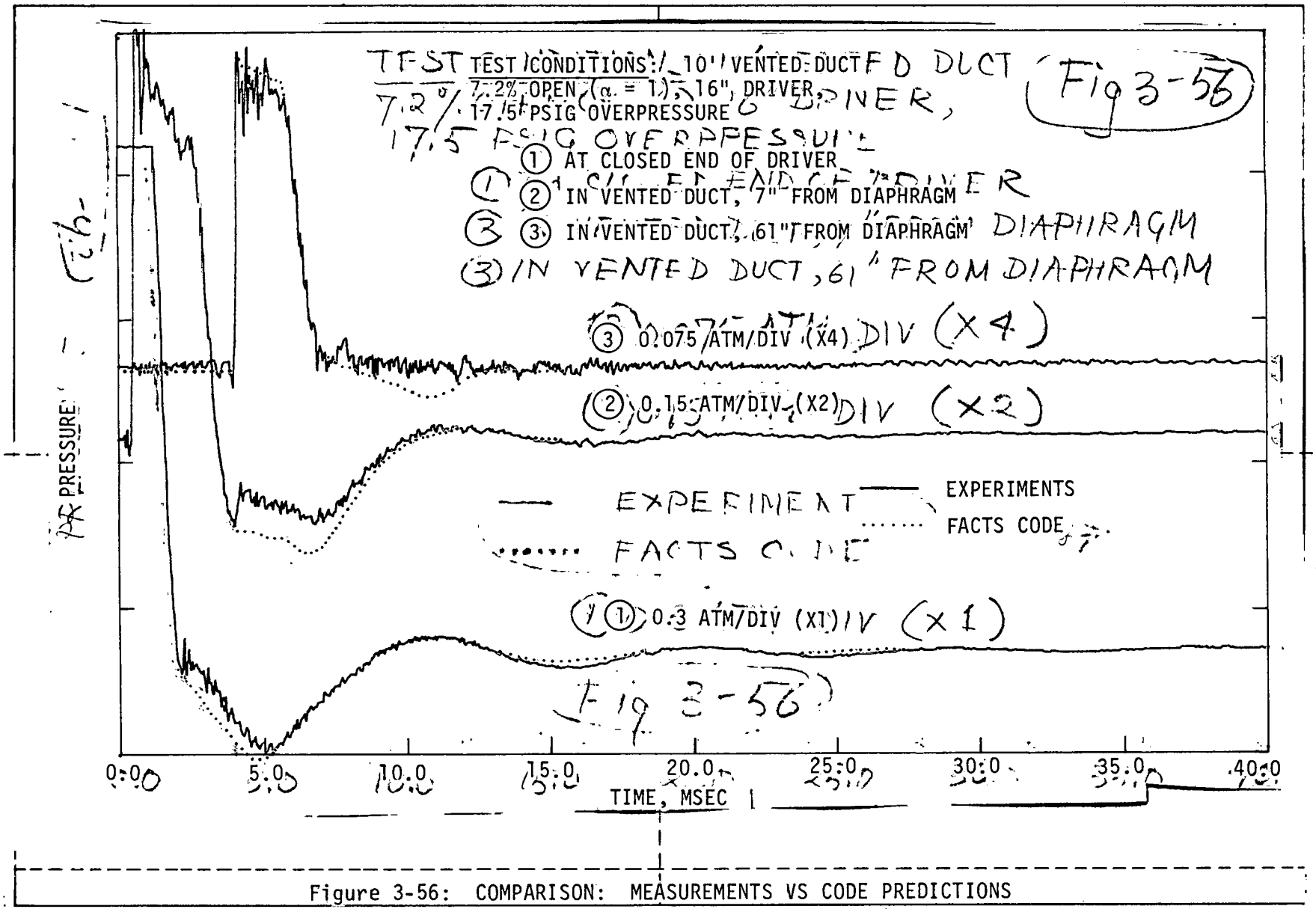

Figure 3-56: COMPARISON: MEASUREMENTS VS CODE PREDICTIONS

Figure 3-57. COMPARISON ON FINE SCALE: TWO OVERPRESSURES

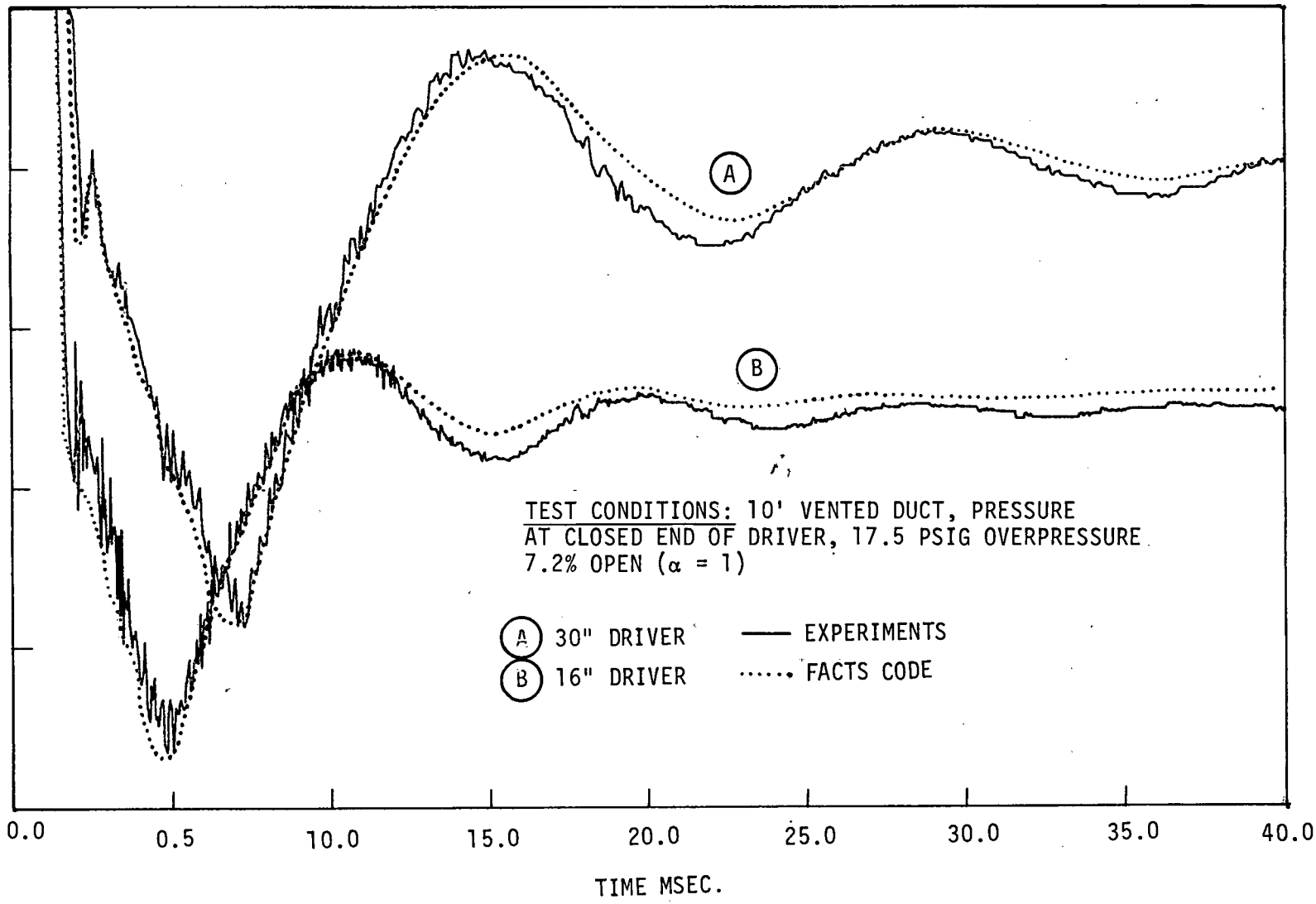

Figure 3-58. COMPARISON OF FINE SCALE: TWO DRIVERLENGTHS

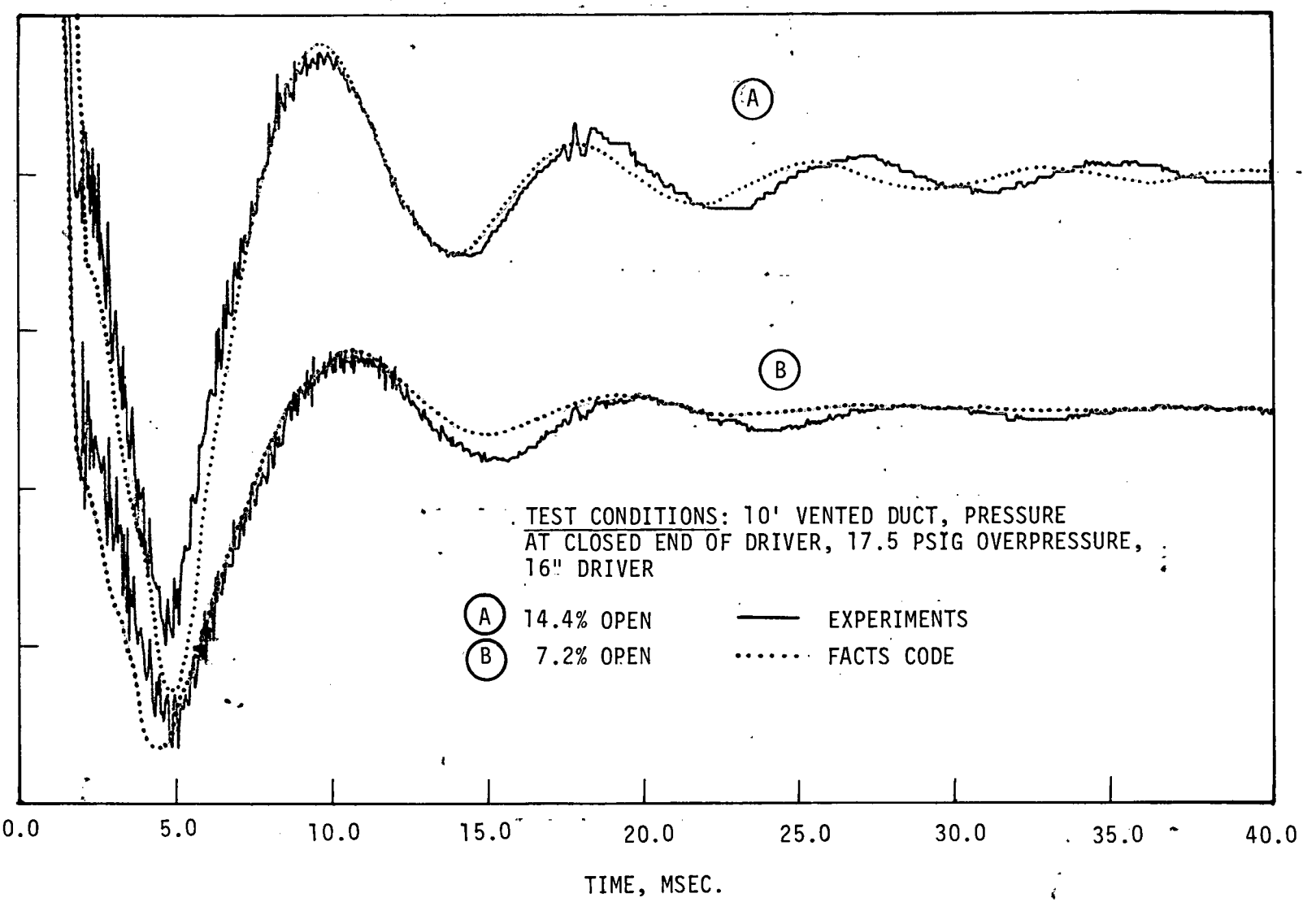

Figure 3-59. COMPARISON ON FINE SCALE: TWO VENT FRACTIONS

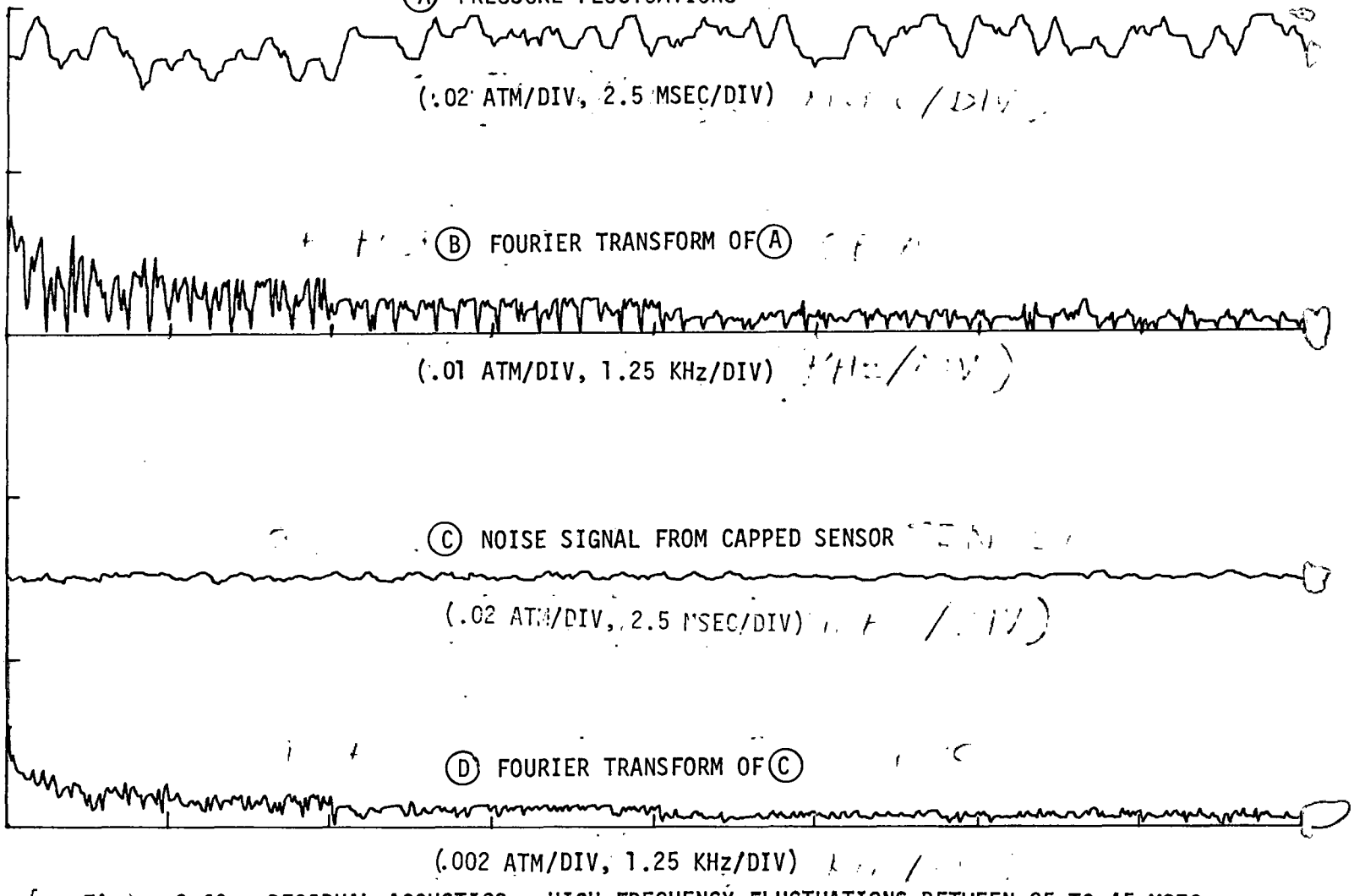

Figure 3-60. RESIDUAL ACOUSTICS: HIGH FREQUENCY FLUCTUATIONS BETWEEN 25 TO 45 MSEC
TEST CONDITIONS: 10' VENTED DUCT, 7.2% OPEN (α = 1), 16" DRIVER
82.5 PSIG OVERPRESSURE, SIGNAL AT 7" FROM DIAPHRAGM IN VENTED DUCT.

3.3.4 Performance Characteristics and Operating Parameters

It is evident that the performance of a suppressor is primarily characterized by the organpipe (or quarter wave) oscillation of the driver or the laser cavity, with its amplitude and its subsequent decay. For long times, the high frequency fluctuations become important. We examine the behavior of the quarter wave oscillation in this section for different operating conditions of a given vented duct suppressor, and in the next section, for different suppressors. The test matrix is shown in Tables 3-1 and 3-2.

In general most of the pressure waves are effectively attenuated by the vented duct, down to about acoustic levels (10^{-3} Atm = 134 dB) in approximately 50 ms. The decay of the initial perturbation is characterized by pressure oscillations of the driver, similar to organ pipe oscillations (quarter-wave mode) at a low frequency (1000 Hz or more), which are initially smaller but persist much longer, and become the dominant component of the residual fluctuations in the 50 ms time scale.

~~The low frequency ringing is measured in terms of initial amplitude,~~ frequency and decay rate, based on the pressure measurements at the closed end of the driver. The initial amplitude is specified here by the peak values of the first undershoot, and the following over-swing of pressure, as it settles to atmospheric pressure. These are scaled relative to the driver overpressure for several cases (Figure 3-61). For the high overpressures, the total pressure perturbation is seen to be suppressed by two orders of magnitude within the first cycle! At low overpressures, this is about one order of magnitude. This emphasizes the nonlinear nature of the vents and their effect on pressure waves, which produce enormous attenuation at large amplitudes, but is far less effective for the weak waves. It is important to note that the absolute level of pressure fluctuation reduces to about 1/20 atm during the first cycle for most cases, irrespective of the driver overpressure. Clearly the effectiveness of the vented tube is excellent for pressure perturbations larger than 1/20 atm level. Also, it should be noticed that the shorter drivers generally show more attenuation during the first period. If there is a driver length which causes minimum undershoot and over-swing for this level of venting,

L" \ ΔP atm	.5		1.2	2.7	5.5
8"				•	
16"			X	X	
30"			X	X	

X Indicates FACTS Code comparison cases

• Indicates addition tests with fiber filled outer duct

Table 3-1. OPERATING CONDITIONS FOR 7.2% VENTED SUPPRESSOR

Venting	14.4%			4.8%	
L" \ ΔP atm	1.2		2.7	1.2	2.7
16"	X		X		
30"	X		X		

X Indicates FACTS Code comparison cases

Table 3-2. OPERATING CONDITIONS FOR OTHER SUPPRESSORS

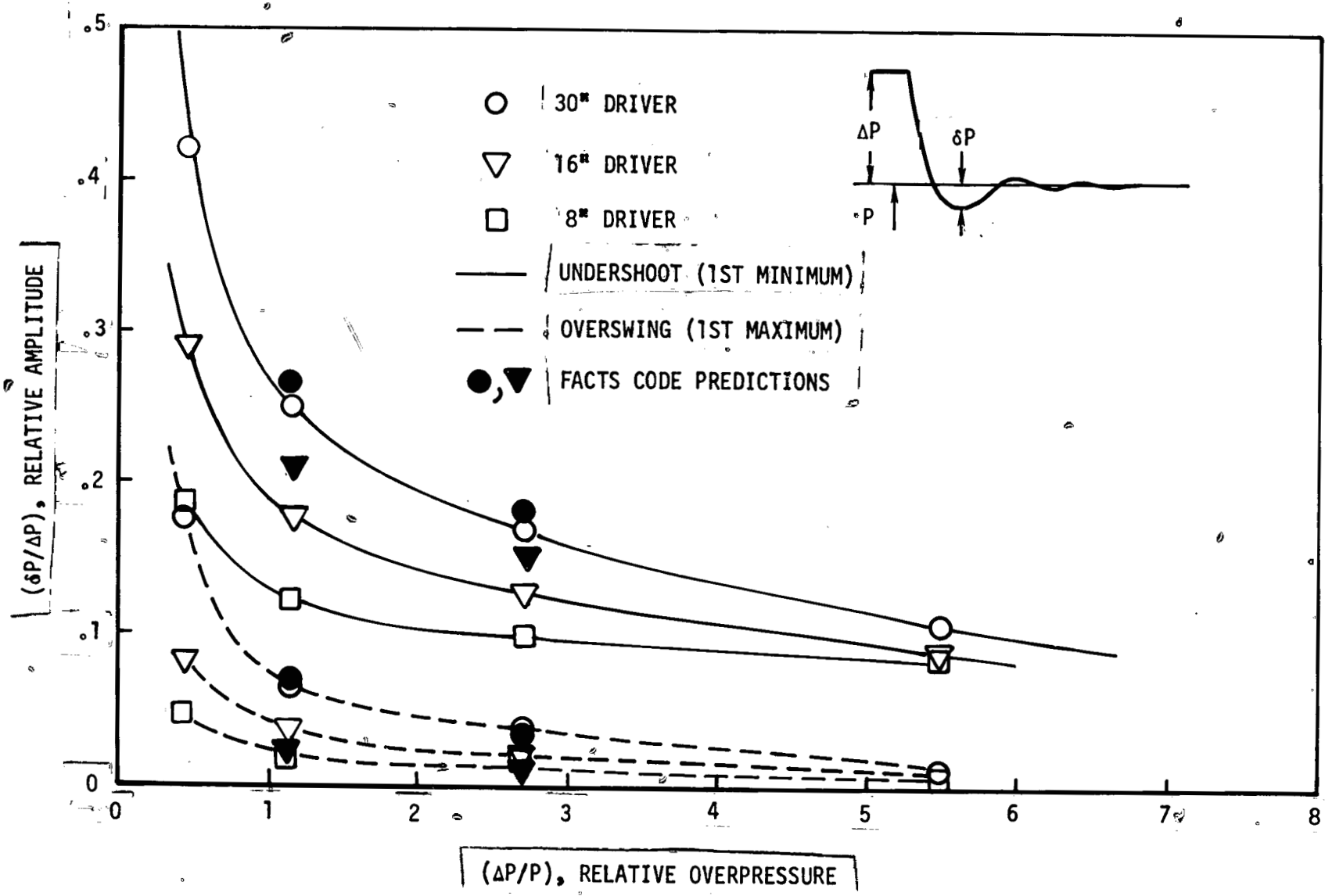

Figure 3-61 INITIAL AMPLITUDES OF QUARTER WAVE OSCILLATION MEASURED AT CLOSED END OF DRIVER

DOCUMENT NO.
PAGE NO.

it is probably shorter than those used here. The computer results marked by solid symbols show the same trends for this initial period.

After the first cycle, in most cases the ringing continues for several cycles at amplitudes lower than 1/20 atm. The frequency and the decay rate of this oscillation are difficult to determine accurately, partly due to the high frequency fluctuations. The other inaccuracy occurs because with increasing time the frequency increases slightly where as the decay rate decreases. The frequency and decay rate averaged over 2-3 cycles are given below for the several cases.

The period of oscillation is scaled with the period of the 1/4 wave mode of the driver (Figure 3-62). The oscillation clearly has a lower frequency in all cases except one. (In the exceptional case, it is found that the 1/4 wave mode is so strongly suppressed that it is unidentifiable; a 3/4 wave mode is observed.) This may be because the vents do not represent a completely open end, and the effective mode of the pressure oscillation occurs farther out into the vented duct. This is consistent with the fact that the ringing is observable in several cases as far out as two duct widths away from the diaphragm station. The frequency of the oscillation decreases slightly for the higher overpressures. This may be attributed to the lowered sound speed in the isentropically expanded driver gas. The temperature gradients in the duct near the driver must also significantly influence the oscillation. It seems likely that the ringing is in part similar also to Helmholtz oscillation of the driver-vent system where the inertia of the fluid in the vents cannot be neglected. This effect is not modeled in the computations which show almost no variation in the scaled period with the driver length.

Decay rate of the oscillation is the ratio of heights of two successive peaks measured from the included minimum, or vice versa (Figure 3-63). In general decay rates for the high overpressures and shorter drivers are higher. The different temperature gradients produced in the vented duct near the driver are probably responsible for the higher decay rate for larger overpressures, in view of the fact that the amplitudes of oscillation are quite comparable for all cases during this phase. Also the decay rates are generally higher for shorter drivers which seems consistent with the trend in the initial amplitude. Thus, small relative undershoots and

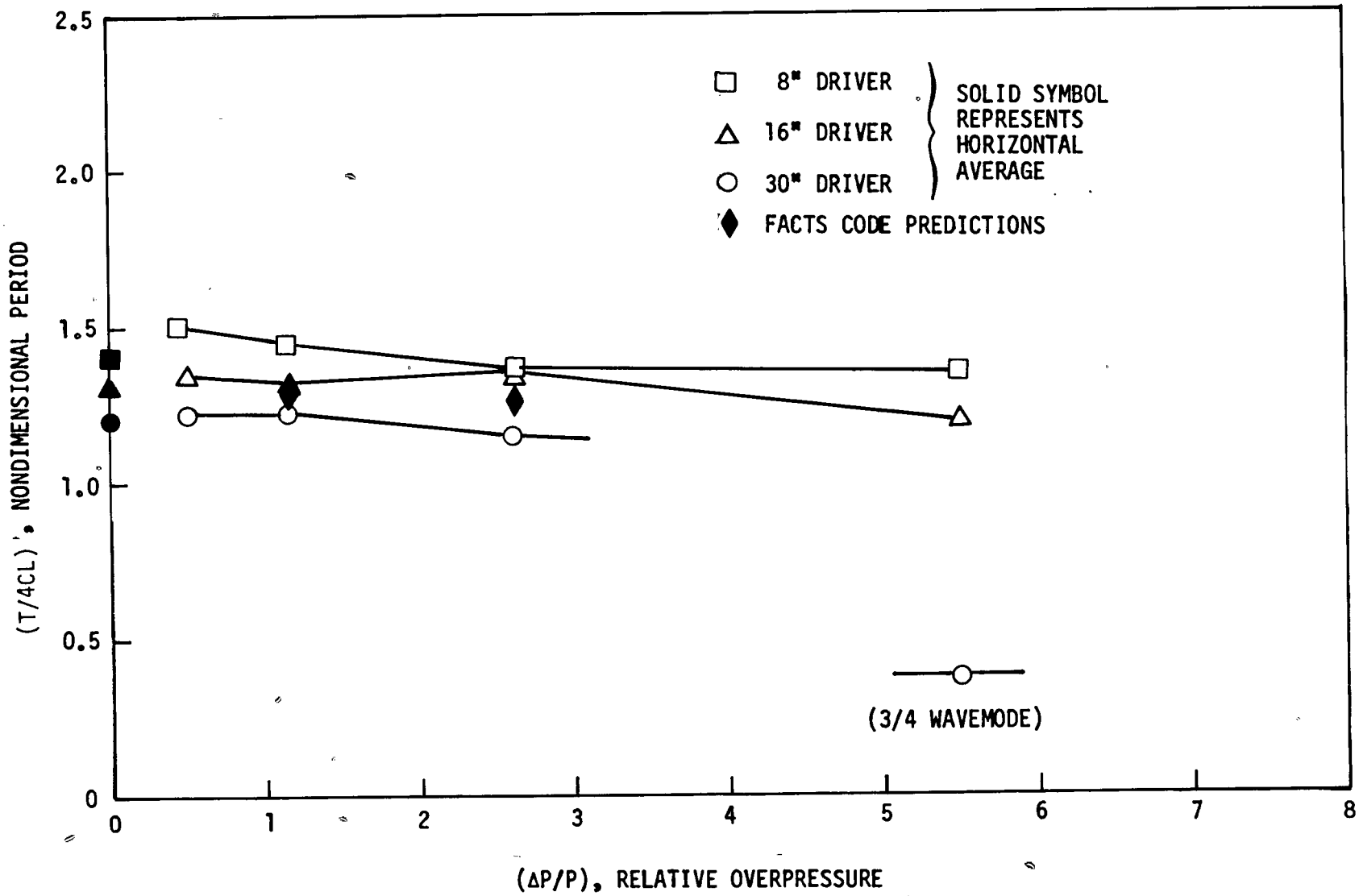

Figure 3-62 : QUARTER WAVE OSCILLATION OF DRIVER AVERAGE TIME PERIODS MEASURED AT CLOSED END OF DRIVER

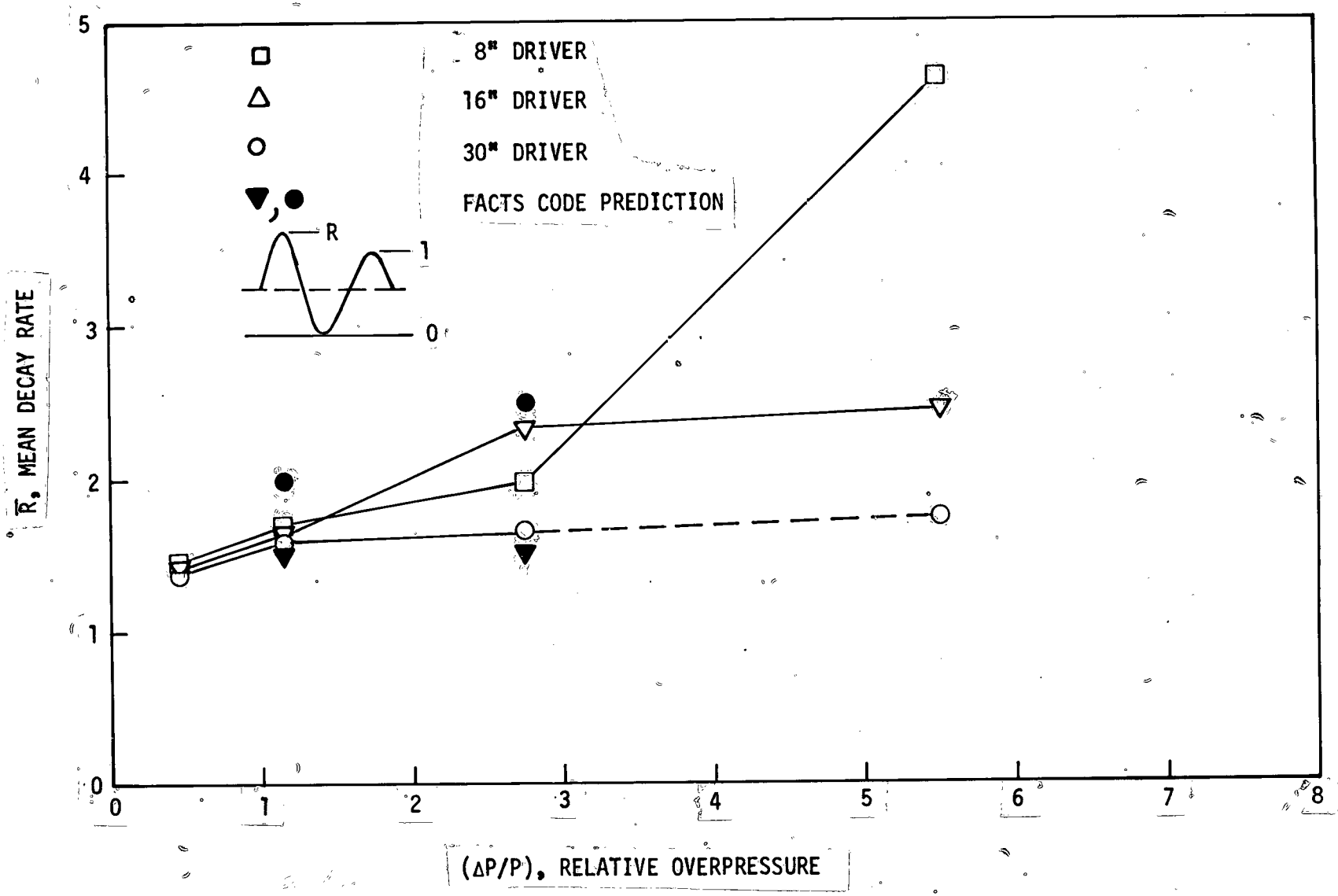

Figure 3-63. QUARTER WAVE OSCILLATION OF DRIVER
AVERAGE DECAY RATE MEASURED AT CLOSED END OF DRIVER

over-swings correlate with high decay rates. The computer results shown with solid symbols exhibit a contrary trend in the decay rate. This is a major sign that the ventflow model is perhaps inaccurate for the long term oscillations, and their decay rate is rather sensitive to the inaccuracy.

3.3.5 Performance Characteristics and Suppressor Parameters

The direct effect of change in the vent area is observed in the low frequency quarter wave oscillation, in terms of the changes in the initial amplitude (undershoot and overswing), the frequency and the decay rate. These are shown in Figures 3-64 through 3-66, respecitvely.

The basic trends in the relative initial amplitudes (i.e., increase with decreasing overpressure and longer driver length) persist for other vent fractions. In addition, it is observed that less venting produces smaller initial amplitudes. This is understandable, since the ringing is minimal in an unvented straight duct, and since the expansion waves returned from the shock-vent interactions are primarily responsible for the pressure undershoot. The more the venting, the stronger the returning expansion wave and the larger the undershoot and subsequent oscillation. This also explains that longer drivers allow longer time between the shock and the expansion, thus, more vent interactions can occur to give a bigger undershoot. There is a major difference, however. With reduced venting, the shock wave attenuates slower and its reflection from the far end may still be of significant amplitude. There is one exceptional case where the returned shock caused abnormally high overswing (Figure 3-64).

The time periods of the quarter wave oscillation show an increase with decreased venting. This is consistent with the idea that the vents represent only a partially open end and therefore the effective pressure node must occur some distance into the vented duct. The less the venting, the larger this distance. (Note: for a completely open ended tube, this distance is approximately 3/4 the tube radius.)

The trends in the decay rate of the quarter wave oscillation are more irregular, although there is no doubt that the decay rate is larger for less venting. At comparable amplitude of oscillation, less vent area would require higher flow velocities and therefore would cause more dissipation giving a higher decay rate.

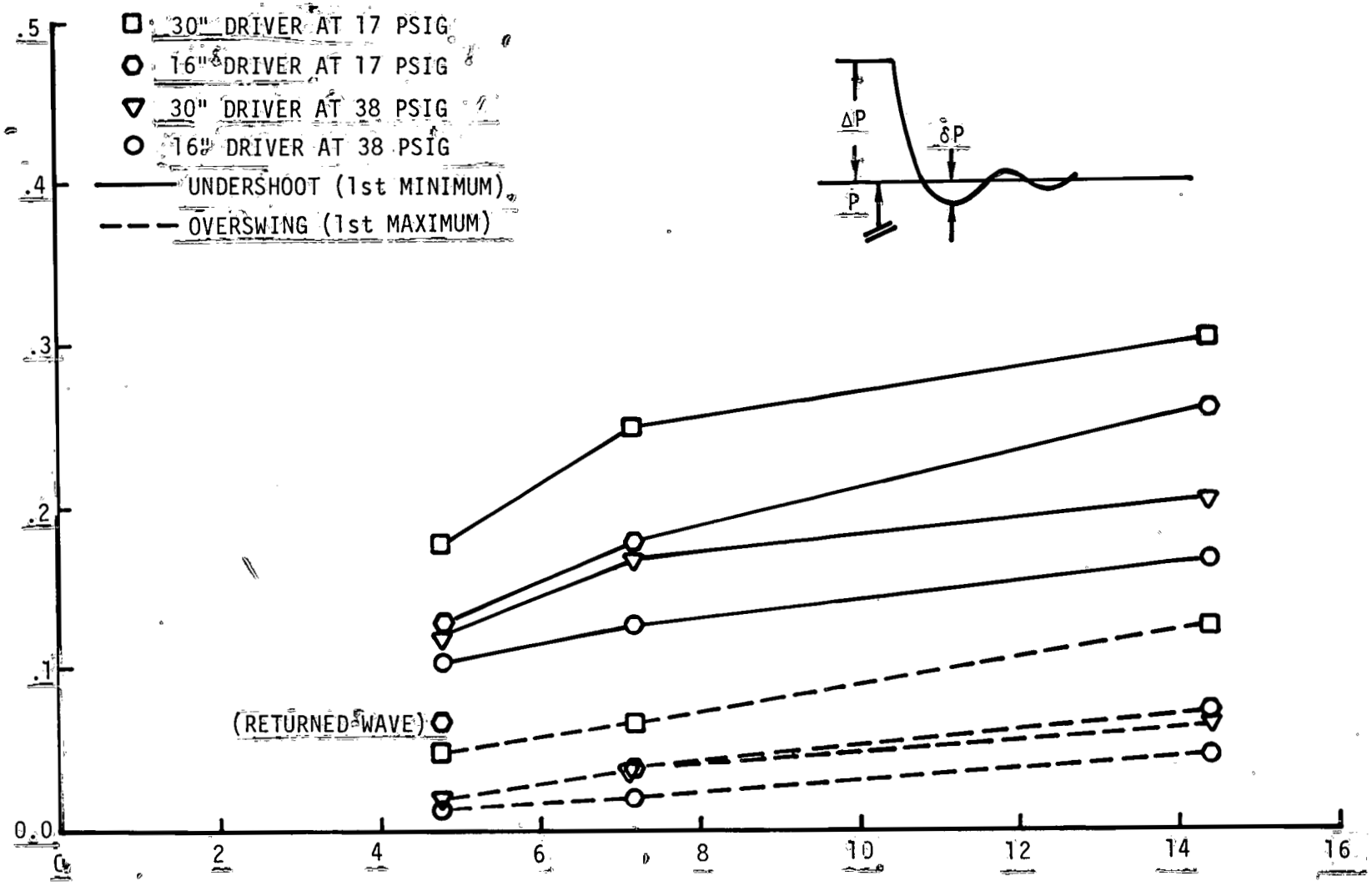

Figure 3-64 INITIAL AMPLITUDES OF QUARTER WAVE OSCILLATION MEASURED AT CLOSED END OF DRIVER

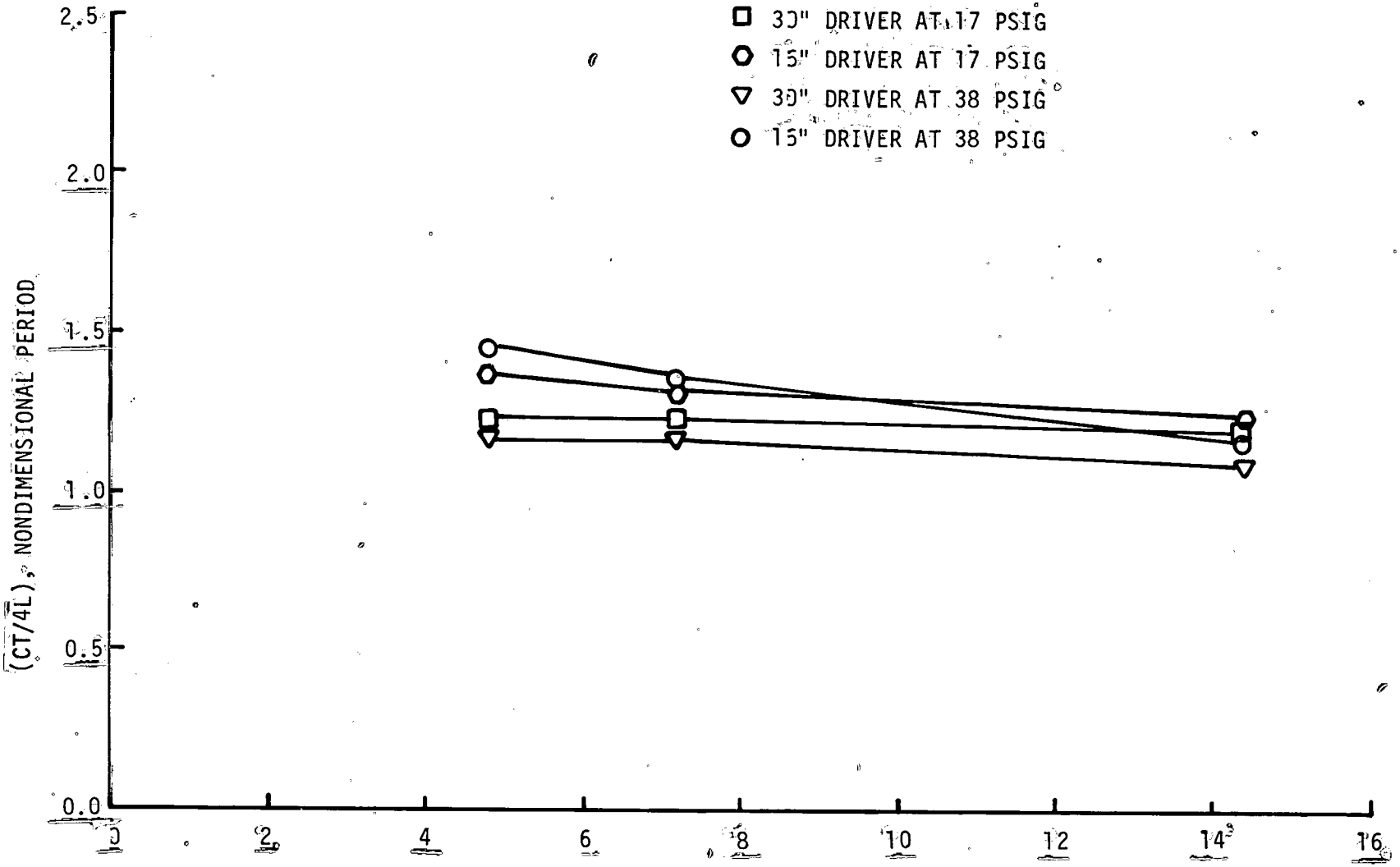

Figure 3-65 QUARTER WAVE OSCILLATION OF DRIVER
AVERAGE TIME PERIODS MEASURED AT CLOSED END OF DRIVER

THIS PAGE

WAS INTENTIONALLY

LEFT BLANK

Thus lower vent area fraction is advantageous in two ways: The initial amplitude of the quarter wave oscillation is lower and its decay rate is higher. The disadvantages is that the shock attenuates slower and thus longer attenuators are required to prevent the return of a substantial reflection from the far end. It should be noticed that the vents closest to the driver contribute mainly to the advantages, where as vents far away can attenuate the wave equally effectively. Perhaps the total performance can be improved with variable venting along the attenuator.

3.3.6 Fiber-Filled Outer Ducts and Long Term Oscillations

It is clear that vents lose their effectiveness for attenuating waves as the waves weaken, basically because they represent a nonlinear device, flow resistence which diminishes with decreasing amplitudes and velocities. Thus the quarter wave oscillation decays slowly, and even after the quarter wave ringing has subsided, high frequency oscillations persist. These residual oscillations were measured in the 30-50 ms interval. Their Fourier spectra show wide band noise with a few broad or indistinct peaks. No clear pattern of recurring frequencies could be found among the different cases. Only a R.M.S. amplitude was recorded (Figure 3-67). This was obtained from the difference between the recorded pressure signal and its smoothed version. Two successive applications of 14 point averaging were used for this purpose (sample interval = 50 ms). The maximum noise from stress waves affecting the pressure gages was also measured similarly, for each overpressure, after mounting a sealed cap over the pressure sensitive surface of the gage nearest to the diaphragm station. Figure 3-67 presents the r.m.s. measurements in comparison to the noise values. There is adequate evidence that acoustic fluctuations at frequencies higher than 1 KHz exist at 10^{-3} atm level betewen 30 to 50 ms.

A porous material can be more effective than vents at further attenuation of the weakened waves. Figure 3-68 shows an example of this behavior by comparing a duct vented to the atmosphere and a duct vented into an outer duct packed with fiberglass (see Figure 3-54). The organpipe oscillation is significantly lower, partly due to the influence of the enclosure and partly due to the increase in ventflow resistence because of the porous material, expecially at the low amplitudes.

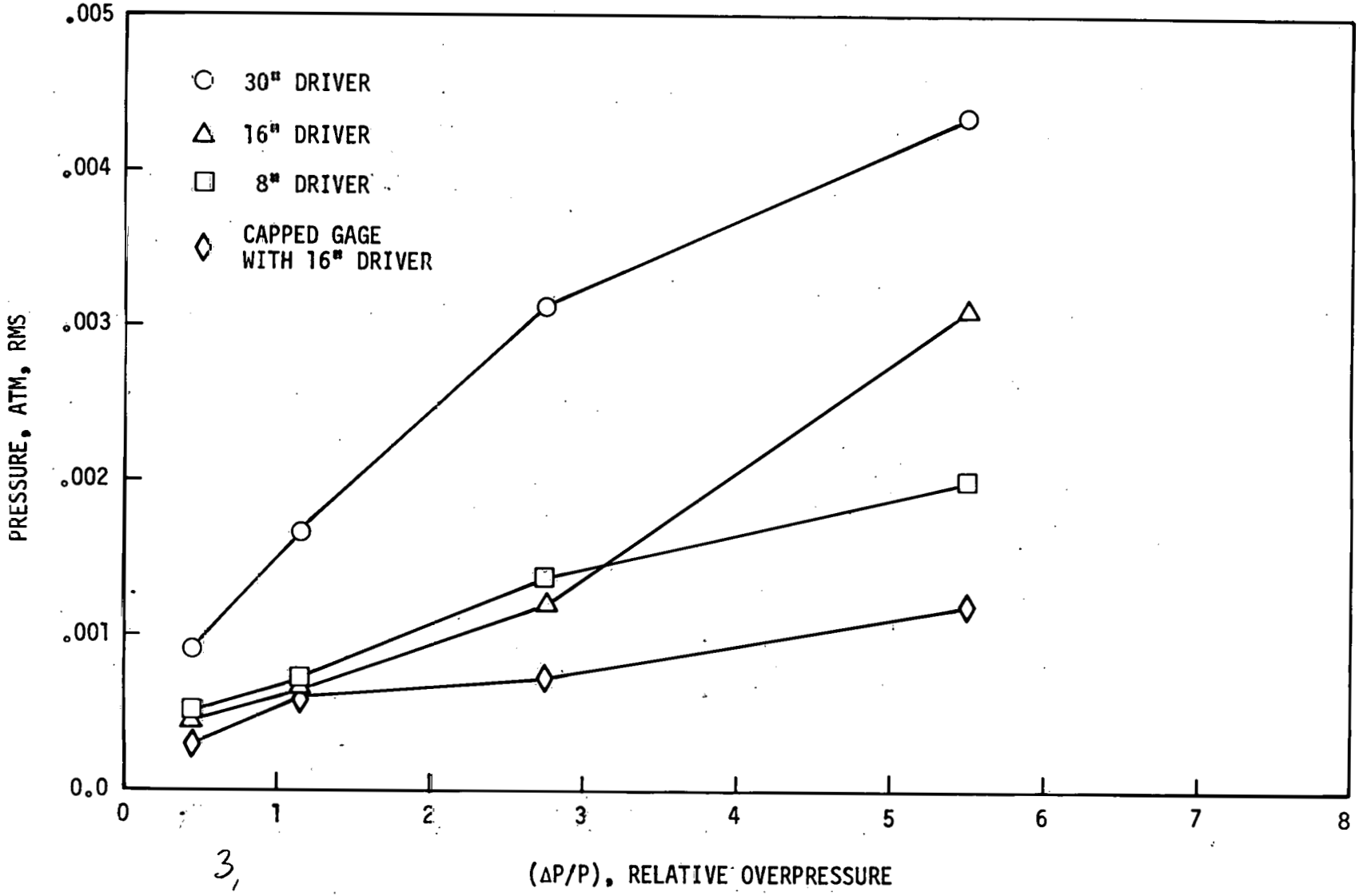

Figure 3-67 RESIDUAL ACOUSTIC FLUCTUATIONS
HIGH FREQUENCIES ABOVE KHz, BETWEEN 25 to 45 MSEC
MEASURED AT 7" FROM DIAPHRAGM IN VENTED DUCT

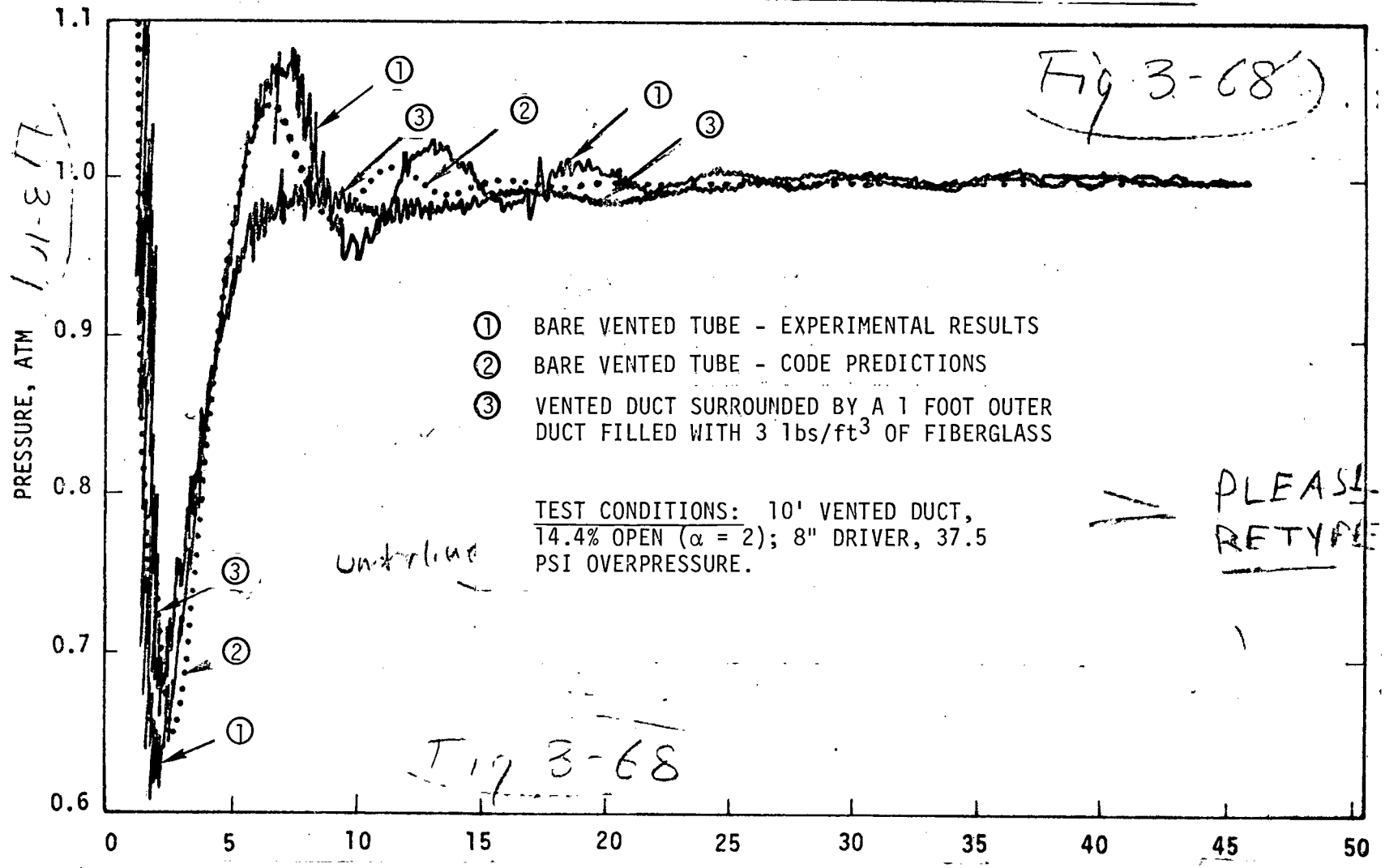

Figure 3-68. TIME AFTER DIAPHRAGM BURST, MSEC
EFFECT OF OUTER DUCT AND FIBERGLASS PACKING

The computations have not modeled these effects so far. It should be noted that the difference between the prediction and the measurement even in the case of the bare vented duct seems substantial in Figure 3-68. This may be because of nonideal behavior of the diaphragm during bursting and subsequent petal motion. These effects are found to have noticable influence when the driver length becomes comparable to the duct cross section.

The porous material also shows signficant attenuation of the high frequency residual oscillations (Figure 3-69). It seems likely that the high frequency fluctuations involve the vents which begin to behave more as inertance than resistance to the flow. This implies transverse modes similar to Helmholtz oscillation, which then would be substantially attenuated by the increase in vent resistance due to the porous material.

Figure 3-69 also shows the wild behavior of pressure fluctuations in the presence of the outer duct without the porous material. Especially large are the fluctuations on a 10 ms timescale. These are oscillation modes of the outer duct. These modes are observable also in the presence of the porous material, but they are damped down to acceptable amplitudes by the viscous dissipation.

3.3.7 Conclusions

The performance of vented duct acoustic suppressors was evaluated in this investigation, both by shock tube simulation and FACTS Code modeling. The basic performance of such suppressors may be qualitatively summarized as follows:

- Most pressure waves are effectively attenuated by the bare vented duct; below .1 atm in about 10 ms, and down to acoustic levels (10^{-3} atm $\simeq$ 134 dB) in approximately 30 ms.
- The initial rapid decay of pressure waves leads into organ-pipe oscillation of the driving cavity (after 10 ms, approximately at 100 Hz below .1 atm), which decays at slightly slower rates.
- High frequency fluctuations (>KHz) are initially smaller, but persist much longer and become the dominant component after about 30 ms at acoustic levels (10^{-3} atm).
- This performance is satisfactory for potential lasers driving inertial confinement fusion reactors (e.g., CO_2 laser), and can be substantially improved further by using an outer duct packed with a porous material.

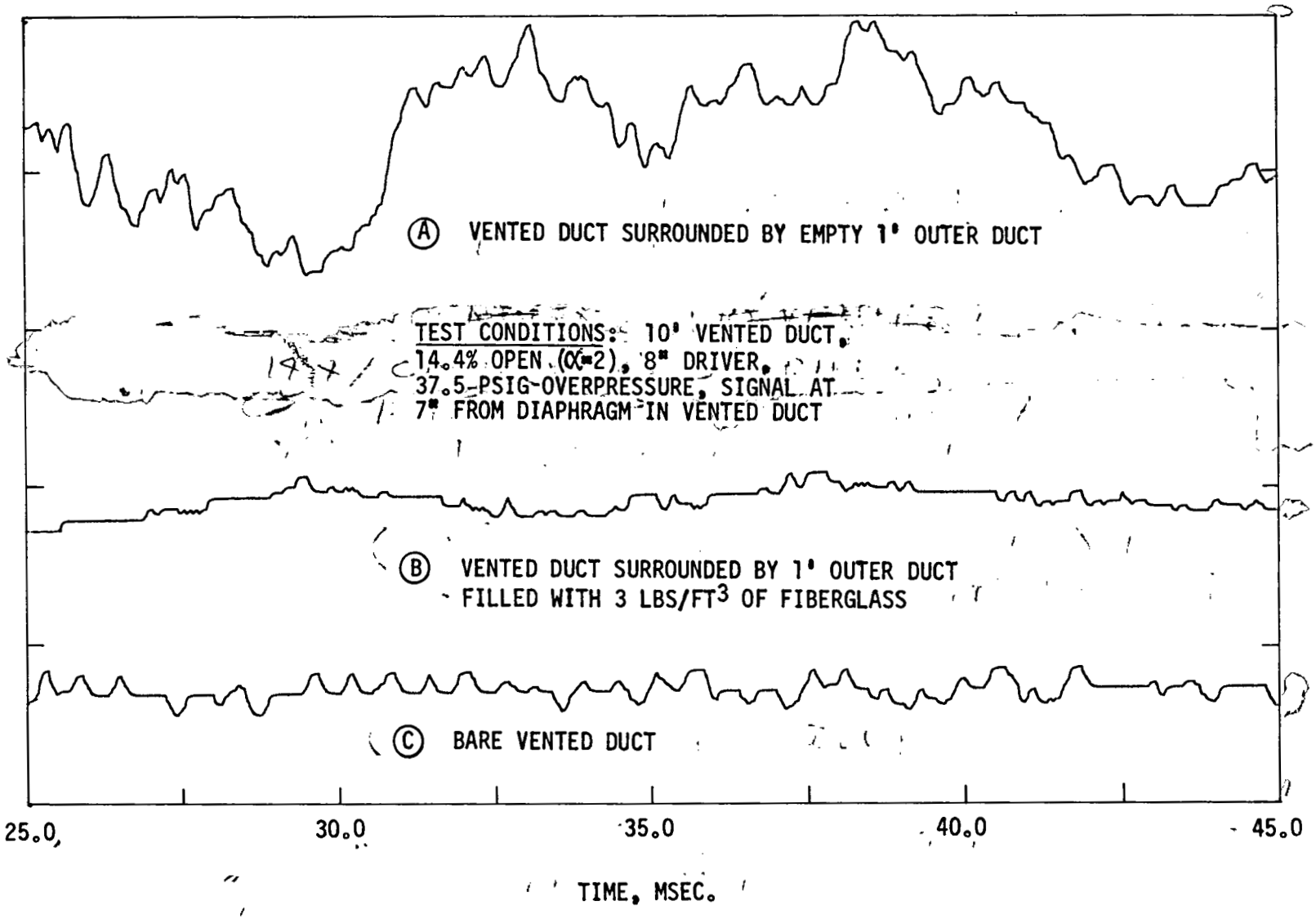

Figure 3-69 . RESIDUAL ACOUSTICS WITH OUTER DUCT AND FIBERGLASS PACKING PRESSURE FLUCTUATIONS AT LATE TIMES

REFERENCES

(Listed by Section)

2-1 G. W. Sutton, "Effect of Turbulent Fluctuations in an Optically Active Fluid Medium," AIAA J., Vol. 7, No. 9, Sept. 1969.

2-2 J. Maniscalo, et al, Civilian Applications of Laser Fusion, Lawrence Livermore Laboratory, UCRL-52343, Nov. 17, 1977.

2-3 J. Shwartz, et al, Fluid Mechanics of Fusion Lasers, Part 1, TRW Inc., 31775-6002-RU-00, April 1978.

2-4 A. Shapiro, The Dynamics and Thermodynamics of Compressible Fluid Flow, Vol. 1, Ronald Press, New York, 1953.

2-5 A. Pope, Wind-Tunnel Testing, John Wiley & Sons, Inc., New York, 1947, Second Edition.

2-6 E. R. Pugh, et al, "Optical Quality of Pulsed Electron-Beam Sustained Lasers," Appl. Optics, Vol. 13, p. 2512, Nov. 1974.

2-7 B. N. Srivastava, C. J. Knight and O. Zappa, "Acoustic Suppression in a Pulsed Laser System," Reprint No. 79-0209, AIAA 17th Aerospace Sciences Meeting, New Orleans, La., Jan. 1979.

2-8 G. L. McAllister, R. E. Equchi and V. G. Dragoo, "Effects of Acoustic Waves on Beam Quality of High Energy CO Lasers," Appl. Optics, Vol. 14, p. 1290, 1975.

2-9 F. E. C. Culick, P. J. Shen and W. S. Griffin, "Acoustic Waves and Heating Due to Molecular Energy Transfer in an Electric Discharge CO Laser," IEEE JQM, Vol. QE-12, No. 10, 1976.

2-10 D. R. Ausherman, E. I. Alber and E. Baum, "Acoustic Suppression in Pulsed Chemical Lasers," Reprint No. 78-237, AIAA 16th Aerospace Sciences Meeting, Huntsville, Al., Jan. 1978.

2-11 W. J. Thayer, V. R. Buonadonna and W. D. Sherman, "Pressure Wave Suppression for a Pulsed Chemical Laser," Reprint 78-1216, AIAA 11th Fluid and Plasma Dynamics Conference, Seattle, Wash., July 1978.

2-12 H. D. Hogge and S. C. Crow, "Flow Design Concepts for High-Power Pulsed Visible-Wavelength Lasers," Poseidon Research Report No. 16, Poseidon Research, Los Angeles, Ca., May 1978.

2-13 K. O. Tong, C. J. Knight and B. N. Srivastava, "Pressure Wave Attenuation in Mufflers with Finite Backing Volume," Reprint No. 76.0602, AIAA 5th Aeroacoustics Conference, Seattle, Wash., March 1979.

2-14 E. E. Stark, Jr., Los Alamos Scientific Laboratory, Private Communication.

2-15 W. T. Leland and M, Kircher, "The Relation of CO_2 Discharge Kinetics to the Efficiency of Short Pulse Amplifiers," Los Alamos Scientific Laboratory Report LA-UR-74-637, 1974.

2-16 J. R. Murray, J. Goldhar and A. Szoke, Appl. Phys. Lett., 32, 551 (1978); and J. R. Murray, J. Goldhar, D. Eimerl and A. Szoke, Appl. Phys. Lett. 33, 339 (1978).

2-17 R. Kung, S. Mani, R. Schaefer and M. Sirchis, "Assessment of Pulse Compressed KrF Lasers as Fusion Drivers," W. J. Schafer Assoc., Report WJAS-78-6-TR1, Nov. 1978.

2-18 (a) J. R. Murray, "Backward Raman Pulse Compressor."
(b) R. A. Haas, "Analytical Assessment of KrF-Raman Compressor Laser System."
(c) J. J. Ewing, "Pulse Compressor Scaling Issues and the Lawrence Livermore Lab Rapier Programs."

Papers presented at the DoE Division of Laser Fusion Workshop on Applications of Rare Gas Halides, and Compiled by W. J. Schafer Assoc., Report WJAS-76-6-SR2, (Sept. 19, 1978).

2-19 E. E. Stark, Jr., "Lasers and Power Systems for Inertial Confinement Fusion Reactors," ANS 3rd Topical Meeting on Fusion Technology, Sante Fe, N.M., May 1978.

2-20 Dryden, H. L., and Abbott, I. H., The Design of Low Turbulence Wind Tunnels, NACA Report 940, 1949.

3-1 E.W.R. Steacie, Atomic and Free Radical Reactions, Reinhold Publishing Corp., New York, 1954, pp. 672-674.

3-2 J. G. Calvert and J. N. Pitts, Photochemistry, John Wiley and Sons, New York, 1966, p. 184.

3-3 D. J. Stevens and L. D. Spicer, "Kinetics and Mechanism of Recoil Chlorine Atom Reactions with Ethylene," J. Phys. Chem., Vol. 81, pp. 1217-1222, 1977.

3-4 N. Cohen and J. F. Bott, "Kinetics of Hydrogen-Halide Chemical Lasers," in Handbook of Chemical Lasers, R.W.F. Gross and J. F. Bott, eds., John Wiley and Sons, New York, 1976, pp. 49-53.

3-5 R. Goldstein, F. N. Mastrup and W. L. Shackleford, Ablating Wall Annular Flash Lamp, TRW Systems Report Nos. AFWL-TR-66-15 and AFWL-TR-67-32 for Wright-Patterson Air Force Base, 1966-67.

3-6 Boris, J. P., and Book D. L., "Flux-Corrected Transport - I. SHASTA, A Fluid Transport Algorithm that Works." Journal of Computational Physics, Vol. II, No. 1, Jan 1973, pp. 38-69.

3-7 Book, D. L., Boris, J. P., and Hain, K., "Generalizations of the Flux-Corrected Transport Technique," Naval Research Laboratory, Washington, D.C., NRL Memorandum Rept. No. 3021, April 1975.

3-8 Szumowski, Andrzej P., "Discharge Coefficients for Air Outflow Through a Single Orifice in the Wall of a Tube," Archiwum Budowy Maszyn, Tom XIX, Zeszyt 4, 1972 (Archive of Mechanical Engineering, Vol. 19, No. 4, 1972).

3-9 Szumowski, Andry P., "Motion of a Shock Wave Along a Uniform Perforated Duct," Prace Naukowe Politechniki Warstawskiej, No. 18, Mechanika, 1973.

3-10 Rogers, T. and Hersh, A. S., "Effect of Grazing Flow on the Steady-State Resistance of Sqaure Edged Orifices," Paper 75-493, AIAA 2nd Aero-Acoustics Conference, Hampton, Va., March 24-26, 1975. Also Available in: Aeroacoustics: Fan Noise and Control; Duct Analysis; Roter Noise, Vol. 44, Progress in Astronautics and Aeronautics, AIAA/MIT Press. 1975.

3-11 Stokes, George, M., Daves, Jr., Don D., and Sellars, Thomas B., "An Experimental Study of Porisity Characteristics of Perforated Materials in Normal and Parallel Flow," NACA TN 3085, April 1954.

3-12 Perry, Jr., J. A., "Critical Flow Through Sharp-Edged Orifices," Transactions of the ASME, Paper No. 48-A-146, October 1949.

3-13 Rudinger, George, "The Reflection of Pressure Waves of Finite Amplitude from an Open End of a Duct," Journal of Fluid Mechanics, Vol. 3, Part 1, October 1957.

3-14 Progelhof, R. C., and Owczarek, J. A., "The Rapid Discharge of a Gas from a Cylindrical Vessel Through an Orifice," ASME Paper 63-WA-10, Philadelphia Mtg., 1963.

3-15 Anon., "Friction Losses for Fully Developed Flow in Straight Pipes," Engineering Sciences Data, Item 66027, September 1966.

3-16 Kays, W. M., Convective Heat and Mass Transfer, McGraw-Hill, 1966.

A-1 Whitham, G. B., Linear and Nonlinear Waves, Wiley-Interscience (1974).

A-2 Friedlander, F. G., Sound Pulses, Cambridge Univ. Press (1958).